Novel Phosphorus Precursors to Group III-V Semiconductor Nanoparticles



Jack Howley

The Queen's College

University of Oxford

A thesis submitted for the degree of

Doctor of Philosophy

Trinity 2023

Abstract

Novel Phosphorus Precursors to Group III-V Semiconductor Nanoparticles

Jack Howley — The Queen's College

DPhil Inorganic Chemistry for Future Manufacturing — Trinity 2023

The development of novel phosphorus precursors to group III-V semiconductor nanoparticles is described in this thesis. An overview of semiconductor nanoparticles, colloquially referred to as quantum dots (QDs), is presented in **Chapter 1**, including strategies for the preparation of InP QDs from typical phosphorus precursors.

Chapter 2 explores the reactivity of the parent phosphinecarboxamide ($H_2PC(O)NH_2$) in solution towards common InP QD precursors. The preparation of InP clusters and a novel *N*-functionalised phosphinecarboxamide using $H_2PC(O)NH_2$ is discussed. Both $H_2PC(O)NH_2$ and *N*-functionalised phosphinecarboxamides are found to be effective sources of PH_3 in solution upon thermal decomposition in pyridine at 105 ºC.

Chapter 3 describes the use of an *N*-functionalised phosphinecarboxamide as a novel air-stable phosphorus precursor to core/shell In(Zn)P/ZnS QDs. A synthetic protocol is optimised to afford core/shell In(Zn)P/ZnS QDs with size-dependant photoluminescence emission maxima between 550 and 650 nm, with full width at half maxima (FWHM) between 68 and 128 nm.

Chapter 4 explores the reactivity of *N*-, *N*,*N*-, and *P*-functionalised phosphine-carboxamides in solution. The effect of phosphinecarboxamide side-chain functionalisation on reactivity is also discussed.

Finally, **Chapter 5** discusses the use of functionalised phosphinecarboxamides for the preparation of In(Zn)P/ZnS QDs and the unique size control that they afford. Carboxylate functionalised phosphinecarboxamides are used to prepare core/shell In(Zn)P/ZnS QDs with size-dependant photoluminescence emission maxima between 550 and 620 nm and FWHM between 83 and 114 nm. Additionally, the unexpected use of a *P*-functionalised phosphinecarboxamide as an air-stable precursor to size-uniform InP QDs is described, which display a photoluminescence maximum at 546 nm and a FWHM of 75 nm.

Acknowledgements

It is surreal to be writing this and I would like to take the opportunity to recognise the countless colleagues, peers, friends, and family who have all supported and contributed to this body of work. Firstly, I would like to thank my two supervisors: Professor Jose Goicoechea and Professor Jason Davis, for their encouragement and motivation as we ventured into a new area of chemistry together. I could not be happier, nor prouder, with how the project has progressed and what we have accomplished together, none of which would be possible without their mentorship, support and enthusiasm.

This recognition extends to the members of both research groups that I have been so privileged to be a part of. I would first like to thank Eric, my OxICFM CDT brother. Whether it's demonstrating, crafting bespoke lab playlists, going to the pub, or even founding a new spectroscopy centre together, his friendship and support has made my DPhil that much more enjoyable. I am grateful for Joey, Olie, Steven, Stephanie, Josh, Doruk, Aaron, Matt, Chenyang, Alex, and Lili for creating a fun and positive lab environment, embracing all of my monstrous playlists ideas, and for their company during coffee, lunch, and pub trips together. I owe an extra thanks to Matt and Lili for their help proof-reading my thesis – that's seven (at least) ciders on me. Also, to my Part II student, Sasha Bai, for her contribution to this work and the effort she put into embracing such a quirky new project. To the Davis group, in particular: Robert, Xuanxiao, Mohamed, Connor, Daohe, Felix, and Sophie, who have helped me navigate the world of nanomaterials through all of the time and effort they so selflessly gave me.

This project has also thrived through the support and contribution of colleagues beyond the research groups to which I belong. I would like to thank Amber Thompson, Nick

Rees, Neil Young, Ian Griffiths, Alex Evans, and the team at ePSIC for all of their help and guidance with the assortment of analytical techniques employed in this thesis.

I am grateful for the new friends I have made during my time in Oxford: to the students and staff on the OxICFM CDT, my friends at Queen's, in the Aldridge group, colleagues at OUI, and to Billy and Takvor. Thanks to everyone for the well needed distractions from chemistry. I am also appreciative of Leigh Rees for his mentorship during my time at OUI, for creating a formative experience which has propelled me onto the next stage of my career.

I would not be here without my family, who have championed me throughout my life, supported and encouraged me while living away from home, and who have acted just interested enough in chemistry to be believable. I would like to thank my Mum and Dad, my brothers, my aunts, uncles, and grandparents for everything they have done for me and our family.

Most importantly, to my wife, Hannah. Hannah is the one person without which none of this would be possible. Thank you for your love, kindness, enthusiasm and unwavering belief in me. You have been my inspiration and my aspiration, showing me that hard work and the ability to laugh at life is really all there is to it. Thank you, Hannah, for always making me smile from my liver.

List of abbreviations

°C	-	degrees Celsius
a_0	-	exciton Bohr radius (nm)
acac	-	acetylacetonate
ALD	-	atomic layer deposition
BDE	-	bond dissociation energy
Bn	-	benzyl
b.p.	-	boiling point
Bu	-	butyl
CB	-	conduction band
CVD	-	chemical vapour deposition
Da	-	Dalton (1 Da = 1 g/mol)
DOS	-	density of states
DTC	-	dithiocarbamates
ε	-	permittivity of free space
e	-	elementary charge
E_{bulk}	-	band gap energy of bulk material
EDX	-	energy dispersive X-ray spectroscopy
E_g	-	band gap energy
h	-	Plank's constant
HDA	-	hexadecylamine
HRTEM	-	high-resolution transmission electron microscopy
ICP-MS	-	inductively coupled plasma mass spectrometry
IR	-	infrared
KHMDS	-	potassium bis(trimethylsilyl)amide
LED	-	light emitting diode
MA	-	myristic acid
MALDI-TOF	-	matrix-assisted laser desorption/ionization time of flight
Me	-	methyl
m_e	-	effective mass of electron
m_h	-	effective mass of hole

MOVD	-	metal organic vapour deposition
m.p.	-	melting point
MS	-	mass spectrometry
MSC	-	magic-sized cluster
My	-	myristate
nm	-	nanometre
NMR	-	nuclear magnetic resonance
OA	-	oleate
OAc	-	acetate
OAm	-	oleylamine
ODE	-	1-octadecene
Pa	-	palmitate
Ph	-	phenyl
PL	-	photoluminescence
PLQY	-	photoluminescence quantum yield (%)
PXRD	-	powder X-ray diffraction
QD	-	quantum dot
r	-	particle size (nm)
SA	-	stearic acid
ST	-	stearate
STEM	-	scanning transmission electron microscopy
^{t}Bu	-	*tert*-butyl
TEM	-	transmission electron microscopy
THF	-	tetrahydrofuran
TMS	-	trimethylsilylphosphine
TOP	-	tri-*n*-octylphosphine
TOPO	-	tri-*n*-octylphosphine oxide
UV	-	ultraviolet
UV-Vis	-	ultraviolet-visible
VB	-	valence band
ZDEC	-	zinc diethyldithiocarbamate

Contents

1 Introduction 1

1.1 Semiconductors 2

1.2 Quantum confinement effects on semiconductors 3

1.2.1 Energy level quantization 5

1.2.2 Size-dependence of band gap energy 6

1.2.3 Effect of quantum confinement on the optical properties of quantum dots 8

1.3 Colloidal quantum dots 8

1.3.1 Effect of QD size inhomogeneity on optical spectra 8

1.3.2 Synthesis of monodisperse colloidal quantum dots 9

1.3.3 Thermal decomposition strategies 13

1.3.4 Role of capping ligands 14

1.3.5 Evaluating the monodispersity of colloidal QDs 18

1.4 Indium phosphide quantum dots 19

1.4.1 Bulk indium phosphide 19

1.4.2 Synthesis of near-monodisperse InP QDs 20

1.4.3 Surface passivation of InP QDs 23

1.4.4 Heteroepitaxial shell growth on InP QDs 25

1.4.5 Development of phosphorus precursors to InP QDs 29

1.5 Phosphinecarboxamides 35

1.5.1 Synthesis of urea 35

1.5.2 The parent phosphinecarboxamide 35

1.5.3 Functionalised phosphinecarboxamides 37

1.5.4 Phosphinecarboxamides as phosphorus precursors to inorganic materials 40

1.6 Project aims 41

1.7 References 42

2 Reactivity of phosphinecarboxamide in solution 53

2.1 Introduction and objectives 54

2.1.1 PH_3 generation in solution 54

2.1.2 PH_3 as a precursor to colloidal metal phosphide nanoparticles 55

2.1.3 Phosphinecarboxamide as an *in situ* PH_3 source 56

2.1.4 Chapter outline 57

2.2 Reactions of phosphinecarboxamide in solution 58

2.2.1 Thermal decomposition of phosphinecarboxamide 58

2.2.2 Reaction of phosphinecarboxamide with indium salts 60

2.2.2.1 Synthesis and characterisation of phenylacetate-capped InP MSCs 61

2.2.2.2 Synthesis and characterisation of myristate-capped InP MSCs 67

2.2.3 Reaction of phosphinecarboxamide with hexadecylamine 69

2.3 *N*-hexadecylphosphinecarboxamide (**1**) 73

2.3.1 Synthesis of **1** 73

2.3.2 Characterisation of **1** 73

2.3.3 Thermal decomposition of **1** 76

2.3.4 Air stability of **1** 81

2.4 Conclusions 82

2.5 References 84

3 Synthesis and characterisation of InP quantum dots prepared from phosphinecarboxamides 87

3.1 Introduction and objectives 88

3.1.1 Conditions for InP QD syntheses 88

3.1.2 Chapter outline 90

3.2 Preparation of In(Zn)P QDs from **1** 91

3.2.1 Synthesis and purification of In(Zn)P QDs 91

3.2.2 Characterisation of In(Zn)P QDs 92

3.2.3 Reaction duration optimisation 95

3.2.3.1 Varying reaction duration at 220 °C 95
3.2.3.2 Varying reaction duration at 120 °C 97
3.3 Preparation of core/shell In(Zn)P/ZnS QDs from **1** 98
3.3.1 Synthesis and purification of core/shell In(Zn)P/ZnS QDs from **1** 101
3.3.2 Characterisation of In(Zn)P/ZnS QDs 101
3.3.3 Reaction duration optimisation at 220 °C 105
3.3.4 Reproducibility evaluation 107
3.4 Preparation of In(Zn)P/ZnS QDs from **1** exposed to air 108
3.4.1 Synthesis of In(Zn)P/ZnS QDs 108
3.4.2 Characterisation In(Zn)P/ZnS QDs 109
3.4.3 Oxidation of **1** 111
3.5 Preparation of TOP-capped InP/ZnS QDs from **1** 113
3.5.1 TOP-capped InP QDs 114
3.5.1.1 Synthesis of TOP-capped InP QDs 114
3.5.1.2 Characterisation of TOP-capped InP QDs 114
3.5.2 TOP-capped core/shell InP/ZnS QDs 116
3.5.2.1 Synthesis of TOP-capped InP/ZnS QDs 116
3.5.2.2 Characterisation of TOP-capped InP/ZnS QDs 117
3.6 Preparation of In(Zn)P QDs using phenylacetate-capped InP MSCs 120
3.6.1 Thermal decomposition of InP MSCs prepared from $H_2PC(O)NH_2$ 120
3.6.2 Preparation of In(Zn)P QDs from phenylacetate-capped InP MSCs 121
3.6.3 Effect of zinc doping on photoluminescence spectra 124
3.7 Conclusions 125
3.8 References 126
4 Reactivity of functionalised phosphinecarboxamides in solution 129
4.1 Introduction and objectives 130
4.1.1 Functionalised phosphinecarboxamides 130
4.1.2 Chapter outline 131

4.2 Synthesis and reactivity of carboxylate-functionalised phosphinecarboxamides 132
4.2.1 Synthesis and characterisation 133
4.2.1.1 Characterisation of **2** 134
4.2.1.2 Characterisation of **3** 137
4.2.2 Thermal decomposition of **2**, **4**, and **5** 138
4.2.3 Transamidation of **2** 141
4.3 Synthesis and reactivity of carboxylic acid-functionalised phosphinecarboxamides ... 143
4.3.1 Synthesis and characterisation 144
4.3.2 Thermal decomposition of **6**, **7**, and **8** 146
4.3.3 Transamidation of **6** 148
4.4 Reactivity of difunctionalised phosphinecarboxamides 149
4.4.1 *N*,*N*-functionalised phosphinecarboxamide 149
4.4.1.1 Thermal decomposition of L-proline-phosphinecarboxamide 151
4.4.1.2 Transamidation of L-proline-phosphinecarboxamide 153
4.4.2 *P*-functionalised phosphinecarboxamide 154
4.4.2.1 Thermal decomposition *P*-benzyl-*N*-cyclohexyl-phosphinecarboxamide 155
4.4.2.2 Transamidation of *P*-benzyl-*N*-cyclohexyl-phosphinecarboxamide 157
4.5 Conclusions 159
4.6 References 160
5 Synthesis and characterisation of InP quantum dots prepared from functionalised phosphinecarboxamides 162
5.1 Introduction and objectives 163
5.1.1 Controlling InP QD growth 163
5.1.2 Influence of phosphorus precursors on QD growth 164
5.1.3 Chapter outline 165
5.2 Preparation of In(Zn)P/ZnS QDs using carboxyl-functionalised phosphine-…….. carboxamides 166
5.2.1 Carboxylate-functionalised phosphinecarboxamides 166

5.2.1.1 Preparation of In(Zn)P/ZnS QDs from **2**–**5** 166
5.2.1.2 Exploring the origin of size control 170
5.2.2 Carboxylic acid-functionalised phosphinecarboxamides 179
5.2.3 Preparation of In(Zn)P/ZnS QDs from L-proline-phosphinecarboxamide 183
5.3 Preparation of In(Zn)P/ZnS QDs using *P*-functionalised phosphinecarboxamides 187
5.3.1 Preparation of In(Zn)P/ZnS QDs from *P*-benzyl-*N*-cyclohexyl-phosphinecarboxamide 187
5.3.2 Air stability of *P*-benzyl-*N*-cyclohexyl-phosphinecarboxamide 192
5.3.3 Synthesis and reactivity of *P*,*P*-benzyl-*N*-cyclohexyl-phosphinecarboxamide 195
5.4 Conclusions 198
5.5 References 199
6 Concluding remarks and future work 202
6.1 Conclusions 203
6.2 Future work 205
6.2.1 Understanding and evaluating the QD size control effect 205
6.2.2 Towards monodisperse InP QDs 206
6.3 References 208
7 Experimental 209
7.1 General synthetic considerations 210
7.2 Synthesis methods 213
7.2.1 Chapter 2 – Reactivity of phosphinecarboxamides in solution 213
7.2.1.1 Thermal decomposition studies 213
7.2.1.2 Synthesis of phenylacetate-capped InP magic-sized clusters 213
7.2.1.3 Synthesis of myristate-capped InP magic-sized clusters 213
7.2.1.4 Synthesis of **1** by transamidation of phosphinecarboxamide with hexadecylamine 214
7.2.1.5 Synthesis of **1** 214

7.2.2 Chapter 3 – Synthesis and characterisation of InP quantum dots prepared ..... from phosphinecarboxamides 215
7.2.2.1 Synthesis of In(Zn)P QDs from **1** 215
7.2.2.2 Synthesis of In(Zn)P/ZnS QDs from **1** 215
7.2.2.3 Synthesis of oleylamine-capped In(Zn)P/ZnS QDs from **1** 215
7.2.2.4 Oxidation of **1** by H_2O_2 216
7.2.2.5 Synthesis of TOP-capped InP QDs from **1** 216
7.2.2.6 Synthesis of TOP-capped InP/ZnS QDs from **1** 216
7.2.2.7 Synthesis of In(Zn)P QDs from phenylacetate-capped InP MSCs 217
7.2.2.8 Purification of QDs by precipitation and resuspension 217
7.2.2.9 Purification of QDs by size-exclusion chromatography 217
7.2.3 Chapter 4 – Reactivity of functionalised phosphinecarboxamides in solution 218
7.2.3.1 Synthesis of **2** 218
7.2.3.2 Synthesis of **3** 219
7.2.3.3 Synthesis of **4** 220
7.2.3.4 Synthesis of **5** 220
7.2.3.5 Synthesis of **6** 221
7.2.3.6 Synthesis of **7** 222
7.2.3.7 Synthesis of **8** 223
7.2.3.8 Thermal decomposition studies 223
7.2.3.9 Transamidation studies 224
7.2.4 Chapter 5 – Synthesis and characterisation of InP quantum dots prepared ..... from functionalised phosphinecarboxamides 224
7.2.4.1 Synthesis of In(Zn)P/ZnS QDs from carboxylate-functionalised…… phosphinecarboxamides **2**–**4** 224
7.2.4.2 Synthesis of In(Zn)P/ZnS QDs by varying ratio of **1** and **4** 225
7.2.4.3 Synthesis of In(Zn)P/ZnS QDs from **1** and L-phenylalanine sodium salt 225
7.2.4.4 Synthesis of In(Zn)P/ZnS QDs from **7** 225

7.2.4.5 Synthesis of In(Zn)P/ZnS QDs from *P*-benzyl-*N*-cyclohexyl-phosphinecarboxamide 226
7.2.4.6 Synthesis of **9** 226
7.3 Characterisation techniques 227
7.3.1 NMR spectroscopy 227
7.3.2 UV-Vis and photoluminescence spectroscopy 227
7.3.3 Photoluminescence quantum yield (PLQY) 228
7.3.4 Mass spectrometry 228
7.3.5 Powder X-ray diffraction 229
7.3.6 Transmission electron microscopy 229
7.3.7 Elemental analyses 230
7.3.8 IR Spectroscopy 230
7.4 References 230

Chapter 1

Introduction

1.1 Semiconductors

Semiconductors are materials characteristically defined by their intermediate electrical conductivity, which at room temperature, typically resides between that of a conductor and an insulator. Semiconductors can be made to conduct by the excitation of electrons from the filled valence band to the empty conduction band.[1] The relatively low energy difference between the valence and conduction bands in semiconductors (band gap energy, E_g) allows excitation to be achieved by heating or irradiation with light.

The defining characteristics of semiconductors are exemplified in some of the earliest reports investigating them. In 1821, Thomas Seebeck observed 'thermomagnetism' properties (magnetic field generation upon heating) held by a variety of semiconductive minerals. This phenomenon was later attributed to the magnetic field induced by the thermoelectric current generated through the semiconductors upon heating.[2,3] Michael Faraday soon corroborated these findings, reporting that electrical conductivity increased when heating silver sulfide.[4] Faraday highlighted the perplexing conductivity gain observed upon heating AgS, in contrast to the conductivity decrease observed in metallic samples, commenting: "*there is no other body with which I am acquainted [which bear these properties]".* Shortly after in 1839, Edmond Becquerel reported the use of light to induce electrical conductivity in semiconductors – the first demonstration of the photovoltaic effect. Becquerel showed that an electrical current could be generated by the UV irradiation of AgCl or AgBr coated Pt electrodes connected in an electrochemical cell.[5]

Over 200 years since Seebeck's observation of thermomagnetism, semiconductors are now ubiquitous and ever-present in day-to-day life. The ability to control electrical

conductivity by external stimulation has defined the utility of semiconductors in modern technology. Semiconductors can be found in integrated chips, diodes, transistors, LEDs and photovoltaics. These are widely used in technologies such as computers, mobile phones, displays, and solar cells.[6,7]

Crystalline silicon is the most well-known semiconductor material on Earth, without which, modern information and communication technologies would not exist in their current form.[8] Other common semiconductor materials include group IV (Ge, SiC),[9] III-V (GaP, InP, InAs),[10] II-VI (CdSe, ZnO),[11] and IV-VI (PbSe, SnTe).[12]

The utility of semiconductors in modern technologies is a result of decades of successful development of their electronic properties through material design (e.g. composition, doping, structure). With the emergence of the 'internet of things' – the increasing number and interconnectivity of electronic devices – there remains the need for continuous exploration and development of semiconductor materials.[13]

1.2 Quantum confinement effects on semiconductors

When an electron in a semiconductor is excited from the valence band (VB) to the conduction band (CB), a positive hole is also created in the valence band. The electron and hole are attracted to one another through Coulomb interactions, and thus remain bound. The bound pair are referred to as an exciton and can be treated as a quasiparticle.

The average separation of charges in the exciton is defined as the exciton Bohr radius, a_0. Exciton Bohr radii range in the order of magnitude of tens of nanometres and can be calculated according to Equation 1.1, where h is Plank's constant, ε is the permittivity of

free space, e is the elementary charge, and m_e and m_h are the effective masses of the electron and hole, respectively.[14]

$$a_0 = \frac{h^2 \varepsilon}{4\pi e^2}\left(\frac{1}{m_e} + \frac{1}{m_h}\right) \qquad (1.1)$$

As shown, a_0 depends on the effective masses of the electron and hole, and hence the value is highly material dependant. Table 1.1 details some common semiconductors and their associated exciton Bohr radii.

Table 1.1: Band gap energies and exciton Bohr radii of common semiconductor materials.[14–16]

Type	Material	Energy gap (eV)	Bohr radius (nm)
II-IV	CdS	2.49	5.8
	CdSe	1.74	4.6
	CdTe	1.43	7.3
III-V	GaN	3.44	2.8
	GaAs	1.42	11.5
	InP	1.34	10
	InAs	0.35	34
IV-VI	PbS	0.41	18
	PbSe	0.28	46

When the size of a semiconductor nanocrystal (r) approaches that of the exciton Bohr radius ($r \approx a_0$), the exciton becomes spatially confined.[17] This effect is called quantum confinement, and results in a size-dependent change of the density of electronic states and the band gap energy, as the exciton must 'fit' into the spatially-confined nanocrystal.[18] This 'fit' is modelled theoretically using a quantum mechanical particle-in-a-box model.[19]

Structural changes to the crystal lattice have profound implications on the electronic structure of semiconductors. As a result of the divergence in electronic structure due to

spatial confinement, semiconductor nanocrystals have uniquely distinct optical properties compared to the bulk phase material.

1.2.1 Energy level quantization

Spatial confinement of semiconductor nanostructures induce changes in the density of electronic states (DOS).[20] As it is possible for nanostructures to be spatially confined in one dimension but not another, the dimensionality of a nanocrystal influences its electronic structure.

Figure 1.1 shows nanostructures with 0D, 1D, 2D, and 3D dimensionality and their associated density of states. For 3D particles (no spatial confinement), the density of states resembles that of a bulk semiconductor, with a greater density of electronic states towards the middle of the band. For 2D nanoparticles, where one of the dimensions is spatially confined, the DOS increases in quantized steps. These nanoparticles are referred to as quantum wells, and examples include GaN nanosheets used in LEDs and semiconductor lasers.[21] In 1D nanoparticles, where two spatial dimensions are confined, the DOS falls rapidly between the quantized steps as the exciton can only travel along one axis. These structures are referred to as quantum wires, with carbon nanotubes the most recognizable example.[22] 0D nanoparticles are spatially confined in all three dimensions, and display quantization of the DOS into discrete, atomic-like energy levels at the band edge. 0D nanoparticles are referred to as quantum dots (QDs),[23] owing to their dimensionless, quantum confined character, and include examples such as CdSe, InP, and PbS.[24]

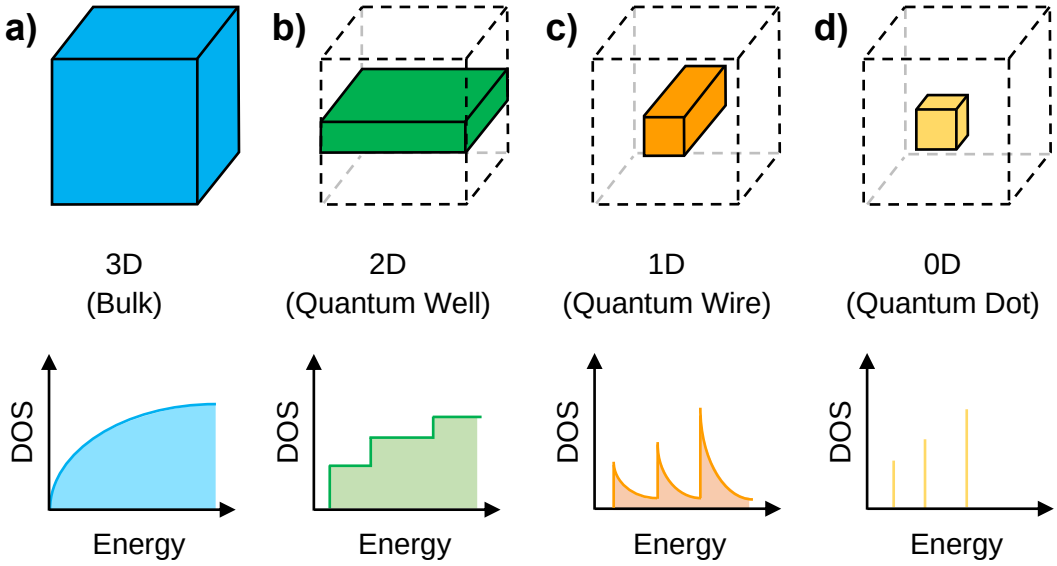


Figure 1.1: Idealised representation of the effect of dimensional confinement on the density of states in: a) 3D; b) 2D; c) 1D; and d) 0D nanostructures.

1.2.2 Size-dependence of band gap energy

In addition to changing the density of electronic states, quantum confinement affects the band gap energy in semiconductors. The quantum confinement effect in semiconductor nanocrystals was first reported by Efros and Ekimov. While investigating CuCl nanocrystals in a glass matrix, Ekimov found that the exciton absorption lines shifted to shorter wavelengths when the crystal size was decreased.[25] Ekimov attributed this to the 'quantum size effect', highlighting the inverse square dependency of crystal size on the exciton binding energy ($E \propto 1/r^2$). In a supporting report, Efros rationalised the onset of quantum confinement in CuCl nanocrystals relative to the exciton Bohr radius.[26] Efros showed that when the nanocrystals were smaller than the exciton Bohr radius ($r << a_0$), the nanocrystals were in a strong quantum confinement regime, with blue-shifted absorption energy consistent with an increase in band gap energy. But when the nanocrystals were larger the exciton Bohr radius ($r >> a_0$), the optical properties aligned more closely to those of the bulk material.

Brus later expanded on these results, devising an equation to calculate the band gap energy of quantum confined spherical semiconductor nanocrystals (QDs) (Equation 1.2).[27]

$$\Delta E_{QD} = \Delta E_{bulk} + \left(\frac{h^2}{8r^2}\right)\left(\frac{1}{m_e} + \frac{1}{m_h}\right) \qquad (1.2)$$

Where ΔE_{bulk} is the band gap energy of the bulk solid, h is Plank's constant, r is the nanocrystal diameter, and m_e and m_h are the effective masses of the electron and hole, respectively. The Brus equation contains a term denoting the band gap energy of the bulk semiconductor and a second term representing the additional energy due to quantum confinement. Physically, this corresponds to smaller QDs experience greater spatial confinement, resulting in a larger band gap energy and blue-shifted excitonic absorption and emission (Figure 1.2).

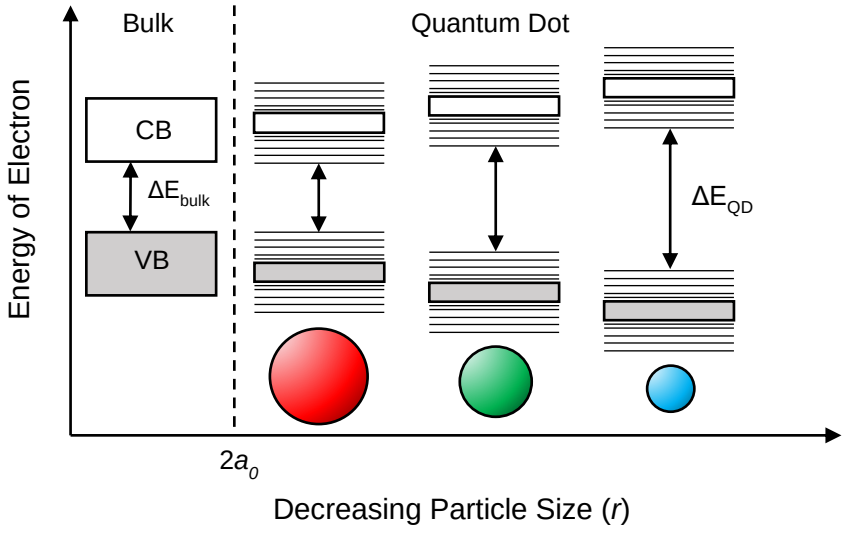


Figure 1.2: Quantum confinement effect on the electronic structure of a bulk semiconductor (left) and quantum dots (right).

1.2.3 Effect of quantum confinement on the optical properties of quantum dots

In QDs, spatial confinement occurs for nanoparticles approximately twice the size of the exciton Bohr radius of a semiconductor material ($r \lesssim 2a_0$).[19] The quantum confinement effect on 0D QDs gives rise to unique, size-dependant optical properties. The resolution of the electronic structure into quantized energy levels results in highly specific absorption and emission, whilst the size-dependence of the band gap energy allows these profiles to be controlled independent of semiconductor composition.

1.3 Colloidal quantum dots

1.3.1 Effect of QD size inhomogeneity on optical spectra

The optical spectra of a QD sample represents the sum of all optically-contributing species present. Owing to the size-dependence on the electronic structure of QDs, each distinct QD size present in a sample will contribute differently.[28] Therefore the optical spectra of a QD sample represents the ensemble of all QD sizes present.

Take for example a sample of QDs of size A which also contain an equal amount of QDs of size B. If the particle size of size B > size A, then the absorption peak of QDs of size A will be blue-shifted relative to size B, due to increased quantum confinement. The resulting absorption spectrum of the sample will be the sum of both respective absorption profiles, smoothing out the two otherwise discrete peaks (Figure 1.3).

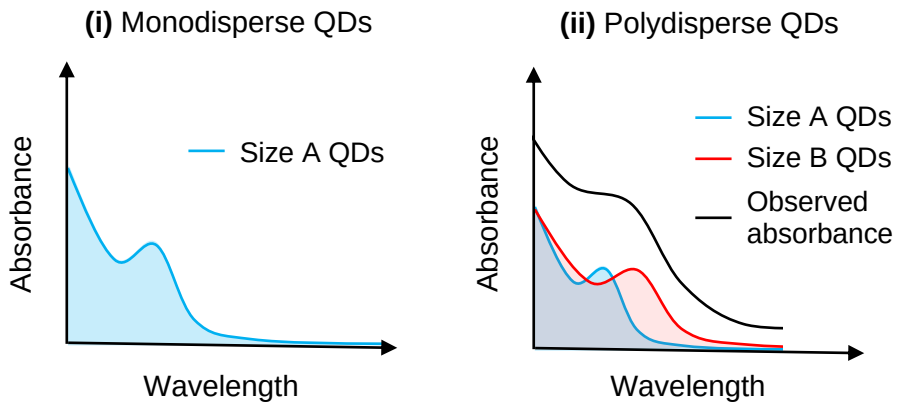


Figure 1.3: Idealised absorption spectra of: (i) monodisperse QDs; (ii) polydisperse QDs composed of two discrete size ensembles, where QD particle size B > A.

The optical quality of a QD sample is generally evaluated by the relative degree of homogeneity in particle size (monodispersity). Due to the intrinsic size-dependence on QD optical spectra, monodispersity is as important as compositional purity in defining their optical characteristics.

1.3.2 Synthesis of monodisperse colloidal quantum dots

Despite the pioneering work of Ekimov, Efros, and Brus in the 1980s, the preparation of QDs by matrix isolation offered minimal size control, resulting in polydisperse QDs. This lack of size control motivated the exploration of new solution phase, colloidal approaches to prepare QDs.[29]

Nanocrystals (NCs) are understood to grow in solution in three stages: (I) solvation of reactive species, (II) nucleation of nanocrystals, and (III) controlled growth of the nuclei to a specific size (Figure 1.4).[30]

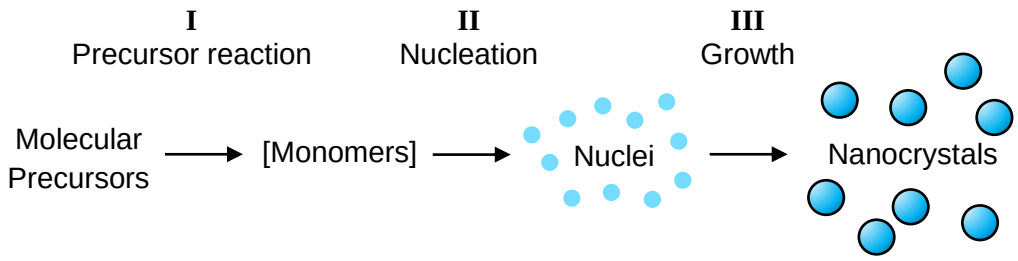


Figure 1.4: Stages of crystallization process: (I) reaction of molecular precursors to form solvated reactive monomers; (II) nucleation of NCs; (III) controlled growth of NCs from nuclei to a specific size.[30]

The LaMer mechanism describes NC growth in solution, and has been applied to understand the growth of colloidal QDs.[31,32] It consists of three stages, as shown in Figure 1.5. First, the precursor monomers are rapidly concentrated in solution (I). Second, the monomers undergo burst-nucleation, as they reach the critical nucleation concentration (nucleation threshold; II).[33] Burst-nucleation results in the rapid consumption of monomers in solution, reducing their concentration below that of the nucleation threshold. Finally, following nucleation, nanocrystal growth occurs under diffusion control (III).

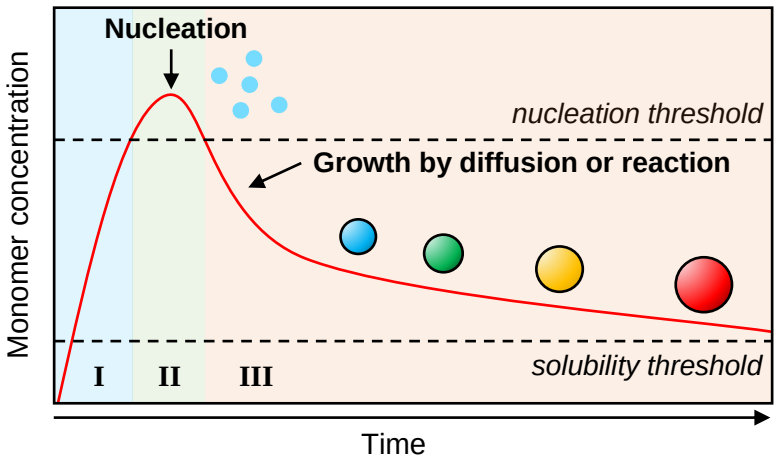
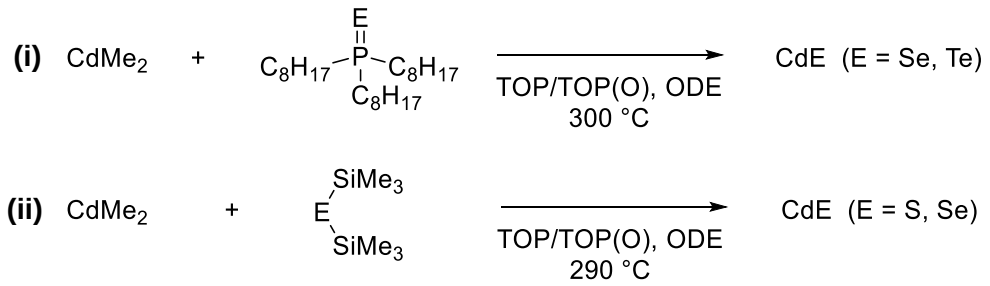


Figure 1.5: LaMer plot showing the change in monomer concentration during NC formation: (I) precursor addition and generation of reactive monomers; (II) supersaturation and nucleation of NCs; (III) diffusion-controlled growth of NCs from nuclei.[32]

It is generally accepted that the separation of nucleation (II) and growth (III) events is required for the growth of monodisperse colloidal NCs.[34] In 1950, LaMer and Dinegar demonstrated that temperature control and modification of the reaction solution could be used to resolve nucleation and growth events of colloids composed of sulphur hydrosols.[31] They found that the nucleation of sulphur hydrosols could be prevented by increasing the reaction temperature (T > 31 °C). By increasing the temperature of the solution, the solubility of sodium thiosulfate precursors increased, reducing saturation and disfavouring nucleation. This enabled them to prepare monodisperse colloidal sulphur hydrosols by exploiting a temporally discrete nucleation event (T < 29 °C), followed by controlled growth (T > 31 °C).

Inspired by LaMer and Dinegar, in 1993 Murray, Norris, and Bawendi pioneered the first surfactant-assisted preparation of near-monodisperse Cd-chalcogenide colloidal QDs (CdE, E = S, Se, Te). In this seminal report, the authors combined organometallic precursors at high temperatures in the presence of organic surfactants to control the growth of CdE QDs (Scheme 1.1).[35] This method of preparation enabled the authors to generate CdE QDs with < 5% particle size distribution, as determined by transmission electron microscopy (TEM).



Scheme 1.1: Preparation of CdE QDs (E = S, Se, Te) by reaction of $CdMe_2$ with: (i) TOP(E) (E = Se or Te); and (ii) $E(SiMe_3)_2$ (E = S or Se).[35] TOP = tri-*n*-octylphosphine, TOP(O) = tri-*n*-octylphosphine oxide, ODE = 1-octadecene.

The key to success in this case was using surfactant stabilising ligands (capping ligands) to control the growth dynamics of QD NCs at elevated temperatures. The use of trialkylphosphine(oxide) (TOP(O)) additives allowed for the temporal resolution of QD nucleation and growth events.

The TOP(O) capping ligands coordinate to the surface of CdE QDs during growth through the phosphine and phosphine oxide groups.[36] The long alkyl chain present in the surfactants presents a significant steric barrier to the addition of new material to the QD surface during growth. Consequently, energy is required to overcome this steric barrier and remove the ligand.[37,38] Bawendi and co-workers demonstrated this, showing that by varying the surfactant chain length, and hence the steric barrier on CdE QD surfaces, the QD growth temperature could be controlled. By changing the trialkylphosphine substituent from octyl to butyl, ethyl, or methyl groups, a reduction in QD growth temperature from 280 °C to 230 °C, 100 °C, and 50 °C, respectively, was found.[35] A similar decrease in growth temperature has been shown for cobalt(0) NCs by substituting trioctylphosphine capping ligands for tributylphosphine.[39] This method of slow, temperature controlled nanocrystal growth by aid of surfactants is commonly referred to as arrested precipitation.[40]

The method pioneered by Murray, Norris, and Bawendi employs the 'hot-injection' of molecular precursors to achieve temporal separation of nucleation and growth. First solutions of $CdMe_2$ and TOP(E) (E = Se or Te) in TOP were combined into a hot solution of TOP(O) capping ligands in 1-octadecene (ODE) at 300 °C (Scheme 1.1(i)). The rapid increase in reagent concentration upon addition results in abrupt supersaturation of the solution, causing burst-nucleation to occur. The nucleation event rapidly self-terminates

due to the concurrent decrease in monomer concentration upon nucleation, as well as the swift temperature decrease as cooler precursor solutions (25 °C) are added to the ODE solution (> 290 °C). It is this temporally discrete nucleation event, aided by TOP(O) capping ligands, that allows for the slow controlled growth of uniformly-sized QDs.

1.3.3 Thermal decomposition strategies

The hot-injection approach is the most popular method for preparing monodisperse colloidal QDs due to effective temporal separation of nucleation and growth events.[34] Materials generated using this method include transition metal NCs (e.g. Cu, Co),[39,41] II-VI QDs (e.g. CdSe, ZnSe), IV-VI QDs (e.g. PbS, PbSe, PbTe), III-V QDs (e.g. InP, InAs),[42] and metal halide perovskites (e.g. $CsPbX_3$, X = Cl, Br, I).[43,44]

An alternative approach is the heat-up technique, where precursors are combined in solution at lower temperatures, and then heated up to initiate nucleation. Heat-up methods are generally less effective at separating nucleation and growth events. To help resolve the events, careful selection of precursors, additives, concentrations, heating temperature and rates are required.[45] The heat-up method has been used to generate monodisperse colloidal QDs for III-V materials (e.g. GaP, InP, InAs), where high precursor reactivity can result in uncontrolled decomposition kinetics using the hot-injection method.[46–48] Heat-up is also used in the solvothermal preparation of various metal oxide NCs (e.g. CdO, CuO, MnO, NiO).[49,50]

Inert organic solvents with high boiling points are required in both hot-injection and heat-up QD synthetic procedures, as ligand-assisted QD growth commonly occurs at temperatures ranging from 200–300 °C. ODE is the most popular solvent for QD growth, as it is non-coordinating, offers a wide liquid temperature range (m.p. = 14–16 °C, b.p. =

315 °C), and is available with few impurities.[51] Other common solvents include the use of neat liquid surfactants such as trioctylphosphine or oleylamine, which may also act as capping ligands.[52,53]

1.3.4 Role of capping ligands

Capping ligands are crucial components in the preparation of monodisperse colloidal QDs. Organic capping ligands typically consist of a coordinating anchor group and a lipophilic tail (Figure 1.6). Whilst trialkylphosphines were preferred ligands for the growth of CdSe QDs,[54,55] and popularised by Murray *et al.*,[35] a variety of capping ligands are routinely used for the preparation of colloidal QDs. Common coordinating motifs include amine ($–NH_2$), thiol (–SH), phosphine ($–PR_2$), phosphonyl ($–PO(OH)_2$), and carboxyl (–COOH) groups, with lipophilic tails consisting of alkyl, olefinic (–C=C–), and aromatic substituents.[56,57]

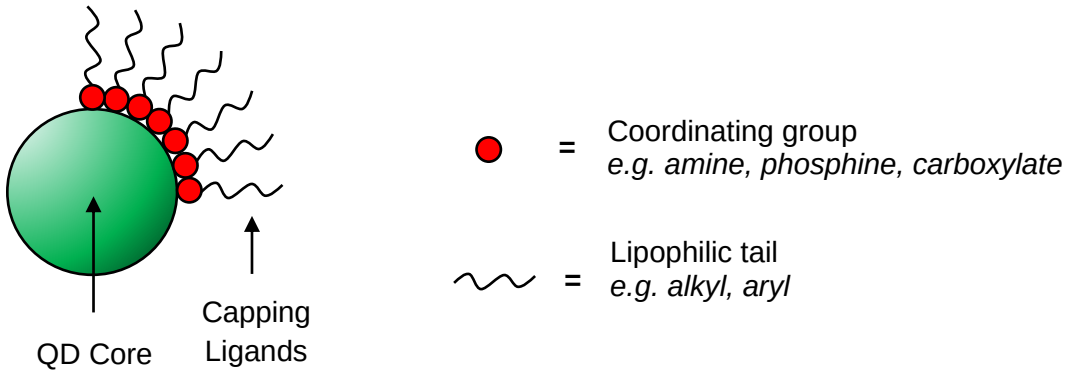
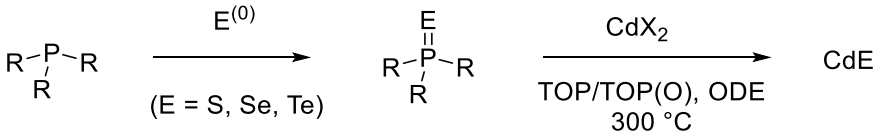


Figure 1.6: Schematic representation of a colloidal quantum dot, consisting of a semiconductor core and a surface passivated by organic capping ligands.

Inorganic precursors are often metal salts (metal halides, carboxylates, acetates, alkoxides) and insoluble in the apolar solvents used in colloidal preparations. Capping ligands solubilise these inorganic precursors through coordination of the anchoring group to the metal ions. Therefore capping ligands must be selected such that they have a high

binding affinity to the metals present. For example, thiols are common capping ligands for gold nanoparticles,[58] whilst amines and carboxyls are used for metal oxides.[57]

The chemical functionality of capping ligands can also be exploited for delivering reactive species into solution. For example, trialkylphosphines can be oxidised by elemental chalcogens to form the corresponding trialkylphosphine chalcogenides. As seen earlier, trialkylphosphine chalcogenides can then react as a chalcogenide source when heated with cadmium salts, forming CdE QDs (E = S, Se, Te; Scheme 1.2).[35,59] Carboxylate capping ligands can also be used to produce reactive oxide species. The high temperature decomposition of iron and zinc carboxylate complexes affords the corresponding metal oxide NCs Fe_3O_4 and ZnO, respectively.[60,61] Furthermore, thermolytic C–S bond cleavage within various thioalkanes allow them to act as a sulphide source in the preparation of CoPdS 'nano-acorns'.[62]



Scheme 1.2: Oxidation of trialkylphosphine by sulphur, selenium, or tellurium to form the corresponding trialkylphosphine chalcogenide, which reacts with cadmium salts to form CdE QDs (R = octyl; X = Me or (acac)).[35,59]

During NC growth, capping ligands play an important role in controlling particle morphology. For example, by varying the length of alkylphosphonic acid ligands, the elongation, length, and degree of branching in CdSe nanorods can be controlled.[63] In addition, the binding energies of ligands on different nanocrystal facets effect their relative growth rates, consequently enabling control over the geometry of the resulting nanoparticles.[64–66] For example, by varying the capping ligand used to prepare gold

nanoparticles, nanorod, nanostar, and triangular prism morphologies can be obtained.[67] The weak-affinity for the {111} facet of 4-(2-hydroxyethyl)-1-piperazineethanesulfonic acid (HEPES)[68] and poly(pyromellitic dianhydride-p-phenylenediamine) (PPDD)[69] ligands promotes growth in the [111] direction; however laurylsulfobetaine (LSB)[70] preferentially adsorbs onto {111} facets, promoting growth in the [220] and [002] directions.

Capping ligands continue to play an important role after synthesis, providing structural integrity and colloidal stability during work up. QDs are commonly purified by precipitation and washing with an anti-solvent to remove residual solvent, capping ligands, and by-products, followed by centrifugation and resuspension. Capping ligand retention on the surface of the QDs is critical for isolating the materials after purification, and solubilising the QDs in organic solvents.[71,72]

Finally, capping ligands have a drastic effect on QD photoluminescence quantum yield (PLQY) due to their ability to passivate surface trap states. Surface traps are electronic states that are contributed to the QD electronic structure by surface species. The bonding environments of typically undercoordinated surface species present in QDs are intrinsically distinct from that of core atoms, and result in poorly mixed electronic states (Figure 1.7). Surface traps reside between the valence and conduction bands and can quench excited carriers (electrons and holes) through recombination, reducing the PLQY. Electron traps originate from vacant orbitals of electron-deficient metals on the surface (e.g. Cd, In, Pb, Zn), whilst hole traps are contributed by lone-pair electrons of electron-rich species (e.g. S, Se, P, As, O).

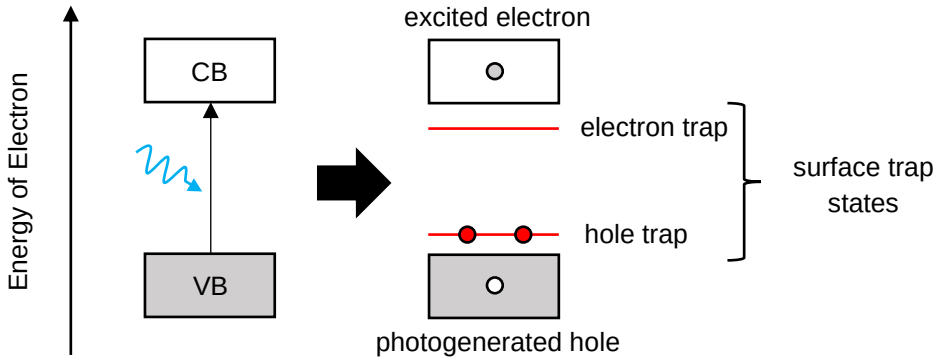


Figure 1.7: Idealised electronic structure of a QD containing mid-gap electron and hole traps, from which photogenerated carriers may recombine.

Capping ligands are used extensively to passivate surface traps. Through dative bonding and orbital mixing, capping ligands 'push' surface traps into the band gap, thus passivating their ability to quench excitonic charge carriers.

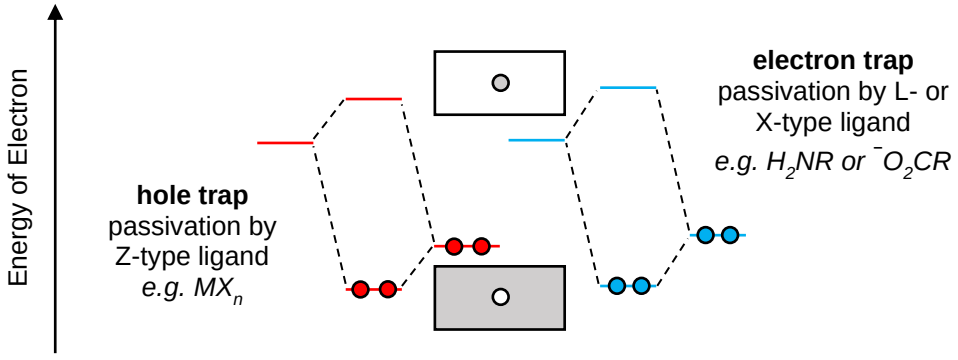


Figure 1.8: Idealised QD surface trap passivation by capping ligands. Blue: electron traps passivated by L- or X-type ligands. Red: hole traps passivated by Z-type ligands.

Electron traps are commonly passivated by Lewis basic L-type (e.g. amine, thiol, phosphine) or X-type ligands (carboxylate, phosphonate, halide; Figure 1.8). Weller and co-workers pioneered this passivation approach when they found that the use of thiol capping ligands induced significantly greater PLQY in CdTe QDs compared to native TOP ligands.[73] Meijerink *et al*. developed this further, showing that the thioalkane capping ligands could be introduced by post-synthetic ligand exchange.[74] The use of L-

and X-type capping ligands to passivate surface traps is used extensively across a variety of QD materials, including II-VI, III-V,[75] and metal halide perovskites.[76]

Conversely, hole traps can be passivated by Lewis acidic Z-type ligands. Houtepen *et al.* showed that the post-synthetic addition of $CdCl_2$ or $InCl_3$ to CdCh (Ch = Se, Te) and InP QDs results in an over 10-fold increase in PLQY.[77] Surface passivation by Z-type ligands is common for covalent QD materials such as II-VI and III-V.

1.3.5 Evaluating the monodispersity of colloidal QDs

Particle size uniformity, or monodispersity, is a critical metric when evaluating the optical purity of QDs. The degree of monodispersity of a given QD sample can be measured in a number of ways.

Particle size distributions can be obtained using transmission electron microscopy (TEM), by directly measuring the diameters of a statistically significant number of particles (> 200).[78]

Photoluminescence (PL) spectroscopy provides a rapid, but qualitative assessment of particle size dispersity. As QDs with different sizes fluoresce at different wavelengths, the full width at half maximum (FWHM) of the PL peak reflects the degree of polydispersity in a given sample. A monodisperse QD sample with uniform particle size distribution (< 5%) presents a narrow PL emission peak, with a low FWHM (Figure 1.9). In contrast, a polydisperse QD sample will be have a broader PL peak with larger FWHM due to the greater particle size distribution and their associated PL contributions (Figure 1.9). PL line broadness only provides a qualitative estimate of particle size

dispersity however, as the FWHM also varies by other factors, such as native defects within the nanocrystal,[79] surface passivation,[80] and surface interactions.[81]

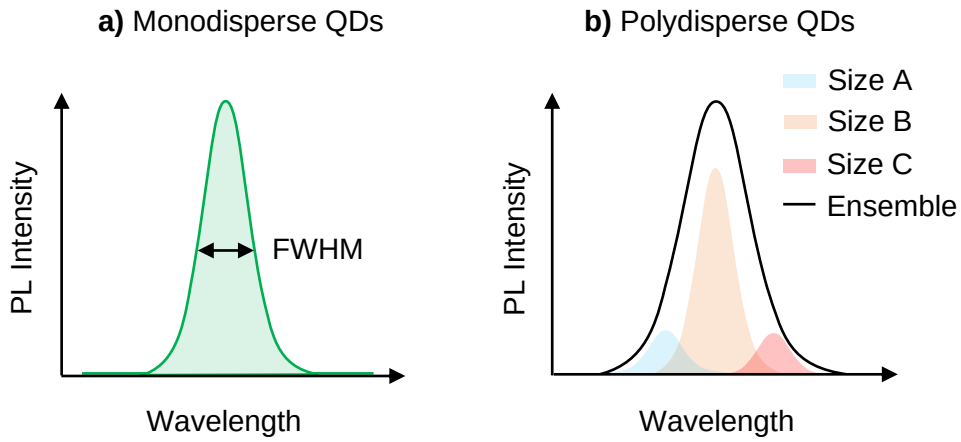


Figure 1.9: Idealised photoluminescence peaks for: a) monodisperse QDs b) polydisperse QD ensemble composed of three different QD sizes, where size A < size B < size C.

1.4 Indium phosphide quantum dots

1.4.1 Bulk indium phosphide

InP materials were originally developed in the 1980s for use in solar cells, having several advantages over archetypal silicon substrates. InP has a band gap energy of 1.34 eV, which is more optimal for solar-to-electricity conversion compared with Si.[82] It is also a direct band gap semiconductor, with excellent optical absorbance, meaning that InP solar cells can be thinner.[83] Furthermore, InP substrates have high temperature and radiation resistance, making them less susceptible to thermal- and photo-degradation during operation. Other applications of InP materials include in optoelectronics devices, such as high-speed digital circuits and photodetectors.[84]

More recently, InP QDs have emerged as a popular alternative to Cd-based QDs, due to their comparably low toxicity.[85] The uptake in their development has been motivated by

the successful commercialisation of QD display technologies, and recent EU legislation effectively prohibiting the use of Cd-containing materials in consumer goods.[86]

1.4.2 Synthesis of near-monodisperse InP QDs

The pioneering work of Efros and Ekimov in revealing quantum confinement in matrix isolated CuCl NCs motivated the exploration of quantum size effects in III-V materials. Early studies of InP NCs also employed matrix isolation approaches for their generation and stabilisation. Yoneyama and co-workers showed that InP NCs could be generated within a zeolite matrix by annealing In^{3+}-exchanged mordenite ($Na_8[(AlO_2)_8(SiO_2)_{76.8}]$) with PH_3 at > 175 °C.[87] A similar strategy was used by Berry *et al.*, but with porous permeable Vycor glass (96% silica, 4% BO_3). They showed that InP NCs could be isolated within Vycor glass treated with trimethylindium followed by annealing with PH_3 at > 300 °C for 28 hr.[88] Much like the CuCl NCs prepared by Ekimov, matrix isolation approaches to InP NCs resulted in poor particle size uniformity.

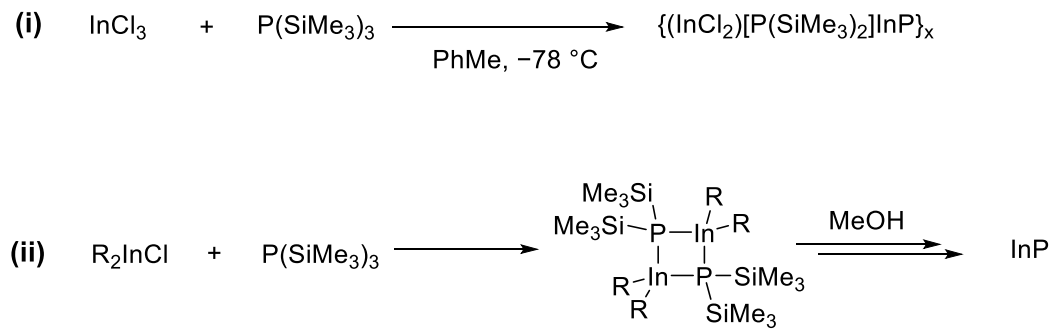
One of the first successful steps towards size-uniform III-V QDs was the development of Wells's dehalosilylation reaction between metal trihalides and silylphosphines.[89] Wells and co-workers initially developed the dehalosilylation reaction for the preparation of arsinogallanes and arsinoindanes (Scheme 1.3).[90–92]

$$MX_3 + As(SiMe_3)_3 \xrightarrow[C_xH_{(2x+1)}]{} MAs + 3\,XSiMe_3$$

Scheme 1.3: Dehalosilylation reaction between group III metal trihalides (M = Ga, In, X = Cl, Br) and tris(trimethylsilyl)arsine to form the corresponding metal arsenide and chlorosilane.[90] x = 5−8.

Barron *et al.* were first to use dehalosilylation reactions to prepare InP phases. They showed that tris(trimethylsilyl)phosphine ($P(SiMe_3)_3$) reacts with $InCl_3$ in solution to

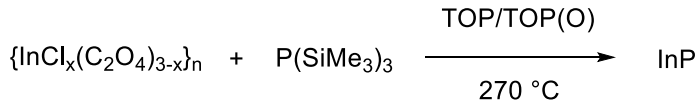
form InP, although were unable to identify the exact product (Scheme 1.4(i)).[93] Shortly after, Douglas and Theopold reported the reaction of alkylindium chlorides with silylphosphines to form molecular indium phosphides containing In_2P_2 units (Scheme 1.4(ii)). They showed that these complexes could be hydrolysed with methanol to form InP NCs, with absorbance maxima between 450 and 650 nm. They estimated the particle diameter of the InP NCs (absorbance peak at 615 nm) to be 5.4 nm.[94]



Scheme 1.4: Dechlorosilylation strategies for the preparation of InP phases by the reaction of indium chlorides and tris(trimethylsilyl)phosphine.[93] R = CH_2SiMe_3 or CH_2CMe_3.

Whilst in both cases the dehalosilylation strategy proved effective in forming InP, the resulting material had poor phase purity, where X-ray diffraction analysis showed considerable In_2O_3 formation. Moreover, the broad, featureless absorption spectra observed is consistent with the formation of polydisperse NCs. To overcome these challenges, Nozik and co-workers combined Wells's dehalosilylation route with the surfactant-assisted method pioneered by Murray, Norris, and Bawendi.[35] Nozik showed that by reacting chloroindium oxalate complexes with $P(SiMe_3)_3$, followed by high temperature annealing in the presence of TOP and TOP(O) capping ligands, InP QDs with uniform size distribution could be isolated (Scheme 1.5).[95] The mean diameter of the InP QDs obtained were measured to be 2.61 nm with a size distribution of ±0.75 nm, as determined by TEM. Alivisatos and Wells improved this procedure shortly after

Nozik, showing that indium halides (X = Cl, Br, I) could be used instead of the oxalate precursor, reducing surface oxidation and improving QD crystallinity.[96,97] The surfactant-assisted dehalosilylation approach has also been successfully employed for the preparation of GaP and $GaInP_2$ NCs.[98]



Scheme 1.5: Formation of InP QDs from the desilylation reaction of chloroindium oxalate complexes with tris(trimethylsilyl)phosphine.[95]

The robustness of the dehalosilylation strategy for the preparation of near-monodisperse InP QDs in solution can be attributed, in part, to the strong silicon-halide bond formed during the reaction. The Si–Cl and Si–Br bond dissociation energies in $XSiMe_3$ are 472 kJ mol^{-1} and 401 kJ mol^{-1},[99] respectively, considerably stronger in comparison to the Si–P bond (*ca.* 167−376 kJ mol^{-1}).[100,101]

The exploitation of the formation of strong Si–E bonds to drive the reaction of indium and phosphorus precursors in solution has also motivated the use of indium carboxylate precursors. The resulting Si–O bond formed upon reaction of $P(SiMe_3)_3$ with $In(O_2CR)_3$ is comparably strong to the Si–X homologues (478 kJ mol^{-1}).[102] Indium carboxylates have emerged as popular indium precursors to InP QDs as they enable the incorporation of surfactants to further control NC growth kinetics.[103] Popular indium carboxylates are derived from fatty acids, such as oleate ($^-OOC(CH_2)_7HC{=}CH(CH_2)_7CH_3$), stearate ($^-OOC(CH_2)_{16}CH_3$), palmitate ($^-OOC(CH_2)_{14}CH_3$), and myristate ($^-OOC(CH_2)_{12}CH_3$).[56]

1.4.3 Surface passivation of InP QDs

Advancements in desilylative protocols enabled the preparation of homogeneously sized InP QDs (particle size distribution < 20% by TEM), but showed poor PLQYs (< 0.5%) compared to CdSe QDs (*ca.* 10%), despite having similar band gap energies.[104,105]

The efficiency of QD photoluminescence can be described by its quantum yield. Quantum yield is the number of photons emitted relative to the number of photons absorbed. The photoluminescence quantum yield (PLQY; Φ) is described by Equation 1.3, where Γ is the emissive rate of the fluorophore and k_{nr} is the rate of non-radiative decay.[106]

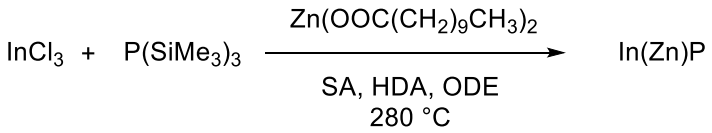
$$\Phi = \frac{\Gamma}{\Gamma + k_{nr}} \qquad (1.3)$$

Native CdSe QDs prepared by Murray *et al.* had PLQYs of *ca*. 10%, compared to the non-emissive InP QDs prepared by Nozik, Alivisatos, and Wells.[35] The low PLQY observed in InP QDs is attributed to poor passivation of the InP surface.

As described in Section 1.3.4, unpassivated surface species introduce mid-gap states (traps) into the electronic structure. The traps provide non-radiative energy loss mechanisms for photoexcited carriers (electrons and holes).[107] These non-radiative pathways tend to be more efficient than direct recombination, consequently quenching photoluminescence. In the case of InP, the emission quenching traps are largely attributed to electron rich surface phosphides and phosphates.[108]

Low PLQY in InP QDs was first resolved by Nozik and co-workers by etching the surface with fluoride ions. They showed that by treating InP QDs with HF or NH_4F, surface traps were removed and a PLQY of 30% could be achieved.[109]

Recognition of the high dependency of InP QD PLQY on the presence of surface traps inspired the development of less aggressive passivation methods. Nann *et al.* prepared highly luminescent InP QDs (PLQY = 30%) by the addition of zinc carboxylate and hexadecylamine additives during synthesis (Scheme 1.6).[110] The authors showed that PLQY increased with zinc doping, and attributed this to the replacement of the surface indium layer with zinc. This hypothesis is consistent with other reports which show that carboxylates play a crucial role in the localisation of zinc atoms on InP QD surfaces.[111,112] The effectiveness of Zn^{2+} doping to enhance PLQY is due to its ability to bind to under-coordinated P atoms on the surface, in turn passivating hole traps.[113] A similar PLQY enhancement can be achieved with Cd^{2+} ion passivation by the post-synthetic modification of InP QDs with cadmium oleate ($Cd(OOC(CH_2)_7HC{=}CH(CH_2)_7CH_3)_2$).[114]



Scheme 1.6: Preparation of Zn-passivated InP QDs using zinc undecylate and hexadecylamine. SA = stearic acid ($HOOC(CH_2)_{16}CH_3$), HDA = hexadecylamine ($H_2N(CH_2)_{15}CH_3$), ODE = 1-octadecene ($H_2C{=}CH_2(CH_2)_{15}CH_3$).[110]

The use of amine surfactants was also important in improving the PLQY. Hexadecylamine was found to disfavour the formation of In_2O_3 phases during the reaction which are known to diminish the PLQY. Similar enhancements in PLQY have been reported using hexylamine and trioctylamine capping ligands.[115,116]

1.4.4 Heteroepitaxial shell growth on InP QDs

By far the most effective method for passivating surface traps and improving InP QD PLQY is the epitaxial growth of a passivating inorganic shell onto the InP surface. The overcoating of a lattice-matched shell material onto InP passivates the surface in an analogous, yet more effective way, to surface etching, ion passivation, and ligand capping.

Shelling InP QDs has several advantages over other passivation strategies. Growth of inorganic shells can efficiently passivate both anionic and cationic surface sites uniformly.[14] Moreover, shells are unlikely to desorb, and impart significant solution processability and chemical stability to the final core/shell QD.[117] Finally, the band gap energy and alignment of the shell material can be tuned, offering added control over photophysical properties.

In selecting a shell material, there are two important parameters that must be considered: the relative band alignment of the InP core and shell; and the relative mismatch in the lattice parameters of the two materials.

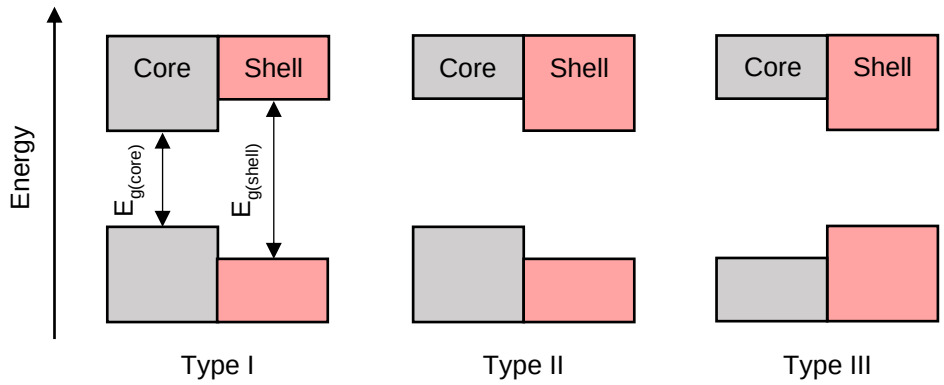


Figure 1.10: Band alignment regimes in core/shell quantum dots.

There are several different band gap alignments core/shell QDs can adopt depending on the respective materials used. A type I band alignment is achieved when the shell material is a wider band gap semiconductor ($E_{g(shell)} > E_{g(core)}$), such that the energy of the valence band is lower and the conduction band higher than that of the core (Figure 1.10). In a type I band structure, photoexcited charge carriers are localised within the QD core by energy potentials. This enhances InP QD PLQY, as the shell insulates the core-localised charge carriers from environmental factors, whilst passivating the core surface through chemical bonding.

Other core/shell band alignments exist, such as off-set type II structures, which localise one of the charge carriers within the shell, or type III structures, which can be considered an inverse-type I, where both charge carriers are localised in the shell (Figure 1.10).[117] These alignments are desirable when charge mobility is important, such as in conductive composite materials for LEDs or chemical sensing.[118]

For a shell to effectively passivate the surface of an InP QD, lattice mismatch between the two materials must be minimised.[119] Lattice mismatch between the QD core and shell will create strain at the interfacial boundary, which in turn is relieved through the formation of crystal defects (e.g. dislocations and vacancies).[120] Interfacial defects contribute mid-gap energy states which diminish PLQY, therefore diligent material selection is crucial to avoid this.[121]

To minimise the lattice mismatch, the shell material must adopt the same crystal packing structure as the core – cubic zinc blende for InP. Secondly, the difference in the respective lattice parameters of the core and shell must be minimised. Lattice mismatch is often

quantified as the ratio of the lattice parameter of the shell material compared to InP ($a_{(shell)}/a_{InP}$).

Nozik *et al.* were first to show that InP QD PLQY could be enhanced by the epitaxial growth of a lattice-matched $ZnCdSe_2$ shell.[122] They found that the InP/$ZnCdSe_2$ core/shell QDs showed 5−10% PLQYs, whilst bare InP QDs showed no photoluminescence. The authors attribute the enhancement in PLQY to the minimisation of interfacial defects between the core and shell, consistent with observations made for InP/$ZnCdSe_2$ thin films prepared by molecular-beam epitaxy.[123]

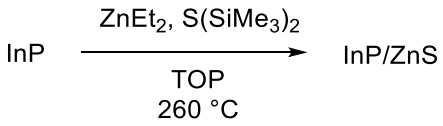
Table 1.2: Physical data of common shell materials used to prepare type I core/shell InP QDs.

Type	Material	Structure	Energy Gap (eV)	Lattice Parameter (Å)[124]	Lattice Mismatch with InP (%)[125–127]
III-V	InP	Zinc blende	1.35	5.869	-
	GaP	Zinc blende	2.27	5.450	6.82
II-V	ZnS	Zinc blende	3.61	5.410	7.7
	ZnSe	Zinc blende	2.69	5.668	3.4
	CdS	Zinc blende	2.42	5.832	0.7

Since Nozik's first report, a variety of shell materials have been employed to improve the poor photoluminescence of bare InP QDs, such as GaP, CdS, ZnSe, and ZnS (Table 1.2).[24,128] Of these, ZnS has emerged as one of the most popular.

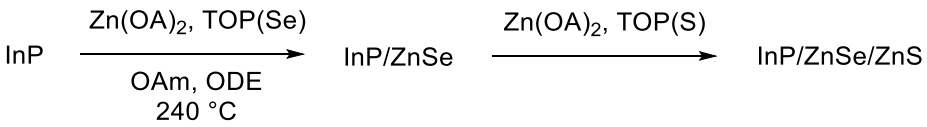
Weller and co-workers first achieved the epitaxial growth of ZnS on TOP-capped InP cores by high temperature annealing with $ZnEt_2$ and $S(SiMe_3)_2$ (260 °C; Scheme 1.7).[129] They showed that the PLQY of the resulting core/shell InP/ZnS QDs could be increased to 23% after shell growth – a 73-fold increase compared to the native InP cores. This synthesis has evolved over the years, employing safer, more accessible precursors such

as zinc carboxylates and trialkylphosphine sulfides.[130] ZnS is an ideal shell material due to its chemical robustness, being relatively tolerant to surface oxidation and photodegradation.[131]



Scheme 1.7: Preparation of core/shell InP/ZnS QDs using diethylzinc and bis(trimethylsilyl)sulphide. TOP = trioctylphosphine.

Materials with lower lattice mismatch than ZnS such as ZnSe (3.4%) can also be exploited to improve PLQYs further using multi-shell architectures. For example, Dennis *et al.* showed that a ZnSe interlayer could be grown between InP and ZnS by the stepwise addition of zinc and selenide precursors, followed by zinc and sulphide (Scheme 1.8). They showed that the addition of a ZnSe interlayer resulted in a 10-fold increase in PLQY, compared to the core/shell InP/ZnS counterparts.[132]



Scheme 1.8: Preparation of core/shell/shell InP/ZnSe/ZnS QDs from InP cores using trioctylphosphine selenide (TOP(Se)), trioctylphosphine sulphide (TOP(S)) and zinc oleate. ODE = 1-octadecene, OAm = oleylamine ($H_2N(CH_2)_8HC{=}CH(CH_2)_7CH_3$), OA = oleate ($OOC(CH_2)_7HC{=}CH(CH_2)_7CH_3$).

Finally, lattice mismatch may also be minimised by alloying the core/shell and shell/shell interfaces. The addition of dopant ions into QD layers can be used to ‘smooth’ the change in lattice constant across a greater distance, reducing interfacial strain and thus defects. Liem and Reiss showed that zinc carboxylates could be used to lattice dope InP QD cores during synthesis.[133] The alloyed In(Zn)P QDs, once overcoated with ZnS, displayed

remarkably high PLQYs between 60–70%. Similar enhancements can be attained by alloying ZnSe interlayers with sulphide ions in the core/shell/shell InP/ZnSe/ZnS QDs described above. Lee *et al.* showed that by smoothing the change in lattice constant between ZnSe and ZnS shells by gradual sulphide doping with TOP(S), PLQYs of up to 80% were possible.[134]

1.4.5 Development of phosphorus precursors to InP QDs

Significant advancements have been made in controlling the optical properties of InP QDs using band engineering and maturing synthetic methodologies, attaining near-unity PLQY (> 90%).[135,136] However, the preparation of InP QDs with narrow size distributions remains a major challenge.[137] The intrinsic size-dependence of QD emission profiles and colour purity make achieving size control an essential goal for their use in optoelectronic applications, such as for consumer displays. For context, CdSe and Pb-based perovskite QDs can be isolated with FWHM below 20 nm, whilst the most monodisperse InP QDs prepared to date trail with a FWHM of > 34 nm.[138]

One theory as to why InP QDs suffer from greater polydispersity compared to other QD materials is the poor resolution of nucleation and growth events during synthesis. Whilst hot-injection approaches have been successful for other QD systems, the highly reactive phosphorus precursors used in InP QD preparations, such as $P(SiMe_3)_3$, are usually fully consumed during the nucleation stage.[139] It is believed that the rapid depletion of molecular precursors upon addition ultimately inhibits control over uniform size growth. Some reports also attribute poor size control to the more covalent nature of the InP lattice, and consequently the lack of reversibility in the nucleation stage and during growth,[140] however to date there is no consensus on this matter.[141]

Moreover, whilst silylphosphines have supported the majority of research into InP QDs over the last three decades, they are highly pyrophoric and challenging to handle safely. For these reasons, a variety of phosphorus precursors have been developed for the preparation of InP QDs. Table 1.3 details common phosphorus precursors to InP QDs.

Table 1.3: Common phosphorus precursors to InP QDs and their respective oxidation states. E = Sn or Ge; R = alkyl, aryl; R' = methyl, pyrazole.

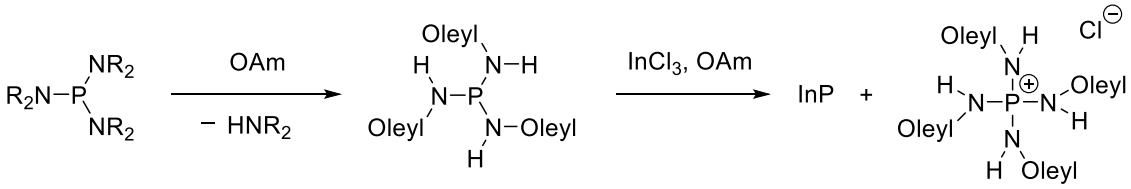
Phosphorus precursor[142–144]	**Phosphorus oxidation state**
$P(SiR_3)_3$	−3
$P(EMe_3)_3$	−3
$P(NR'_2)_3$	+3
P_4	0
PCl_3	+3
PH_3	−3
Na(PCO)	−1
InP 'magic-sized' clusters	−3

Tin and germanium analogues of $P(SiMe_3)_3$ have been explored due to the increased stability of the P–Sn and P–Ge bonds, in the hope that this will decrease their reactivity.[145] Bawendi and Harris showed that using $P(GeMe_3)_3$ resulted in slower InP QD growth, however did not improve particle size distribution, due to its conversion rate remaining fast compared to particle growth. It was also shown that $P(SnMe_3)_3$ did not produce QDs with sharp absorption features, likely due to the formation of the competing tin phosphide phase.[142]

Aminophosphines have also been explored as phosphorus precursors, owing to the stronger P–N bond compared to the respective P–Si bond of $P(SiMe_3)_3$.[14] Yamaguchi *et al.* first reported the use of $P(NMe_2)_3$ as a safer and cheaper alternative to $P(SiMe_3)_3$, showing that polydisperse TOP/TOP(O)-capped InP QDs could be generated upon

reaction with $InCl_3$ (PL FWHM > 100 nm).[146] This preparation has since been improved, employing amine capping ligands to achieve PLQYs of 30−70% and FWHM of 46−65 nm.[47,147,148]

Amine capping ligands have been found to play an important role in the reactivity of aminophosphines in solution. Weigand and co-workers revealed that tri(pyrazolyl)phosphanes undergo transamination reactions with oleylamine additives during QD growth conditions, forming the corresponding oleylaminophosphine (Scheme 1.9). Oleylamine was also found to act as a co-reductant, converting aminophosphines in their +3 oxidation state to InP in the −3 oxidation state. Hens, Dubertret, and Weigand demonstrated that by heating trioleylaminophosphine formed after transamination with $InCl_3$, the aminophosphine disproportionates into InP (−3) and tetra(oleylamino)phosphonium chloride (+5).[149–151]

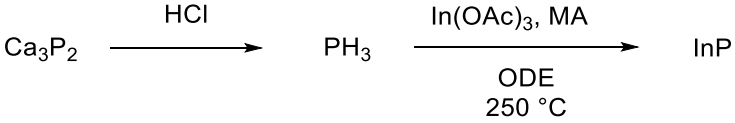


Scheme 1.9: Transamination of aminophosphines with oleylamine and subsequent disproportionation upon reaction with $InCl_3$ to form InP QDs and tetra(oleylamino)phosphonium chloride. NR_2 = NMe_2, pyrazole; OAm = oleylamine; Oleyl = $(CH_2)_8HC{=}CH(CH_2)_7CH_3$.

The use of a co-reductant to reduce phosphide sources to the correct oxidation state for InP QD synthesis has been employed for the development of a variety of inorganic phosphorus sources. Xie *et al.* first reported that potassium borohydride (KBH_4) could reduce mixtures of white and red phosphorus in the presence of $InCl_3$ to form InP NCs.[152] Mézailles and co-workers showed that indium halides could first be reduced by sodium

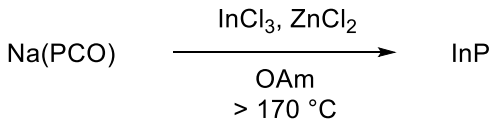
naphthalenide ($NaC_{10}H_8$) in solution with capping ligands, and that the resulting In^0 nanoparticles react with P_4 to form InP NCs.[153] Alternatively, Park *et al.* showed that oleylamine is a suitable co-reductant to enable the reaction of P_4 with indium (III) halides to form InP QDs.[144]

Phosphorus trichloride (PCl_3) and phosphine (PH_3) are both widely used in the semiconductor industry as phosphide sources because of their volatility and relatively low bond dissociation energies (356 kJ mol^{-1} and 351 kJ mol^{-1}, respectively).[102] Inspired by the early work of Xie, Fang and co-workers showed that the simultaneous reduction of indium acetate and PCl_3 with superhydride ($LiBH(C_2H_5)_3$) in the presence of stearic acid capping ligands afforded InP QDs.[143] Reiss and co-workers were first to demonstrate that PH_3 is also a competent phosphorus precursor, and unlike PCl_3, does not require use of a co-reductant. Reiss showed that PH_3 generated by the acidification of calcium phosphide (Ca_3P_2) and bubbled into a solution of ODE containing indium carboxylates reacts to form large InP QDs (PL emission maxima = 570–720 nm; Scheme 1.10).[154] Dorofeev later improved the relatively low PLQYs reported by Reiss using PH_3 from 20% up to 50% by growing a ZnSe/ZnS multi-shell onto the InP QDs.[155] Whilst PCl_3 and PH_3 are attractive phosphorus sources for InP QDs, being inexpensive and widely available, they remain highly pyrophoric and toxic if inhaled, necessitating similar hazard mitigations to $P(SiMe_3)_3$.[156]



Scheme 1.10: Preparation of InP QDs using PH_3 formed from the acidification of calcium phosphide by hydrochloric acid. MA = myristic acid ($HOOC(CH_2)_{12}CH_3$).

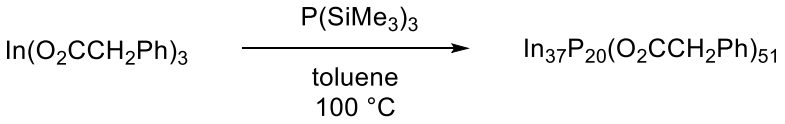
Even thirty years after Nozik's first characterisation of InP QDs, the pursuit of more accessible, safer phosphorus precursors remains highly active. In 2021, Zhao and co-workers reported sodium phosphaethynolate, Na(PCO), as a new phosphorus precursor. Zhao demonstrated that Na(PCO) can be used to prepare zinc-alloyed InP QDs by reaction with $InCl_3$ and $ZnCl_2$ in oleylamine (Scheme 1.11).[157] The QDs formed had size-tuneable emission between 465 and 620 nm and high PLQYs of 43−97%. The authors highlight that Na(PCO) is less expensive than popular silyl- and amino-phosphines currently used, and is also non-pyrophoric.



Scheme 1.11: Preparation of InP QDs using sodium phosphaethynolate as a phosphorus precursor. OAm = oleylamine.

In recent years, the use of single-source precursors to InP QDs has been explored, inspired by the elucidation and isolation of intermediate InP cluster phases. InP clusters, commonly referred to as 'magic-sized' clusters (MSCs), are thermodynamically stable phases observed during QD growth conditions, and also exist in II-VI systems.[158] Peng *et al.* were first to identify InP cluster evolution during QD growth by their characteristic high energy absorption peak at *ca.* 390 nm.[159] InP clusters were shown to form from the reaction of long chain indium carboxylates and $P(SiMe_3)_3$ at low temperatures relative to QD growth (< 200 °C). The identity of these clusters was later corroborated by Cossairt and co-workers. By substituting the long chain carboxylates with phenylacetate ligands and reducing the reaction temperature to 100 °C, an $In_{37}P_{20}(O_2CCH_2Ph)_{51}$ MSC could be isolated and crystallographically characterised (Scheme 1.12).[160] Regardless of

carboxylate choice, the InP MSCs prepared are shown to act as suitable single-source precursors for the synthesis of InP QDs, decomposing above 200 °C.



Scheme 1.12: Preparation of a magic-sized InP cluster from indium phenylacetate and tris(trimethylsilyl)phosphine.[160]

InP MSCs are receiving significant attention due to their crystallographically distinct polytwistane structure, compared to the zinc blende structure of InP QDs.[161–164] The non-zinc blende structure of InP MSCs has cast doubt over the accuracy of using classical nucleation theory to describe QD growth, which assumes the NCs adopt the same crystallographic structure as their parent nuclei.[165] InP MSCs have played an important role in developing an understanding of NC nucleation and cluster to nanocrystal phase transformations.[166]

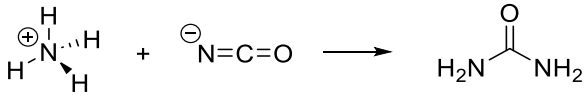
Although $P(SiMe_3)_3$ has been crucial in the development of InP QD chemistry, the emerging commercial applications of these materials demands innovation and the continuous evolution of phosphorus precursors.[167] While companies such as Samsung and Nanosys have pioneered InP QD thin films in television display panels, the necessity of expensive and pyrophoric $P(SiMe_3)_3$ remains a persistent challenge at scale.

The phosphorus precursors described in this section, whilst effective phosphide sources for InP QDs, are all air- and moisture-sensitive. For this reason, the search continues for a phosphorus precursor that is: air- and moisture-stable, convenient to prepare and handle,

and compatible with existing InP QD synthetic methodologies. This motivated us to explore phosphinecarboxamides as a potential new class of phosphorus precursor to InP QDs.

1.5 Phosphinecarboxamides

1.5.1 Synthesis of urea

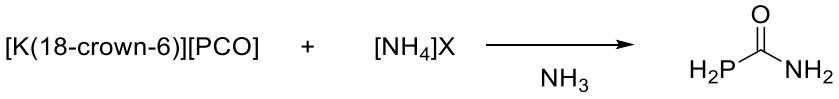


Scheme 1.13: Preparation of urea from ammonium and cyanate salts.

Wöhler first reported the synthesis of urea in 1828 while attempting to form ammonium cyanate from silver cyanate and ammonium chloride (Scheme 1.13).[168] The significance of this finding is underscored by Hermann Kopp, an important chronicler of the history of chemistry at the time. Kopp hailed this accomplishment as "*the first example [of] an organic substance… produced through chemical means alone from inorganic materials; this discovery destroyed the till-then accepted distinction between the organic and inorganic bodies*".[169] Wöhler's contemporaries largely met his work with indifference, yet it is widely considered a founding moment of organic chemistry.[170]

1.5.2 The parent phosphinecarboxamide

Our group was inspired by Wöhler's synthesis of urea, and the potential for the phosphaethynolate anion, a heavier cyanate analogue, to demonstrate analogous reactivity.[171] Jupp and Goicoechea showed that the reaction of [K(18-crown-6)][PCO] with ammonium salts afforded the parent phosphinecarboxamide, a phosphorus containing analogue of urea (Scheme 1.14).[172]

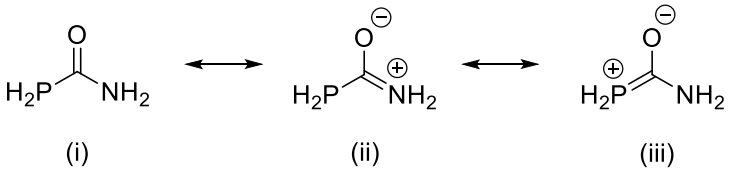


Scheme 1.14: Synthesis of the parent phosphinecarboxamide. X = Cl or BPh_4.

The mechanism for the reaction is postulated to be analogous to that of Wöhler's urea synthesis, and involves protonation of the 2-phosphaethynolate anion followed by nucleophilic attack of HPCO by ammonia.[173]

Unlike most primary phosphines, the parent phosphinecarboxamide is remarkably stable in air and moisture.[174] Phosphinecarboxamide can be prepared in aqueous solution, and has a half-life of nine days in d_5-pyridine exposed to air.[172]

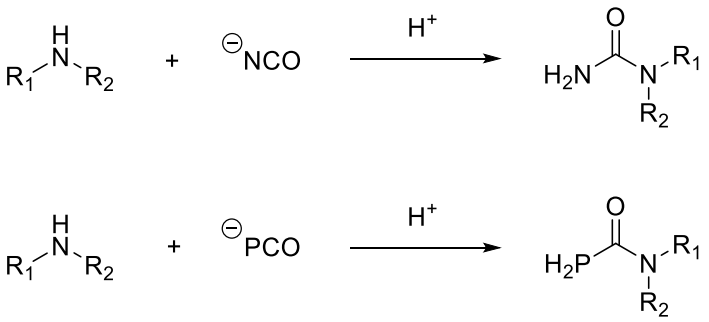
This air stability may be rationalised by phosphorus lone-pair delocalisation into the carbamoyl moiety (Scheme 1.15). However, spectroscopic data, bond metrics, and the computed electronic structure all suggest that phosphorus lone-pair delocalisation is minimal.[175] For example, X-ray crystallographic characterisation reveals the trigonal pyramidal geometry at phosphorus, whilst trigonal planar at nitrogen, consistent with a greater degree of nitrogen lone-pair delocalisation into the C=O π* orbital. Moreover, the HOMO of phosphinecarboxamide is computed to have considerable phosphorus lone-pair character (44.4%), suggesting that resonance structures (i) and (ii) contribute significantly to the final structure.



Scheme 1.15: Proposed resonance structures of the parent phosphinecarboxamide.

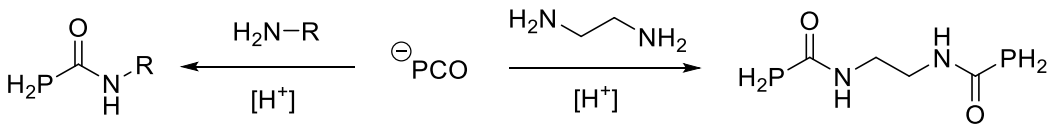
1.5.3 Functionalised phosphinecarboxamides

The synthetic similarities of urea and phosphinecarboxamide extend to their functionalisation. *N*-Functionalised ureas can be synthesised by reaction of isocyanates with amines under acid conditions (Scheme 1.16).[176–178] Analogously, *N*-functionalised phosphinecarboxamides can be prepared by the facile reaction of the 2-phosphaethynolate anion with amines.



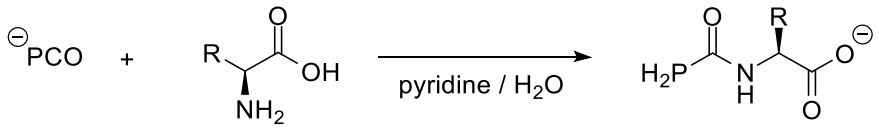
Scheme 1.16: Formation of *N*-functionalised ureas and phosphinecarboxamides by reaction of amines with cyanate and phosphaethynolate salts, respectively.

Jupp *et al.* showed that novel *N*-functionalised phosphinecarboxamides can be prepared from primary amines in the presence of pyridinium triflate.[179] It was found that the equivalent reaction with secondary amines does not proceed as readily, and only *N*,*N*-diethylphosphinecarboxamide ($H_2PC(O)NEt_2$) can be isolated. This approach was later extended to use diamines, affording the corresponding disubstituted phosphine-carboxamide (Scheme 1.17).[180]



Scheme 1.17: Preparation of *N*-functionalised phosphinecarboxamides from alkylamines (left) and ethylenediamine (right). R = Et, cyclohexyl, ^{t}Bu; [H^+] = pyridinium triflate.

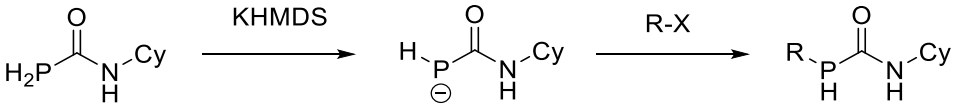
Additional functionality may also be incorporated into phosphinecarboxamide molecules. Faria and Jupp showed that PCO^- reacts with enantiomerically pure α-amino acids to form the corresponding carboxylate-functionalised phosphinecarboxamides (Scheme 1.18).[181] In this case, no exogenous acid is required to protonate PCO^- during synthesis, as the amino acid precursor contains a carboxylic acid group.



Scheme 1.18: Preparation of carboxylate-functionalised phosphinecarboxamides from amino acids.

These studies have highlighted the promising functional group tolerance of the phosphinecarboxamide motif, which include thiol, hydroxyl, alkynyl, carboxylate, and carboxylic acid groups. The facile formation and stability of *N*-functionalised phosphinecarboxamides has even enabled mechanochemical synthetic methods to be employed. Quan and co-workers showed that the reaction of PCO^- and primary amines can be achieved by mechanochemical ball-milling, affording the corresponding *N*-alkyl- and *N*-aryl-phosphinecarboxamides.[182]

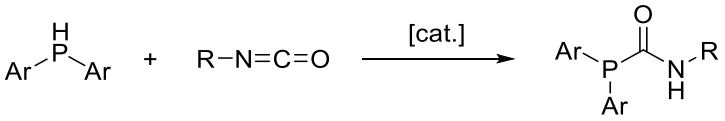
Functionalisation is not only limited to the nitrogen atom − *P*-functionalisation can also be achieved in several ways. Our group has found that primary phosphinecarboxamides can be deprotonated by potassium bis(trimethylsilyl)amide (KHMDS), which occurs at the phosphine P–H bond. Whilst it may be expected that deprotonation occur at the more polarized E–H bond (E = N, P), the total bonding energies of the computed structures reveal that the phosphide is 29.0 kJ mol^{-1} more stable than the amide. The deprotonated phosphinecarboxamide can subsequently react with bromoalkanes to form the corresponding *P*-functionalised derivatives (Scheme 1.19).[180]



Scheme 1.19: *P*-functionalisation of primary phosphinecarboxamides by deprotonation and reaction with an electrophile. R = Me, Bn (CH_2Ph); X = Br.

Quan and co-workers achieved similar results using potassium carbonate, a weaker base than KHMDS. They reported the *P*-arylation of primary phosphinecarboxamides upon deprotonation and reaction with aryl triflates.[183] Quan also highlighted that this procedure could be repeated on the *P*-arylated product, affording the *P*,*P*-functionalised tertiary phosphinecarboxamide. *P*-functionalisation of phosphinecarboxamides is also not limited to intermolecular reactions. Robinson *et al.* showed that deprotonation of an *N*-functionalised phosphinecarboxamide bearing alkyne functionalities results in an intramolecular cyclisation reaction, forming five- and six-membered heterocycles.[184]

Alternatively, *P*-functionalised phosphinecarboxamides may be obtained by the hydrophosphination of isocyanates. In the late 1960s, Buckler and Lindsey first reported the hydrophosphination of isocyanic acid with diphenylphosphine.[185,186] More recently, metal-catalysed approaches have been popularised due to the low yield (13%) and long reaction time (4 days) of the original preparations. Lanthanum, iron, copper, and zinc all effectively catalyse hydrophosphination reactions, forming metal-phosphide intermediates that afford *P*-functionalised phosphinecarboxamides upon reaction with isocyanates in solution (Scheme 1.20).[187–190] Liptrot and co-workers have also demonstrated that a carbene-ligated Cu(I) catalyst can hydrophosphinate isocyanates using phosphinite esters ($P(OR)_3$), vastly expanding the substrate scope.[191]



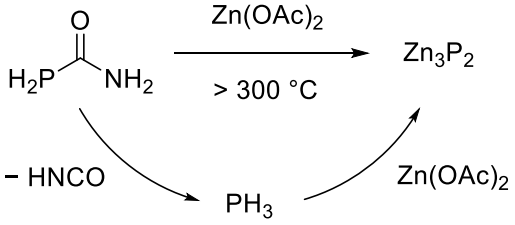
Scheme 1.20: Preparation of *P*-functionalised phosphinecarboxamides from the hydrophosphination of isocyanates. [cat.] = α-La(DMBA)$_3$ (dimethylbenzylamine), CpFe(CO)$_2$(Me), (IPr)CuO-*t*-Bu (IPr = 1,3-bis(2,6-diisopropylphenyl)imidazol-2-ylidene), ZnEt$_2$.

Hydrophosphination and phosphaethynolate derivatisation are two complementary routes to *P*-functionalised phosphinecarboxamides, offering their own respective advantages and disadvantages. For example, the hydrophosphination route can be accomplished with commercially available precursors, but is limited to the isolation of secondary and tertiary phosphine products. Conversely, PCO^- derivatisation offers greater functionalisation control, yet phosphaethynolate salts are not yet commercially available.

1.5.4 Phosphinecarboxamides as phosphorus precursors to inorganic materials

The remarkable air and moisture stability of phosphinecarboxamides compared to the common phosphorus precursors described (Section 1.4.5) has inspired their exploration for the preparation of metal phosphides.

Recently, Hyett and co-workers described using the parent phosphinecarboxamide as an unexpected phosphorus precursor in the chemical vapour deposition of zinc phosphide thin films.[192] They found that upon heating, $H_2PC(O)NH_2$ decomposes to generate PH_3, which reacts with zinc acetate to produce a thin film (Scheme 1.21). Here, phosphine-carboxamide can be considered a ‘masked’ PH_3 source that is stable under ambient conditions.



Scheme 1.21: Chemical vapour deposition of Zn_3P_2 thin films using the parent phosphinecarboxamide as a phosphide source.

1.6 Project aims

At the onset of this project, we were inspired by Hyett's first successful demonstration of phosphinecarboxamide as a novel phosphorus source in materials chemistry. The suggestion that phosphinecarboxamide acts as a 'masked' PH_3 source upon thermal decomposition motivated us to explore whether this reactivity could be reproduced in the solution phase. In particular, we were interested in its viability for the preparation of InP QDs as PH_3 is already a known phosphorus source. We believe that the air and moisture stability of phosphinecarboxamides, combined with their robust functionalisation chemistry, make them promising candidates to explore in the synthesis of InP QDs.

1.7 References

1 A. Rockett, Ed., *The Physics of Solids BT - The Materials Science of Semiconductors*, Springer US, Boston, MA, 2008.

2 S. T. J, *Abh. Akad. Wiss.*, 1822, **1820**–**21**, 289–346.

3 Enn Velmre, *Proc. Est. Acad. Sci. Eng.*, 2007, **13**, 276–282.

4 M. Faraday, *Philos. Trans. R. Soc. London*, 1833, **123**, 507–522.

5 A. E. Becquerel, *Comptes Rendus L´Academie des Sci.*, 1839, **9**, 145–149.

6 T. Taki and M. Strassburg, *ECS J. Solid State Sci. Technol.*, 2020, **9**, 15017.

7 A. A. F. Husain, W. Z. W. Hasan, S. Shafie, M. N. Hamidon and S. S. Pandey, *Renew. Sustain. Energy Rev.*, 2018, **94**, 779–791.

8 W. Heywang and K. H. Zaininger, eds. P. Siffert and E. F. Krimmel, Springer Berlin Heidelberg, Berlin, Heidelberg, 2004, pp. 25–42.

9 J.-L. Autran and D. Munteanu, *Radiation Response of Group-IV and III-V Semiconductors Subjected to D–D and D–T Fusion Neutrons*, IntechOpen, Rijeka, 2022.

10 K. Y. Cheng, ed. K. Y. Cheng, Springer International Publishing, 2020, pp. 161–202.

11 M. Afzaal and P. O'Brien, *J. Mater. Chem.*, 2006, **16**, 1597–1602.

12 M. L. Cohen and J. R. Chelikowsky, eds. M. L. Cohen and J. R. Chelikowsky, Springer Berlin Heidelberg, Berlin, Heidelberg, 1988, pp. 172–188.

13 C. A. Irfana Parveen, O. Anjali and R. Sunder, eds. A. Joshi, M. Mahmud and R. G. Ragel, Springer Nature Singapore, Singapore, 2023, pp. 123–134.

14 B. Chen, D. Li and F. Wang, *Small*, 2020, **16**, 1–20.

15 H. Landolt, R. Börnstein, K. H. Hellwege, D. Bimberg, M. Schulz, H. Weiss and O. Madelung, *Landolt-Börnstein numerical data and functional relationships in science and technology. Group 3, Crystal and solid state physics. Vol. 17, Semiconductors*, Springer, Berlin, New series., 1982.

16 J. Singh, *Physics of semiconductors and their heterostructures*, McGraw-Hill, New York, 1993.

17 D. Aldakov and P. Reiss, *J. Phys. Chem. C*, 2019, **123**, 12527–12541.

18 P. Reiss, *Semicond. Nanocrystal Quantum Dots Synth. Assem. Spectrosc. Appl.*,

2008, 35–72.

19 A. L. Efros, M. Rosen, M. Kuno, M. Nirmal, D. Norris and M. Bawendi, *Phys. Rev. B*, 1996, **54**, 4843–4856.

20 F. T. Rabouw and C. de Mello Donega, *Top. Curr. Chem.*, 2016, **374**, 1–30.

21 S. Kasap and R. K. Sinha, *Optoelectronics and photonics : principles and practices*, Pearson Education, Harlow, Essex, 2013.

22 T. W. Odom, J.-L. Huang, P. Kim and C. M. Lieber, *J. Phys. Chem. B*, 2000, **104**, 2794–2809.

23 M. A. Reed, J. N. Randall, R. J. Aggarwal, R. J. Matyi, T. M. Moore and A. E. Wetsel, *Phys. Rev. Lett.*, 1988, **60**, 535–537.

24 P. Reiss, M. Protière and L. Li, *Small*, 2009, **5**, 154–168.

25 A. Ekimov and A. Onushchehko, *JETP Lett.*, 1981, **34**, 363.

26 A. Efros and A. Efros, *Sov. Phys. Semicond.*, 1982, **16**, 772–775.

27 L. E. Brus, *J. Chem. Phys.*, 1984, **80**, 4403–4409.

28 R. Toufanian, X. Zhong, J. C. Kays, A. M. Saeboe and A. M. Dennis, *Chem. Mater.*, 2021, **33**, 7527–7536.

29 W. Baek, H. Chang, M. S. Bootharaju, J. H. Kim, S. Park and T. Hyeon, *JACS Au*, 2021, **1**, 1849–1859.

30 *Colloidal Quantum Dot Optoelectronics and Photovoltaics*, Cambridge University Press, Cambridge, 2013.

31 V. K. Lamer and R. H. Dinegar, *J. Am. Chem. Soc.*, 1950, **72**, 4847–4854.

32 N. T. K. Thanh, N. Maclean and S. Mahiddine, *Chem. Rev.*, 2014, **114**, 7610–7630.

33 T. Sugimoto, *J. Colloid Interface Sci.*, 2007, **309**, 106–118.

34 J. Park, J. Joo, G. K. Soon, Y. Jang and T. Hyeon, *Angew. Chem. Int. Ed.*, 2007, **46**, 4630–4660.

35 C. B. Murray, D. J. Norris and M. G. Bawendi, *J. Am. Chem. Soc.*, 1993, **115**, 8706–8715.

36 L. R. Becerra, C. B. Murray, R. G. Griffin and M. G. Bawendi, *J. Chem. Phys.*, 1994, **100**, 3297–3300.

37 D. H. Napper, *J. Colloid Interface Sci.*, 1977, **58**, 390–407.

38 E. B. Zhulina, O. V Borisov and V. A. Priamitsyn, *J. Colloid Interface Sci.*, 1990, **137**, 495–511.

39 S. Sun and C. B. Murray, *J. Appl. Phys.*, 1999, **85**, 4325–4330.

40 P. S. Shah, S. Husain, K. P. Johnston and B. A. Korgel, *J. Phys. Chem. B*, 2001, **105**, 9433–9440.

41 J. Hambrock, R. Becker, A. Birkner, J. Weiß and R. A. Fischer, *Chem. Commun.*, 2002, 68–69.

42 C. de Mello Donegá, P. Liljeroth and D. Vanmaekelbergh, *Small*, 2005, **1**, 1152–1162.

43 K. Vighnesh, S. Wang, H. Liu and A. L. Rogach, *ACS Nano*, 2022, **16**, 19618–19625.

44 L. Protesescu, S. Yakunin, M. I. Bodnarchuk, F. Krieg, R. Caputo, C. H. Hendon, R. X. Yang, A. Walsh and M. V Kovalenko, *Nano Lett.*, 2015, **15**, 3692–3696.

45 J. Van Embden, A. S. R. Chesman and J. J. Jasieniak, *Chem. Mater.*, 2015, **27**, 2246–2285.

46 M. Green and P. O'Brien, *J. Mater. Chem.*, 2004, **14**, 629–636.

47 L. Li and P. Reiss, *J. Am. Chem. Soc.*, 2008, **130**, 11588–11589.

48 A. A. Guzelian, U. Banin, A. V Kadavanich, X. Peng and A. P. Alivisatos, *Appl. Phys. Lett.*, 1996, **69**, 1432–1434.

49 M. Ghosh and C. N. R. Rao, *Chem. Phys. Lett.*, 2004, **393**, 493–497.

50 M. Ghosh, K. Biswas, A. Sundaresan and C. N. R. Rao, *J. Mater. Chem.*, 2006, **16**, 106–111.

51 E. Dhaene, J. Billet, E. Bennett, I. Van Driessche and J. De Roo, *Nano Lett.*, 2019, **19**, 7411–7417.

52 N. G. Mbewana-Ntshanka, M. J. Moloto and P. K. Mubiayi, *Heliyon*, 2020, **6**, e05130.

53 E. N. Lang, A. G. Porter, T. Ouyang, A. Shi, T. R. Hayes, T. C. Davis and S. A. Claridge, *ACS Nano*, 2021, **15**, 10275–10285.

54 M. G. Bawendi, P. J. Carroll, W. L. Wilson and L. E. Brus, *J. Chem. Phys.*, 1992, **96**, 946–954.

55 M. G. Bawendi, W. L. Wilson, L. Rothberg, P. J. Carroll, T. M. Jedju, M. L. Steigerwald and L. E. Brus, *Phys. Rev. Lett.*, 1990, **65**, 1623–1626.

56 M. Green, *J. Mater. Chem.*, 2010, **20**, 5797–5809.

57 A. Heuer-Jungemann, N. Feliu, I. Bakaimi, M. Hamaly, A. Alkilany, I. Chakraborty, A. Masood, M. F. Casula, A. Kostopoulou, E. Oh, K. Susumu, M. H. Stewart, I. L. Medintz, E. Stratakis, W. J. Parak and A. G. Kanaras, *Chem. Rev.*, 2019, **119**, 4819–4880.

58 S. R. K. Perala and S. Kumar, *Langmuir*, 2013, **29**, 9863–9873.

59 S. Chen, X. Zhang, Q. Zhang and W. Tan, *Nanoscale Res. Lett.*, 2009, **4**, 1159.

60 W. W. Yu, J. C. Falkner, C. T. Yavuz and V. L. Colvin, *Chem. Commun.*, 2004, 2306–2307.

61 G. Rodríguez-Gattorno, P. Santiago-Jacinto, L. Rendon-Vázquez, J. Németh, I. Dékány and D. Díaz, *J. Phys. Chem. B*, 2003, **107**, 12597–12604.

62 T. Teranishi, Y. Inoue, M. Nakaya, Y. Oumi and T. Sano, *J. Am. Chem. Soc.*, 2004, **126**, 9914–9915.

63 W. Wang, S. Banerjee, S. Jia, M. L. Steigerwald and I. P. Herman, *Chem. Mater.*, 2007, **19**, 2573–2580.

64 Y. Xia, Y. Xiong, B. Lim and S. E. Skrabalak, *Angew. Chem. Int. Ed.*, 2009, **48**, 60–103.

65 A. Puzder, A. J. Williamson, N. Zaitseva, G. Galli, L. Manna and A. P. Alivisatos, *Nano Lett.*, 2004, **4**, 2361–2365.

66 E. Drijvers, J. De Roo, J. C. Martins, I. Infante and Z. Hens, *Chem. Mater.*, 2018, **30**, 1178–1186.

67 A. L. Siegel and G. A. Baker, *Nanoscale Adv.*, 2021, **3**, 3980–4004.

68 J. A. Webb, W. R. Erwin, H. F. Zarick, J. Aufrecht, H. W. Manning, M. J. Lang, C. L. Pint and R. Bardhan, *J. Phys. Chem. C*, 2014, **118**, 3696–3707.

69 V. M. Kariuki, J. C. Hoffmeier, I. Yazgan and O. A. Sadik, *Nanoscale*, 2017, **9**, 8330–8340.

70 P. Pallavicini, G. Chirico, M. Collini, G. Dacarro, A. Donà, L. D'Alfonso, A. Falqui, Y. Diaz-Fernandez, S. Freddi, B. Garofalo, A. Genovese, L. Sironi and A. Taglietti, *Chem. Commun.*, 2011, **47**, 1315–1317.

71 A. J. Morris-Cohen, M. D. Donakowski, K. E. Knowles and E. A. Weiss, *J. Phys. Chem. C*, 2010, **114**, 897–906.

72 A. Hassinen, I. Moreels, K. De Nolf, P. F. Smet, J. C. Martins and Z. Hens, *J. Am. Chem. Soc.*, 2012, **134**, 20705–20712.

73 N. Gaponik, D. V Talapin, A. L. Rogach, K. Hoppe, E. V Shevchenko, A. Kornowski, A. Eychmüller and H. Weller, *J. Phys. Chem. B*, 2002, **106**, 7177–7185.

74 S. F. Wuister, C. de Mello Donegá and A. Meijerink, *J. Phys. Chem. B*, 2004, **108**, 17393–17397.

75 Y. Kim, J. H. Chang, H. Choi, Y.-H. Kim, W. K. Bae and S. Jeong, *Chem. Sci.*, 2020, **11**, 913–922.

76 L. Liu, K. Pan, K. Xu and J. Z. Zhang, *ACS Phys. Chem. Au*, 2022, **2**, 156–170.

77 N. Kirkwood, J. O. V Monchen, R. W. Crisp, G. Grimaldi, H. A. C. Bergstein, I. du Fossé, W. van der Stam, I. Infante and A. J. Houtepen, *J. Am. Chem. Soc.*, 2018, **140**, 15712–15723.

78 D. Segets, *KONA Powder Part. J.*, 2016, **33**, 48–62.

79 D. K. Sharma, S. Hirata, L. Bujak, V. Biju, T. Kameyama, M. Kishi, T. Torimoto and M. Vacha, *Nanoscale*, 2016, **8**, 13687–13694.

80 J. Zhang and H. Gu, *Dalton Trans.*, 2020, **49**, 6119–6126.

81 M. J. Fernée, C. Sinito, Y. Louyer, P. Tamarat and B. Lounis, *Nanotechnology*, 2013, **24**, 465703.

82 B. Gupta, M. M. Shehata, Y. Lee, L. E. Black, F. Ma, B. Hoex, C. Jagadish, H. H. Tan and S. Karuturi, *Sol. RRL*, 2023, **7**, 2200868.

83 M. Yamaguchi, A. Yamamoto, N. Uchida and C. Uemura, *Sol. Cells*, 1986, **19**, 85–96.

84 F. Zafar and A. Iqbal, *Proc. R. Soc. A Math. Phys. Eng. Sci.*, 2016, **472**, 20150804.

85 V. Brunetti, H. Chibli, R. Fiammengo, A. Galeone, M. A. Malvindi, G. Vecchio, R. Cingolani, J. L. Nadeau and P. P. Pompa, *Nanoscale*, 2013, **5**, 307–317.

86 European Commission, *COMMISSION DELEGATED DIRECTIVE (EU) 2015/863*, 2015.

87 H. Uchida, T. Ogata and H. Yoneyama, *Chem. Phys. Lett.*, 1990, **173**, 103–106.

88 D. G. Hendershot, D. K. Gaskill, B. L. Justus, M. Fatemi and A. D. Berry, *Appl. Phys. Lett.*, 1993, **63**, 3324–3326.

89 B. M. Cossairt, *Chem. Mater.*, 2016, **28**, 7181–7189.

90 R. L. Wells, C. G. Pitt, A. T. McPhail, A. P. Purdy, S. Shafieezad and R. B. Hallock, *Chem. Mater.*, 1989, **1**, 4–6.

91 C. G. Pitt, A. P. Purdy, K. T. Higa and R. L. Wells, *Organometallics*, 1986, **5**, 1266–1268.

92 R. L. Wells, *Coord. Chem. Rev.*, 1992, **112**, 273–291.

93 M. D. Healy, P. E. Laibinis, P. D. Stupik and A. R. Barron, *J. Chem. Soc. Chem. Commun.*, 1989, **6**, 359–360.

94 T. Douglas and K. H. Theopold, *Inorg. Chem.*, 1991, **30**, 594–596.

95 O. I. Mićić, C. J. Curtis, K. M. Jones, J. R. Sprague and A. J. Nozik, *J. Phys. Chem.*, 1994, **98**, 4966–4969.

96 A. A. Guzelian, J. E. B. Katari, A. V. Kadavanich, U. Banin, K. Hamad, E. Juban, A. P. Alivisatos, R. H. Wolters, C. C. Arnold and J. R. Heath, *J. Phys. Chem.*, 1996, **100**, 7212–7219.

97 R. L. Wells, S. R. Aubuchon, S. S. Kher, M. S. Lube and P. S. White, *Chem. Mater.*, 1995, **7**, 793–800.

98 O. I. Micic, J. R. Sprague, C. J. Curtis, K. M. Jones, J. L. Machol, A. J. Nozik, H. Giessen, B. Fluegel, G. Mohs and N. Peyghambarian, *J. Phys. Chem.*, 1995, **99**, 7754–7759.

99 R. Walsh, *Acc. Chem. Res.*, 1981, **14**, 246–252.

100 A. G. Baboul and H. B. Schlegel, *J. Am. Chem. Soc.*, 1996, **118**, 8444–8451.

101 S. Joung, S. Yoon, C.-S. Han, Y. Kim and S. Jeong, *Nanoscale Res. Lett.*, 2012, **7**, 93.

102 Y.-R. Luo, *Comprehensive handbook of chemical bond energies*, CRC Press, Boca Raton , 2007.

103 S. Tamang, C. Lincheneau, Y. Hermans, S. Jeong and P. Reiss, *Chem. Mater.*, 2016, **28**, 2491–2506.

104 M. T. Clarke, F. N. Viscomi, T. W. Chamberlain, N. Hondow, A. M. Adawi, J. Sturge, S. C. Erwin, J. S. G. Bouillard, S. Tamang and G. J. Stasiuk, *Commun. Chem.*, 2019, **2**, 1–7.

105 H. Zhu, A. Prakash, D. N. Benoit, C. J. Jones and V. L. Colvin, *Nanotechnology*, 2010, **21**, 255604.

106 J. R. Lakowicz, ed. J. R. Lakowicz, Springer US, Boston, MA, 1999, pp. 1–23.

107 E. M. Janke, N. E. Williams, C. She, D. Zherebetskyy, M. H. Hudson, L. Wang, D. J. Gosztola, R. D. Schaller, B. Lee, C. Sun, G. S. Engel and D. V Talapin, *J. Am. Chem. Soc.*, 2018, **140**, 15791–15803.

108 S. Adam, D. V Talapin, H. Borchert, A. Lobo, C. McGinley, A. R. B. de Castro, M. Haase, H. Weller and T. Möller, *J. Chem. Phys.*, 2005, **123**, 84706.

109 O. I. Mićić, J. Sprague, Z. Lu and A. J. Nozik, *Appl. Phys. Lett.*, 1996, **68**, 3150–3152.

110 S. Xu, J. Ziegler and T. Nann, *J. Mater. Chem.*, 2008, **18**, 2653–2656.

111 N. Kirkwood, A. De Backer, T. Altantzis, N. Winckelmans, A. Longo, F. V. Antolinez, F. T. Rabouw, L. De Trizio, J. J. Geuchies, J. T. Mulder, N. Renaud, S. Bals, L. Manna and A. J. Houtepen, *Chem. Mater.*, 2020, **32**, 557–565.

112 Y. Choi, D. Kim, Y. S. Shin, W. Lee, S. Orr, J. Y. Kim and J. Park, *Nanoscale*, 2022, **14**, 2771–2779.

113 K. C. Dümbgen, J. Leemans, V. De Roo, M. Minjauw, C. Detavernier and Z. Hens, *Chem. Mater.*, 2023, **35**, 1037–1046.

114 J. L. Stein, E. A. Mader and B. M. Cossairt, *J. Phys. Chem. Lett.*, 2016, **7**, 1315–1320.

115 J. M. Nedeljković, O. I. Mićić, S. P. Ahrenkiel, A. Miedaner and A. J. Nozik, *J. Am. Chem. Soc.*, 2004, **126**, 2632–2639.

116 O. I. Mićić, S. P. Ahrenkiel and A. J. Nozik, *Appl. Phys. Lett.*, 2001, **78**, 4022–4024.

117 M. Green, *Semiconductor Quantum Dots*, The Royal Society of Chemistry, 2014.

118 G. O. Eren, S. Sadeghi, H. Bahmani Jalali, M. Ritter, M. Han, I. Baylam, R. Melikov, A. Onal, F. Oz, M. Sahin, C. W. Ow-Yang, A. Sennaroglu, R. T. Lechner and S. Nizamoglu, *ACS Appl. Mater. Interfaces*, 2021, **13**, 32022–32030.

119 P. A. Gabrys, S. E. Seo, M. X. Wang, E. Oh, R. J. Macfarlane and C. A. Mirkin, *Nano Lett.*, 2018, **18**, 579–585.

120 C. J. Palmstrom, *Annu. Rev. Mater. Sci.*, 1995, **25**, 389–415.

121 H. Zhang, N. Hu, Z. Zeng, Q. Lin, F. Zhang, A. Tang, Y. Jia, L. S. Li, H. Shen, F. Teng and Z. Du, *Adv. Opt. Mater.*, 2019, **7**, 1801602.

122 O. I. Mićić, B. B. Smith and A. J. Nozik, *J. Phys. Chem. B*, 2000, **104**, 12149–12156.

123 N. Dai, A. Cavus, R. Dzakpasu, M. C. Tamargo, F. Semendy, N. Bambha, D. M. Hwang and C. Y. Chen, *Appl. Phys. Lett.*, 1995, **66**, 2742–2744.

124 P. Reiss, M. Carrière, C. Lincheneau, L. Vaure and S. Tamang, *Chem. Rev.*, 2016, **116**, 10731–10819.

125 S. Kim, T. Kim, M. Kang, S. K. Kwak, T. W. Yoo, L. S. Park, I. Yang, S. Hwang, J. E. Lee, S. K. Kim and S.-W. Kim, *J. Am. Chem. Soc.*, 2012, **134**, 3804–3809.

126 R. Toufanian, M. Chern, V. H. Kong and A. M. Dennis, *Chem. Mater.*, 2021, **33**, 1964–1975.

127 C. T. Smith, M. A. Leontiadou, P. C. J. Clark, C. Lydon, N. Savjani, B. F. Spencer, W. R. Flavell, P. O'Brien and D. J. Binks, *J. Phys. Chem. C*, 2017, **121**, 2099–2107.

128 S. H. Wei and A. Zunger, *Appl. Phys. Lett.*, 1998, **72**, 2011–2013.

129 S. Haubold, M. Haase, A. Kornowski and H. Weller, *ChemPhysChem*, 2001, **2**, 331–334.

130 R. Xie, D. Battaglia and X. Peng, *J. Am. Chem. Soc.*, 2007, **129**, 15432–15433.

131 J. Kim, Y. Kim, C. Boeffel, H. S. Choi, A. Taubert and A. Wedel, in *2022 IEEE 12th International Conference Nanomaterials: Applications & Properties (NAP)*, 2022, pp. 1–9.

132 R. Toufanian, M. Chern, V. H. Kong and A. M. Dennis, *Chem. Mater.*, 2021, **33**, 1964–1975.

133 U. T. D. Thuy, P. Reiss and N. Q. Liem, *Appl. Phys. Lett.*, 2010, **97**, 2–4.

134 D. A. Taylor, J. A. Teku, S. Cho, W.-S. Chae, S.-J. Jeong and J.-S. Lee, *Chem. Mater.*, 2021, **33**, 4399–4407.

135 Y. Li, X. Hou, X. Dai, Z. Yao, L. Lv, Y. Jin and X. Peng, *J. Am. Chem. Soc.*, 2019, **141**, 6448–6452.

136 Y.-H. Won, O. Cho, T. Kim, D.-Y. Chung, T. Kim, H. Chung, H. Jang, J. Lee, D. Kim and E. Jang, *Nature*, 2019, **575**, 634–638.

137 P. Ramasamy, N. Kim, Y.-S. Kang, O. Ramirez and J.-S. Lee, *Chem. Mater.*, 2017, **29**, 6893–6899.

138 X. Jiang, Z. Fan, L. Luo and L. Wang, *Micromachines*, 2022, 13, 709.

139 D. C. Gary and B. M. Cossairt, *Chem. Mater.*, 2013, **25**, 2463–2469.

140 D. C. Gary, B. A. Glassy and B. M. Cossairt, *Chem. Mater.*, 2014, **26**, 1734–1744.

141 P. M. Allen, B. J. Walker and M. G. Bawendi, *Angew. Chem. Int. Ed.*, 2010, **49**, 760–762.

142 D. K. Harris and M. G. Bawendi, *J. Am. Chem. Soc.*, 2012, **134**, 20211–20213.

143 Z. Liu, A. Kumbhar, D. Xu, J. Zhang, Z. Sun and J. Fang, *Angew. Chem. Int. Ed.*, 2008, **47**, 3540–3542.

144 E. Bang, Y. Choi, J. Cho, Y.-H. Suh, H. W. Ban, J. S. Son and J. Park, *Chem. Mater.*, 2017, **29**, 4236–4243.

145 E. Amberger and R. W. Salazar G, *J. Organomet. Chem.*, 1967, **8**, 111–114.

146 T. Matsumoto, S. Maenosono and Y. Yamaguchi, *Chem. Lett.*, 2004, **33**, 1492–1493.

147 H.-J. Byun, W.-S. Song and H. Yang, *Nanotechnology*, 2011, **22**, 235605.

148 W.-S. Song, H.-S. Lee, J. C. Lee, D. S. Jang, Y. Choi, M. Choi and H. Yang, *J. Nanoparticle Res.*, 2013, **15**, 1750.

149 R. Panzer, C. Guhrenz, D. Haubold, R. Hübner, N. Gaponik, A. Eychmüller and J. J. Weigand, *Angew. Chem. Int. Ed.*, 2017, **56**, 14737–14742.

150 A. Buffard, S. Dreyfuss, B. Nadal, H. Heuclin, X. Xu, G. Patriarche, N. Mézailles and B. Dubertret, *Chem. Mater.*, 2016, **28**, 5925–5934.

151 M. D. Tessier, K. De Nolf, D. Dupont, D. Sinnaeve, J. De Roo and Z. Hens, *J. Am. Chem. Soc.*, 2016, **138**, 5923–5929.

152 P. Yan, Y. Xie, W. Wang, F. Liu and Y. Qian, *J. Mater. Chem.*, 1999, **9**, 1831–1833.

153 S. Carenco, M. Demange, J. Shi, C. Boissière, C. Sanchez, P. Le Floch and N. Mézailles, *Chem. Commun.*, 2010, **46**, 5578–5580.

154 L. Li, M. Protière and P. Reiss, *Chem. Mater.*, 2008, **20**, 2621–2623.

155 N. Mordvinova, A. Vinokurov, T. Kuznetsova, O. I. Lebedev and S. Dorofeev, *Dalton Trans.*, 2017, **46**, 1297–1303.

156 T. M. Hood, S. Lau and R. L. Webster, *J. Am. Chem. Soc.*, 2022, **144**, 16684–16697.

157 P. Yu, Y. Shan, S. Cao, Y. Hu, Q. Li, R. Zeng, B. Zou, Y. Wang and J. Zhao, *ACS Energy Lett.*, 2021, **6**, 2697–2703.

158 J. R. McBride, A. D. Dukes, M. A. Schreuder and S. J. Rosenthal, *Chem. Phys. Lett.*, 2010, **498**, 1–9.

159 R. Xie, Z. Li and X. Peng, *J. Am. Chem. Soc.*, 2009, **131**, 15457–15466.

160 D. C. Gary, S. E. Flowers, W. Kaminsky, A. Petrone, X. Li and B. M. Cossairt, *J. Am. Chem. Soc.*, 2016, **138**, 1510–1513.

161 M. R. Friedfeld, J. L. Stein, A. Ritchhart and B. M. Cossairt, *Acc. Chem. Res.*, 2018, **51**, 2803–2810.

162 A. Ritchhart and B. M. Cossairt, *Angew. Chem. Int. Ed.*, 2018, **57**, 1908–1912.

163 M. R. Friedfeld, J. L. Stein and B. M. Cossairt, *Inorg. Chem.*, 2017, **56**, 8689–8697.

164 Y. Kwon, J. Oh, E. Lee, S. H. Lee, A. Agnes, G. Bang, J. Kim, D. Kim and S. Kim, *Nat. Commun.*, 2020, **11**, 1–15.

165 D. Erdemir, A. Y. Lee and A. S. Myerson, *Acc. Chem. Res.*, 2009, **42**, 621–629.

166 J. L. Stein, M. I. Steimle, M. W. Terban, A. Petrone, S. J. L. Billinge, X. Li and B. M. Cossairt, *Chem. Mater.*, 2017, **29**, 7984–7992.

167 J.-H. Jo, D.-Y. Jo, S.-H. Lee, S.-Y. Yoon, H.-B. Lim, B.-J. Lee, Y. R. Do and H. Yang, *ACS Appl. Nano Mater.*, 2020, **3**, 1972–1980.

168 F. Wöhler, *Ann. Phys. (Leipzig)*, 1828, **87**, 253–256.

169 H. Kopp, *Histroy of Chemistry*, Braunschweig, 1843.

170 P. S. Cohen and S. M. Cohen, *J. Chem. Educ.*, 1996, **73**, 883.

171 J. M. Goicoechea and H. Grützmacher, *Angew. Chem. Int. Ed.*, 2018, **57**, 16968–16994.

172 A. R. Jupp and J. M. Goicoechea, *J. Am. Chem. Soc.*, 2013, **135**, 19131–19134.

173 C. A. Tsipis and P. A. Karipidis, *J. Am. Chem. Soc.*, 2003, **125**, 2307–2318.

174 B. Stewart, A. Harriman and L. J. Higham, *Organometallics*, 2011, **30**, 5338–5343.

175 M. B. Geeson, A. R. Jupp, J. E. McGrady and J. M. Goicoechea, *Chem. Commun.*, 2014, **50**, 12281–12284.

176 L. Tiwari, V. Kumar, B. Kumar and D. Mahajan, *RSC Adv.*, 2018, **8**, 21585–21595.

177 E. J. Jacobsen, R. E. TenBrink, L. S. Stelzer, K. L. Belonga, D. B. Carter, H. K. Im, W. Bin Im, V. H. Sethy, A. H. Tang, P. F. VonVoigtlander and J. D. Petke, *J. Med. Chem.*, 1996, **39**, 158–175.

178 C. L. Cioffi, N. Dobri, E. E. Freeman, M. P. Conlon, P. Chen, D. G. Stafford, D. M. C. Schwarz, K. C. Golden, L. Zhu, D. B. Kitchen, K. D. Barnes, B. Racz, Q. Qin, E. Michelotti, C. L. Cywin, W. H. Martin, P. G. Pearson, G. Johnson and K. Petrukhin, *J. Med. Chem.*, 2014, **57**, 7731–7757.

179 A. R. Jupp, G. Trott, É. Payen De La Garanderie, J. D. G. Holl, D. Carmichael and J. M. Goicoechea, *Chem. Eur. J.*, 2015, **21**, 8015–8018.

180 E. N. Faria, A. R. Jupp and J. M. Goicoechea, *Dalton Trans.*, 2021, **50**, 6991–6996.

181 E. N. Faria, A. R. Jupp and J. M. Goicoechea, *Chem. Commun.*, 2017, **53**, 7092–7095.

182 Y. H. Wu, Z. F. Li, W. P. Wang, X. C. Wang and Z. J. Quan, *Eur. J. Org. Chem.*, 2017, **2017**, 5546–5553.

183 W.-P. Wang, X.-H. Cui, M. Li, X.-C. Wang and Z.-J. Quan, *Asian J. Org. Chem.*, 2022, **11**, e202200124.

184 T. P. Robinson and J. M. Goicoechea, *Chem. Eur. J.*, 2015, **21**, 5727–5731.

185 G. P. Papp and S. A. Buckler, *J. Org. Chem.*, 1966, **31**, 588–589.

186 L. G. Vaughan and R. V. J. Lindsey, *J. Org. Chem.*, 1968, **33**, 3088–3089.

187 A. C. Behrle and J. A. R. Schmidt, *Organometallics*, 2013, **32**, 1141–1149.

188 M. Itazaki, T. Matsutani, T. Nochida, T. Moriuchi and H. Nakazawa, *Chem. Commun.*, 2020, **56**, 443–445.

189 T. M. Horsley Downie, J. W. Hall, T. P. Collier Finn, D. J. Liptrot, J. P. Lowe, M. F. Mahon, C. L. McMullin and M. K. Whittlesey, *Chem. Commun.*, 2020, **56**, 13359–13362.

190 B. Zhang, X. Ma, B. Yan, C. Ni, H. Yu, Z. Yang and H. W. Roesky, *Dalton Trans.*, 2021, **50**, 15488–15492.

191 T. M. Horsley Downie, M. F. Mahon, J. P. Lowe, R. M. Bailey and D. J. Liptrot, *ACS Catal.*, 2022, **12**, 8214–8219.

192 S. V. F. Beddoe, S. D. Cosham, A. N. Kulak, A. R. Jupp, J. M. Goicoechea and G. Hyett, *Dalton Trans.*, 2018, **47**, 9221–9225.

Chapter 2

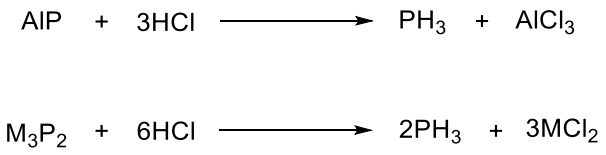
Reactivity of phosphinecarboxamide in solution

2.1 Introduction and objectives

2.1.1 PH_3 generation in solution

Phosphine gas is widely used in the semiconductor industry, with up to 40 million pounds (lbs) produced in the US alone in 2019.[1] However, its handling and storage in research laboratories remains challenging as PH_3 is a highly toxic and pyrophoric gas. Motivated by these challenges, recent years have seen the development of *in situ* PH_3 generation methods for its safer handling.

PH_3 can be produced by the acidification of metal phosphides, and then used immediately *in situ* or *ex situ*. PH_3 can be generated *in situ* from AlP, Mg_3P_2, Ca_3P_2, and Zn_3P_2 upon addition of HCl (Scheme 2.1).[2,3] For *ex situ* use, the PH_3 produced is commonly dried through a P_2O_5 column to remove residual water.



Scheme 2.1: *in situ* PH_3 generation by the acidification of metal phosphides (M = Mg, Ca, or Zn).

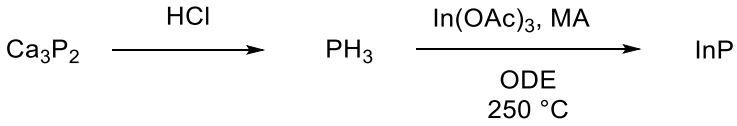
Facile *in situ* generation methods have made conducting research with PH_3 more accessible, avoiding the need to handle pressurised gas cylinders containing a toxic, highly flammable gas. *In situ* PH_3 generation by the acidification of Zn_3P_2 has gained popularity in organophosphorus chemistry, for example in the *C*-phosphorylation of pyridine,[4] as well as enabling novel umpolung strategies for preparing di-*tert*-alkylphosphine derivatives.[5]

2.1.2 PH_3 as a precursor to colloidal metal phosphide nanoparticles

Phosphine gas is a ubiquitous phosphide source in atomic layer deposition (ALD),[6] metal-organic vapour deposition (MOVD),[7] and chemical vapour deposition (CVD).[8] The utility of PH_3 in the preparation of semiconductor materials in gas and solid-gas phase reactions has motivated exploration for its use in analogous colloidal nanoparticle systems.

Preparations of various colloidal metal phosphide nanoparticles take advantage of *ex situ* PH_3 generation for several reasons. Firstly, the inorganic metal phosphide precursors used to generate PH_3 are insoluble in apolar solvents. Their introduction into the reaction mixture would destabilise colloidal nanoparticles and result in precipitation out of solution.[9] Secondly, strong acids such as HCl are required to produce PH_3, which in turn also react with most metal phosphide nanoparticles. Addition of HCl to the metal phosphide source in solution (e.g. Zn_3P_2) would also result in the decomposition of any colloidal metal phosphide nanoparticles formed. Hence, the use of *ex situ* PH_3 is preferred, as it prevents product decomposition and colloidal destabilisation.

Reiss and co-workers were first to report using *ex situ* prepared PH_3 as a precursor to InP QDs. They showed that upon acidification with HCl, Ca_3P_2 generates PH_3, which in turn can be bubbled into a 1-octadecene (ODE) solution containing indium acetate and myristic acid at 250 °C to form InP QDs (Scheme 2.2).[3] In their preparation, PH_3 produced was first passed through a column containing P_2O_5 to remove residual water, before bubbling into solution. Drying of the gas was critical to minimise QD surface hydrolysis and oxidation, which InP is particularly susceptible to.[10]



Scheme 2.2: Preparation of InP QDs using PH_3 formed from the acidification of calcium phosphide by hydrochloric acid. MA = myristic acid ($HOOC(CH_2)_{12}CH_3$). ODE = 1-octadecene.

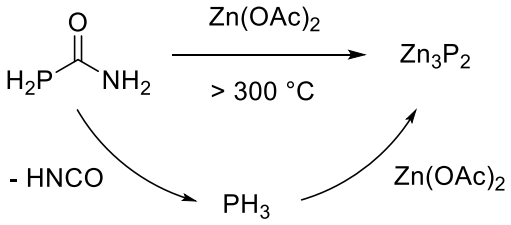
Reiss's *ex situ* PH_3 method using calcium phosphide has been successfully applied in the preparation of various colloidal metal phosphide nanoparticles. Maio *et al.* reported the preparation of monodisperse Cd_6P_7 nanoparticles this way, revealing their unusual stoichiometry by energy dispersive X-ray (EDX) spectroscopic analysis.[11] Mana *et al.* prepared Cu_3P nanoparticles with unique platelet morphology using *ex situ* PH_3,[12] while Eychmüller and co-workers showed that Zn_3P_2 QDs could also be prepared by this method.[13]

2.1.3 Phosphinecarboxamide as an *in situ* PH_3 source

Phosphinecarboxamides are an attractive phosphorus precursor from a materials perspective. They are relatively easy to prepare and handle compared to typical phosphorus precursors, being stable in air for several days. Moreover, a substantial library of *N*-functionalised phosphinecarboxamides are known by derivatisation of the 2-phosphaethynolate salt from a variety of primary amines.[14,15] Most importantly, our early work studying the parent phosphinecarboxamide revealed that it decomposes above 75 °C to form PH_3, as observed by ^{31}P NMR spectroscopy.

Hyett and co-workers were inspired by these observations, and were interested in whether the PH_3 produced upon heating phosphinecarboxamide could be used *in situ* to form zinc phosphide. They showed that Zn_3P_2 thin films could be prepared by the chemical vapour deposition of phosphinecarboxamide with zinc acetate at > 300 °C.[16] The authors

suggested that phosphinecarboxamide acts as a 'masked' phosphine source, rapidly decomposing upon heating to release PH_3, which then reacts with zinc salts to produce a thin film (Scheme 2.3).



Scheme 2.3: Chemical vapour deposition of Zn_3P_2 thin films by the *in situ* generation of PH_3 by thermal decomposition of phosphinecarboxamide.[16]

The *in situ* generation of PH_3 by phosphinecarboxamide upon heating motivated us to explore whether this unique reactivity could be reproduced in the solution phase. Moreover, we were encouraged by well-established methods using PH_3 as a phosphide source for colloidal metal phosphide nanoparticles, in particular, the preparation of InP QDs. In addition to the air- and moisture-tolerance of phosphinecarboxamides, their potential to act as an *in situ* PH_3 source has distinct advantages over *ex situ* methods, avoiding the generation of the highly flammable and toxic gaseous species, that in turn must be transferred into solution.

2.1.4 Chapter outline

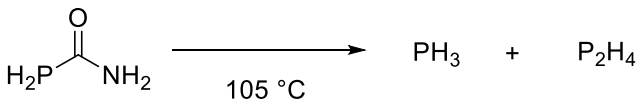
This chapter will describe the solution phase reactivity of phosphinecarboxamide. The use of phosphinecarboxamide as a masked PH_3 source in solution is explored, in addition to its reactivity with indium salts and amine capping ligands.

The synthesis of the novel air-stable *N*-hexadecylphosphinecarboxamide (**1**) is also reported. The ability of **1** to act as a source of PH_3 in solution is discussed.

2.2 Reactions of phosphinecarboxamide in solution

2.2.1 Thermal decomposition of phosphinecarboxamide

To explore *in situ* PH_3 reactivity in solution, a d_5-pyridine solution of phosphinecarboxamide (0.25 M) was heated at 105 °C and monitored by ^{31}P NMR spectroscopy (Scheme 2.4).



Scheme 2.4: Thermal decomposition of $H_2PC(O)NH_2$ in d_5-pyridine.

Upon heating, the phosphinecarboxamide signal at −134.0 ppm decreases in intensity relative to the PPh_3 internal standard (−5.0 ppm; Figure 2.1). In addition, after 10 minutes of heating two new peaks emerge at −211.2 ppm and −242.1 ppm. The proton-coupled ^{31}P NMR spectra reveal a complex multiplet at −211.2 ppm and a quartet at −242.1 ppm (Figure 2.2). The quartet is assigned to dissolved phosphine (PH_3) with $^1J_{H–P}$ = 189 Hz, whilst the multiplet is characteristic of dissolved diphosphane (P_2H_4), arising from a $A_2XX'A'_2$ splitting system due to magnetic nonequivalence.[17]

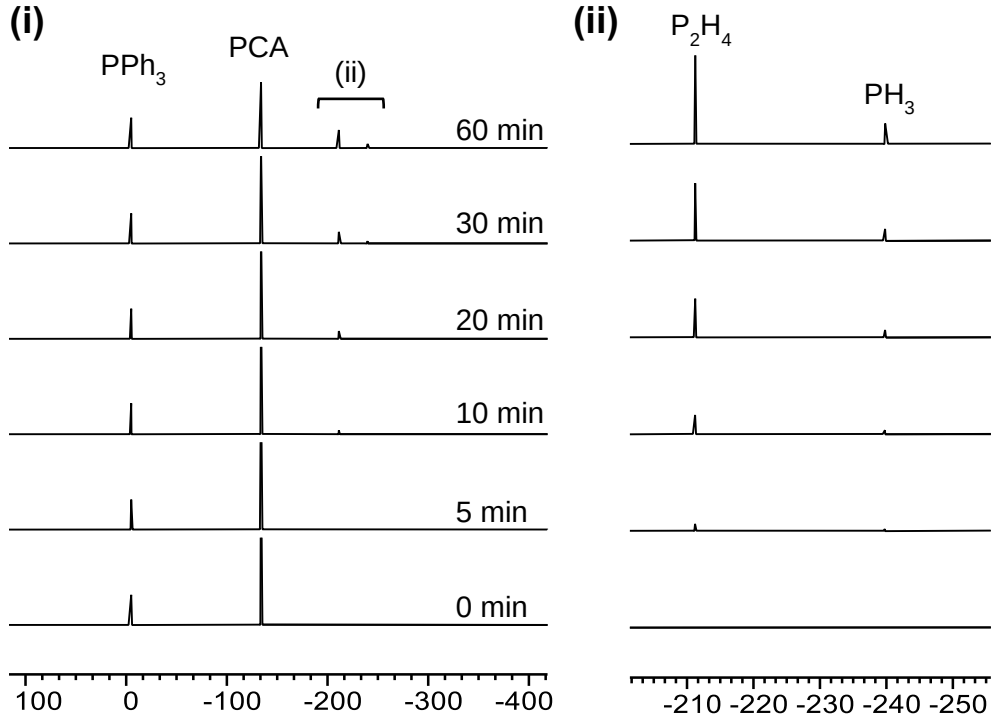


Figure 2.1: $^{31}P\{^{1}H\}$ NMR spectra of (i) d_5-pyridine containing phosphinecarboxamide heated at 105 °C for 0–60 min; (ii) expanded region to show characteristic PH_3 and P_2H_4 resonances. PPh_3 is present as an internal standard.

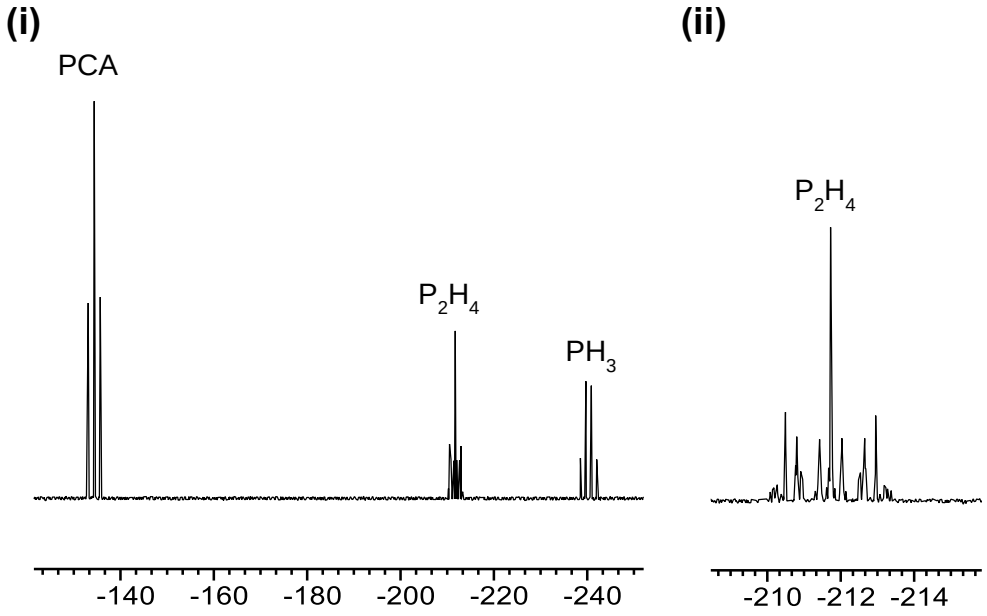
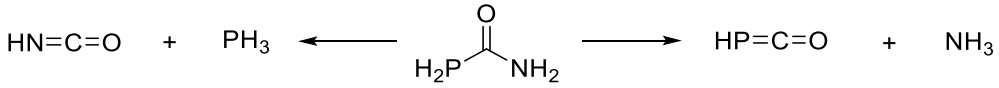


Figure 2.2: ^{31}P NMR spectrum of (i) d_5-pyridine containing phosphinecarboxamide heated at 105 °C for 60 min; (ii) expanded region to show the multiplet corresponding to P_2H_4.

The formation of PH_3 and P_2H_4 upon thermal decomposition of phosphinecarboxamide can be rationalised by several plausible mechanisms (Scheme 2.5). Thermal decomposition could result in the formation of PH_3 and isocyanic acid. Whilst in this case P_2H_4 is not formally produced, it is a known product of the photolytic disproportionation of PH_3, therefore could feasibly be formed at the elevated temperature of this experiment.[18] Alternatively, phosphinecarboxamide could decompose to form the phosphorus analogue of isocyanic acid, HPCO, and ammonia. HPCO is unstable, even at low temperature, and decomposes rapidly into PH_3 and P_2H_4.[19] A base-assisted mechanism, whereby the weakly basic pyridine solvent deprotonates phosphinecarboxamide, also cannot be ruled out. Our group has shown that the deprotonation of phosphinecarboxamide results in the rapid formation of PH_3 and NCO^-.[20] Further discussion on the mechanism of phosphinecarboxamide decomposition will be detailed later in this chapter (Section 2.3.3).



Scheme 2.5: Potential thermal decomposition pathways of phosphinecarboxamide.

2.2.2 Reaction of phosphinecarboxamide with indium salts

Having demonstrated the formation of PH_3 upon heating phosphinecarboxamide in solution, we sought to investigate utilising the PH_3 generated as a phosphide source by reaction with indium salts.

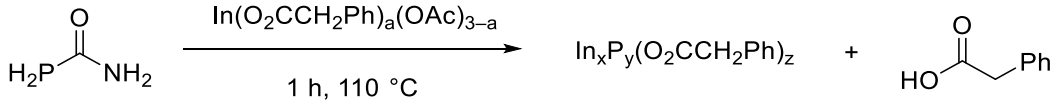
As discussed in Chapter 1, thermodynamically stable magic-sized clusters (MSCs) of InP are known to form at > 100 °C, well below common QD growth temperatures. InP MSCs are typically prepared by reacting $P(SiMe_3)_3$ with indium carboxylates.[21–23] Moreover,

the clusters may be characterised by common molecular analytical techniques, such as NMR spectroscopy, mass spectrometry, and single crystal X-ray diffraction. The formation of MSCs from common phosphorus precursors, and their associated role in QD particle growth evolution, makes them relevant targets for evaluating whether phosphinecarboxamide-generated PH_3 can be utilised as a phosphide source.

To investigate this, reactions were carried out following the procedure reported by Cossairt and co-workers.[21] In their procedure, phenylacetate ligands ($OOCCH_2Ph$) were used instead of carboxylates with long-chain alkyl substituents to prepare the InP MSCs. Phenylacetate was found to both stabilise the MSCs and enable the isolation of single crystals. MSCs with surfactant ligands (myristate, $OOC(CH_2)_{12}CH_3$) are also accessible, although not crystallographically characterised.[23]

2.2.2.1 Synthesis and characterisation of phenylacetate-capped InP MSCs

In a typical reaction, indium phenylacetate and phosphinecarboxamide were heated in a solution of toluene at 110 °C for 1 hour, during which time the solution turned yellow, then orange (Scheme 2.6).



Scheme 2.6: Reaction of $H_2PC(O)NH_2$ with indium phenylacetate (a = 0.40−0.62).

$^{31}P\{^1H\}$ NMR analysis initially showed a broad, featureless resonance around –200 ppm, as well as complete consumption of phosphinecarboxamide (–134.0 ppm). To improve the resolution of the broad peak, the NMR experiment was repeated with an increased pulse delay (0.8039 s) to account for changes in T_1 and T_2 relaxation times and a greater number of scans (22,131) to improve signal-to-noise. Our motivation for selecting these

parameters was informed by Stein *et al.*, who used long relaxation delays (20 s) in their ^{31}P NMR analysis monitoring $In_{37}P_{20}(O_2CCH_2Ph)_{51}$ cluster conversion reactions.[24] Although the authors did not comment on their rationale for using a longer relaxation delay, it alludes to the fact that the relaxation times of ^{31}P nuclei in InP MSCs are relatively long.

Using the modified NMR experimental parameters described, numerous peaks between –180 and –250 ppm could be resolved in the $^{31}P\{^1H\}$ NMR spectrum (Figure 2.3). The resonances in this region are characteristic of In-rich InP clusters, and closely agree with spectra of literature known MSCs reported by Cossairt and Kim.[21,22,25]

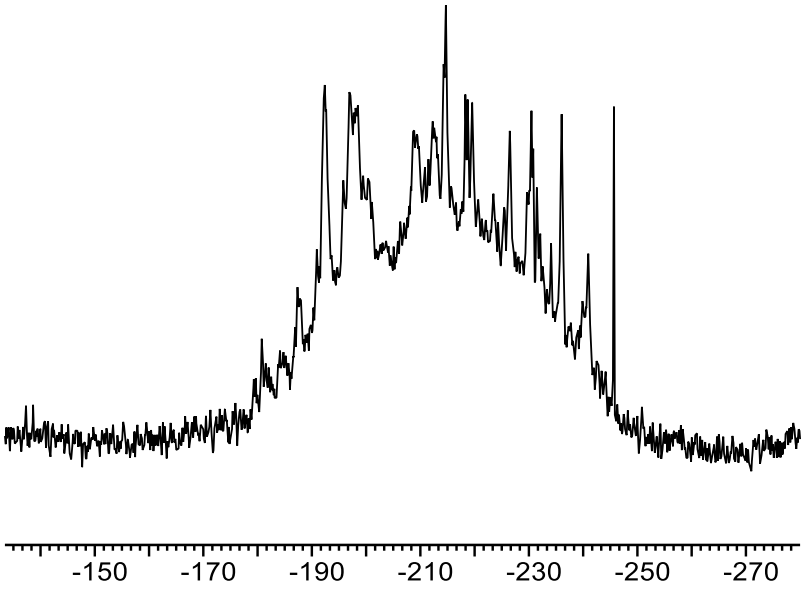


Figure 2.3: $^{31}P\{^1H\}$ NMR spectrum of d_8-THF containing phenylacetate-capped InP MSCs.

The $^{31}P\{^1H\}$ NMR spectrum obtained for phenylacetate-capped InP MSCs prepared from phosphinecarboxamide contains considerably more peaks than would be expected for a single, atomically defined product. For example, NMR analysis of $In_{37}P_{20}(O_2CR)_{51}$ MSCs (O_2CR = phenylacetate or myristate) reported by Cossairt and co-workers reveal

only ten distinct phosphorus cluster environments. In our case, the observation of many signals may be rationalised by the formation of multiple InP cluster products. Several cluster compositions are known, including the smaller $In_{29}P_{14}(O_2CC_{13}H_{27})_{45}$ cluster, which Ritchhart *et al.* show forms when excess $P(SiMe_3)_3$ is added to the parent $In_{37}P_{20}(O_2CR)_{51}$ MSC.[25] Kim and co-workers also showed that substitution of carboxylate ligands with chloride ions results in the formation of new InP MSCs with distinct ^{31}P NMR environments compared to the parent cluster.[22] The presence of multiple cluster products in our case seems reasonable, considering that the indium precursor used also contains residual acetate groups. The additional signals may arise from clusters with differing stoichiometries of phenylacetate and acetate capping ligands. Due to the unknown composition of the InP MSCs formed, assignment of individual ^{31}P NMR environments is not possible.

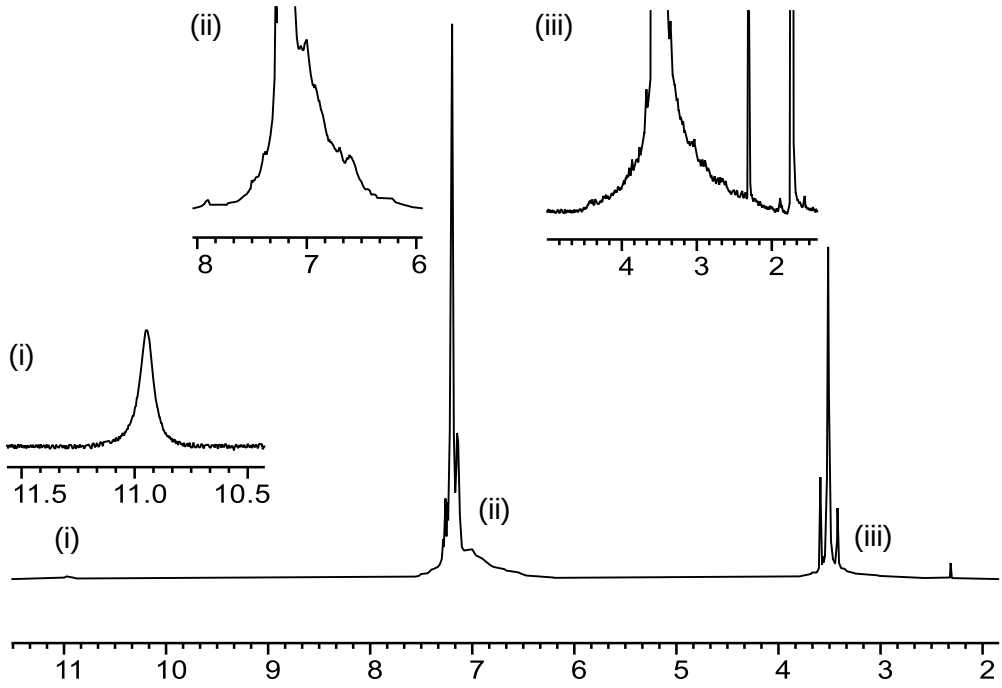


Figure 2.4: ^1H NMR spectrum of d_8-THF containing phenylacetate-capped InP MSCs. Insets show broad resonances corresponding to: (i) carboxylic acid group; (ii) aromatic region; and (iii) methylene peaks.

^{1}H NMR spectroscopy analysis also supports the formation of InP MSCs, revealing broad peaks at 3.50 ppm and 7.00 ppm. These broad peaks correspond to the methylene CH_2 and aromatic CH environments, respectively, and are characteristic of non-equivalent phenylacetate capping ligands (Figure 2.4). Broadening of ^{1}H NMR signals is expected, as the phenylacetate surface ligands may adopt multiple coordination modes, as well as different orientations of the benzyl side chain. Cossairt and co-workers highlighted this, showing that the phenylacetate ligands could adopt: bidentate; bidentate and dative; symmetric bridging; and asymmetric bridging modes (Figure 2.5).[21] In addition to the broad resonances attributed to InP MSCs, residual phenylacetic acid produced by the reaction as a by-product is observed. Phenylacetic acid is characterised by the low intensity, broad peak at 10.95 ppm, a multiplet at 7.15−7.25 ppm, and a singlet at 3.51 ppm, corresponding to the acidic COOH proton, aromatic CH protons, and the methylene CH_2 protons, respectively.

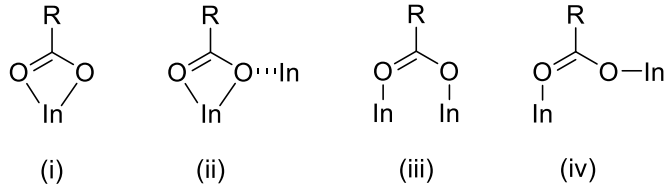


Figure 2.5: Schematic representation of observed binding modes of phenylacetate ligands on InP MSCs: (i) bidentate; (ii) bidentate + dative; (iii) symmetric bridging; (iv) asymmetric bridging.[21]

UV-Vis spectroscopy can also be used to characterise InP MSCs, which typically have dominant absorption peaks between 360 and 408 nm.[26] UV-Vis characterisation shows a broad absorption shoulder at 414 nm (Figure 2.6). The absence of a well-defined absorption peak is consistent with our assumption that several cluster species are present in the sample. Inhomogeneity in particle size is known to cause peak broadening in the absorption spectra of both QDs and MSCs.[26,27] Whilst this value is on the higher end for

known InP MSCs, it is still considerably blue-shifted from expected wavelengths for InP QDs (*ca.* 450−500 nm). Hence, the absorption shoulder at 414 nm supports characterisation of the products as highly quantum confined InP clusters, and not QDs.

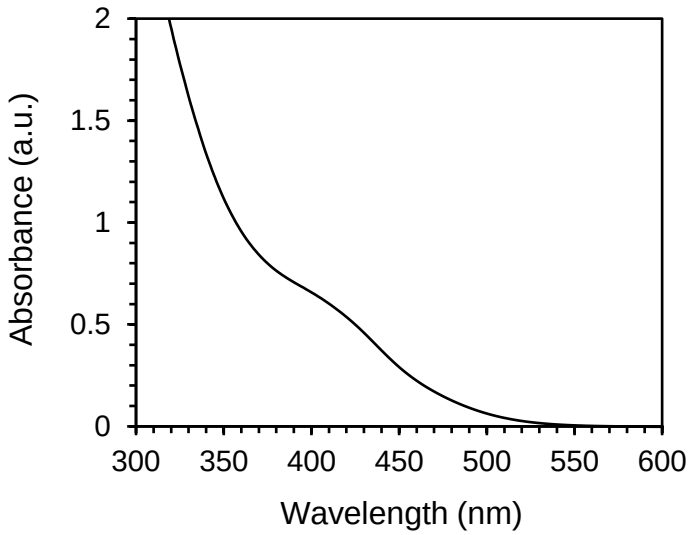


Figure 2.6: UV-Vis spectrum of a toluene solution containing phenylacetate-capped InP MSCs.

Matrix-assisted laser desorption/ionization time-of-flight (MALDI-TOF) mass spectrometry (MS) has been applied to analyse a variety of inorganic materials, including gold nanoclusters, metal oxide nanoparticles, and QDs.[28–30] Soft ionization techniques, such as MALDI-TOF MS, are preferred for colloidal materials which are particularly sensitive to ligand ablation, owing to their high concentration on particle surfaces.[31] The use of a matrix, such as *trans*-2-[3-(4-*tert*-butylphenyl)-2-methyl-2-propenylidene]-malononitrile (DCTB) or dithranol (DT) to ionize the colloidal nanoparticles in MALDI-TOF MS helps to minimise sample ablation and fragmentation.

Whilst NMR and UV-Vis spectroscopic data is consistent with known InP MSCs, we were inspired by reports using mass spectrometry to unambiguously confirm the identity InP MSCs in the absence of single crystal X-ray diffraction data. Jensen and co-workers

recently monitored the evolution, and subsequent consumption of InP MSCs during QD growth.[32] They used MALDI-TOF MS to reveal small InP clusters with masses of around 10 kDa, and found that despite the soft ionization method employed, the clusters produced broad, heterogenous *m*/*z* peaks. More recently, Stein *et al.* used this technique to follow the conversion of InP MSCs into Cd_3P_2 nanoclusters upon topotactic cation exchange with Cd^{2+}.[24]

MALDI-TOF MS analysis of a 1:1 mixture of the phenylacetate-capped InP MSCs and DCTB matrix revealed a broad mass peak at around 8000 Da (Figure 2.7), in addition to an intense peak at 8492 Da. Cossairt and co-workers observed a similarly sharp peak at 8500 Da, tentatively assigning it to a $[In_{31}P_{20}(O_2CCH_2Ph)_{32}]^+$ fragment.[24] Once again, without knowing the composition of InP MSCs present in the sample, it is difficult to assign the peak accurately. However, the presence of the broad heterogeneous peak at 8000 Da is consistent with the presence of InP MSCs, similar in composition to those discussed earlier. This assignment is strengthened by the absence of any mass peaks in the higher mass region (> 25 kDa), confirming that the sample does not contain larger nanoparticles.[32]

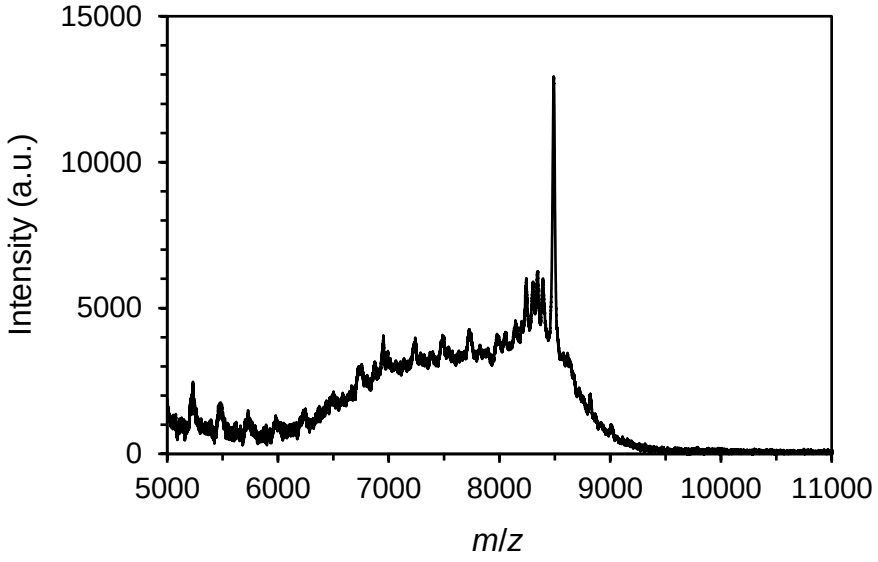
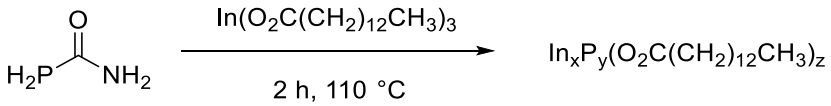


Figure 2.7: MALDI-TOF mass spectrum of a THF solution containing a 1:1 v/v mixture of phenylacetate-capped InP MSCs and DCTB matrix.

Further confirmation of the character of the MSCs is their ability to act as single-source precursors to InP QDs, which will be discussed in Chapter 3.

2.2.2.2 Synthesis and characterisation of myristate-capped InP MSCs

In a bid to further validate the production of InP MSCs using phosphinecarboxamides, myristate-capped InP MSCs were also targeted in a test reaction. Following a similar preparation to the phenylacetate-capped InP MSCs, indium myristate and phosphinecarboxamide were combined at 110 °C in toluene, and stirred for 2 hours (Scheme 2.7).



Scheme 2.7: Reaction of $H_2PC(O)NH_2$ with indium myristate.

The $^{31}P\{^{1}H\}$ NMR spectrum of the crude product showed two singlets at −134.5 ppm and −242.2 ppm, as well as broad peaks between −190 ppm and −240 ppm (Figure 2.8). The

singlet at −134.5 ppm is assigned to phosphinecarboxamide, while the peak at −242.2 ppm is consistent with dissolved PH_3. Once again, the signals between −190 ppm and −240 ppm suggest the formation of InP MSCs, and closer inspection of the weak signals reveal at least seven broad resonances. Unlike the phenylacetate-capped MSCs, the myristate-capped InP MSCs contain much fewer resonances, suggesting the formation of potentially just one cluster product.

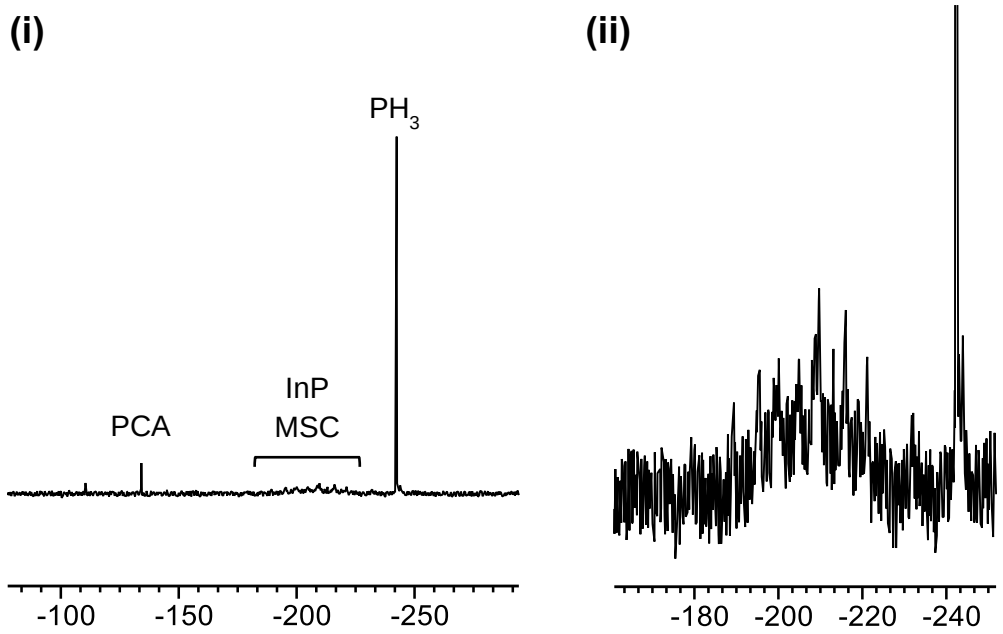


Figure 2.8: $^{31}P\{^{1}H\}$ NMR spectrum of (i) C_6D_6 solution of myristate-capped InP MSCs; (ii) expanded region to show signals corresponding to InP MSCs.

The NMR, UV-Vis, and MALDI-TOF MS data presented in this section are consistent with the successful preparation of phenylacetate- and myristate-capped InP MSCs. The successful preparation of InP MSCs from phosphinecarboxamide offers a new approach to their isolation and study. Whilst no further investigation of the clusters was carried out, there may be the potential to identify new InP MSC compositions and chemistries through this novel approach.

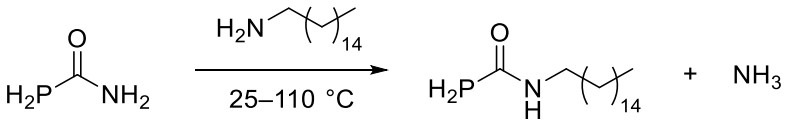
The preparation of InP MSCs using phosphinecarboxamide represents relevant proof-of-concept for its suitability as a phosphorus precursor to InP QDs. Moreover, it represents the first example of using phosphinecarboxamide as an *in situ* PH_3 source in solution.

2.2.3 Reaction of phosphinecarboxamide with hexadecylamine

We were interested in understanding the compatibility of phosphinecarboxamide with common amine capping ligands used in the preparation of InP QDs, given the promising reactivity shown with indium carboxylates.

Amines are known to be effective capping ligands for InP QDs, binding strongly to InP {111} facets, whilst providing colloidal stability through long-chain hydrocarbon subtituents.[33] Common examples of amine capping ligands used in InP QD preparation include hexadecylamine, oleylamine, and trioctylamine.[34,35] Of these, we chose to study hexadecylamine as it is a solid which can be easily transferred into an inert atmosphere for use in the glovebox. In contrast, oleylamine and trioctylamine are both liquids and require more rigorous drying and degassing.

No reaction was observed when phosphinecarboxamide and hexadecylamine were combined in d_5-pyridine. However, upon heating the formation of the transamidated product *N*-hexadecylphosphinecarboxamide (**1**) was observed (Scheme 2.8).



Scheme 2.8: Reaction of $H_2PC(O)NH_2$ with hexadecylamine to afford **1**.

The ^{1}H NMR spectra shows the doublet corresponding to the phosphanyl PH_2 environment of phosphinecarboxamide (3.84 ppm, $^{1}J_{P–H}$ = 209 Hz) decreasing in intensity upon heating, as well as the emergence of a new doublet at 3.81 ppm ($^{1}J_{P–H}$ = 208 Hz), assigned to the PH_2 group of **1** (Figure 2.9). As the solution is heated, the non-equivalent NH amide protons of phosphinecarboxamide (8.52 and 9.01 ppm) also decrease in intensity, whilst the NH environment of **1** emerges at 9.20 ppm. The formation of **1** can also be monitored by changes in intensity of the CH_2 proton environments adjacent to the amine and amide in hexadecylamine and **1**, respectively. As the reaction proceeds, the multiplet at 2.74 ppm, corresponding to the CH_2 group adjacent to the amine of hexadecylamine decreases in intensity, whilst a new multiplet at 3.48 ppm increases in intensity. The multiplet at 3.48 ppm is assigned to the methylene moiety adjacent to the amide environment of **1**. This multiplet appears at a higher chemical shift than that of the free amine, consistent with its close proximity to the deshielding phosphinecarboxamide π-system. The new amide and adjacent methylene peaks of **1** are clearly visible above 40 °C, and continue to grow with heating.

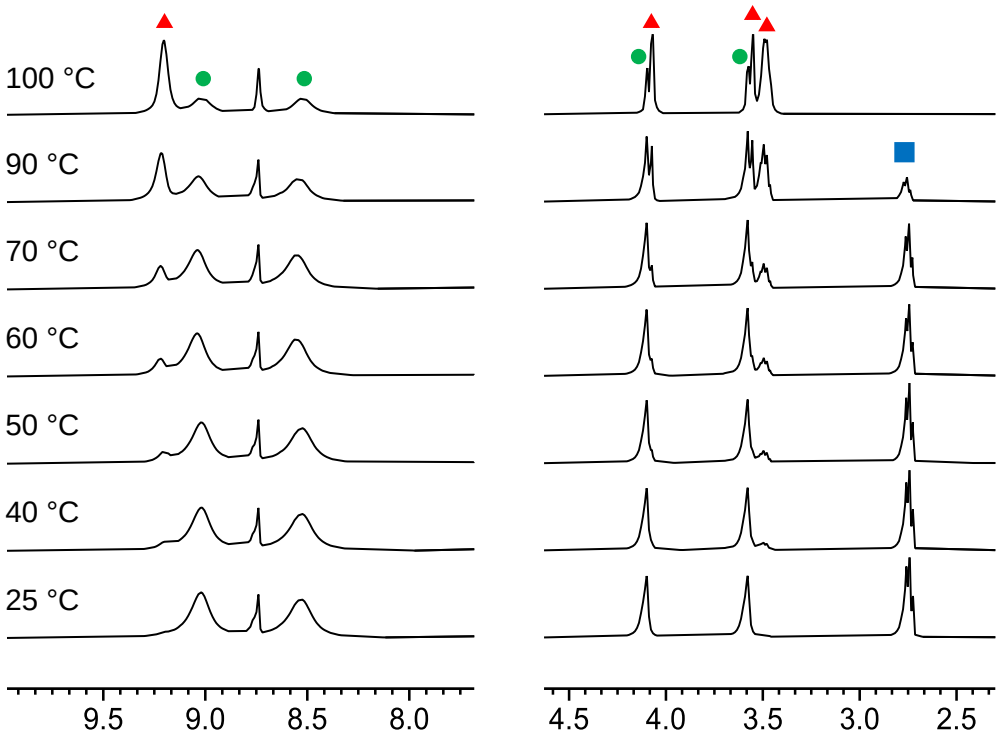


Figure 2.9: ^{1}H NMR spectra of d_5-pyridine containing phosphinecarboxamide and hexadecylamine after heating at 25−100 °C for two minutes. Red triangle = **1**; green circle = $H_2PC(O)NH_2$; blue square = hexadecylamine.

The ^{31}P NMR spectra show the phosphinecarboxamide peak at −134.5 ppm decrease in intensity, whilst a new peak emerges at −133.0 ppm (Figure 2.10). The peak at −133.0 ppm is unambiguously assigned to the PH_2 group in **1** by the proton-coupled ^{31}P NMR spectrum, which reveals a triplet splitting pattern with $^{1}J_{H-P}$ = 208 Hz. This coupling is equal to the coupling constant measured for the PH_2 doublet by ^{1}H NMR, and is characteristic of an *N*-functionalised phosphinecarboxamide.[14,36]

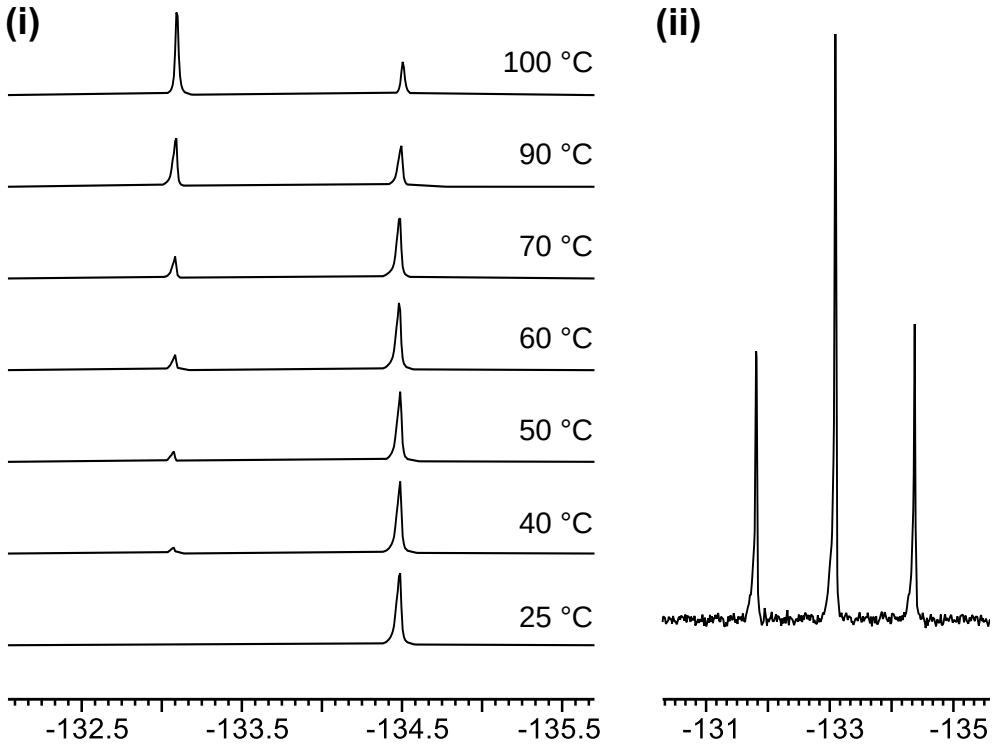
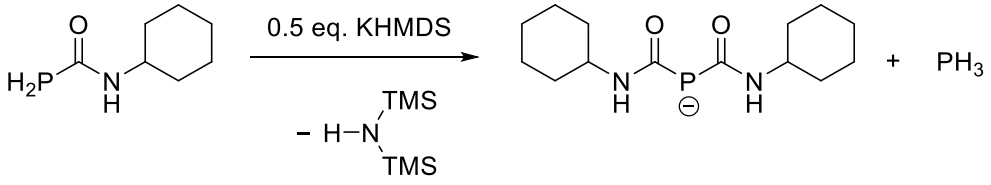


Figure 2.10: (i) $^{31}P\{^{1}H\}$ NMR spectra of d_5-pyridine containing phosphinecarboxamide and hexadecylamine after heating at 25−100 °C for two minutes; (ii) ^{31}P NMR of **1** after heating to 100 °C.

The transamidation of phosphinecarboxamide by hexadecylamine to form **1** is the first example of this type of reactivity for the phosphinecarboxamide moiety. In unpublished work, our group has shown that the phosphinecarboxamide moiety is susceptible to nucleophilic attack. For example, when *N*-cyclohexylphosphinecarboxamide is deprotonated by half an equivalent of KHMDS, the resulting phosphide will attack remaining unreacted molecules to form the di(cyclohexylcarboxamido)phosphide (Scheme 2.9). [37]



Scheme 2.9: Example of nucleophilic reaction at *N*-cyclohexylphosphinecarboxamide.[37] TMS = $SiMe_3$.

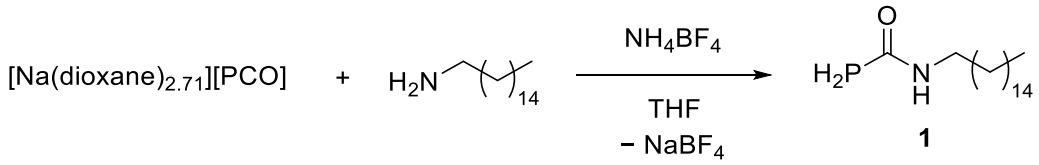
In this case the reaction favours transamidation, presumably due to the fact that hexadecylamine is a weak base (pK_a = 10.63) and unable to deprotonate phosphinecarboxamide.

2.3 *N*-hexadecylphosphinecarboxamide (1)

The facile transamidation of phosphinecarboxamide with hexadecylamine requires examination of **1** as a potential *in situ* PH_3 source in solution. If **1** does not display the same thermal decomposition characteristics as phosphinecarboxamide, then avoiding amine capping ligands in subsequent experiments may be necessary.

2.3.1 Synthesis of 1

1 was independently prepared from the 2-phosphaethynolate anion and hexadecylamine in the presence of ammonium tetrafluoroborate (Scheme 2.10). The reaction proceeded quickly, as evidenced by the change in colour of the solution from orange to yellow after 30 minutes of stirring. The hexadecyl substituent solubilises **1** in non-polar solvents, allowing for its straightforward separation from the $NaBF_4$ by-product by extraction with toluene.



Scheme 2.10: Synthesis of **1** from hexadecylamine and the 2-phosphaethynolate anion.

2.3.2 Characterisation of 1

The ^{1}H NMR spectrum of a C_6D_6 solution containing **1** reveals a characteristic doublet at 3.30 ppm, with a large coupling constant ($^1J_{P–H}$ = 204 Hz), which collapses into a singlet

upon phosphorus-decoupling (Figure 2.11). The doublet is characteristic of the phosphanyl protons (PH_2) of the phosphinecarboxamide moiety in **1**. A broad singlet is also observed at 4.73 ppm, and is assigned to the amide environment. Numerous multiplet resonances are observed between 0.90 and 1.60 ppm, as well as a multiplet at 2.98 ppm. The resonance at 2.98 ppm is assigned to the methylene group adjacent to the amide group, as this environment will be the most deshielded due to its close proximity to the carbonyl fragment. The remaining peaks between 0.90 and 1.60 ppm are assigned to the remaining environments of the alkyl chain ($C_{15}H_{31}$; 14 × CH_2 and 1 × CH_3).

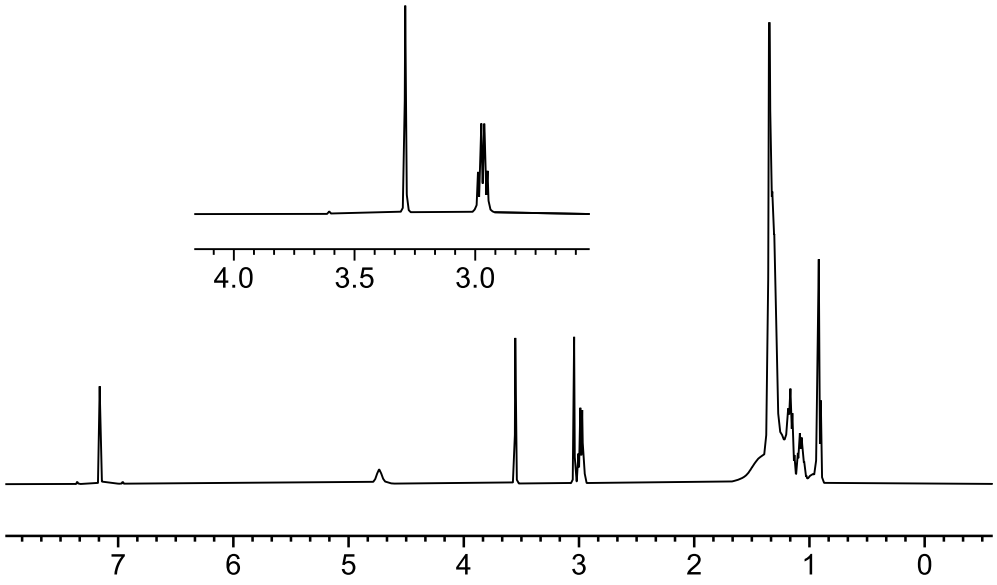


Figure 2.11: ^{1}H NMR spectrum of C_6D_6 solution containing **1**. Inset shows the $^{1}H\{^{31}P\}$ spectrum, where the doublet at 3.30 ppm collapses into a singlet.

^{31}P NMR spectroscopy provides unambiguous confirmation of the formation of **1**, showing a triplet at −132.5 ppm corresponding to the phosphorus atom of the phosphinecarboxamide fragment, which collapses into a singlet upon proton-decoupling (Figure 2.12). The coupling constant of the triplet is $^{1}J_{H-P}$ = 205 Hz, equal to that of the doublet observed in the ^{1}H NMR spectrum.

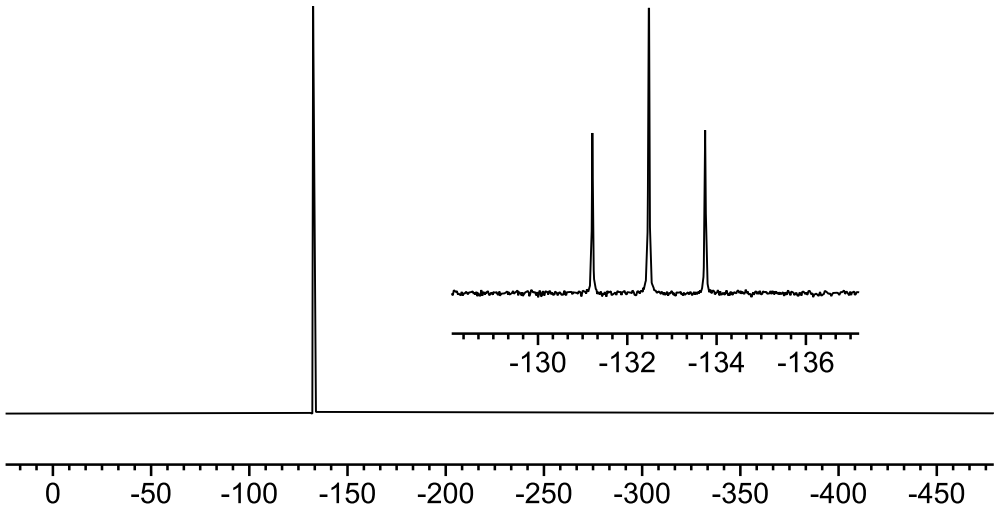


Figure 2.12: $^{31}P\{^{1}H\}$ NMR spectrum of C_6D_6 solution containing **1**. Inset shows the ^{31}P NMR spectrum of **1**.

The $^{13}C\{^{1}H\}$ NMR spectrum is also consistent with the proposed structure of **1**, showing a doublet at 172.4 ppm ($^{1}J_{P-C}$ = 6 Hz), corresponding to the carbonyl carbon atom coupling to the phosphorus atom of the phosphinecarboxamide (Figure 2.13).[14,36,38]

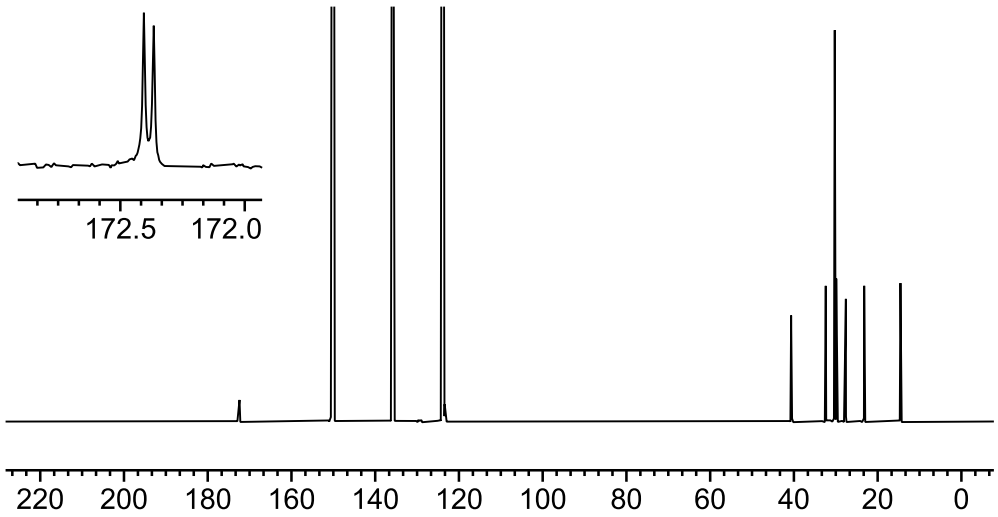


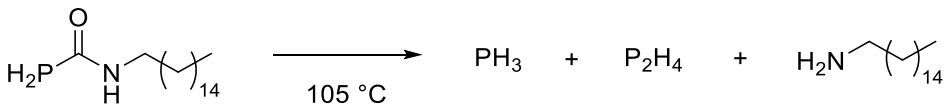
Figure 2.13: $^{13}C\{^{1}H\}$ spectrum of d_5-pyridine containing **1**. Inset shows the doublet corresponding to the carbon atom of the phosphinecarboxamide moiety.

NMR spectroscopic characterisation of independently prepared **1** is consistent with our assignment of it as a product of the transamidation reaction between phosphinecarboxamide and hexadecylamine upon heating (Section 2.2.3).

2.3.3 Thermal decomposition of 1

Motivated by the formation of **1** upon reaction of phosphinecarboxamide and hexadecylamine upon heating, we were interested in whether **1** may also show *in situ* PH_3 production upon heating.

To investigate this, a d_5-pyridine solution containing **1** was heated and monitored by ^{31}P and ^{1}H NMR spectroscopy (Scheme 2.11). No decomposition was observed below 105 °C, but after heating **1** at 105 °C for a short time, new peaks emerged in both the ^{31}P and ^{1}H NMR spectra.



Scheme 2.11: Thermal decomposition of **1** in d_5-pyridine.

$^{31}P\{^{1}H\}$ NMR spectra show the gradual consumption of **1** through a decrease in intensity of the peak at −133.0 ppm (Figure 2.14). In addition, new peaks emerge at −211.7 and −240.4 ppm, corresponding to P_2H_4 and PH_3, respectively.

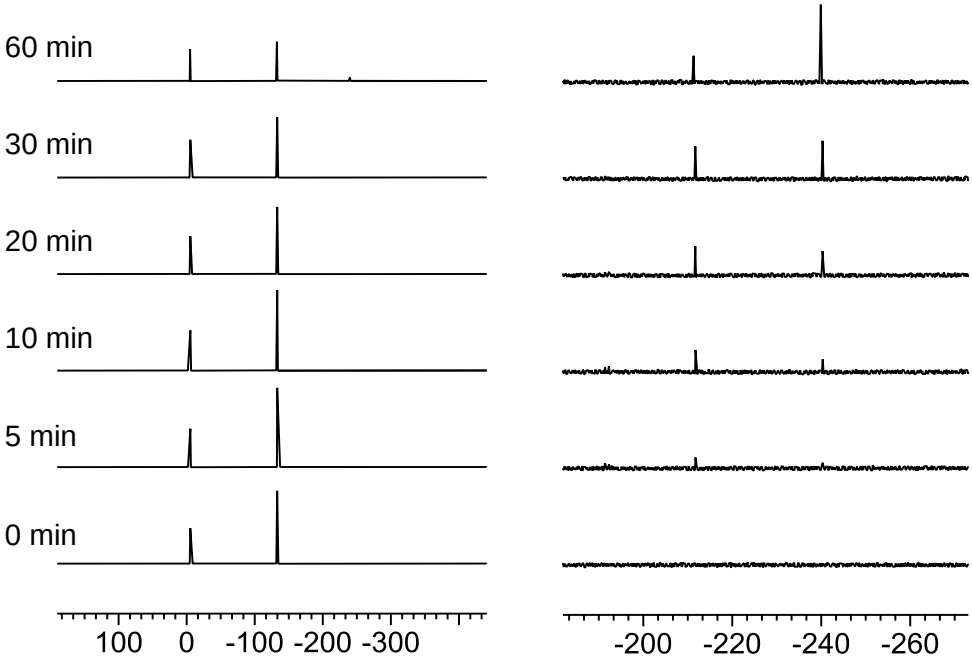


Figure 2.14: $^{31}P\{^{1}H\}$ NMR spectra of d_5-pyridine solution containing **1** heated at 105 °C for 0–60 min. Expanded region to show characteristic PH_3 and P_2H_4 resonances. The peak at −5 ppm corresponds to the PPh_3 internal standard.

The ^{1}H NMR spectra also reveals the formation of a new triplet at 2.75 ppm and a multiplet at 1.47 ppm after heating **1** for 30−180 minutes (Figure 2.15). The new product formed can confidently be characterised as free hexadecylamine by comparing the ^{1}H NMR spectrum of a d_5-pyridine solution containing hexadecylamine. The triplet at 2.75 ppm is assigned to the methylene protons adjacent to the amine group, showing three-bond coupling ($^{3}J_{H–H}$ = 6.8 Hz) to the two protons of the neighbouring CH_2 group. The neighbouring CH_2 group ($H_2NCH_2C\underline{H_2}$) in turn gives rise to the multiplet at 1.47 ppm.

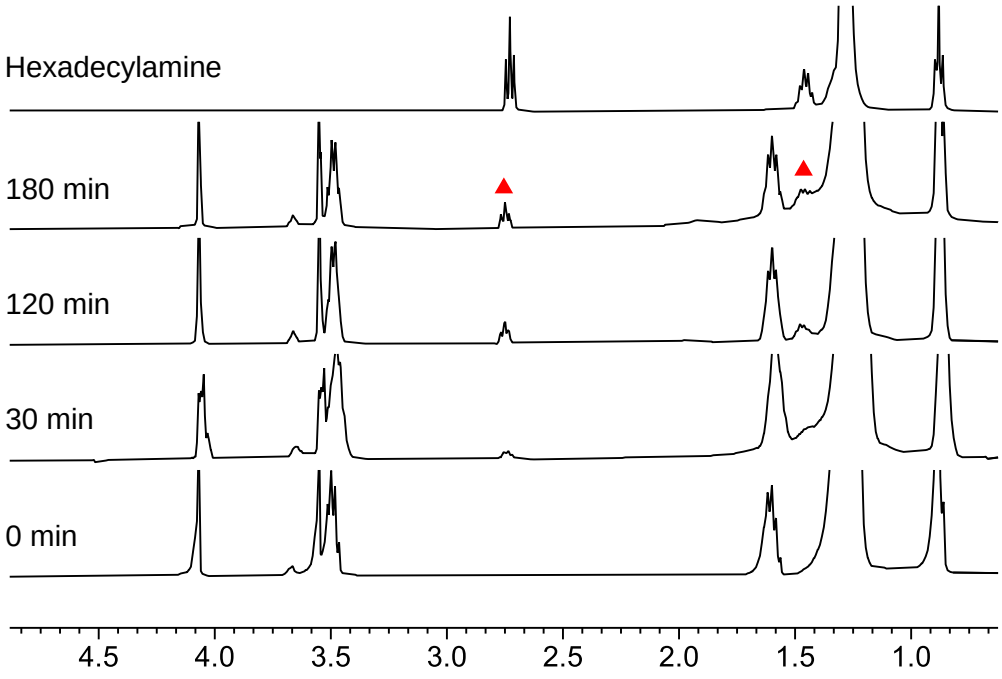
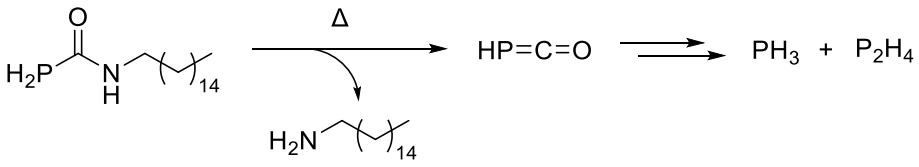


Figure 2.15: ^{1}H NMR spectra of a d_5-pyridine solution containing **1** heated at 105 °C for 0–180 min. The red triangles highlight the new peaks that emerge.

The observation of hexadecylamine as a product of the decomposition of **1** provides valuable insight into the mechanism by which **1** decomposes. In Hyett's report using phosphinecarboxamide as a PH_3 source for Zn_3P_2 thin films, the authors hypothesised that $H_2PC(O)NH_2$ decomposes to form PH_3 and isocyanic acid.[16] However, no evidence is given for this decomposition mechanism, which is carried out in the gas phase. In this work, the formation of HNCO was also not observed by ^{1}H NMR during solution phase decomposition studies of phosphinecarboxamide.

The regeneration of amine in solution upon decomposition suggests that **1** decomposes to form HPCO and hexadecylamine, and not PH_3 and the corresponding hexadecylisocyanate (Scheme 2.12). Whilst this reaction does not directly yield PH_3, as noted earlier, HPCO is known to decompose in solution to form PH_3. Hinz *et al.* showed that HPCO generated by the protonation of PCO^- with stearic acid is unstable in solution,

forming PH_3 and P_2H_4, even at low temperatures.[19] Schreiber and Goicoechea also showed during investigations of aqueous solutions containing Na(PCO) that the PCO^- anion is unstable in acidic conditions, forming PH_3 upon decomposition of the postulated HPCO intermediate.[39]



Scheme 2.12: Proposed thermal decomposition mechanism of **1**.

The thermal decomposition of **1** to form PH_3 and P_2H_4 in solution is exciting for numerous reasons. First, it supports PH_3 release in solution as being a novel mode of reactivity of the phosphinecarboxamide functional group itself. Moreover, by demonstrating that *N*-functionalisation of a phosphinecarboxamide does not prevent this reactivity, it presents the potential for a variety of structural and functional characteristics to be incorporated into the molecules, whilst conserving the ability to produce PH_3 *in situ*.

Although **1** decomposes similarly to phosphinecarboxamide to form PH_3 and P_2H_4, the relative rate of thermal decomposition varies between the two. By comparing the change in integral upon heating at 105 °C, $^{31}P\{^1H\}$ NMR spectra show that phosphinecarboxamide decomposes at a faster rate than **1** (Figure 2.16). After 1 hour of heating, 41% of phosphinecarboxamide remains, whilst **1** appears to have greater thermal stability, with 61% present after the same duration.

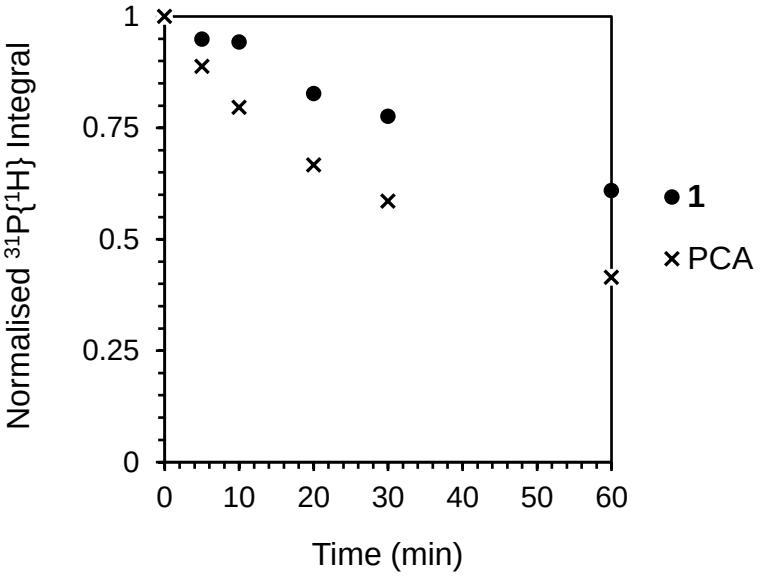
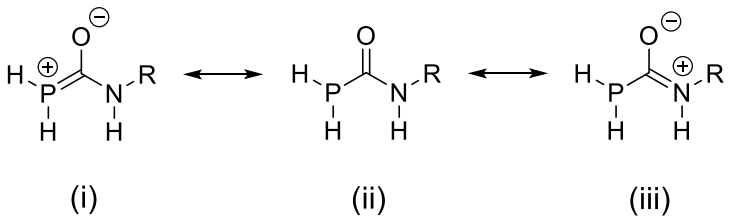


Figure 2.16: Change in normalised $^{31}P\{^{1}H\}$ NMR integrals of phosphinecarboxamide (−134.0 ppm) and **1** (−133.0 ppm) upon heating at 105 °C over 1 hour. Integrals normalised against PPh_3 internal standard.

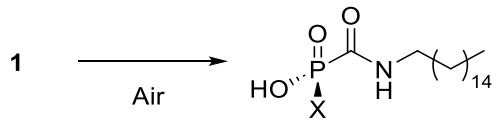
The improved thermal stability of **1** compared to the parent phosphinecarboxamide is rationalised by the change in electronics of the phosphinecarboxamide moiety upon *N*-functionalisation. Delocalisation of π-electron density of the amide lone pair into the carbonyl group is known to provide a significant resonance contribution.[38] As a hexadecyl group is a better electron donating group than a hydrogen atom, it should increase the π-character of the C−N bond, further favouring resonance structure (iii) (Scheme 2.13). As the C−N bond must be cleaved to form hexadecylamine and HPCO, the additional stabilisation afforded to this bond by the hexadecyl group rationalises the disparity in decomposition rates between **1** and the parent phosphinecarboxamide.



Scheme 2.13: Resonance structures of phosphinecarboxamides.

2.3.4 Air stability of 1

Motivated by the observation of PH_3 formation upon thermal decomposition of **1** in solution, and with the aim to exploit this to prepare InP QDs, we wanted to evaluate the air stability of **1**. To do so, solid samples of **1** were stored in vials on the bench and exposed to air. Samples were then analysed by ^{31}P NMR after 1 month and 17 months of air exposure (Scheme 2.14).



Scheme 2.14: Oxidation of **1** in air for 1–17 months (X = H or OH).

The ^{31}P NMR spectrum shows little change in **1** after exposure to air for 1 month, as evidenced by the prominent triplet at −132.5 ppm, which collapses into a singlet upon proton-decoupling (Figure 2.17). Low intensity peaks are observed around 3.00 ppm, which increase in intensity in the 17 month sample, and are characteristic of oxidised phosphinecarboxamides.[37]

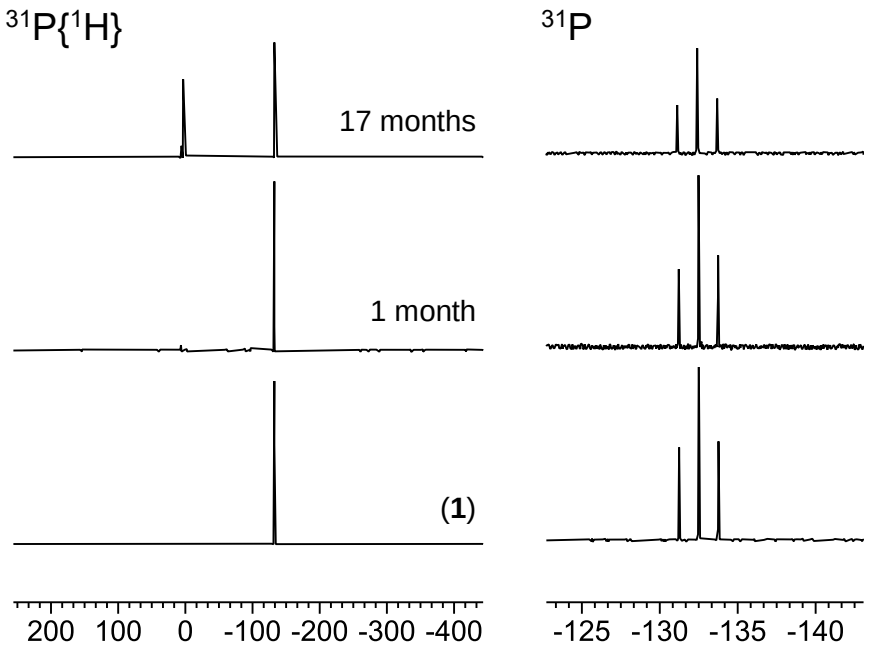


Figure 2.17: ^{31}P NMR spectra of C_6D_6 solutions containing **1** after exposure to air for 1 month and 17 months.

1 is found to be remarkably stable in air for a primary phosphine and shows minimal decomposition after 1 month of exposure. Whilst more oxidation is observed after 17 months, **1** remains the major species present in solution.

2.4 Conclusions

This chapter has described the solution phase reactivity of phosphinecarboxamide. Heating phosphinecarboxamide ($H_2PC(O)NH_2$) at 105 °C in d_5-pyridine was found to form PH_3 and P_2H_4. By exploiting this thermal decomposition, phosphinecarboxamide could be used as an *in situ* PH_3 source by reacting with indium carboxylates, forming magic-sized clusters. The phenylacetate-capped InP MSCs were characterised by ^{31}P NMR spectroscopy, UV-Vis spectroscopy, and MALDI-TOF mass spectrometry, and were consistent with thermodynamically stable intermediate InP phases reported in the

literature. The successful preparation of InP MSCs from phosphinecarboxamide is encouraging for its application in the preparation of InP QDs.

This chapter also described the synthesis and characterisation of the novel *N*-hexadecylphosphinecarboxamide (**1**). **1** was prepared by the reaction of hexadecylamine with PCO^- under acidic conditions. **1** was also found to form as a result of the transamidation reaction of hexadecylamine and $H_2PC(O)NH_2$. **1** is shown to act as an *in situ* PH_3 source upon thermal decomposition, and was found to release PH_3 at a slower rate than the parent phosphinecarboxamide. Finally, **1** is shown to be remarkably air stable, with negligible oxidation occurring after one month of air exposure.

2.5 References

1 Chemical Data Reporting under the Toxic Substances Control Act, https://www.epa.gov/chemical-data-reporting, (accessed 31 July 2023).

2 T. M. Hood, S. Lau and R. L. Webster, *J. Am. Chem. Soc.*, 2022, **144**, 16684–16697.

3 L. Li, M. Protière and P. Reiss, *Chem. Mater.*, 2008, **20**, 2621–2623.

4 Y. A. Dorfman and L. V Levina, *Chem. Heterocycl. Compd.*, 1992, **28**, 111–112.

5 T. Barber, S. P. Argent and L. T. Ball, *ACS Catal.*, 2020, **10**, 5454–5461.

6 H. Zhang, D. J. Hagen, X. Li, A. Graff, F. Heyroth, B. Fuhrmann, I. Kostanovskiy, S. L. Schweizer, F. Caddeo, A. W. Maijenburg, S. Parkin and R. B. Wehrspohn, *Angew. Chem. Int. Ed.*, 2020, **59**, 17172–17176.

7 C. Hetherington, D. Jacobsson, K. A. Dick and L. R. Wallenberg, *Semicond. Sci. Technol.*, 2020, **35**, 34004.

8 D. E. Bost and J. G. Ekerdt, *Thin Solid Films*, 2014, **558**, 160–164.

9 W. B. Russel, D. A. Saville and W. R. Schowalter, *Colloidal Dispersions*, Cambridge University Press, Cambridge, 1989.

10 A. Cros-Gagneux, F. Delpech, C. Nayral, A. Cornejo, Y. Coppel and B. Chaudret, *J. Am. Chem. Soc.*, 2010, **132**, 18147–18157.

11 S. Miao, S. G. Hickey, C. Waurisch, V. Lesnyak, T. Otto, B. Rellinghaus and A. Eychmüller, *ACS Nano*, 2012, **6**, 7059–7065.

12 G. Manna, R. Bose and N. Pradhan, *Angew. Chem. Int. Ed.*, 2013, **52**, 6762–6766.

13 S. Miao, T. Yang, S. G. Hickey, V. Lesnyak, B. Rellinghaus, J. Xu and A. Eychmüller, *Small*, 2013, **9**, 3415–3422.

14 E. N. Faria, A. R. Jupp and J. M. Goicoechea, *Chem. Commun.*, 2017, **53**, 7092–7095.

15 Y. H. Wu, Z. F. Li, W. P. Wang, X. C. Wang and Z. J. Quan, *Eur. J. Org. Chem.*, 2017, **2017**, 5546–5553.

16 S. V. F. Beddoe, S. D. Cosham, A. N. Kulak, A. R. Jupp, J. M. Goicoechea and G. Hyett, *Dalton Trans.*, 2018, **47**, 9221–9225.

17 M. Baudler and K. Glinka, *Chem. Rev.*, 1993, **93**, 1623–1667.

18 J. P. Ferris and R. Benson, *Nature*, 1980, **285**, 156–157.

19 A. Hinz, R. Labbow, C. Rennick, A. Schulz and J. M. Goicoechea, *Angew. Chem. Int. Ed.*, 2017, **56**, 3911–3915.

20 A. R. Jupp, G. Trott, É. Payen De La Garanderie, J. D. G. Holl, D. Carmichael and J. M. Goicoechea, *Chem. Eur. J.*, 2015, **21**, 8015–8018.

21 D. C. Gary, S. E. Flowers, W. Kaminsky, A. Petrone, X. Li and B. M. Cossairt, *J. Am. Chem. Soc.*, 2016, **138**, 1510–1513.

22 Y. Kwon, J. Oh, E. Lee, S. H. Lee, A. Agnes, G. Bang, J. Kim, D. Kim and S. Kim, *Nat. Commun.*, 2020, **11**, 1–15.

23 D. C. Gary, M. W. Terban, S. J. L. Billinge and B. M. Cossairt, *Chem. Mater.*, 2015, **27**, 1432–1441.

24 J. L. Stein, M. I. Steimle, M. W. Terban, A. Petrone, S. J. L. Billinge, X. Li and B. M. Cossairt, *Chem. Mater.*, 2017, **29**, 7984–7992.

25 A. Ritchhart and B. M. Cossairt, *Angew. Chem. Int. Ed.*, 2018, **57**, 1908–1912.

26 Y. Kwon and S. Kim, *NPG Asia Mater.*, 2021, **13**, 37.

27 S. A. Tovstun, A. V Gadomska, M. G. Spirin and V. F. Razumov, *J. Lumin.*, 2022, **252**, 119420.

28 A. Dass, A. Stevenson, G. R. Dubay, J. B. Tracy and R. W. Murray, *J. Am. Chem. Soc.*, 2008, **130**, 5940–5946.

29 C. Peng, Q. Zhang, J. Liu, Z. Wang, Z. Zhao, N. Kang, Y. Chen and Q. Huo, *Green Process. Synth.*, 2021, **10**, 700–710.

30 J. Li, T. Yang, W. H. Chan, M. M. F. Choi and D. Zhao, *J. Phys. Chem. C*, 2013, **117**, 19175–19181.

31 G. A. Khitrov and G. F. Strouse, *J. Am. Chem. Soc.*, 2003, **125**, 10465–10469.

32 L. Xie, Y. Shen, D. Franke, V. Sebastián, M. G. Bawendi and K. F. Jensen, *J. Am. Chem. Soc.*, 2016, **138**, 13469–13472.

33 K. Kim, D. Yoo, H. Choi, S. Tamang, J.-H. Ko, S. Kim, Y.-H. Kim and S. Jeong, *Angew. Chem. Int. Ed.*, 2016, **55**, 3714–3718.

34 Y. Dou, L. Wang, Y. Wang, Q. Wu, F. Cao, S. Wang, Q. Huang, Y. Ma and X. Yang, *Adv. Opt. Mater.*, 2023, **11**, 2300133.

35 Y. Kim, J. H. Chang, H. Choi, Y.-H. Kim, W. K. Bae and S. Jeong, *Chem. Sci.*, 2020, **11**, 913–922.

36 E. N. Faria, A. R. Jupp and J. M. Goicoechea, *Dalton Trans.*, 2021, **50**, 6991–6996.

37 A. Jupp, 2016, Thesis (D.Phil.), University of Oxford.

38 A. R. Jupp and J. M. Goicoechea, *J. Am. Chem. Soc.*, 2013, **135**, 19131–19134.

39 R. E. Schreiber and J. M. Goicoechea, *Angew. Chem. Int. Ed.*, 2021, **60**, 3759–3767.

Chapter 3

Synthesis and characterisation of InP quantum dots prepared from phosphinecarboxamides

3.1 Introduction and objectives

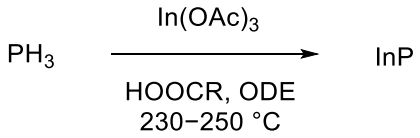
The use of the parent phosphinecarboxamide, $H_2PC(O)NH_2$, for the preparation of InP QDs was studied by our group in collaboration with colleagues at King's College London, and is described in our recent paper.[1] Given that *N*-hexadecyl-phosphinecarboxamide (**1**) forms upon heating $H_2PC(O)NH_2$ with hexadecylamine (HDA), our investigations focussed the use of **1** for the preparation of InP QDs. Moreover, the parent phosphinecarboxamide, whilst air- and moisture-tolerant, decomposes in air after one day of exposure. In contrast, **1** is remarkably bench stable, showing negligible decomposition after one month in air with a half-life greater than 17 months.

3.1.1 Conditions for InP QD syntheses

As surveyed in Chapter 1, there are numerous methodologies for the preparation of QDs. Due to the novelty of using phosphinecarboxamides for the preparation of InP QDs, for efficient evaluation it is important to minimise the number of variables in our synthetic protocol. For this reason, conditions were selected from the literature to aid our evaluation and characterisation of the material formed when using phosphinecarboxamides. Where possible, the parameters and conditions chosen were fixed and deviations were avoided to minimise experiment-to-experiment variance.

Hexadecylamine (HDA) is the most rational choice of capping ligand for use in our protocol since it is observed as a decomposition product of **1**. The use of HDA offers additional benefits, such as its ability to minimise In_2O_3 formation during the reaction which is known to diminish the PLQY.

Previous reports using PH_3 as a phosphorus precursor guided our selection of optimal starting conditions. Reiss and Dorofeev took advantage of myristate and oleate capping ligands in their respective InP QD preparations from *ex situ* generated PH_3 (Scheme 3.1).[2,3] Long-chain carboxylates are effective at solubilising metal ions in apolar solvents, in particular In^{3+} and Zn^{2+} ions. Moreover, carboxylates are popular capping ligands for InP QDs and are frequently employed to achieve near-monodispersity.[4–6]



Scheme 3.1: Preparation of InP QDs from *ex situ* generated PH_3.[2,3] HOOCR = oleic acid or myristic acid; ODE = 1-octadecene.

Zinc-alloying of InP QDs has been popularised over the last decade, offering superior PLQYs compared to native InP and straightforward reaction protocols.[7–11] Dicationic Zn^{2+} ions are effective at passivating surface traps on bare InP QDs, supressing trap emission while enhancing band edge emission.[12] Furthermore, alloying with zinc reduces the lattice constant of the resulting In(Zn)P nanocrystal, optimising lattice-matched shell growth (e.g. with ZnSe or ZnS). The reduction in lattice constant has been found to reduce interfacial defects and enhance PLQY upon shell growth.[13]

For this work, the ability to induce photoluminescence in bare InP QDs was particularly appealing, offering an additional point of characterisation during development. Zinc stearate is selected for use as both a Zn^{2+} ion and long-chain carboxylate capping ligand source. Kirkwood *et al.* have shown that long-chain carboxylates localise zinc ions on the surface of InP QDs, resulting in more effective surface passivation.[10]

Halide ion passivation of InP QD surfaces is also popular for enhancing PLQY.[14,15] Small, electronegative halide ions (e.g. F^- or Cl^-) are more effective at removing negative charge from the surface than carboxylates and amines, in turn suppressing electron rich hole traps and improving photoluminescence. Small halide ions are also better at passivating undercoordinated surface species due to their reduced steric encumbrance compared to traditional capping ligands.[16] For these reasons, $InCl_3$ was selected as the indium precursor to supply chloride ions into solution.

To minimise the evaporation of volatile PH_3 out of solution, a heat-up synthesis was elected. The observation of InP MSC formation at low temperatures (110 °C) described in Chapter 2 motivated us to exploit this reaction as a discrete nucleation event. An initial reaction temperature of 120 °C was chosen to begin nucleating the QDs through MSC formation, followed by high temperature annealing at 220 °C. Reiss and Dorofeev also employed reaction temperatures of 230–250 °C to ensure slow, controlled QD growth. Park *et al.* employed a similar heat-up protocol for the preparation of core/shell/shell InP/GaP/ZnS QDs from $P(SiMe_3)_3$ with narrow particle size distribution (FWHM = 40−60 nm).[17]

To facilitate such high reaction temperatures 1-octadecene (ODE) was selected as a reaction solvent. ODE is non-coordinating, has a high boiling point (315 °C), and is commercially available in good purity (> 90%).

3.1.2 Chapter outline

This chapter will describe the preparation of HDA-capped In(Zn)P and core/shell In(Zn)P/ZnS QDs using *N*-hexadecylphosphinecarboxamide (**1**). The development of a synthetic protocol using **1** and optimisation of reaction conditions towards size-uniform

InP QDs will be discussed. The use of **1** exposed to air for one month for the preparation of In(Zn)P/ZnS QDs is also investigated.

This chapter will also explore the use of phenylacetate-capped InP magic-sized clusters (MSCs) prepared from the parent phosphinecarboxamide, $H_2PC(O)NH_2$ detailed in Chapter 2, as single-source precursors to In(Zn)P QDs.

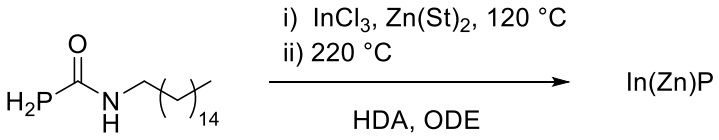
3.2 Preparation of In(Zn)P QDs from 1

3.2.1 Synthesis and purification of In(Zn)P QDs

The promising *in-situ* reactivity of **1** motivated us to explore its use for the preparation of InP QDs. It is common when using heat-up methods for the preparation of QDs to nucleate the nanocrystals at low temperatures (*ca*. 110 °C) whilst the reaction mixture is under dynamic vacuum. This is done to ensure that the solvent is fully degassed, removing dissolved oxygen before heating at elevated temperatures (> 200 °C). Degassing liquid reagents and solvents is critical for minimising the formation of oxide impurities during synthesis, such as In_2O_3 and $InPO_x$, as these defects are well-known to diminish InP QD PLQY.[18–20]

Initial attempts to prepare In(Zn)P QDs by degassing the reaction mixture at 120 °C failed, presumably due to the removal of volatile PH_3 produced upon thermal decomposition of **1**. To circumvent this challenge, ODE was degassed prior to use by heating under reflux under reduced pressure overnight. The degassed ODE was subsequently stored in a gas-tight glass ampule and transferred under an inert atmosphere into the reaction mixture when required.

A degassed ODE solution containing **1**, $InCl_3$, zinc stearate, and HDA was heated at 120 °C for 30 minutes, followed by 220 °C for a further 30 minutes, and results in the formation of In(Zn)P QDs (Scheme 3.2, experimental details described in Section 7.2.1.1). The formation of InP QDs is evidenced by the change in colour of the reaction mixture from colourless to yellow and ultimately to deep red upon heating to 120 °C, then 220 °C, respectively.



Scheme 3.2: Synthesis of In(Zn)P QDs from **1**. St = stearate ($O_2C(CH_2)_{16}CH_3$); HDA = hexadecylamine ($H_2N(CH_2)_{15}CH_3$); ODE = 1-octadecene ($H_2C=CH(CH_2)_{15}CH_3$).

The In(Zn)P QDs prepared were purified by several precipitation and redissolution cycles, washing with ethanol to remove excess ODE and capping ligands, followed by centrifugation to isolate the QDs.

3.2.2 Characterisation of In(Zn)P QDs

To evaluate the In(Zn)P QDs prepared from **1**, purified samples were analysed by UV-Vis, absorption and photoluminescence (PL) spectroscopy, powder X-ray diffraction (PXRD), and inductively coupled plasma mass spectrometry (ICP-MS).

A broad, featureless absorption edge is observed at *ca.* 550 nm in the UV-Vis spectrum of a toluene solution containing HDA-capped In(Zn)P QDs (Figure 3.1). The absence of a well-resolved absorption peak is common for InP QDs.[21,22] Broadening in absorption spectra can occur as a consequence of particle size polydispersity, as well as competing surface ligand absorption. In this case, the use of HDA capping ligands likely contributes

significantly to the presence of an absorption edge. HDA is known to compete with band edge absorption in III-V QDs due to its high extinction coefficient below 450 nm.[23] Lee *et al*. report a similar effect for HDA-capped CdSe QDs, whereby the addition of HDA capping ligands masks the otherwise distinguishable CdSe QD absorption peak.[24]

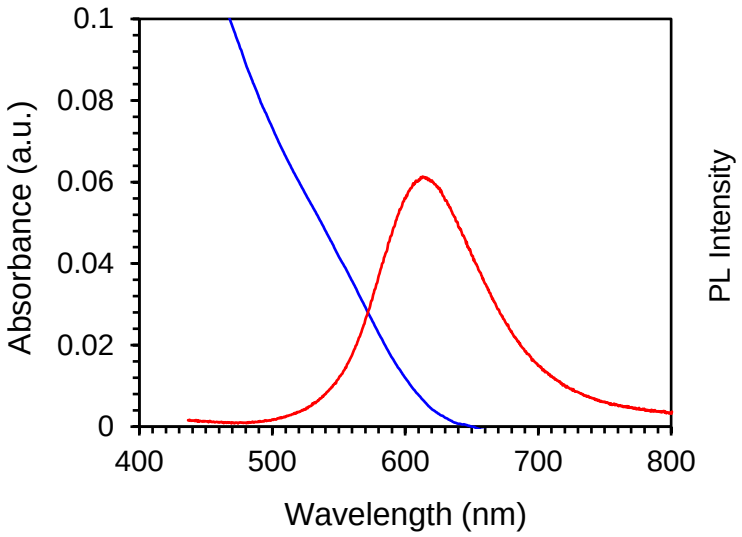


Figure 3.1: UV-Vis absorption (blue) and PL emission (red) spectra of a toluene solution containing HDA-capped In(Zn)P QDs prepared from **1**.

Nonetheless, the PL emission spectrum provides more convincing evidence of In(Zn)P QD formation, revealing a sharp emission peak at 613 nm. The emission peak is consistent with physical observations, as the sample fluoresces orange upon irradiation with a UV lamp (365 nm). The relatively symmetrical emission peak is characteristic of zinc-doped InP QDs, and supports the isolation of a single QD size ensemble. The full-width at half maximum (FWHM) of the PL emission peak is 91 nm, and although not significantly broad, does imply a degree of polydispersity in QD particle size.

PXRD analysis of the In(Zn)P QDs reveals several broad, low intensity peaks at 26.7 and 43.5°, in addition to shoulders at 20.7 and 51.3° (Figure 3.2). The peaks at 26.7 43.5, and 51.3° are in good agreement with the (111), (220), and (311) reflections of cubic zinc

blende InP (26.3, 43.6, and 51.7°, respectively). The peak broadening observed is a consequence of Scherrer line broadening, due to the small crystallite size (< 5 nm). The small QDs nanocrystals have fewer Bragg planes compared to the bulk phase, therefore there is less destructive interference at non-Bragg angles and increased broadening of diffraction peaks.[25,26] The additional shoulder at 20.7° is characteristic of well-ordered aliphatic ligands bound to the QD surface, in this case HDA capping ligands.[27]

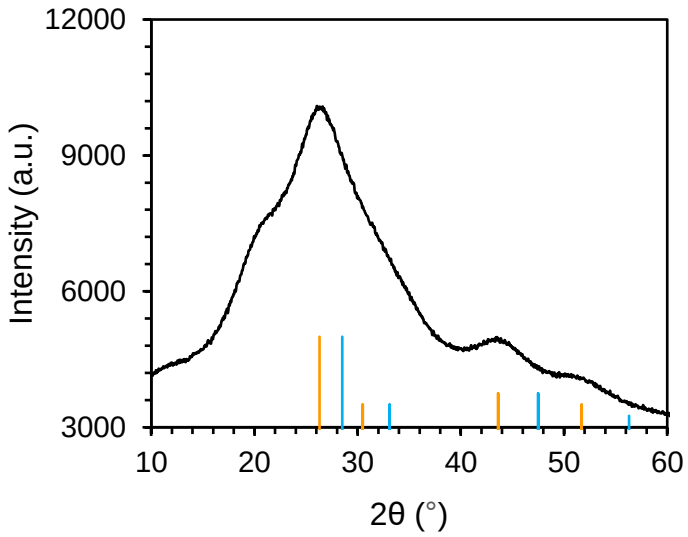


Figure 3.2: Powder X-ray diffraction pattern of In(Zn)P QDs prepared from **1**. Diffraction patterns of zinc blende InP (orange) and ZnS (blue) shown for reference.

ICP-MS analysis of the In(Zn)P QDs confirmed the incorporation of In, Zn, and P into the final product, revealing an In:Zn:P stoichiometry of 3.34:1:4.61. The low zinc content is expected for zinc-doped InP QDs. ICP-MS analysis cannot however provide information regarding the location of the Zn^{2+} ions within the QDs.

The photoluminescence observed for In(Zn)P QDs prepared from **1** highlights the effectiveness of Zn^{2+} doping in passivating surface traps. The addition of zinc stearate during synthesis is clearly validated, enabling PL spectroscopy to be used to characterise the InP QDs which are otherwise non-emissive. In addition, the close match of the X-ray

diffraction peaks with those expected for bulk phase InP further supports the surface localisation of Zn^{2+} ions on the InP QDs, resulting in minimal change to the lattice parameters. These results, coupled with the relatively low Zn content found by ICP-MS, support that the ions are localised on the QD surface, as expected.[10]

3.2.3 Reaction duration optimisation

3.2.3.1 Varying reaction duration at 220 °C

As discussed in Chapter 1, a defining characteristic of InP QDs is size-tuneable emission. To further confirm the formation of In(Zn)P QDs, QD growth was monitored by changes in the emission profile throughout the reaction.

In(Zn)P QD samples were prepared as before by heating at 120 °C for 30 minutes, before warming to 220 °C. QD samples were then analysed using PL spectroscopy after heating at 220 °C for 0 minutes, 5 minutes, 15 minutes, and 30 minutes.

HDA-capped In(Zn)P QDs prepared by heating to 220 °C, followed by immediate cooling display a PL peak (λ_{max}) at 550 nm (FWHM = 84 nm; Figure 3.3(i)). The λ_{max} value is observed to increase to 551 nm, 589 nm, and finally 613 nm upon heating at 220 °C for 5 minutes, 15 minutes, and 30 minutes, respectively. The red-shift of the emission peak with increasing reaction duration is consistent with the growth of InP QDs in solution.[28] As the reaction at 220 °C proceeds, QD nanocrystals grow larger, experience decreased quantum confinement, which decreases their band gap energy, resulting in red-shifted emission. The FWHM of the QDs prepared after heating for 5 minutes, 15 minutes, and 30 minutes remains relatively constant (83 nm, 82 nm, and 91 nm, respectively), suggesting that the particle growth profile over the 30 minute reaction duration is uniform.

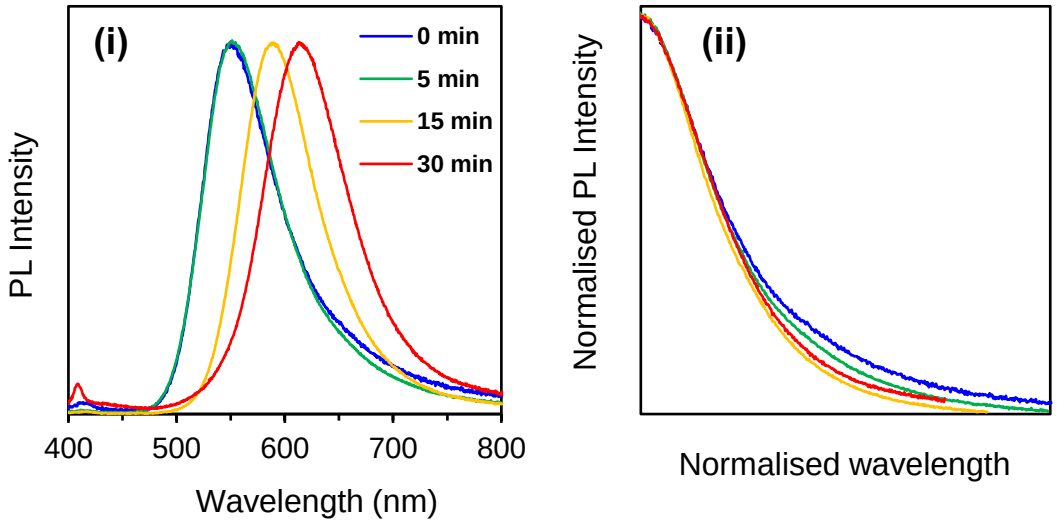


Figure 3.3: (i) PL emission spectra of HDA-capped In(Zn)P QDs grown for 0–30 minutes at 220 °C; (ii) normalised PL emission spectra showing reduction in defect emission peak.

Further insight into the growth of In(Zn)P QDs during the reaction is afforded by the change in homogeneity of the PL peak with increasing reaction duration. As can be seen for the 0 minute sample, there appears to be emission at wavelengths longer than the PL peak, creating a 'red tail' (Figure 3.3(ii)).[29] Red tails in emission spectra are characteristic of defect emission due to incomplete passivation of the InP QD surface. In fact, these are the defect emission peaks that are largely being supressed by alloying the QDs with Zn^{2+} ions. Zhang and Gu showed that zinc-alloying is highly effective at supressing surface defects in InP QDs.[12] It is also observed that as the reaction proceeds the red tail diminishes in intensity. This reduction is due to a decrease in the surface-to-volume ratio as the QDs increase in size, resulting in lower defect emission relative to band edge emission.[30]

Whilst a red-shift in absorption spectra was also observed upon increasing the reaction duration at 220 °C, the broad, featureless nature of the absorption edge does not offer additional insight.

3.2.3.2 Varying reaction duration at 120 °C

In heat-up reactions, nucleation occurs at low temperatures, where precursor monomers are converted into nuclei. The duration of the first annealing stage at 120 °C is important in dictating the particle size and dispersity of the In(Zn)P QDs formed, as this will determine what concentration of precursor monomers remain for subsequent crystal growth during high temperature annealing (220 °C). To investigate the effect of the initial heat-up temperature on QD optical properties, In(Zn)P QDs were prepared as described in Section 3.2.1, varying the reaction duration at 120 °C.

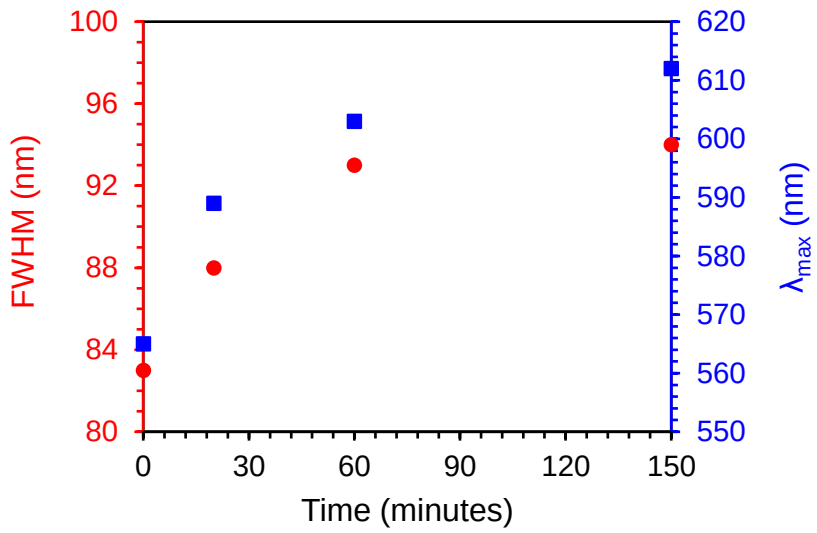


Figure 3.4: PL emission maxima (blue) and FWHM (red) of In(Zn)P QDs grown for 0–150 minutes at 120 °C.

When the reaction duration at 120 °C is increased from 0 to 150 minutes, the PL λ_{max} values increase from 565 to 612 nm, consistent with the growth of larger QDs (Figure 3.4). This can be rationalised by the greater consumption of precursors to form InP clusters upon prolonged heating at 120 °C, in addition to some amount of QD growth occurring. The greater degree of monomer consumption at low temperatures prevents slow, controlled particle growth at higher temperatures. This is also reflected in the

increase in FWHM observed upon increasing the reaction duration at 120 °C. The increase in FHWM is indicative of greater particle size dispersity as a result of less controlled QD growth.

The formation of InP clusters at low temperatures, and their subsequent decomposition, is one reason for the greater polydispersity observed. Friedfeld *et al.* have shown InP clusters release multiple monomer species upon decomposition with varying reactivities, and that these differences in reactivity result in increased InP QD polydispersity.[31]

Another possible reason for the increase in polydispersity is the production of acid by-products from the reaction of PH_3 with $InCl_3$ and zinc stearate. Mézailles and co-workers showed that by using acid-free indium carboxylate precursors, core/shell InP/ZnSeS QDs with PL emission FWHM of 40 nm could be prepared.[5] The authors also showed that by progressively increasing the concentration of extraneous free acid in the reaction mixture, the FWHM steadily increased by up to 50% to 60 nm. The deterioration in optical properties observed is attributed to the destabilisation of $(Me_3Si)_3P{\rightarrow}In(OOCR)_3$ precursor complexes, disrupting nanocrystal size focussing.

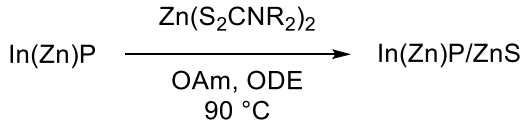
3.3 Preparation of core/shell In(Zn)P/ZnS QDs from 1

The preparation of In(Zn)P QDs using **1** validates that PH_3 generated *in situ* can be utilised as a phosphide source. Motivated to the demonstrate the effectiveness of **1** as a novel alternative phosphorus source, the preparation of core/shell In(Zn)P/ZnS QDs was investigated. Moreover, successful shell growth would provide supporting evidence for the successful formation of In(Zn)P QDs from **1** described in Section 3.2.

As highlighted in Chapter 1, there are several approaches for the epitaxial growth of ZnS shells onto InP QDs. The most popular method is to anneal InP QDs at high temperature (> 250 °C) with zinc carboxylate and trioctylphosphine sulphide (TOP(S)) precursors. The drawback to this approach is that TOP(S) introduces tri-*n*-octylphosphine (TOP) capping ligands into the reaction mixture upon decomposition. As the system described and optimised thus far employs hexadecylamine capping ligands, we wished to avoid the introduction of additional capping ligands into solution.

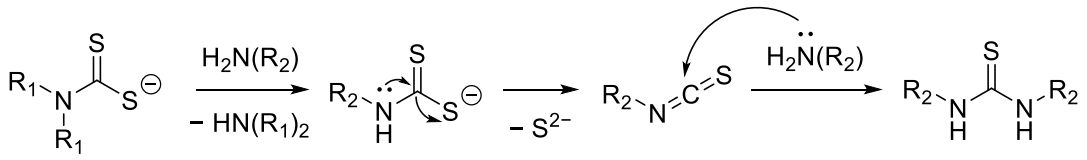
Metal dithiocarbamate complexes (DTCs) are widely employed as single-source precursors for the preparation of metal sulphide QDs and thin films.[32] DTCs are cheap and commercially available precursors, making them attractive for materials applications. Pertinent to this work, Malik *et al.* demonstrated the successful use of zinc diethyldithiocarbamate (ZDEC) as a single-source precursor for the preparation of trioctylphosphine oxide-capped ZnS QDs.[33]

In recent years, zinc DTCs have emerged as popular precursors for the growth of epitaxial ZnS shells onto InP QDs. For example, Nann and co-workers used ZDEC in place of TOP(S) and zinc carboxylates to prepare core/shell InP/ZnS QDs.[34] This method is also effective for shelling zinc-alloyed InP QDs. Xi *et al.* showed that zinc dialkyldithiocarbamates (R = Me, Et, Bu, or benzyl) may be employed for the growth of ZnS shells onto In(Zn)P QDs (Scheme 3.3).[35]



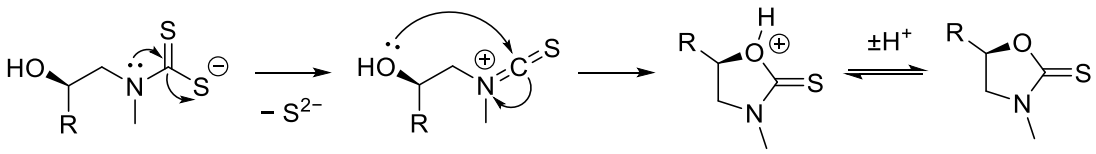
Scheme 3.3: Synthesis of core/shell In(Zn)P/ZnS QDs using zinc dialkyldithiocarbamate precursors (R = Me, Et, Bu, or benzyl). OAm = oleylamine ($H_2N(CH_2)_8HC{=}CH(CH_2)_7CH_3$); ODE = 1-octadecene.

Zinc DTC complexes are commonly used in combination with amine capping ligands. This is due to the transamidation reaction that occurs when the DTCs are heated in the presence of primary amines, which can be used to help solubilise the single-source precursors (Scheme 3.4).[36] Zinc DTC complexes are postulated to react via initial transamidation with primary amine capping ligands in solution, followed by subsequent S^{2-} elimination and isothiocyanate formation. The isothiocyanates in turn may undergo a further reaction with additional amine ligands, forming the corresponding thiourea.[32]



Scheme 3.4: Postulated decomposition mechanism of DTCs, initiating with a transamidation reaction, followed by the formation of sulphide ions, isothiocyanates, and thioureas.[32]

Further evidence for this mechanism is given by Green *et al.*, who crystallographically characterised the decomposition product of cadmium(II) bis(*N*-methyl-D-glucamine-dithiocarbamate) as the 'trapped' isothiocyanate, which is observed in the form of a oxazolidine-2-thione (Scheme 3.5).[37] In this example, the authors postulate that upon elimination of the sulphide group, the *N*-methyl-D-glucamineisothiocyanate undergoes an intramolecular cyclisation reaction, forming the heterocyclic oxazolidine-2-thione product.

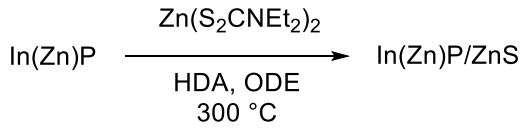


Scheme 3.5: Postulated mechanism of *N*-methyl-D-glucaminedithiocarbamate decomposition to from sulphide ions and 3-methyl-5-(1,2,3,4-tetrahydroxybuty-l)oxazolidine-2-thione, via an isothiocyanate intermediate (R = $(CHOH)_3CH_2OH$).[37]

The effectiveness of zinc DTCs as single-source precursors to ZnS and their synergistic compatibility with primary amine capping ligands motivated us to employ them for shell growth on HDA-capped In(Zn)P QDs prepared from **1**.

3.3.1 Synthesis and purification of core/shell In(Zn)P/ZnS QDs from 1

To avoid the oxidation of the In(Zn)P QD surface between reactions, ZnS shell growth was carried out on the crude QD core reaction mixture prepared from **1** without further purification. In a typical reaction, zinc diethyldithiocarbamate (ZDEC) was added to an ODE solution containing In(Zn)P QDs and HDA capping ligands. The solution was then heated to 300 °C and stirred for 30 minutes (Scheme 3.6). The core/shell In(Zn)P/ZnS QD products were purified by precipitation and redissolution cycles, in addition to size-exclusion chromatography (SEC; experimental details described in Section 7.2.2.9).[38]



Scheme 3.6: Synthesis of core/shell In(Zn)P/ZnS QDs from ZDEC and In(Zn)P QD cores prepared from **1**.

3.3.2 Characterisation of In(Zn)P/ZnS QDs

As observed for the In(Zn)P QD cores, the UV-Vis spectrum of the core/shell In(Zn)P/ZnS QDs reveals a broad, featureless absorption edge (Figure 3.5). Once again the PL spectrum proves more informative, displaying a prominent peak at 595 nm with a FWHM of 116 nm. An 18 nm blue-shift in the PL peak position is observed compared to that of the In(Zn)P cores. Blue-shifts in PL spectra usually arise from a decrease in QD size, and in this case may be a result of topotactic P^{3-} exchange for S^{2-} ions on the alloyed In(Zn)P surface upon shell growth.[7] The increase in FWHM from *ca.* 90 nm for the QD

cores to 116 nm for the core/shell QDs suggests that particle size polydispersity has increased upon shell growth. This is also reflected by the persistence of the broad absorption edge in the UV-Vis spectrum.

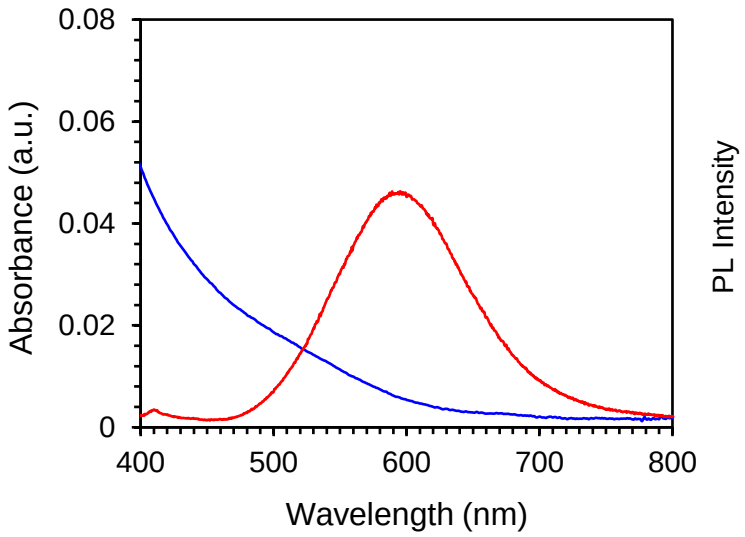


Figure 3.5: UV-Vis absorption (blue) and PL emission (red) spectra of a toluene solution containing In(Zn)P/ZnS QDs prepared from **1**.

ZnS shell growth also produced a marked visual improvement in the photoluminescence upon irradiation with a UV lamp (365 nm). However, the photoluminescence quantum yield (PLQY) could not be measured due to significant PL line broadness. This broadness resulted in non-zero emission at the excitation wavelength, which introduced significant measurement uncertainty. Use of an integrating sphere would enable measurement of the absolute PLQY, but unfortunately this equipment could not be accessed for this work.

Further evidence of successful shell growth is given by the change in PXRD patterns upon increasing ZDEC addition. Upon addition of 0.1 equivalents and 1.0 equivalents of ZDEC, the (111), (220), and (311) diffraction peaks increase in intensity and shift to higher angles (Figure 3.6). The diffraction peaks observed when 1.0 equivalent of ZDEC is used appear at 28.1, 47.2, and 55.7°. The shift to higher angles is consistent with a

decrease in lattice parameter as the unit cell shrinks, and the positions are in close agreement with the (111), (220), and (311) reflections of bulk zinc blende ZnS (28.5, 47.5, and 56.3°, respectively). The shift implies a lattice contraction occurs to the In(Zn)P core upon deposition of the ZnS shell. This is consistent with overcoating using ZnS, which has a lower lattice constant (5.410 Å) than InP (5.869 Å), and is in agreement with other alloyed In(Zn)P/ZnS core/shell QDs.[10,11,39] The peaks remain broadened due to the small crystallite size. The sharp peak observed at 21.1° when 0.1 equivalents of ZDEC is used is indicative of surface ordered hexadecylamine ligands.[27]

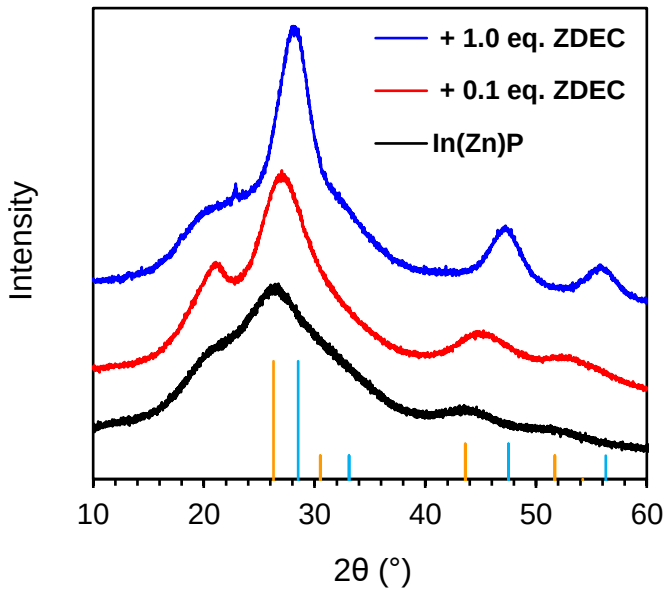
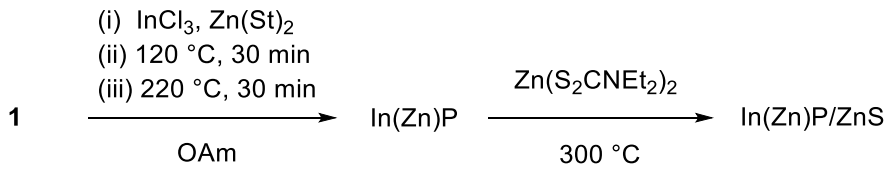


Figure 3.6: Powder X-ray diffraction pattern of core/shell In(Zn)P/ZnS QDs prepared using ZDEC. Diffraction patterns of zinc blende InP (orange) and ZnS (blue) shown for reference.

ICP-MS analysis provides additional insight into the change in composition of the QDs upon ZnS shell growth. The In(Zn)P QD cores were found to have an In:Zn ratio of 3.34:1, but upon shell growth the zinc content increased drastically to a ratio of 1:2.1. This increase is reflective of the additional zinc present within the ZnS shell.

Attempts to characterise the core/shell In(Zn)P/ZnS QDs prepared from **1** by scanning transmission electron microscopy (STEM) were unsuccessful due to extensive radiolysis of the samples. To alleviate these challenges, the synthetic methodology was modified to take advantage of oleylamine capping ligands (Scheme 3.7).



Scheme 3.7: Synthesis of oleylamine-capped In(Zn)P and core/shell In(Zn)P/ZnS QDs from **1**. $ZnSt_2$ = zinc stearate, OAm = oleylamine.

Oleylamine-capped In(Zn)P/ZnS QDs prepared from **1** were less sensitive to radiolysis, enabling successful imaging using high-angle annular dark-field (HAADF) STEM. HAADF-STEM images show the presence of spherical nanoparticles with an average particle diameter of 4.1 (± 0.5) nm (Figure 3.7(i)). This value is in agreement with other single shell InP/ZnS QDs, and provides unambiguous confirmation of the successful preparation of In(Zn)P/ZnS QDs from **1**.[40]

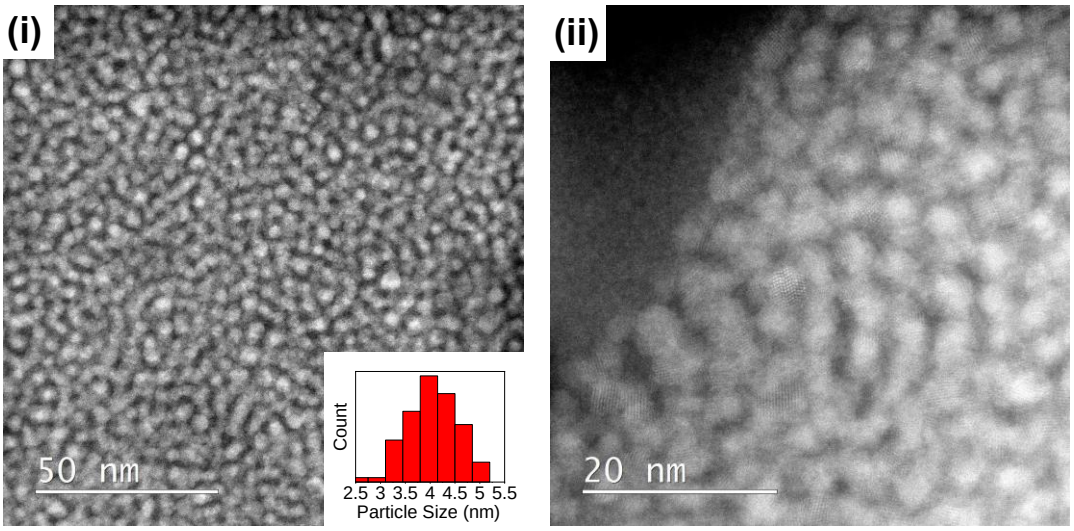


Figure 3.7: HAADF-STEM images of oleylamine-capped In(Zn)P/ZnS QDs prepared from **1**. Inset shows the histogram of particles diameters measured for 200 unique QDs.

Higher magnification imaging also clearly resolves lattice fringes arising from electron diffraction through the crystalline QD sample (Figure 3.7(ii)). Two sets of lattice fringes were observed for the oleylamine-capped In(Zn)P/ZnS QDs, with d-spacings equal to 0.322 nm and 0.182 nm. These lattice fringes can be assigned to the (111) and (220) planes of cubic zinc blende ZnS, respectively, and are in close agreement with d-spacings calculated by PXRD (d_{111} = 0.318 nm, d_{220} = 0.193 nm; Figure 3.8). The majority of the lattices fringes observed by STEM imaging correspond to diffraction of the (111) plane. This is also consistent with PXRD data, where the (111) peak as the most prominent.

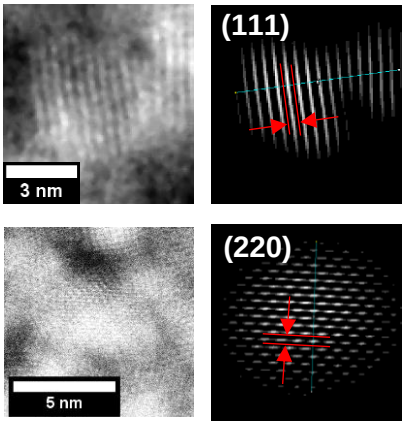


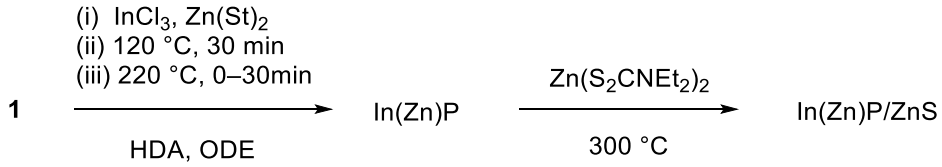
Figure 3.8: HAADF-STEM images of representative (111) and (220) lattice fringes used to estimate d-spacing.

3.3.3 Reaction duration optimisation at 220 °C

Having successfully employed ZDEC for the growth of core/shell In(Zn)P/ZnS QDs prepared from **1**, we were interested in evaluating how robust the shell growth methodology is for QD cores of different sizes.

As per Section 3.2.3.1, In(Zn)P QDs of different sizes were grown for 0–30 minutes at 220 °C, followed by epitaxial ZnS shell growth by annealing at 300 °C with ZDEC

(Scheme 3.8). The resulting core/shell QDs were purified by precipitation and resuspension cycles, and characterised using PL spectroscopy.



Scheme 3.8: Synthesis of core/shell In(Zn)P/ZnS QDs from **1** by varying the reaction duration at 220 °C.

The PL emission spectrum of In(Zn)P/ZnS QDs grown for 0 minutes at 220 °C show a peak at 544 nm (Figure 3.9(i)). As the reaction duration is increased to 5 minutes, 15 minutes, and 30 minutes, the PL λ_{max} values red-shift to 558 nm, 604 nm, and 616 nm, respectively, consistent with the growth of a ZnS shell onto a progressively larger In(Zn)P core. The FWHM of the peaks also gradually increase from 102 nm to 110 nm, 115 nm, and 119 nm.

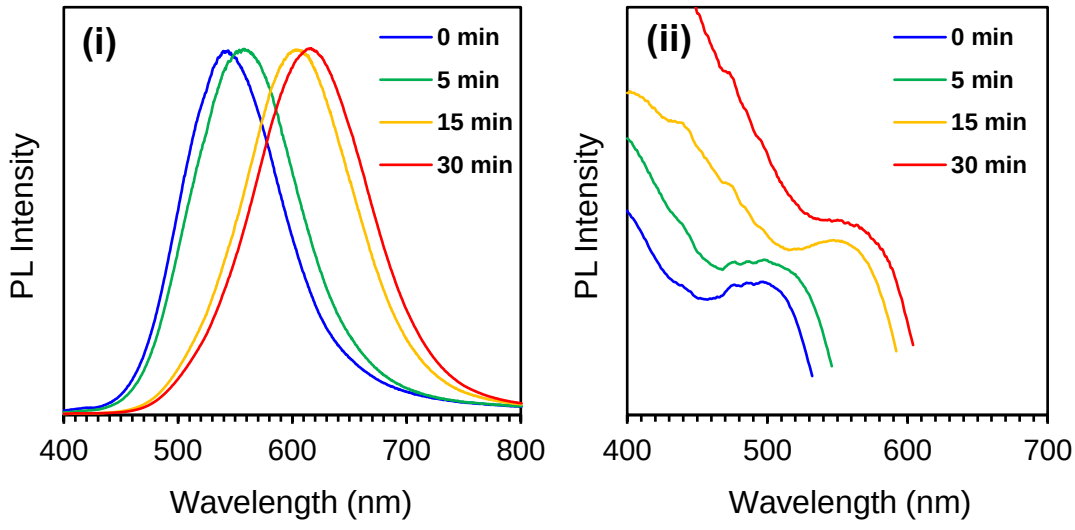


Figure 3.9: (i) PL emission spectra of In(Zn)P/ZnS QDs grown for 0–30 minutes at 220 °C; (ii) corresponding PL excitation spectra.

A similar trend is observed in the PL excitation spectra, where the excitation shoulders are shown to red-shift to higher wavelengths upon increasing the reaction duration at 220 °C (Figure 3.9(ii)). In(Zn)P/ZnS QDs grown at 220 °C for 0 minutes have an excitation shoulder at 497 nm, which increases to 501 nm, 547 nm, and 552 nm for upon heating for 5 minutes, 15 minutes, and 30 minutes, respectively.

3.3.4 Reproducibility evaluation

Given that the reactivity of **1** as a phosphide source is proposed to proceed via *in situ* PH_3 generation, we were cognizant of potential reproducibility challenges as a consequence of utilising volatile PH_3 at high temperatures. To evaluate the reproducibility of the synthetic procedure developed, the PL spectra of core/shell In(Zn)P/ZnS QDs prepared from **1** under identical conditions, as described in Section 3.3.1, are compared (Figure 3.10).

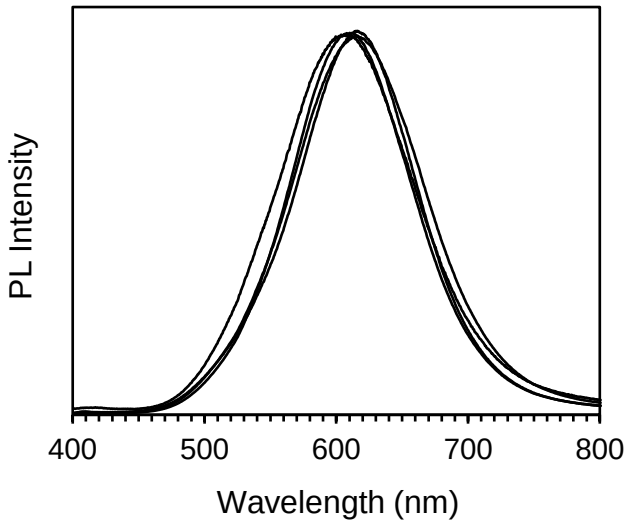


Figure 3.10: PL emission spectra of core/shell In(Zn)P/ZnS QDs prepared from **1**.

The four PL spectra compared are found to be consistent and reproducible, bearing a PL emission λ_{max} value of 613 (± 4.5) nm. The PL peak broadness varies by a slightly larger

margin, with FWHM measured as 114 (± 10.3) nm. However, the variance in FWHM is acceptable, as this reflects the relatively large degree of polydispersity already observed.

The reproducibility of the preparation developed, despite the use of **1** as an *in situ* PH_3 source, is encouraging and further affirms the phosphinecarboxamide group as an effective phosphide source for InP QDs.

3.4 Preparation of In(Zn)P/ZnS QDs from 1 exposed to air

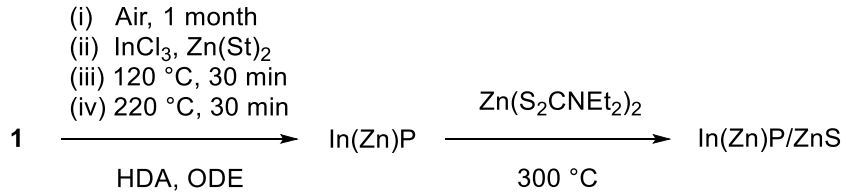
The successful implementation and development of **1** as a novel phosphorus precursor to InP QDs is exciting in its own right. As highlighted in Chapter 1, only a handful of phosphorus precursors to InP QDs are known. The addition of **1** to this group expands the toolset available for the pursuit and development of monodisperse InP QDs, offering a wholly new approach through *in situ* PH_3 generation.

Independent of its novelty as a phosphorus source, **1** is also remarkably air- and moisture-stable, showing minimal decomposition when exposed to air (Chapter 2). This characteristic is unprecedented for phosphorus precursors to InP QDs. Accordingly, we were interested in testing whether **1** exposed to air remains an effective phosphorus precursor to In(Zn)P QDs.

3.4.1 Synthesis of In(Zn)P/ZnS QDs

1 was stored in a glass vial under ambient conditions for one month. The headspace in the vial was periodically refreshed by opening the cap for one hour every week over the course of the experiment. **1** exposed to air was then combined with $InCl_3$, zinc stearate,

and HDA in ODE. Core/shell In(Zn)P/ZnS QD were then prepared following the same protocol described in Section 3.3.1 (Scheme 3.9).



Scheme 3.9: Synthesis of core/shell In(Zn)P/ZnS QDs from **1** exposed to air for one month. St = stearate, HDA = hexadecylamine, ODE = 1-octadecene.

3.4.2 Characterisation In(Zn)P/ZnS QDs

The PL spectrum shows a peak at 617 nm with a FWHM of 128 nm, supporting the successful formation of core/shell In(Zn)P/ZnS QDs (Figure 3.11). The PL peak is consistent with those observed when **1** is used in the absence of air exposure (Section 3.3.4). As seen before, the UV-Vis spectra shows a broad absorption edge, consistent with the presence of polydisperse QDs.

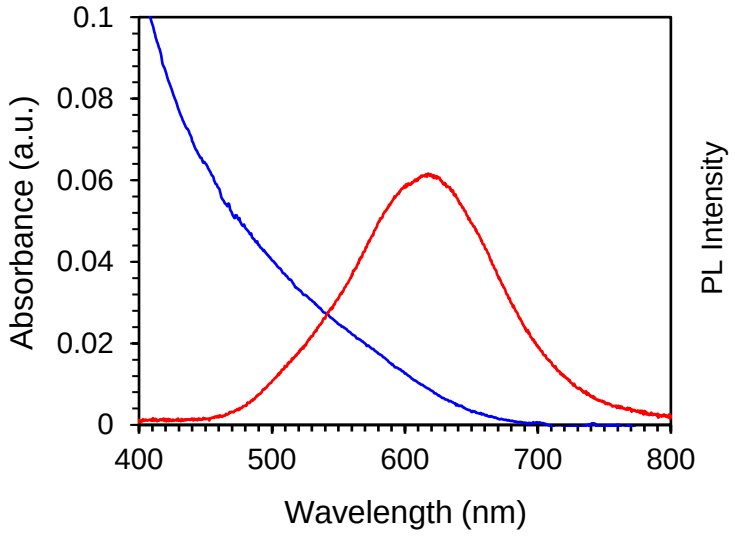


Figure 3.11: UV-Vis absorption (blue) and PL emission (red) spectra of a toluene solution containing In(Zn)P/ZnS QDs prepared from **1** that was exposed to air for 1 month.

Further support for the successful preparation of In(Zn)P and In(Zn)P/ZnS QDs from **1** when exposed to air is the given by PXRD analysis (Figure 3.12). The diffraction pattern of the In(Zn)P QDs cores shows a peak at 26.7°, and two broad shoulders at 43.5 and 51.0°, assigned to the (111), (220), and (311) reflections, respectively. Upon growth of a ZnS shell using ZDEC, the peaks increase in intensity and shift to higher angles as expected (28.1, 47.2, and 55.8°), and are in good agreement with bulk zinc blende ZnS.

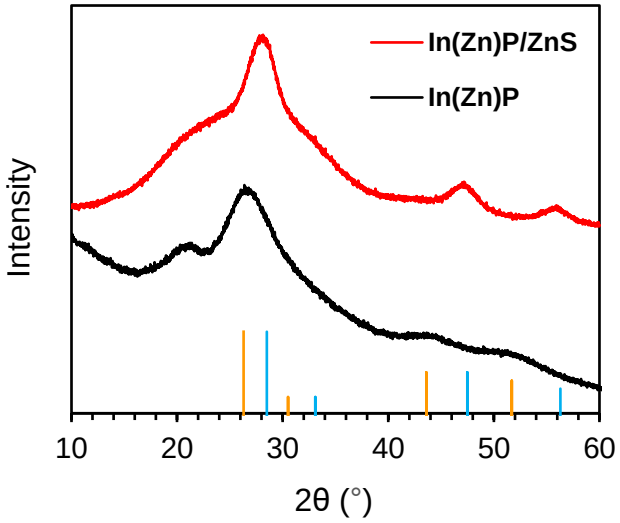
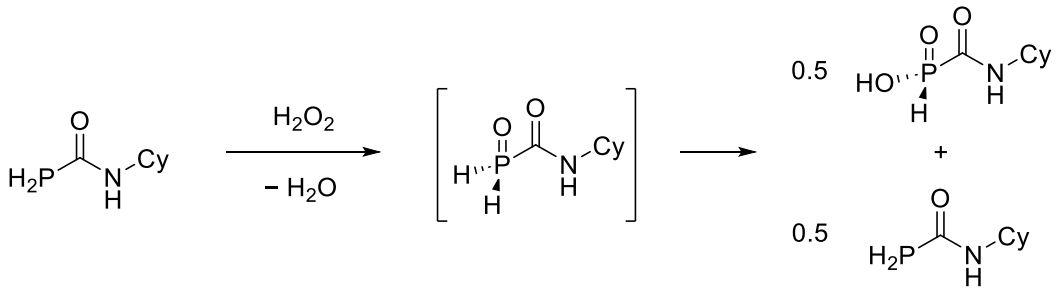


Figure 3.12: Powder X-ray diffraction pattern of In(Zn)P (black) and core/shell In(Zn)P/ZnS (red) QDs prepared from **1** exposed to air for one month. Diffraction patterns of zinc blende InP (orange) and ZnS (blue) shown for reference.

The close agreement of PL spectra and PXRD data with the QDs prepared from **1** without air exposure highlights the unprecedented ability of **1** to act as a bench stable phosphorus precursor to InP QDs. By utilising the *in situ* PH_3 reactivity of the *N*-functionalised phosphinecarboxamide motif, stability is conserved under ambient conditions whilst the ability to act as a phosphorus precursor upon thermal treatment is retained.

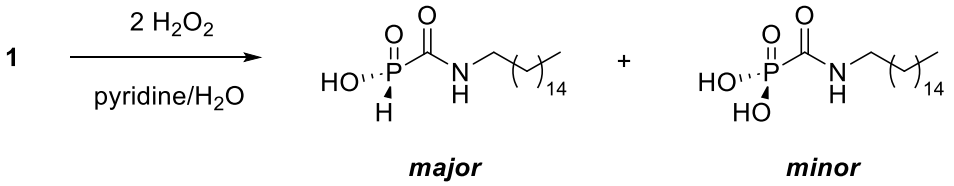
3.4.3 Oxidation of 1

Given the air stability of **1**, we were curious to investigate the reactivity of its oxidised form towards the preparation of InP QDs. Previous work in our group has shown that chemical oxidation of phosphinecarboxamides can be achieved by treatment with hydrogen peroxide.[41] It was found that the direct oxidation product, the phosphinecarboxamide oxide, is not stable and rapidly disproportionates into the corresponding phosphinic acid (Scheme 3.10).



Scheme 3.10: Oxidation of *N*-cyclohexylphosphinecarboxamide by H_2O_2.[41]

To compensate for the disproportionation reaction, **1** was oxidised using two equivalents of H_2O_2 and the crude reaction mixture isolated without further purification (Scheme 3.11).



Scheme 3.11: Oxidation of **1** by H_2O_2.

The ^{31}P NMR spectrum shows a doublet at 5.38 ppm ($^1J_{H–P}$ = 522 Hz) which collapses into a singlet upon proton decoupling (Figure 3.13). This is assigned to the phosphinic acid product and is consistent with spectroscopic data of the analogous oxidised *N*-cyclohexylphosphinecarboxamide (5.8 ppm, $^1J_{H–P}$ = 527 Hz).[41] The large coupling

constant of the oxidised product compared to **1** ($^1J_{H-P}$ = 204 Hz) is a result of the reduced electron density around phosphorus centre in the +5 oxidation state.[42] A singlet is also observed at −0.88 ppm, which is assigned to the phosphonic acid product present as a minor impurity.

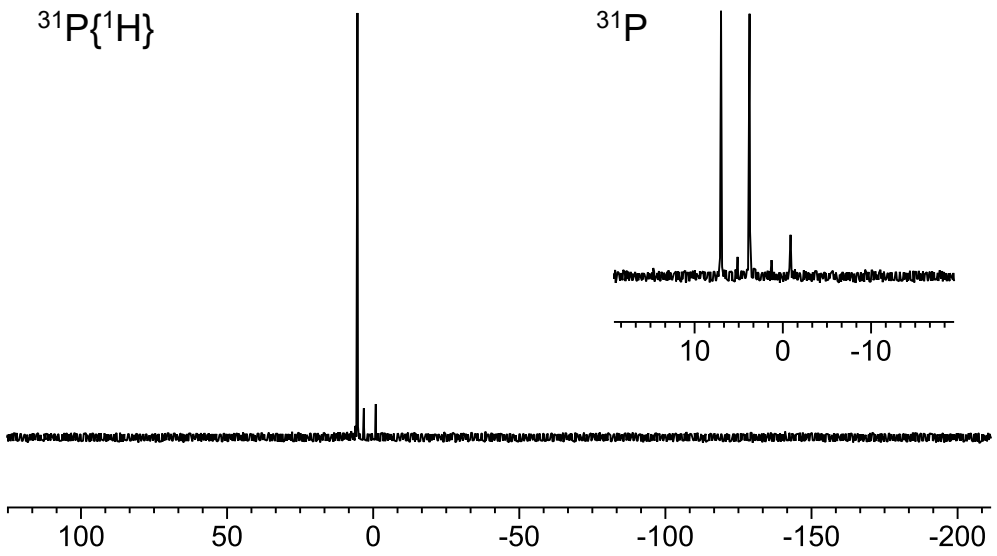
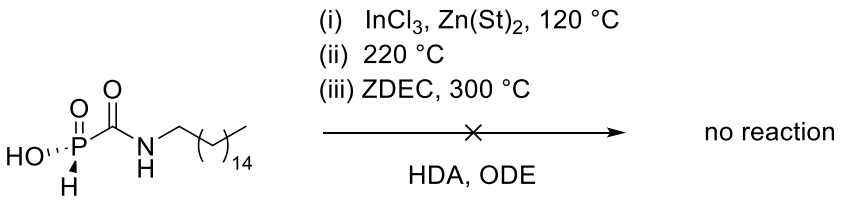


Figure 3.13: $^{31}P\{^1H\}$ NMR spectrum of d_5-pyridine containing the crude product from the oxidation of **1** by H_2O_2. Inset shows the ^{31}P NMR spectrum.

Attempts at using the phosphinic acid derivative of **1** to prepare In(Zn)P QDs resulted in the formation of a grey precipitate, assumed to be In_2O_3 (Scheme 3.12). The failed reaction can be rationalised by the ability of the phosphinic acid derivative of **1** to undergo condensation reactions with itself at elevated temperatures, forming the corresponding phosphinic acid anhydride.[43,44] The release of H_2O from the condensation reaction generates In_2O_3 phases in solution at elevated temperatures, which is consistent with physical observations.[45]



Scheme 3.12: Attempted synthesis of core/shell In(Zn)P/ZnS using the phosphinic acid of **1**.

The inability of the phosphinic acid derivative of **1** to act as a phosphorus precursor to InP QDs is compounded by the greater thermodynamic stability of the P(V) species. This is supported by the fact that no other phosphorus precursors to InP QDs in the +5 oxidation state are known.

3.5 Preparation of TOP-capped InP/ZnS QDs from 1

So far we have reported on the development of **1** for the preparation of HDA-capped In(Zn)P and core/shell In(Zn)P/ZnS QDs, in addition to its effectiveness for the reproducible production of a single ensemble of QDs. Yet as discussed, the QDs isolated display PL emission peaks with relatively large FWHM, indicative of polydispersity in QD particle size.

To address this, we were motivated to adapt our synthetic procedure to take advantage of conditions reported in the literature for the preparation of near-monodisperse InP QDs. We were particularly interested in the report by Angelé *et al.*, who developed a methodology using tri-*n*-octylphosphine (TOP) ligands and indium carboxylate precursors to prepare core/shell InP/ZnSeS QDs with PL emission FWHM as low as 40 nm.[5]

3.5.1 TOP-capped InP QDs

3.5.1.1 Synthesis of TOP-capped InP QDs

TOP-capped InP QDs were prepared using a modified preparation of that reported by Angelé *et al.*, substituting $P(SiMe_3)_3$ for **1** as the phosphorus precursor.[5] **1** was combined with indium palmitate ($In(O_2C(CH_2)_{14}CH_3)_3$) in a solution of TOP and ODE, and warmed to 250 °C (Scheme 3.13). The reaction mixture was stirred at 250 °C for 20 minutes, during which time an orange colour evolved, which quickly turned to dark red.



Scheme 3.13: Synthesis of TOP-capped In(Zn)P QDs from **1**. Pa = palmitate ($O_2C(CH_2)_{12}CH_3$); TOP = tri-*n*-octylphosphine; ODE = 1-octadecene.

3.5.1.2 Characterisation of TOP-capped InP QDs

UV-Vis analysis of the TOP-capped InP QD cores shows an absorption peak at 480 nm (Figure 3.14). The presence of a well-resolved absorption peak contrasts with the featureless absorption spectra obtained for HDA-capped In(Zn)P QDs. The resolution observed in the absorption spectrum is likely due to the substitution of HDA capping ligands with TOP. As discussed above, HDA capping ligands are highly absorbing and are known to mask absorption peaks in CdSe and III-V QDs.[24]

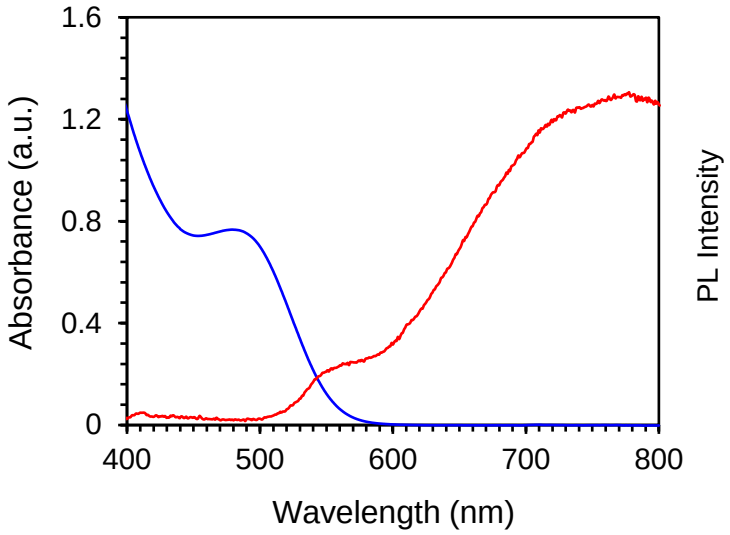


Figure 3.14: UV-Vis absorption (blue) and PL emission (red) spectra of a toluene solution containing TOP-capped InP QDs prepared from **1**.

The PL spectrum reveals a shoulder at 552 nm, as well as a broad and intense peak above 600 nm (Figure 3.14). The shoulder at 552 nm is attributed to band edge emission of the InP QDs, whilst the broad feature is characteristic of InP surface trap emission.[12] The low intensity of QD band edge emission, and conversely the high intensity of trap emission, is reflective of the absence of Zn^{2+} alloying in this procedure. By removing zinc stearate, the InP QD surface is no longer passivated with Zn^{2+} ions, resulting in a greater density of surface traps and an associated reduction in band edge emission.

The assignment of the broad peak above 600 nm as surface trap emission can be verified by interrogation of the corresponding PL excitation spectra. The PL excitation spectrum measured for QD band edge emission (λ_{max} = 552 nm) shows a peak at 526 nm, with a 26 nm Stokes shift characteristic of InP QD band gap excitation (Figure 3.15).[46] The PL excitation spectrum of the surface trap emission (λ_{max} = 760 nm) bears a peak at 512 nm. The large Stokes shift (248 nm) eliminates the possibility that the broad emission feature is a consequence of large polydisperse QDs. Instead, this is indicative of an energy loss

mechanism whereby photoexcited carriers charge transfer to surface trap states, consequently quenching band edge PL.[47]

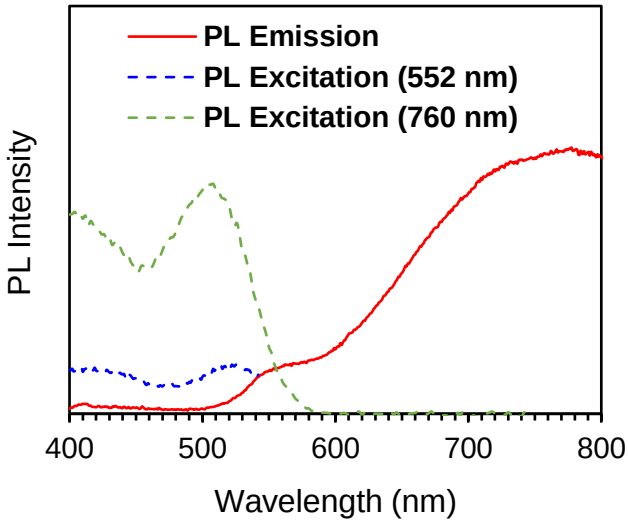


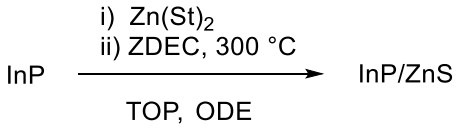
Figure 3.15: PL emission and excitation spectra of a toluene solution containing TOP-capped InP QDs prepared using **1**.

3.5.2 TOP-capped core/shell InP/ZnS QDs

3.5.2.1 Synthesis of TOP-capped InP/ZnS QDs

The low intensity of the PL peak and significant surface trap emission observed for TOP-capped InP QDs prepared from **1** prevented further evaluation of their optical properties. To address this a ZnS shell was grown onto the InP cores in an analogous manner to the HDA-capped In(Zn)P QDs (Section 3.3).

Zinc stearate was added to a crude solution containing TOP-capped InP QDs in TOP and ODE, and warmed to 300 °C (Scheme 3.14). When the solution temperature reached 260 °C a solution of ZDEC in ODE was added. The solution was then stirred at 300 °C for 30 minutes before cooling and purification.



Scheme 3.14: Synthesis of TOP-capped core/shell InP/ZnS QDs from InP QDs prepared from **1**. St = stearate; ZDEC = zinc diethyldithiocarbamate; TOP = tri-*n*-octylphosphine; ODE = 1-octadecene.

3.5.2.2 Characterisation of TOP-capped InP/ZnS QDs

The UV-Vis spectrum once again reveals a well-resolved absorption peak at 489 nm, 9 nm higher that the corresponding peak in the InP QD cores (Figure 3.16). The small increase is due to QD particle growth occurring as the temperature ramps up to 260 °C, before addition of ZDEC.

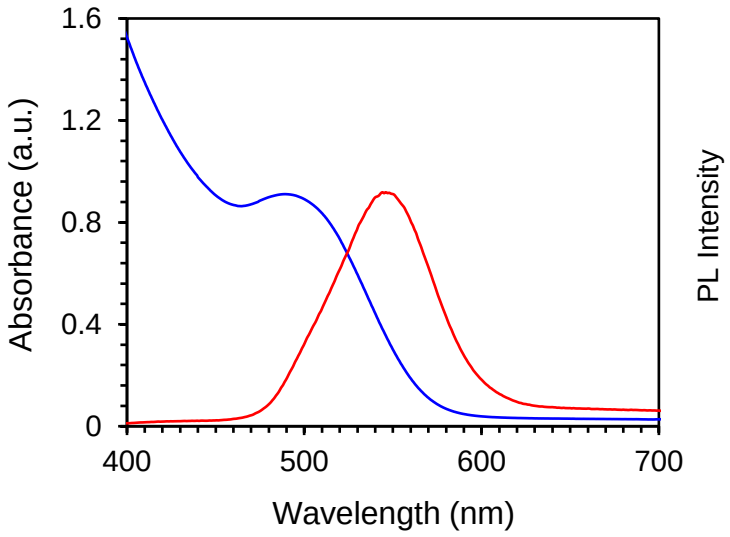


Figure 3.16: UV-Vis absorption (blue) and PL emission (red) spectra of a toluene solution containing TOP-capped core/shell InP/ZnS QDs prepared using **1**.

The PL spectrum shows a strong PL peak at 546 nm with FWHM of 68 nm (Figure 3.16). Moreover, the broad surface trap emission peak observed in the InP QD core spectra (*ca.* 760 nm) is absent. The suppression of surface trap emission is indicative of successful ZnS shell growth and surface passivation.

The narrow PL line width reflects a substantial improvement in particle size dispersity compared with the HDA-capped In(Zn)P/ZnS QDs presented earlier (FWHM >100 nm; Section 3.3). The improvement will inevitably be due to a combination of numerous changes in the synthetic procedure made upon adopting the preparation of Angelé *et al.*. These include for example: replacement of HDA capping ligands with TOP, substitution of the indium precursor, removal of zinc stearate, as well as changes in concentration, reagent stoichiometry, and heating profile.

The narrow PL emission linewidth enabled measurement of the PLQY of the TOP-capped InP/ZnS QDs, which was calculated to be 2.8%, determined relative to the coumarin 153 reference dye (PLQY = 53%). The PLQY, albeit low, supports the successful InP surface passivation by ZnS shell growth, given the non-emissive properties of unpassivated InP QDs. The low PLQY measured is due to the lack of optimisation of this protocol for the use of **1**. The shell growth protocol reported by Angelé *et al.* was optimised for the epitaxial growth of a ternary ZnSeS shell onto InP QDs prepared from $P(SiMe_3)_3$. In this case, we use **1**, which releases HDA upon decomposition, and subsequently grew a binary ZnS shell onto the InP QD cores. As discussed in Chapter 1, ZnSe and selenide-doped ZnSeS shells have lower lattice mismatches to InP compared to ZnS, resulting in fewer internal defects, improved surface passivation, and greater PLQYs.[28]

Further evidence of the successful formation of TOP-capped core/shell InP/ZnS QDs is given by PXRD analysis. Broad diffraction peaks are observed at 27.5, 45.7, and 53.9°, in good agreement to those of the HDA-capped core/shell In(Zn)P/ZnS QDs, and correspond to the (111), (220), and (311) reflections (Figure 3.17).

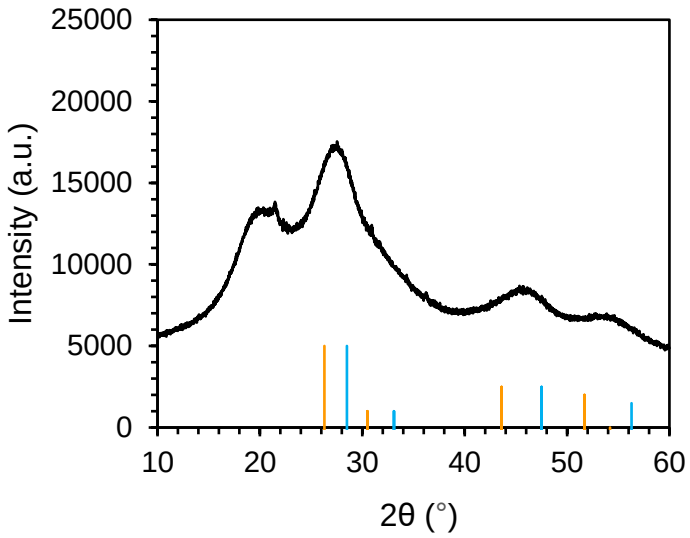


Figure 3.17: Powder X-ray diffraction pattern of TOP-capped core/shell InP/ZnS QDs prepared from **1**. Diffraction patterns of zinc blende InP (orange) and ZnS (blue) shown for reference.

The successful preparation of TOP-capped core/shell InP/ZnS QDs from **1** demonstrates its utility as a suitable substitute to traditional phosphorus precursors and compatibility with existing methodologies. The TOP-capped InP/ZnS QDs showed superior optical characteristics compared to the HDA-capped In(Zn)P/ZnS QDs detailed in Section 3.3 as a result of the greater degree of monodispersity in particle size. The purified TOP-capped InP/ZnS QDs showed comparably high solubility in apolar solvents, such as hexane and toluene (*ca.* 30 mg/ml), as the HDA-capped QDs described earlier. The success of the TOP-capped QD preparation highlights the potential for further synthetic optimisation to improve the optical quality of InP QDs prepared from **1**.

Despite these improvements, precursor challenges precluded the further development of **1** using the TOP-capped QD system. These challenges include TOP availability constraints, batch-to-batch inconsistencies in purity, as well as purification issues.

3.6 Preparation of In(Zn)P QDs using phenylacetate-capped InP MSCs

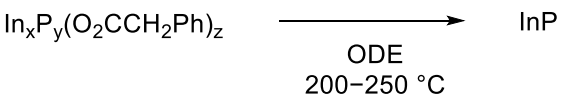
Our successful development of several protocols for the preparation of InP QDs from **1** motivated us to return to the phenylacetate-capped InP magic-sized clusters (MSCs) prepared in Chapter 2.

As discussed, InP MSCs are single-source precursors to InP QDs. InP MSCs are known to adopt crystallographically-distinct phases from that of the zinc blende structure of InP QDs. The structural difference between InP MSCs and QDs has implications for their potential role in templating nanocrystal growth and in dictating reaction kinetics. For this reason, InP MSCs are widely studied as precursors to InP QDs.

Chapter 2 discussed the synthesis and characterisation of phenylacetate-capped InP MSCs from the parent phosphinecarboxamide, $H_2PC(O)NH_2$. Using the synthesis protocol development and insights discussed in this chapter, in particular the successful preparation of HDA-capped In(Zn)P QDs, the phenylacetate-capped InP MSCs were studied as single-source precursors to InP QDs.

3.6.1 Thermal decomposition of InP MSCs prepared from $H_2PC(O)NH_2$

Phenylacetate-capped InP MSCs prepared from $H_2PC(O)NH_2$ were heated in ODE at 200 °C and 250 °C for 30 minutes and the crude reaction mixture was analysed by UV-Vis spectroscopy (Scheme 3.15).



Scheme 3.15: Thermal decomposition of phenylacetate-capped InP MSCs.

UV-Vis analysis reveals the resolution of the characteristic InP MSC peak at 414 nm after heating at 200 °C for 30 minutes, in addition to the formation of a new absorption shoulder at 599 nm (Figure 3.18). After heating at 250 °C the peak at 414 nm is completely consumed, while the absorption shoulder at 599 nm increases in wavelength to 627 nm. The consumption of the MSC and formation of a new, red-shifting absorption feature is characteristic of heterogenous InP QD growth directly from the InP MSCs. Moreover these results are consistent to those reported by Gary *et al*., who observed the evolution of InP QDs upon heating phenylacetate-capped InP MSCs in ODE at 160 °C for 40 minutes.[48]

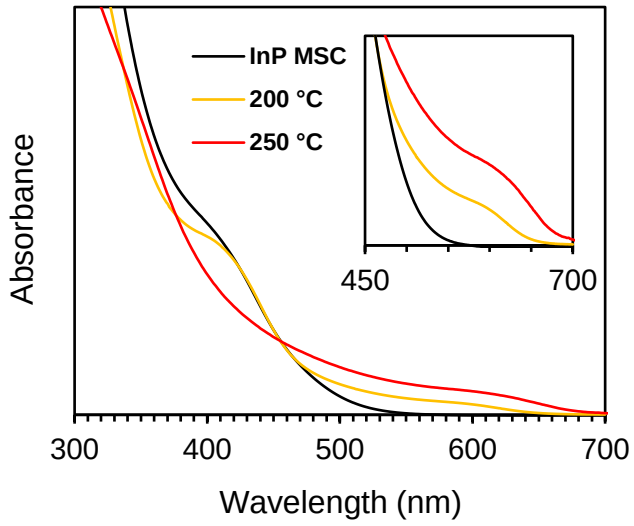
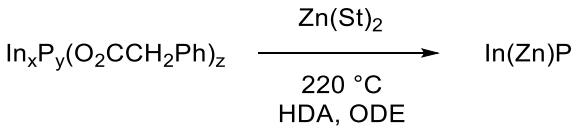


Figure 3.18: UV-Vis absorption spectra of phenylacetate-capped InP MSCs prepared from $H_2PC(O)NH_2$ (black) after heating at 200 °C (yellow) and 250 °C (red) for 30 minutes.

3.6.2 Preparation of In(Zn)P QDs from phenylacetate-capped InP MSCs

To further support the formation of InP QDs from phenylacetate-capped InP MSCs, In(Zn)P QDs were prepared using a modified method to that described in Section 3.2. Phenylacetate-capped InP MSCs prepared from $H_2PC(O)NH_2$ were combined with zinc

stearate and HDA, and suspended in ODE. The reaction mixture was then heated to 220 °C and stirred for 1 minute before the solution was rapidly cooled and purified for analysis (Scheme 3.16).



Scheme 3.16: Synthesis of In(Zn)P QDs from phenylacetate-capped InP MSCs. St = stearate; HDA = hexadecylamine; ODE = 1-octadecene.

UV-Vis analysis shows broad, featureless band edge absorption similar to that observed for HDA-capped In(Zn)P QDs prepared using **1** (Figure 3.19). PL spectroscopy reveals an emission peak at 611 nm, with a significant red-tail at longer wavelengths. The presence of an emission peak confirms the formation of In(Zn)P QDs, with the red-tail indicative of defect emission due to incomplete surface passivation by Zn^{2+} ions. This will be discussed further in Section 3.6.3.

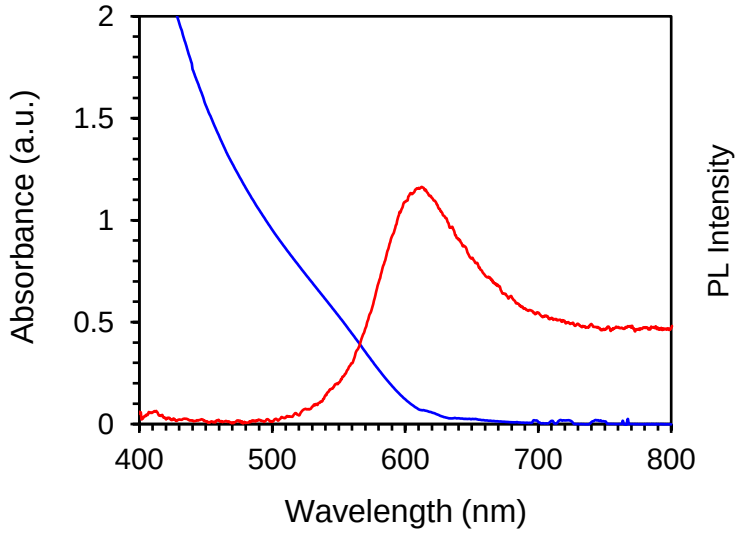


Figure 3.19: UV-Vis absorption (blue) and PL emission (red) spectra of a toluene solution containing In(Zn)P QDs prepared from phenylacetate-capped InP MSCs.

PXRD analysis of the HDA-capped In(Zn)P QDs prepared provides further evidence of their identity, showing broad diffraction peaks corresponding to the (111), (220), and (311), as anticipated for zinc blende InP QDs (Figure 3.20).

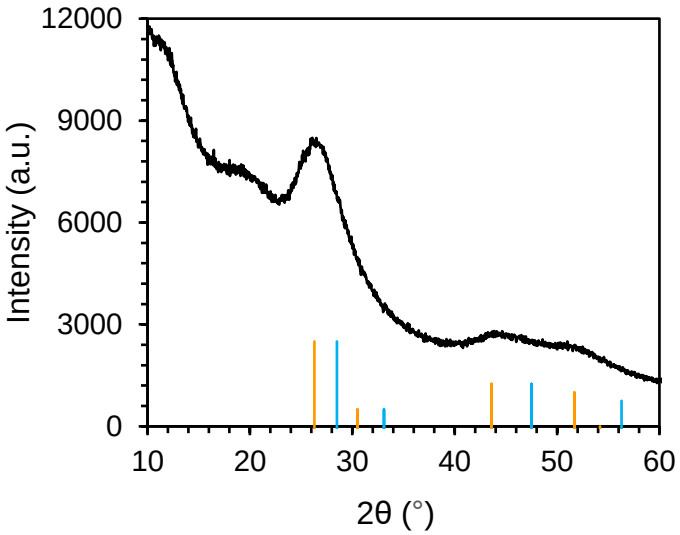


Figure 3.20: Powder X-ray diffraction pattern of In(Zn)P QDs prepared from phenylacetate-capped InP MSCs. Diffraction patterns of zinc blende InP (orange) and ZnS (blue) shown for reference.

ICP-MS analysis also supports successful zinc-alloying of InP QDs formed from the heterogenous growth of phenylacetate-capped InP MSCs, where an In:Zn ratio of 4.29:1 was measured. The high indium content of the In(Zn)P QDs is due to the InP MSC precursor itself being indium-rich.[49] The high In:Zn ratio is consistent with the red-tail observed in the PL emission spectrum, and indicates poor surface passivation as a consequence of low zinc incorporation. These results are also consistent with the HDA-capped In(Zn)P QDs prepared from **1** discussed earlier (Section 3.2.2), which had a comparably lower In:Zn ratio of 3.34:1 and showed substantially supressed defect emission.

The ability of phenylacetate-capped InP MSCs prepared from $H_2PC(O)NH_2$ to act as a single-source precursor to InP QDs supports the characterisation proposed and discussed in Chapter 2.

3.6.3 Effect of zinc doping on photoluminescence spectra

As highlighted in this chapter, the addition of zinc stearate strongly influences the PL emission profile of InP QDs. Zinc stearate was selected for its ability to alloy the InP surface with Zn^{2+} ions and passivate surface defects. This passivation is clearly observed when comparing the PL emission spectra of InP QDs prepared with differing Zn:In precursor stoichiometries. When the Zn:In precursor stoichiometry is increased, surface defect emission, red-shifted with respect to band edge emission, is progressively quenched (Figure 3.21). The decrease in defect emission is accompanied by an increase in intensity and resolution of the QD band edge emission peak. This observation is consistent with results reported by Zhang and Gu, who used zinc halides to dope In(Zn)P QDs and supress surface trap emission.[12]

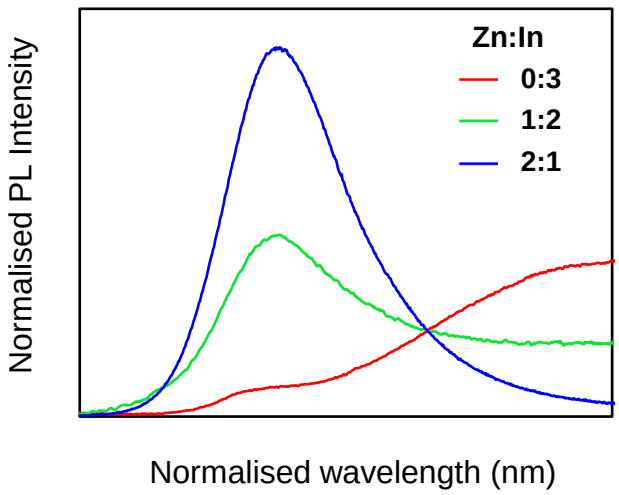


Figure 3.21: Normalised PL emission spectra showing a decrease in surface defect emission upon varying the Zn:In precursor stoichiometry.

3.7 Conclusions

This chapter has reported the preparation of HDA-capped In(Zn)P and core/shell In(Zn)P/ZnS QDs using *N*-hexadecylphosphinecarboxamide (**1**). The QDs prepared were characterised by UV-Vis and photoluminescence spectroscopy, powder X-ray diffraction, ICP-MS, and scanning transmission electron microscopy to provide conclusive evidence of their identity. The preparation of In(Zn)P/ZnS QDs from **1** stored in air for one month is also described. The QDs are shown to have comparable optical properties to those prepared from **1** when stored under an inert atmosphere. This unprecedented result represents the first example of an air-stable phosphorus precursor to InP QDs.

This chapter also details the optimisation and development of reaction conditions for the preparation of InP QDs using **1**. The sensitivity of QD particle size dispersity to the heating profile during QD nucleation and growth is discussed. While the results obtained suggest that In(Zn)P/ZnS QDs prepared from **1** are polydisperse, an improved method using TOP and palmitate capping ligands afforded InP and core/shell InP/ZnS QDs with greater size uniformity.

Finally, the InP QD preparation method described is applied for the use of the phenylacetate-capped InP magic-sized clusters (MSCs) described in Chapter 2 as precursors. The InP MSCs are shown to act as suitable single-source precursors to In(Zn)P QDs, which are characterised using spectroscopic, spectrometric, and X-ray crystallography methods.

3.8 References

1 Y. Wang, J. Howley, E. N. Faria, C. Huang, S. Carter-Searjeant, S. Fairclough, A. Kirkland, J. J. Davis, F. Naz, M. T. Sajjad, J. M. Goicoechea and M. Green, *Nanoscale Horiz.*, 2023, **8**, 1411–1416.

2 L. Li, M. Protière and P. Reiss, *Chem. Mater.*, 2008, **20**, 2621–2623.

3 N. Mordvinova, A. Vinokurov, T. Kuznetsova, O. I. Lebedev and S. Dorofeev, *Dalton Trans.*, 2017, **46**, 1297–1303.

4 Z. Xu, Y. Li, J. Li, C. Pu, J. Zhou, L. Lv and X. Peng, *Chem. Mater.*, 2019, **31**, 5331–5341.

5 L. Angelé, S. Dreyfuss, B. Dubertret and N. Mézailles, *Inorg. Chem.*, 2021, **60**, 2271–2278.

6 D. A. Taylor, J. A. Teku, S. Cho, W.-S. Chae, S.-J. Jeong and J.-S. Lee, *Chem. Mater.*, 2021, **33**, 4399–4407.

7 S. Xu, J. Ziegler and T. Nann, *J. Mater. Chem.*, 2008, **18**, 2653–2656.

8 L. Xi, D.-Y. Cho, A. Besmehn, M. Duchamp, D. Grützmacher, Y. M. Lam and B. E. Kardynał, *Inorg. Chem.*, 2016, **55**, 8381–8386.

9 F. Pietra, L. De Trizio, A. W. Hoekstra, N. Renaud, M. Prato, F. C. Grozema, P. J. Baesjou, R. Koole, L. Manna and A. J. Houtepen, *ACS Nano*, 2016, **10**, 4754–4762.

10 N. Kirkwood, A. De Backer, T. Altantzis, N. Winckelmans, A. Longo, F. V. Antolinez, F. T. Rabouw, L. De Trizio, J. J. Geuchies, J. T. Mulder, N. Renaud, S. Bals, L. Manna and A. J. Houtepen, *Chem. Mater.*, 2020, **32**, 557–565.

11 U. T. D. Thuy, P. Reiss and N. Q. Liem, *Appl. Phys. Lett.*, 2010, **97**, 2–4.

12 J. Zhang and H. Gu, *Dalton Trans.*, 2020, **49**, 6119–6126.

13 Y. Choi, D. Kim, Y. S. Shin, W. Lee, S. Orr, J. Y. Kim and J. Park, *Nanoscale*, 2022, **14**, 2771–2779.

14 H. Yoo, K.-S. Lee, S. Nahm, G. W. Hwang and S. Kim, *Appl. Surf. Sci.*, 2022, **578**, 151972.

15 J. J. Calvin, J. K. Swabeck, A. B. Sedlak, Y. Kim, E. Jang and A. P. Alivisatos, *J. Am. Chem. Soc.*, 2020, **142**, 18897–18906.

16 T.-G. Kim, D. Zherebetskyy, Y. Bekenstein, M. H. Oh, L.-W. Wang, E. Jang and A. P. Alivisatos, *ACS Nano*, 2018, **12**, 11529–11540.

17 J. P. Park, J.-J. Lee and S.-W. Kim, *Sci. Rep.*, 2016, **6**, 30094.

18 A. Cros-Gagneux, F. Delpech, C. Nayral, A. Cornejo, Y. Coppel and B. Chaudret, *J. Am. Chem. Soc.*, 2010, **132**, 18147–18157.

19 H. Virieux, M. Le Troedec, A. Cros-Gagneux, W.-S. Ojo, F. Delpech, C. Nayral, H. Martinez and B. Chaudret, *J. Am. Chem. Soc.*, 2012, **134**, 19701–19708.

20 E. Jang, Y. Kim, Y. H. Won, H. Jang and S. M. Choi, *ACS Energy Lett.*, 2020, **5**, 1316–1327.

21 D. A. Granada-Ramirez, J. S. Arias-Cerón, M. L. Gómez-Herrera, J. P. Luna-Arias, M. Pérez-González, S. A. Tomás, P. Rodríguez-Fragoso and J. G. Mendoza-Alvarez, *J. Mater. Sci. Mater. Electron.*, 2019, **30**, 4885–4894.

22 E. M. Janke, N. E. Williams, C. She, D. Zherebetskyy, M. H. Hudson, L. Wang, D. J. Gosztola, R. D. Schaller, B. Lee, C. Sun, G. S. Engel and D. V. Talapin, *J. Am. Chem. Soc.*, 2018, **140**, 15791–15803.

23 M. Furis, Y. Sahoo, D. J. MacRae, F. S. Manciu, A. N. Cartwright and P. N. Prasad, *J. Phys. Chem. B*, 2003, **107**, 11622–11625.

24 J.-W. Lee, H.-S. Yang, K. S. Hong and S. M. Kim, *J. Korean Phys. Soc.*, 2013, **63**, 2301–2304.

25 P. Scherrer, *Math. Phys.*, 1918, **2**, 98–100.

26 X. Xing, R. Liu, X. Yu, G. Zhang, H. Cao, J. Yao, B. Ren, Z. Jiang and H. Zhao, *J. Mater. Chem. A*, 2013, **1**, 1488–1494.

27 J. J. Calvin, T. M. Kaufman, A. B. Sedlak, M. F. Crook and A. P. Alivisatos, *Nat. Commun.*, 2021, **12**, 1–8.

28 B. Chen, D. Li and F. Wang, *Small*, 2020, **16**, 1–20.

29 R. Yadav, Y. Kwon, C. Rivaux, C. Saint-Pierre, W. L. Ling and P. Reiss, *J. Am. Chem. Soc.*, 2023, **145**, 5970–5981.

30 M. Kushwaha, A. P. Srivastava and M. K. Singh, *Mater. Lett.*, 2013, **109**, 23–26.

31 M. R. Friedfeld, J. L. Stein, A. Ritchhart and B. M. Cossairt, *Acc. Chem. Res.*, 2018, **51**, 2803–2810.

32 J. C. Sarker and G. Hogarth, *Chem. Rev.*, 2021, **121**, 6057–6123.

33 M. Azad Malik, P. O'Brien and N. Revaprasadu, *J. Mater. Chem.*, 2001, **11**, 2382–2386.

34 T. J. Macdonald, D. D. Tune, M. R. Dewi, J. C. Bear, P. D. McNaughter, A. G. Mayes, W. M. Skinner, I. P. Parkin, J. G. Shapter and T. Nann, *J. Mater. Chem.*

C, 2016, **4**, 3379–3384.

35 L. Xi, D. Y. Cho, M. Duchamp, C. B. Boothroyd, J. Y. Lek, A. Besmehn, R. Waser, Y. M. Lam and B. Kardynal, *ACS Appl. Mater. Interfaces*, 2014, **6**, 18233–18242.

36 Y. K. Jung, J. Il Kim and J.-K. Lee, *J. Am. Chem. Soc.*, 2010, **132**, 178–184.

37 M. Green, L. Sandiford, K. M. Anderson and Y. Ma, *Chempluschem*, 2012, **77**, 192–195.

38 Y. Shen, M. Y. Gee, R. Tan, P. J. Pellechia and A. B. Greytak, *Chem. Mater.*, 2013, **25**, 2838–2848.

39 U. T. D. Thuy, A. Maurice, N. Q. Liem and P. Reiss, *Dalton Trans.*, 2013, **42**, 12606–12610.

40 W. Zhang, S. Ding, W. Zhuang, D. Wu, P. Liu, X. Qu, H. Liu, H. Yang, Z. Wu, K. Wang and X. W. Sun, *Adv. Funct. Mater.*, 2020, **30**, 2005303.

41 A. Jupp, 2016, Thesis (D.Phil.), University of Oxford.

42 O. Kühl, ed. O. Kühl, Springer Berlin Heidelberg, Berlin, Heidelberg, 2008, pp. 25–29.

43 N. Z. Kiss, R. Henyecz and G. Keglevich, *Molecules*, 2020, 25.

44 K. Moedritzer, *J. Am. Chem. Soc.*, 1961, **83**, 4381–4384.

45 I. G. Nielsen, S. Sommer and B. B. Iversen, *Nanoscale*, 2021, **13**, 4038–4050.

46 E. M. Janke, N. E. Williams, C. She, D. Zherebetskyy, M. H. Hudson, L. Wang, D. J. Gosztola, R. D. Schaller, B. Lee, C. Sun, G. S. Engel and D. V Talapin, *J. Am. Chem. Soc.*, 2018, **140**, 15791–15803.

47 C. Giansante and I. Infante, *J. Phys. Chem. Lett.*, 2017, **8**, 5209–5215.

48 D. C. Gary, M. W. Terban, S. J. L. Billinge and B. M. Cossairt, *Chem. Mater.*, 2015, **27**, 1432–1441.

49 D. C. Gary, S. E. Flowers, W. Kaminsky, A. Petrone, X. Li and B. M. Cossairt, *J. Am. Chem. Soc.*, 2016, **138**, 1510–1513.

Chapter 4

Reactivity of functionalised phosphinecarboxamides in solution

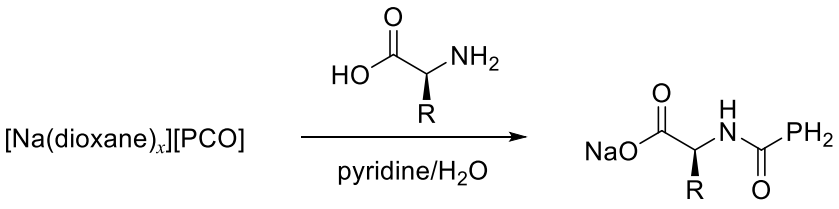
4.1 Introduction and objectives

The successful utilisation of **1** for the preparation of InP QDs described in Chapter 3 warrants the exploration of other phosphinecarboxamides as phosphorus precursors. By demonstrating that an *N*-functionalised phosphinecarboxamide effectively acts as an *in situ* PH_3 source, we were interested in investigating the effect of functionalisation on this reactivity profile. In particular, we were interested in incorporating capping ligand functionality into the phosphinecarboxamide precursor as a means to control the optical properties of the resulting InP QDs.

4.1.1 Functionalised phosphinecarboxamides

As highlighted in Chapter 1, a variety of functionalised phosphinecarboxamides can be accessed through the facile reaction of the 2-phosphaethyneolate anion (PCO^-) with amines under acidic conditions.[1]

Faria and Jupp showed that carboxylate functionality may be introduced through the *N*-substituent by derivation with amino acids (Scheme 4.1).[2] The phosphinecarboxamide derived from L-alanine was also found to be air- and moisture-tolerant. ^{1}H NMR analysis of a d_5-pyridine solution containing L-alanine-phosphinecarboxamide exposed to air reveals only 9% decomposition to free L-alanine after a period of two weeks.



Scheme 4.1: Carboxylate-functionalised primary phosphinecarboxamides prepared from L-amino acids (R = Me, CH_2OH, CH_2SH, $CH_2C(O)NH_2$, or $(CH_2)_2C(O)NH_2$).

Further functionalisation at both the nitrogen and phosphorus centres is also known. *P*-functionalisation can be achieved using several strategies: by the hydrophosphination of isocyanates;[3–7] or by the deprotonation of an *N*-functionalised phosphinecarboxamide, followed by reaction with a suitable electrophile.[8,9] These approaches have afforded a plethora of secondary and tertiary phosphinecarboxamides decorated with alkyl, benzyl, and aryl substituents at phosphorus.

In contrast to *P*,*P*-functionalisation, few *N*,*N*-functionalised phosphinecarboxamides exist. Jupp e*t al.* reported the preparation of *N*,*N*-diethylphosphinecarboxamide ($H_2PC(O)NEt_2$) from diethylamine, while Faria described the synthesis of an *N*,*N*-functionalised phosphinecarboxamide derived from L-proline.[10,11]

4.1.2 Chapter outline

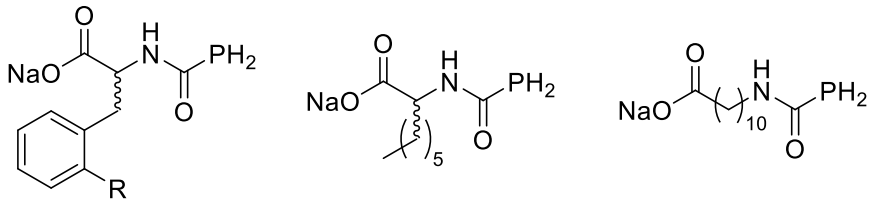
This chapter will describe the solution phase reactivity of *N*-, *N*,*N*-, and *P*-functionalised phosphinecarboxamides. Novel *N*-functionalised phosphinecarboxamides bearing carboxyl functional groups (**2**–**8**) are prepared and characterised by ^{1}H, ^{13}C, ^{19}F, ^{31}P NMR and infrared (IR) spectroscopy. The thermal decomposition of these compounds and transamidation reactions with hexadecylamine are also described.

The effect of *N*,*N*- and *P*-functionalisation on the reactivity of the phosphinecarboxamide moiety is also studied. The thermal decomposition and transamidation with hexadecylamine of L-proline-phosphinecarboxamide and *P*-benzyl-*N*-cyclohexyl-phosphinecarboxamide is described.

Xuechun Bai contributed experimentally to this work under my supervision, and submitted a thesis on their work in fulfilment of Part II of the M.Chem. degree.

4.2 Synthesis and reactivity of carboxylate-functionalised phosphinecarboxamides

In order to appropriately evaluate the effect of *N*-substituent functionalisation on the optical properties of InP QDs, several novel phosphinecarboxamides were targeted. Chapter 2 detailed the use of phenylacetate capping ligands for the preparation and stabilisation of InP magic-sized clusters from $H_2PC(O)NH_2$, and in Chapter 3 these were successfully employed as single-source precursors to InP QDs. Inspired by these results, we sought to incorporate phenylacetate functionality into a phosphinecarboxamide. At the time that this work was conducted, supply issues precluded the acquisition of L-phenylglycine, therefore the structurally-related L-phenylalanine was used instead (**2**; Figure 4.1). The structural congener of **2** containing a CF_3 substituent on the phenyl ring was also targeted to provide an additional ^{19}F NMR spectroscopic handle during analysis.



2 (R = H)
3 (R = CF_3)

4

5

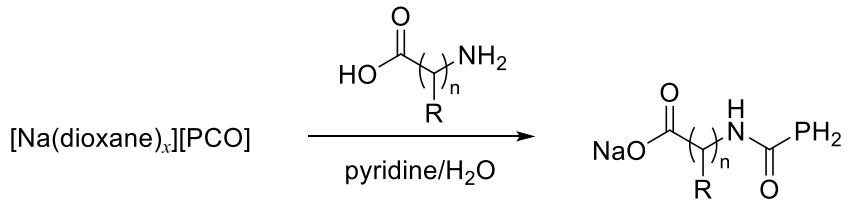
Figure 4.1: Compounds **2**–**5**.

We were inspired by the success of introducing capping-ligand character into phosphinecarboxamide **1** through the hexadecyl *N*-substituent. **4** was derived from DL-2-aminocaprylic acid, which replaces the CH_2Ph substituent in **2** with an aliphatic C_6H_{13} group. It is envisioned that the addition of a long chain aliphatic hydrocarbon substituent should aid the solubilisation of **4** in apolar reaction media.

Finally, **5** was derived from 11-aminoundecanoic acid, thereby increasing the distance between the phosphinecarboxamide and carboxyl moieties. **5** is reminiscent of bi-functional capping ligands used to stabilise nanoparticles in hydrophilic conditions, as well as those employed for tethering nanoparticles to one another.[12]

4.2.1 Synthesis and characterisation

Phosphinecarboxamides **2**–**5** were prepared following the procedure of Faria and Jupp from [Na(dioxane)$_x$][PCO] and the respective amino acid (**2**–**4**) or amino-carboxylic acid (**5**) precursors in pyridine and water (Scheme 4.2).[2]



Scheme 4.2: Synthesis of **2**–**5**. R = CH_2Ph (**2**), $CH_2C_6H_4(CF_3)$ (**3**), C_6H_{13} (**4**), or H (**5**); n = 1 (**2**, **3**, **4**), or 10 (**5**); x = 2.50–2.71.

The reactions were monitored by ^{1}H, ^{13}C, ^{19}F and ^{31}P NMR spectroscopy, which revealed the formation of the expected phosphinecarboxamides. The ^{31}P NMR spectra of **2**–**5** show a characteristic triplet between –131.1 and –132.2 ppm ($^1J_{H–P}$ = 207.1–211.9 Hz) that collapses to a singlet upon proton-decoupling (Table 4.1).

Due to the presence of a chiral centre in the backbone of **2**–**4**, the products displayed two diastereotopic phosphine protons in ^{1}H NMR spectra. These resonances appear between 3.68 and 3.94 ppm, and have the same large one-bond phosphorus coupling as observed in their respective ^{31}P NMR spectra ($^1J_{H–P}$ = 207.0–212.0 Hz). Upon phosphorus-decoupling the signals collapse into doublets ($^2J_{H–H}$ = 11.6–11.7 Hz) as expected.

Finally, $^{13}C\{^{1}H\}$ NMR spectra of **2**–**5** reveal a doublet between 173.4 and 176.7 ppm corresponding to the carbonyl carbon which couples to the phosphorus in the phosphinecarboxamide fragment.

Selected NMR data are summarised in Table 4.1 for d_5-pyridine solutions containing **2**–**5** with a drop of distilled H_2O to aid solubility. The resonances found are in line with other carboxylate-functionalised phosphinecarboxamides reported.[2,11]

Table 4.1: Selected NMR spectroscopic data for **2**–**5**. Chemical shifts are given in ppm and coupling constants in Hz. General structure $H_2PC(O)NH(CHR)_nCOONa$.

Compound	R	n	^{31}P	$^{1}J_{H–P}$	^{1}H	$^{13}C\{^{1}H\}$	$^{1}J_{P–C}$
2	CH_2Ph	1	−131.8	207.1	3.68; 3.74	173.5	7.6
3	$CH_2(C_4H_6$-o-$CF_3)$	1	−131.8	209.0	3.75; 3.82	173.7	7.1
4	C_6H_{13}	1	−131.1	209.1	3.86; 3.94	173.4	7.1
5	H	10	−132.2	211.9	4.04	176.7	8.2

All of the phosphinecarboxamides described in Table 4.1 were fully characterised by NMR spectroscopy and complete data can be found in Chapter 7. Herein only the results obtained for **2** and **3** will be discussed in significant detail as representative examples. Despite several attempts, no crystal structures were obtained for the compounds listed.

4.2.1.1 Characterisation of 2

The ^{1}H NMR spectrum of **2** shows four doublet of doublets (Figure 4.2). One pair appear centred at 3.68 and 3.74 ppm, each with one large ($^{1}J_{P–H}$ = 207.1 Hz) and one small ($^{2}J_{H–H}$ = 11.2, 11.6 Hz) coupling constant. The peaks are assigned to the two diastereotopic phosphine protons, and collapse to two doublets upon phosphorus-

decoupling ($^2J_{Ha–Hb}$; Figure 4.3). The second pair of doublet of doublets at 3.57 and 3.77 ppm are attributed to the two non-equivalent benzylic protons by their shared geminal coupling ($^2J_{Ha–Hb}$ = 13.7 Hz). The appearance of two doublet of doublets and not one single doublet arises due to restricted C–C bond rotation in the backbone causing non-equivalence ((OOC)(NH)HC–CH_2Ph). This is reflected by the difference in the vicinal coupling constants to the adjacent CH proton environment (5.28 ppm; $^3J_{H–Ha}$ = 4.9 Hz versus $^3J_{H–Hb}$ = 7.1 Hz). This non-equivalence is also observed in the ^{1}H NMR spectra of **3** and **4**. However, the methylene protons in **5** are equivalent due to free C–C bond rotation afforded as a result of the greater distance between the bulky substituents. The other resonances in the ^{1}H NMR spectrum of **2** correspond to the aromatic (7.21–7.58 ppm), amide (7.70 ppm), and methyne (5.28 ppm) proton environments.

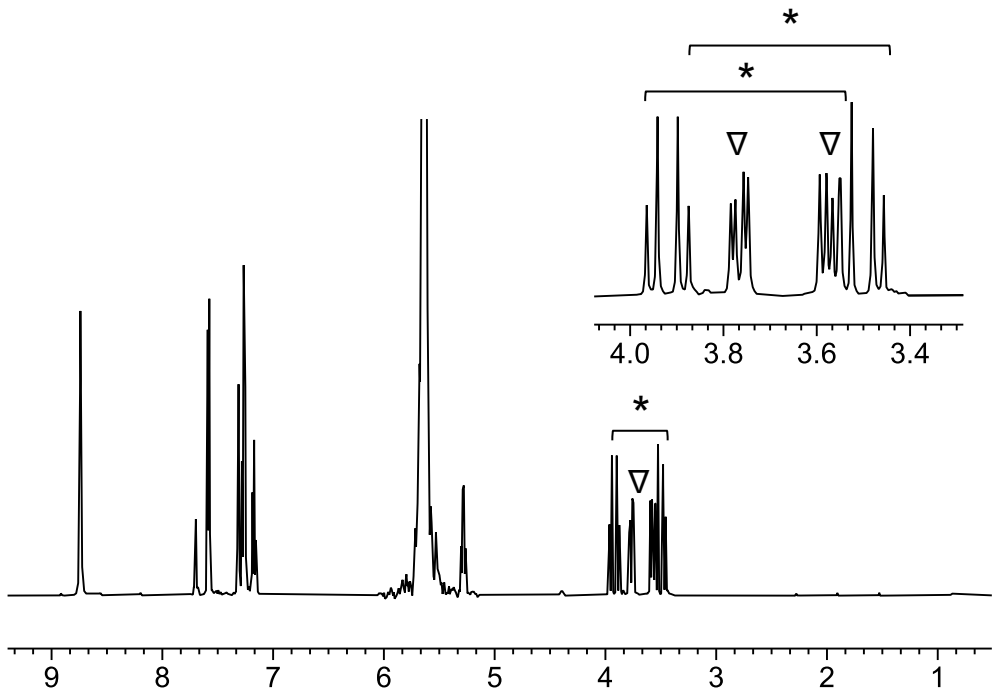


Figure 4.2: ^{1}H NMR spectrum of a d_5-pyridine solution of **2**. Inset showing diastereotopic phosphine protons of the phosphinecarboxamide moiety (*) and benzylic protons (∇). Intense peak at 5.64 ppm corresponds to H_2O.

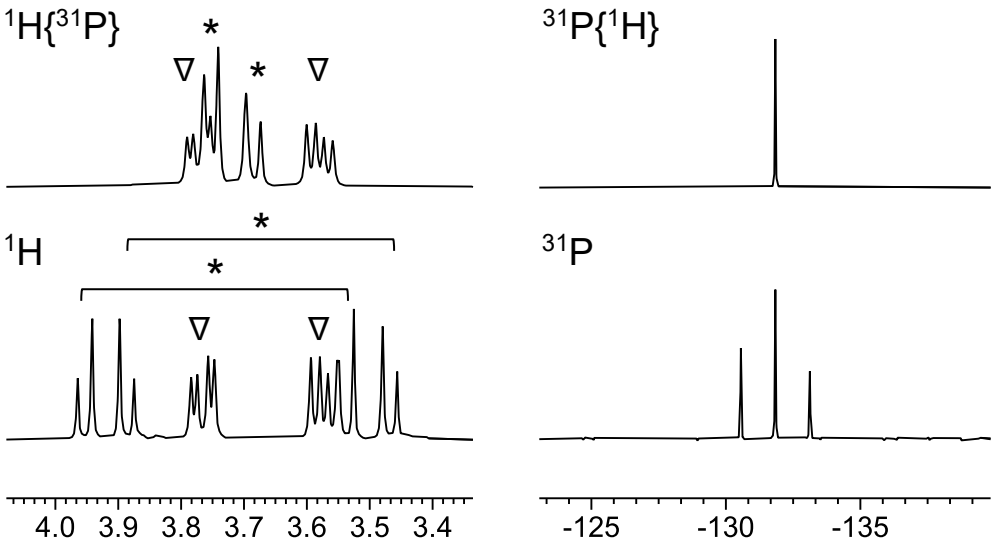


Figure 4.3: ^{1}H and ^{31}P NMR spectra of **2**. Phosphine protons of the phosphinecarboxamide moiety (*) and benzylic protons (∇) highlighted for clarity.

The formation of **2** is also evidenced in the ^{31}P NMR spectrum by a characteristic triplet at –131.8 ppm ($^{1}J_{P–H}$ = 207.1 Hz) which collapses to a singlet upon proton-decoupling (Figure 4.3). Moreover, the $^{13}C\{^{1}H\}$ NMR spectrum shows a doublet at 173.5 ppm with a coupling constant of $^{1}J_{P–C}$ = 7.6 Hz, corresponding to the phosphinecarboxamide moiety (Figure 4.4). A singlet at 177.5 ppm is also observed and is assigned to the carboxylate carbon environment. The results obtained are in good agreement with other carboxylate-functionalised phosphinecarboxamides.[2,11]

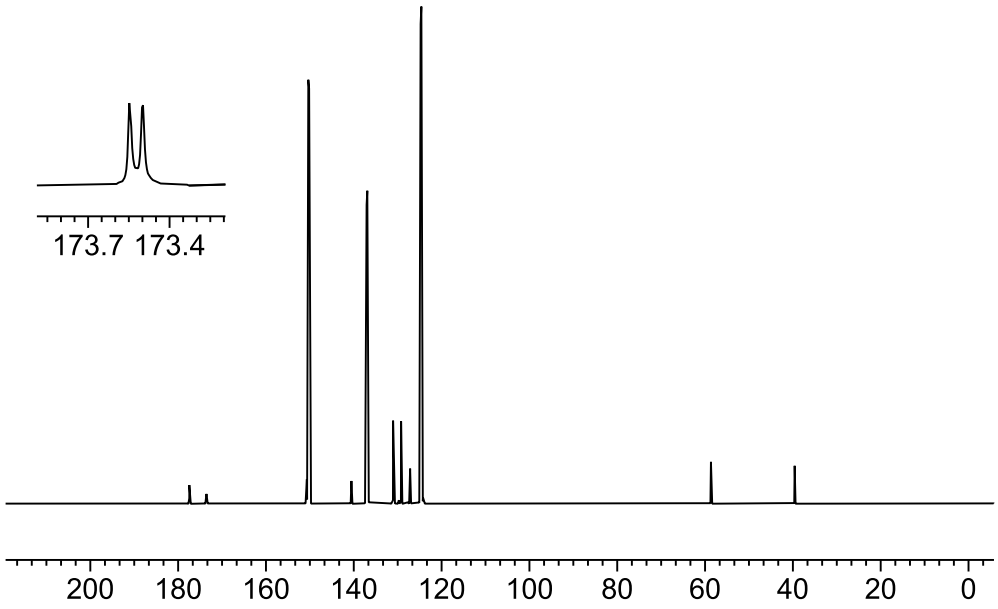


Figure 4.4: $^{13}C\{^{1}H\}$ NMR spectrum of **2**. Inset showing carbon resonance corresponding to the phosphinecarboxamide moiety.

4.2.1.2 Characterisation of 3

Compound **3**, the structural congener of **2**, was prepared with a CF_3 substituent on the phenyl ring in order to incorporate an additional ^{19}F NMR spectroscopic handle for use in further reactivity studies. ^{1}H and ^{31}P NMR spectra obtained for **3** were consistent with **2** and the corresponding data are highlighted in Table 4.1. The ^{19}F NMR spectrum shows a singlet at −58.1 ppm which is assigned to the CF_3 substituent on the o-phenylene ring (Figure 4.5). The presence of the CF_3 group in the product is also evidenced in the $^{13}C\{^{1}H\}$ NMR spectrum by the presence of a quartet resonance at 126.8 ppm ($^{1}J_{F–C}$ = 5.2 Hz).

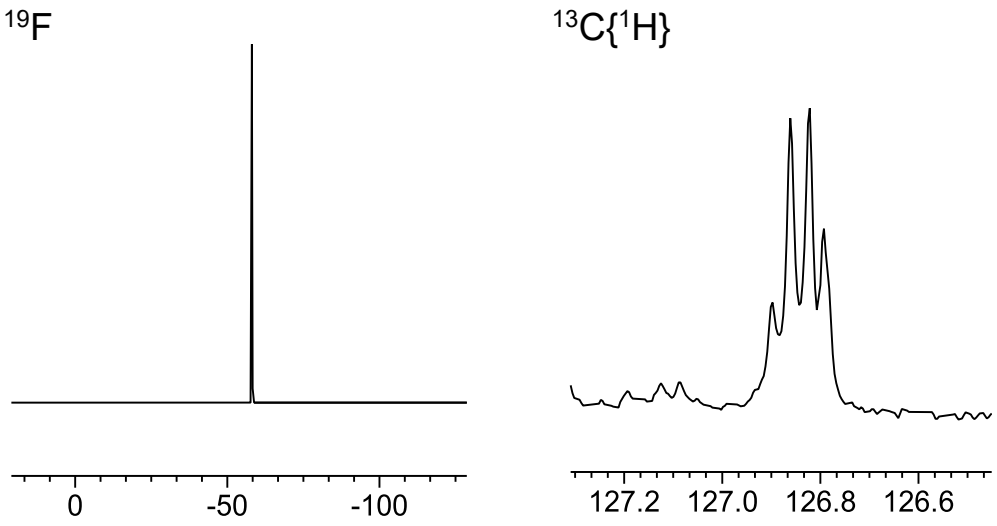
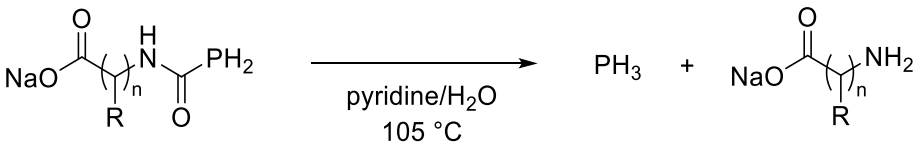


Figure 4.5: ^{19}F and $^{13}C\{^{1}H\}$ NMR spectra highlighting the CF_3 environment of **3**.

4.2.2 Thermal decomposition of 2, 4, and 5

To determine whether *N*-functionalised phosphinecarboxamides bearing carboxylate functional groups decompose to form PH_3 *in situ* as observed for **1**, the thermal decomposition of **2**, **4**, and **5** was investigated. The compounds were heated in d_5-pyridine at 105 °C for 0–120 minutes and monitored by ^{31}P NMR spectroscopy (Scheme 4.3). No thermal decomposition was observed below 105 °C.



Scheme 4.3: Thermal decomposition of carboxylate-functionalised phosphinecarboxamides **2**, **4**, and **5** in d_5-pyridine and H_2O.

The $^{31}P\{^{1}H\}$ NMR spectra show that upon heating **2**, the phosphinecarboxamide peak at −131.8 ppm decreases in intensity relative to the triphenylphosphine (PPh_3) internal standard (Figure 4.6). In addition, a new peak forms at −239.5 ppm and increases in

intensity as the experiment proceeds. The peak is characteristic of dissolved PH_3 and is consistent with the *in situ* PH_3 generation observed for **1** (Chapter 2).

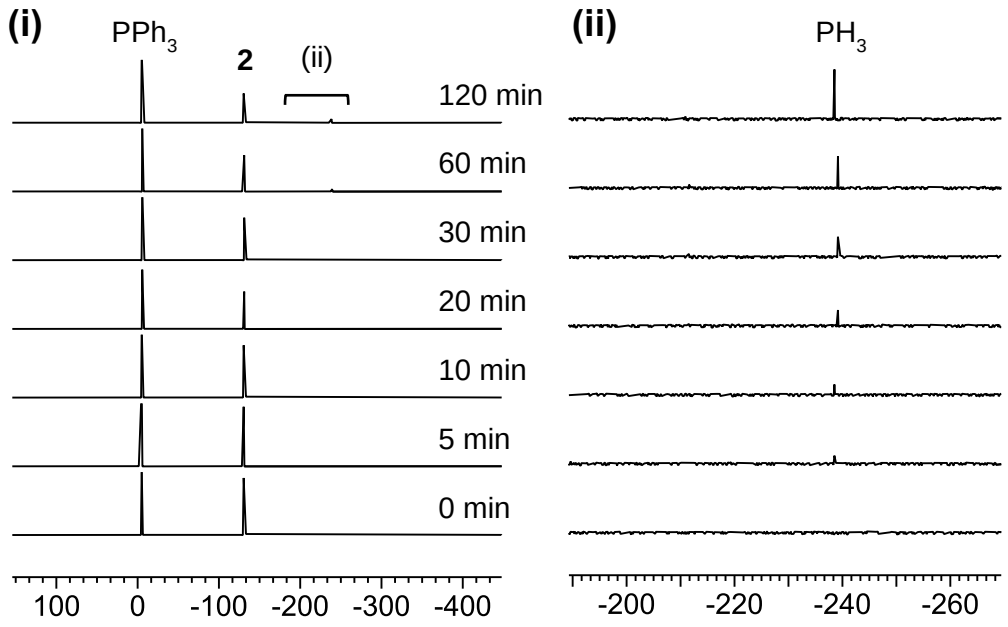


Figure 4.6: (i) $^{31}P\{^1H\}$ NMR spectra of a d_5-pyridine solution of **2** heated at 105 °C for 0–120 min; (ii) expanded region to show characteristic PH_3 resonance. PPh_3 is present as an internal standard.

Congruent reactivity is observed for **4** and **5** upon heating at 105 °C for 120 minutes, showing consumption of the phosphinecarboxamide peak and concomitant PH_3 evolution (Figure 4.7). **2**, **4**, and **5** appear to decompose at varying rates, however this is likely due to the poor solubility of the compounds in d_5-pyridine and sensitivity to the amount of H_2O added.

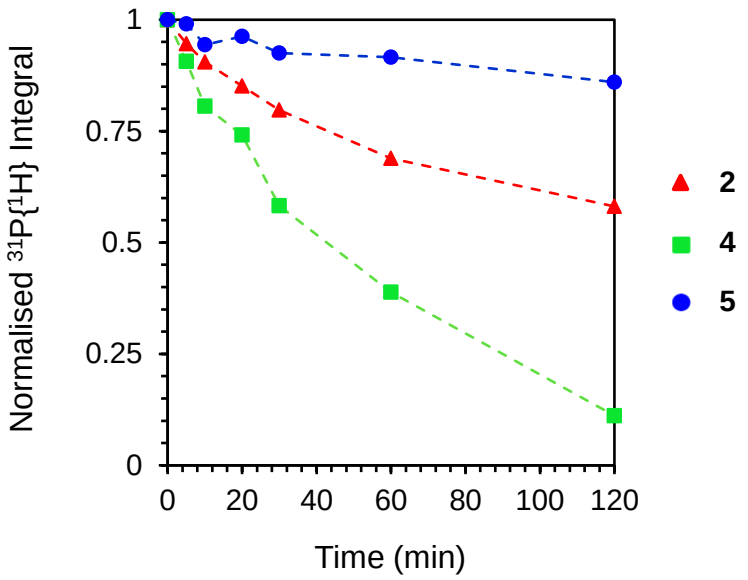


Figure 4.7: Normalised $^{31}P\{^{1}H\}$ NMR integrals of **2**, **4**, and **5** upon heating at 105 °C over 120 minutes. Integrals normalised against a PPh_3 internal standard.

With the mechanism of PH_3 generation upon thermal decomposition proposed to proceed through a HPCO intermediate, subtle differences in the concentration of H_2O, a protic solvent, likely gives rise to the differing decomposition profiles observed. Hinz and Schreiber have both reported the sensitivity of PCO^- to decomposition under acidic conditions.[13,14]

In fact, further evidence of the intermediacy of PCO^- in the thermal decomposition of phosphinecarboxamides is revealed by **5**. $^{31}P\{^{1}H\}$ NMR spectra show that upon decomposition of **5** (−132.0 ppm), a new peak at −390.0 ppm emerges characteristic of PCO^- (Figure 4.8). As the experiment proceeds, the PCO^- peak diminishes in intensity while PH_3 is formed (−239.0 ppm).

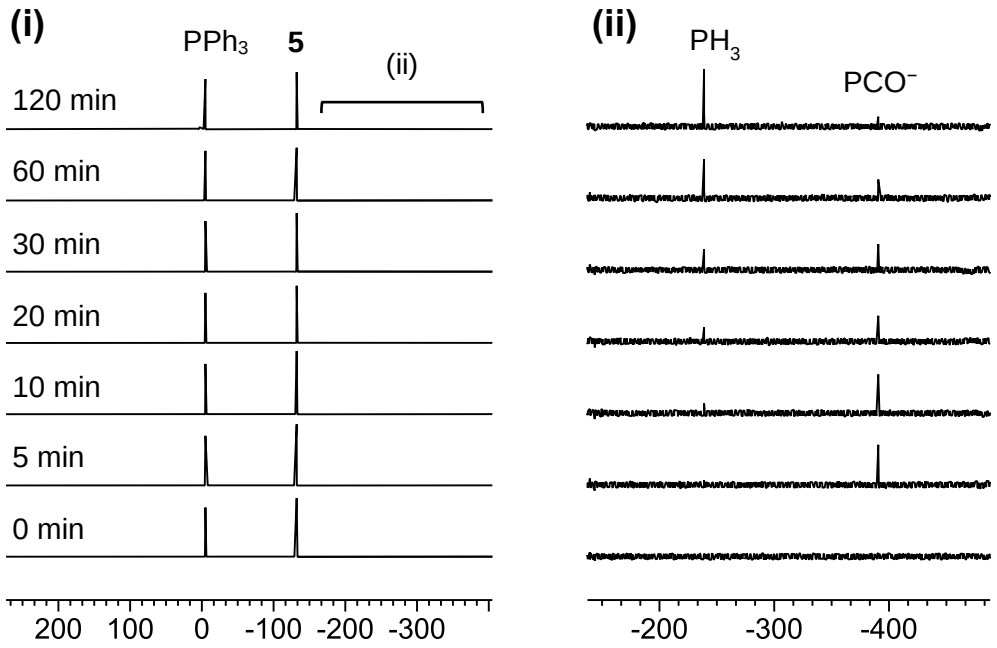


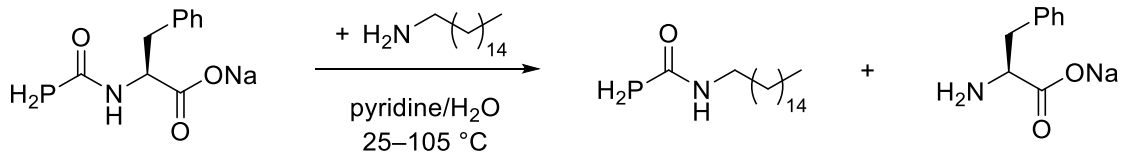
Figure 4.8: (i) $^{31}P\{^{1}H\}$ NMR spectra of a d_5-pyridine solution of **5** heated at 105 °C for 0–120 min; (ii) expanded region to show characteristic PH_3 and PCO^- resonances. PPh_3 is present as an internal standard.

The conservation of *in situ* PH_3 generation observed for **1** upon functionalisation with a carboxylate group confirms this reactivity as characteristic of the phosphinecarboxamide moiety itself. Moreover, the formation of PH_3 upon thermal decomposition is promising for the use of **2**–**5** as phosphorus precursors to InP QDs, which will be discussed in Chapter 5.

4.2.3 Transamidation of 2

The transamidation reaction of $H_2PC(O)NH_2$ with hexadecylamine (HDA) to form **1** described in Chapter 2 was influential in steering the development of this research. This revealed **1** as the active species during InP QD growth conditions when using HDA capping ligands. Considering the analogous transamidation reaction occurring for carboxylate-functionalised phosphinecarboxamides, the reaction of **2** with HDA was studied.

A d_5-pyridine solution containing **2** and HDA was heated at 25–105 °C, following a similar heating profile to that used in the preparation of HDA-capped In(Zn)P QDs (Scheme 4.4).



Scheme 4.4: Formation of **1** from the transamidation of **2** with hexadecylamine.

^{1}H NMR spectra show a decrease in intensity of the phosphine (3.39 and 3.45 ppm) and benzylic (3.40 and 3.70 ppm) proton environments of **2**, in addition to the emergence of a new doublet and multiplet (Figure 4.9). The new peaks are consistent with the formation **1**, with the doublet at 3.53 ppm ($^1J_{P–H}$ = 207.4 Hz) characteristic of the phosphine protons and the multiplet at 3.47 ppm corresponding to the benzylic protons adjacent to the amide group.

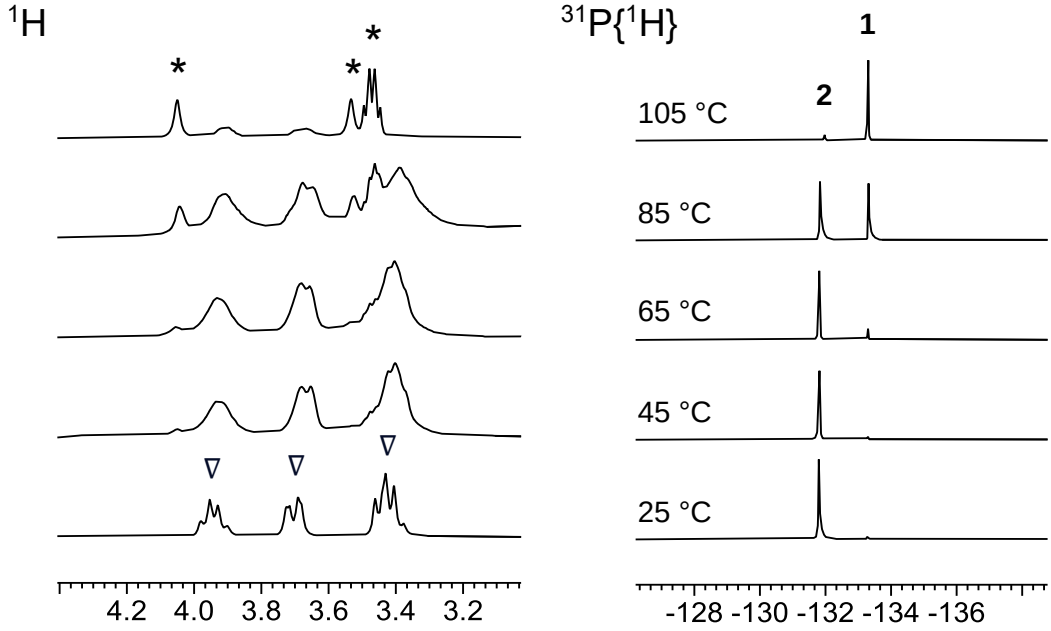


Figure 4.9: ^{1}H and ^{31}P{^{1}H} NMR spectra showing the formation of **1** (*) upon heating a d_5-pyridine solution containing **2** (∇) and hexadecylamine at 25−105 °C for two minutes.

Further evidence for the formation of **1** is observable in the $^{31}P\{^{1}H\}$ NMR spectra. The peak at −131.8 ppm corresponding to **2** is gradually converted into a new signal at −133.3 ppm. The peak at −133.3 ppm appears as triplet with $^{1}J_{H–P}$ = 207.7 Hz in the proton-coupled spectrum, in good agreement with the expected chemical shift of **1**.

As shown, almost complete transamidation of **2** by HDA occurs by the time the reaction reaches 105 °C. This suggests that, similarly to $H_2PC(O)NH_2$, **2** is converted into **1** in the presence of excess HDA capping ligands before reaching typical reaction temperatures for QD nucleation (120 °C).

The transformation of phosphorus precursors to InP QDs upon reaction with amine capping ligands is know, and occurs for aminophosphines. Hens, Dubertret, and Weigand reported the transamination reaction of dialkylaminophosphines ($P(NEt_2)_3$) when heated with oleylamine capping ligands. The reactions are shown to occur at comparably low temperatures compared to QD growth, similar to the results found for **2**.[15–17] The ramifications of the transamidation reaction observed for **2** on QD growth will be discussed in Chapter 5.

4.3 Synthesis and reactivity of carboxylic acid-functionalised phosphinecarboxamides

Capping ligands bearing carboxylic acid functional groups are commonly employed in a variety of nanocrystal syntheses.[18] They are favoured due variety of chain lengths and structural diversity available, allowing for the capping ligand to be tailored for specific material applications.[12] For example, oleic acid is particularly effective at stabilising and dispersing iron oxide ferrofluids. The stability afforded by oleic acid compared to the

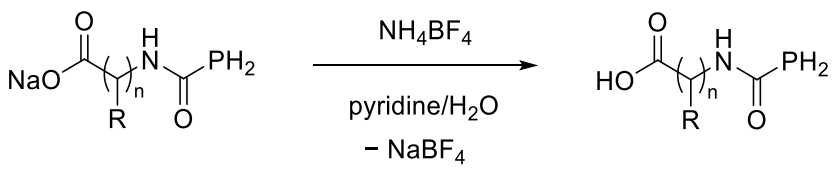
saturated structural isomer stearic acid is attributed to the 'kink' in the alkyl chain, consequent of the internal C=C double bond.[19]

Carboxylic acids are readily incorporated into metal precursors through facile carboxylate exchange reactions and are used to increase the solubility of the metal salts in apolar reaction solvents. Consequently, carboxylic acids are often present as by-products carried forward from the preparation of metal carboxylate precursors. The presence of excess acid has been shown to affect both the reaction kinetics and optical properties of InP QDs. Angelé *et al.* have shown that by reducing the concentration of free acid in solution, InP QDs could be prepared with improved monodispersity.[20] They attribute the effect to the rapid protonation of the $P(SiMe_3)_3$ precursor by palmitic acid, which results in more rapid, less controlled QD growth.

The ubiquity of carboxylic acid capping ligands in QD synthetic protocols motivated us to explore this functionality within the phosphinecarboxamides described thus far.

4.3.1 Synthesis and characterisation

Phosphinecarboxamides **2**, **4**, and **5** were protonated using ammonium tetrafluoroborate to form the corresponding carboxylic acid derivatives **6**, **7**, and **8** (Scheme 4.5). Conversion of the phosphinecarboxamide salts into the carboxylic acid derivatives upon protonation enabled their straight-forward separation from unreacted material and the $NaBF_4$ by-product by extraction with THF.



Scheme 4.5: Synthesis of **6**, **7**, and **8**. R = CH_2Ph (**2**, **6**), C_6H_{13} (**4**, **7**), or H (**8**); n = 1 (**2**, **4**, **6**, **7**), or 10 (**8**).

The reactions were monitored by ^{1}H, ^{13}C, ^{31}P NMR and infrared (IR) spectroscopy. Minimal change to the NMR spectra was observed upon protonation and selected NMR data are summarised in Table 4.2 for d_5-pyridine solutions containing **6**, **7**, and **8**.

Table 4.2: Selected NMR and IR spectroscopic data of **6**, **7**, and **8**. Chemical shifts are given in ppm, coupling constants in Hz, and wavenumber in cm^{-1}.

Compound	^{31}P	$^{1}J_{H-P}$	^{1}H (P$\underline{H}_2$)	^{1}H (COO$\underline{H}$)	$^{13}C\{^{1}H\}$	$^{1}J_{P-C}$	$\nu_{(O-H)}$
6	−132.1	209.4	3.74; 3.77	12.55	173.5	7.6	3281
7	−132.6	209.0	3.88; 3.91	14.95	173.5	6.5	3256
8	−133.1	207.7	3.91	13.78	172.6	6.0	3325

Unequivocal evidence of the successful protonation of the carboxylate moieties is given in ^{1}H NMR spectra, which show a new broad peak at 12.55–14.95 ppm. The peak is characteristic of a carboxylic acid proton environment, and consistent with previous reports.[2] This observation is accompanied by the formation of a new broad peak in the IR spectra at 3281–3325 cm^{-1}, consistent with a carboxylic acid O–H stretch (Table 4.2).

Similarly to **2** and **4**, ^{1}H NMR spectra of **6** and **7** also display two doublet of doublets corresponding to the non-equivalent diastereotopic phosphine protons, which collapse into doublets upon phosphorus-decoupling ($^{2}J_{H-H}$ = 10.8–11.5 Hz). In contrast, **8** shows just one doublet ($^{1}J_{P-H}$ = 207.7 Hz) due to the equivalence of its phosphine protons.

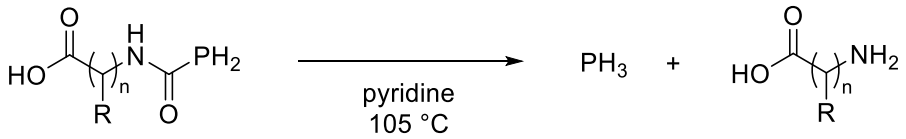
The ^{31}P NMR spectra of **6**, **7**, and **8** once again show a characteristic triplet between –132.1 and –133.2 ppm ($^{1}J_{H-P}$ = 207.7–209.4 Hz) that collapses to a singlet upon proton-decoupling. $^{13}C\{^{1}H\}$ NMR spectra reveal a doublet at 172.6–173.5 ppm corresponding

to the carbon atom of the phosphinecarboxamide carbonyl group coupling to the phosphorus atom in the phosphanyl fragment ($^1J_{P–C}$ = 6.0–7.6 ppm).

All of the phosphinecarboxamides described in Table 4.2 were fully characterised by NMR spectroscopy and are in good agreement with the carboxylic acid-functionalised phosphinecarboxamides reported by Faria and Jupp.[2] Complete spectroscopic data can be found in Chapter 7.

4.3.2 Thermal decomposition of 6, 7, and 8

The thermal decomposition of **6**, **7**, and **8** was studied following a similar protocol to that described in Section 4.2.2. d_5-Pyridine solutions containing **6**, **7**, and **8** were heated at 105 °C for 120 minutes and monitored by $^{31}P\{^1H\}$ NMR spectroscopy (Scheme 4.6).



Scheme 4.6: Thermal decomposition of carboxylic acid-functionalised phosphinecarboxamides **6**, **7**, and **8** in d_5-pyridine.

Upon heating **6**, $^{31}P\{^1H\}$ NMR spectra reveal a similar decomposition profile to that of its sodium salt (**2**). The phosphinecarboxamide peak at −132.1 ppm decreases in intensity relative to the PPh_3 internal standard and is accompanied by the formation of two new signals at −211.8 and −240.4 ppm, characteristic of P_2H_4 and PH_3, respectively (Figure 4.10). Similar decomposition profiles are also observed for **7** and **8**, showing consumption of the phosphinecarboxamide peaks at −132.6 ppm and −133.1 ppm, respectively, and concomitant PH_3 evolution (Figure 4.11).

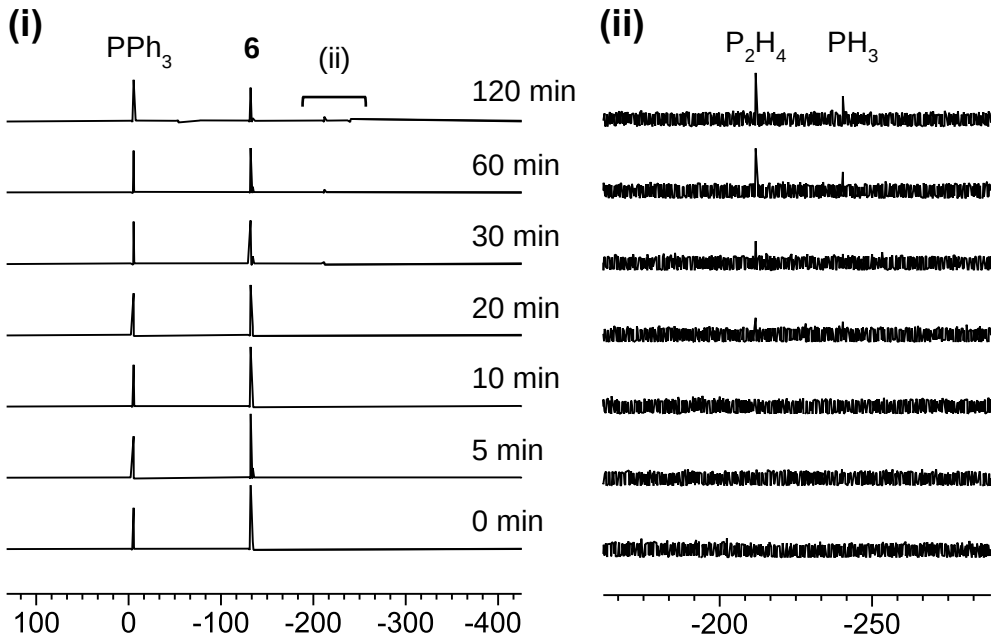


Figure 4.10: (i) $^{31}P\{^{1}H\}$ NMR spectra of a d_5-pyridine solution of **6** heated at 105 °C for 0–120 min; (ii) expanded region to show characteristic P_2H_4 and PH_3 resonances. PPh_3 is present as an internal standard.

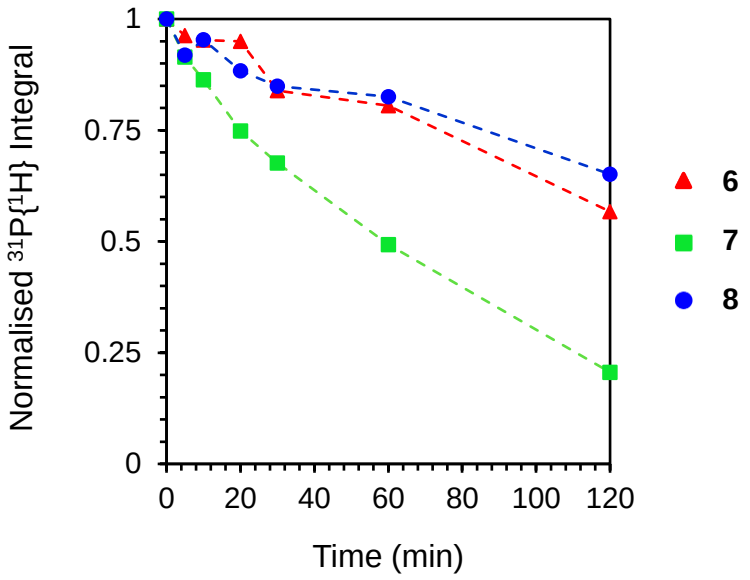


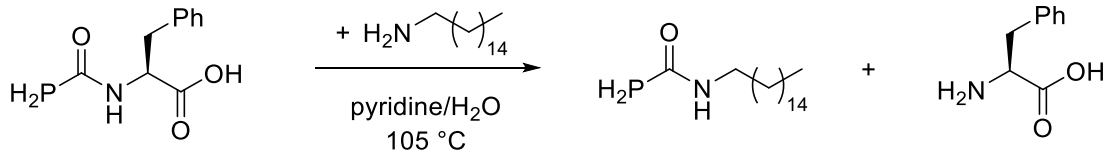
Figure 4.11: Normalised $^{31}P\{^{1}H\}$ NMR integrals of **6**, **7**, and **8** upon heating at 105 °C over 120 minutes. Integrals normalised against a PPh_3 internal standard.

The conservation of *in situ* PH_3 reactivity by **6**, **7**, and **8** after protonation supports the decomposition mechanism proposed proceeding through a HPCO intermediate, which should not be affected by the protonation state of the carboxyl substituent. This is further

corroborated by the formation of precipitate in the NMR tube over time, consistent with the decomposition of HPCO into insoluble phosphorus containing species. The presence of a carboxylic acid moiety is expected to favour the formation and subsequent decomposition of HPCO. The negative charge carried by the PCO^- anion provides stability to the weak C–P π-bond through Coulomb repulsion.[1] Protonation neutralises the charge on the PCO^- anion, reducing Coulomb repulsion and favouring decomposition through oligomerization. This is reflected by the fact that no resonance associated with free PCO^- is observed in any of the $^{31}P\{^1H\}$ NMR spectra measured for **6**, **7**, and **8** (*ca.* −390 ppm), in contrast to **5** where PCO^- was clearly observed upon heating.

4.3.3 Transamidation of 6

2 and **6** both decompose to form PH_3 in solution, regardless of the protonation state of the carboxyl group. This similarity in reactivity extends to the analogous transamidation reaction that occurs when a d_5-pyridine solution containing **6** and HDA is heated at 25–105 °C (Scheme 4.7).



Scheme 4.7: Formation of **1** from the transamidation of **6** with hexadecylamine.

The ^1H NMR spectra shows a decrease in intensity of the phosphine (3.45 ppm) and benzylic (3.56 and 3.73 ppm) proton environments of **6**, in addition to the emergence of new doublet and multiplet (Figure 4.12). The new peaks are consistent with the formation of **1**, with the doublet at 3.54 ppm ($^1J_{P–H}$ = 207.3 Hz) characteristic of the phosphine

protons and the multiplet at 3.48 ppm corresponding to the benzylic protons adjacent to the amide.

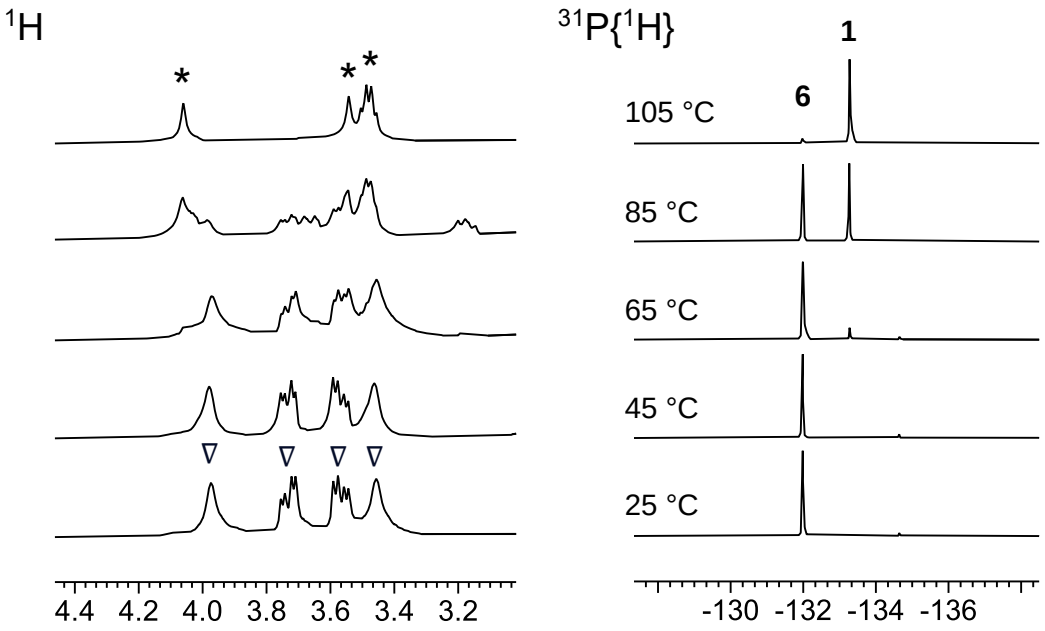


Figure 4.12: ^{1}H and ^{31}P{^{1}H} NMR spectra showing the formation of **1** (*) upon heating a d_5-pyridine solution containing **6** (∇) and hexadecylamine at 25−105 °C for two minutes.

4.4 Reactivity of difunctionalised phosphinecarboxamides

4.4.1 *N,N*-functionalised phosphinecarboxamide

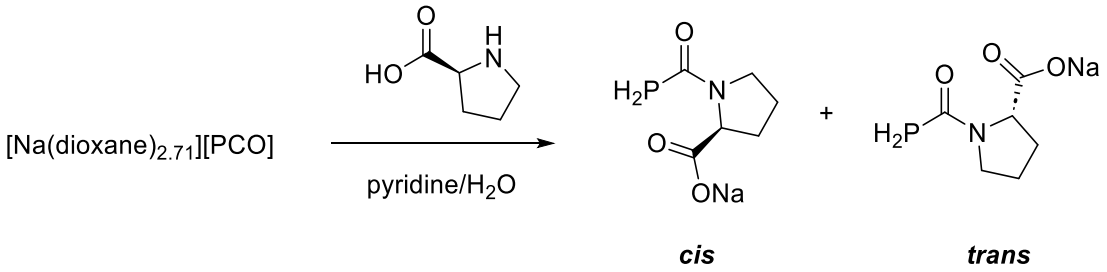
So far, this chapter has described the reproducible generation of PH_3 *in situ* by various *N*-functionalised phosphinecarboxamides bearing carboxyl substituents. The observation of PCO^- upon thermal decomposition of **5** supports its formation as an intermediate before protonation and subsequent decomposition into PH_3. The decomposition of PCO^- must also be accompanied by the production of the corresponding primary amine from which the phosphinecarboxamide is derived. Whilst this was not observed for compounds

2, **4**, and **5**, evidence of amine release was given through the formation of hexadecylamine observed upon thermal decomposition of **1** (Chapter 2).

These findings suggest that *N*,*N*-functionalised phosphinecarboxamides should also decompose to form PCO^-, and ultimately PH_3. This motivated us to compare the reactivity of an *N*,*N*-functionalised phosphinecarboxamide with compounds **2**, **4**, and **5**.

As highlighted, there are relatively few examples of *N*,*N*-functionalised primary phosphinecarboxamides. Our group has previously described the synthesis of *N*,*N*-diethylphosphinecarboxamide; *N*,*N*-di(cyclohexyl)phosphinecarboxamide; and L-proline-phosphinecarboxamide.[11,21] The dearth of examples compared to *N*-functionalised phosphinecarboxamides is attributed to the sluggish reaction kinetics of secondary amines. The steric bulk of secondary amine precursors inhibits their reactivity with HPCO, consequently resulting in a greater degree of HPCO decomposition compared to phosphinecarboxamide formation. Whilst secondary amines are expected to be more nucleophilic than primary amines due to the greater electron donating inductive effect of an additional alkyl substituent, this is outweighed by the effect of steric hinderance of the substituents studied.[22,23]

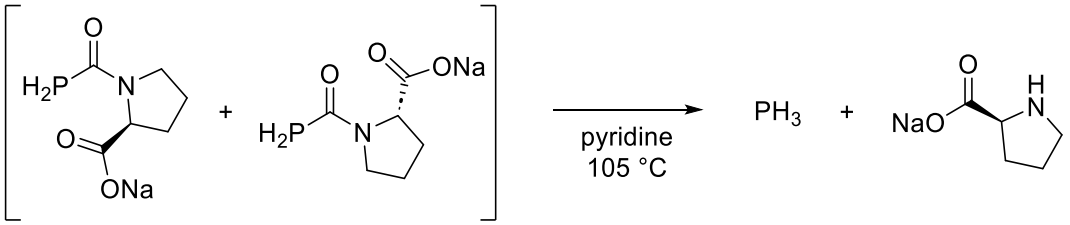
L-Proline-phosphinecarboxamide was selected to study as it can be easily prepared and isolated in excellent yield (97%). In addition, it also contains a carboxylate group, making it a good comparison to compounds **2**–**5**. L-Proline-phosphinecarboxamide was prepared following the procedure described by Faria from $[Na(dioxane)_{2.71}][PCO]$ and L-proline, and isolated as a 0.73:0.27 mixture of the *cis* and *trans* stereoisomers (Scheme 4.8).[11]



Scheme 4.8: Synthesis of L-proline-phosphinecarboxamide.

4.4.1.1 Thermal decomposition of L-proline-phosphinecarboxamide

The thermal decomposition of L-proline-phosphinecarboxamide was studied following the procedure described in Section 4.2.2 for compounds **2**, **4**, and **5** (Scheme 4.9).



Scheme 4.9: Thermal decomposition of (*cis*/*trans*)-L-proline-phosphinecarboxamide in d_5-pyridine.

$^{31}P\{^{1}H\}$ NMR spectra reveal that the two signals at −127.8 ppm and −131.3 ppm, corresponding to the *cis* and *trans* stereoisomers of L-proline-phosphinecarboxamide, rapidly diminish upon heating at 105 °C and are fully consumed after one hour (Figure 4.13). Simultaneously, new signals corresponding to P_2H_4 (−211.8 ppm) and PH_3 (−240.4 ppm) emerge. These results are consistent with those observed for **2**, **4**, and **5**.

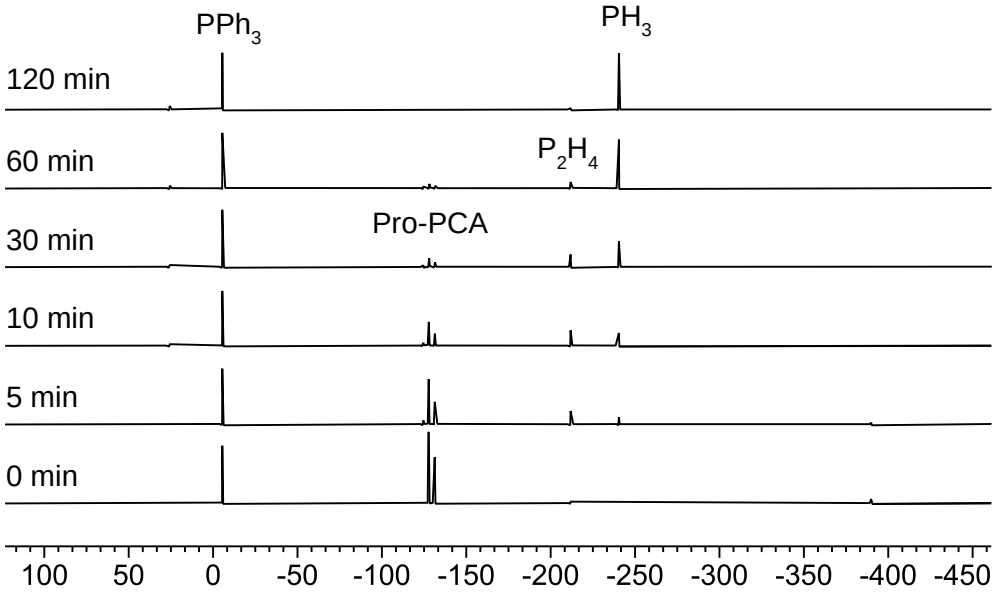
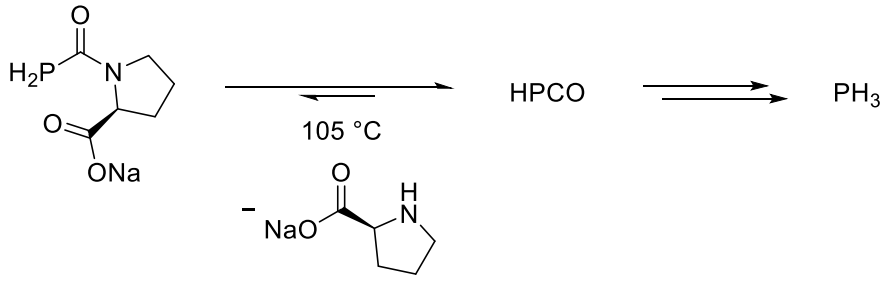


Figure 4.13: $^{31}P\{^{1}H\}$ NMR spectra of a d_5-pyridine solution of L-proline-phosphinecarboxamide (Pro-PCA) heated at 105 °C for 0–120 min. PPh_3 is present as an internal standard.

The fast consumption of L-proline-phosphinecarboxamide is presumably due to the poor nucleophilicity of the sterically bulky secondary amino acid sodium salt formed as a product. Unpublished results from our group have shown that the greater steric bulk of secondary amine substituents (e.g. cyclohexyl or ^{t}Bu) reduces their reactivity with HPCO compared to primary amines.[10,21]

Using this explanation, the fast decomposition of L-proline-phosphinecarboxamide can be rationalised. Upon decomposition, HPCO and L-proline sodium salt are formed. L-Proline sodium salt is a poor nucleophile due to its steric bulk which disfavours the reverse reaction with HPCO to reform L-proline-phosphinecarboxamide. Therefore HPCO is more likely to oligomerise and subsequently decompose to form PH_3, as observed (Scheme 4.10). Additional evidence for this is the rapid production of PH_3 and absence of PCO^- by ^{31}P NMR spectroscopy.

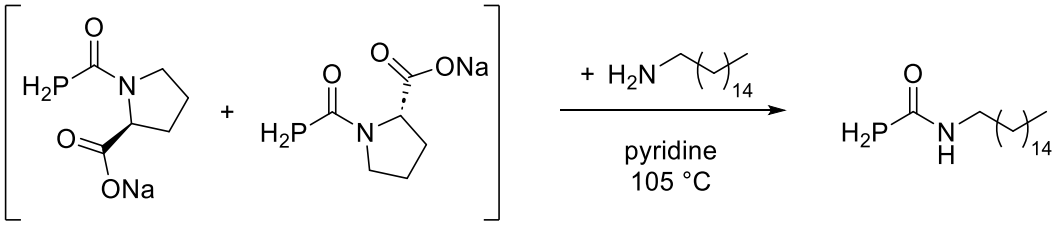


Scheme 4.10: Proposed thermal decomposition mechanism of L-proline-phosphinecarboxamide.

The ability of L-proline-phosphinecarboxamide to act as an *in situ* source of PH_3 provides valuable insight into the mechanism of thermal decomposition of compounds **1**, **2**, **4**, and **5**. Unlike the phosphinecarboxamides derived from primary amines, a decomposition mechanism whereby PH_3 is directly generated in addition to an isocyanate is not possible for secondary amines such as L-proline. Hence, the decomposition of L-proline-phosphinecarboxamide must proceed via HPCO generation. This finding definitively confirms that *N*- and *N,N*-functionalised phosphinecarboxamides act as *in situ* PH_3 source through HPCO formation and decomposition, and not by direct PH_3 generation (Scheme 4.10).

4.4.1.2 Transamidation of L-proline-phosphinecarboxamide

The *in situ* PH_3 reactivity displayed by L-proline-phosphinecarboxamide warrants its study for the preparation of In(Zn)P QDs, which will be discussed in Chapter 5. Accordingly, the reaction of L-proline-phosphinecarboxamide with HDA was investigated following the protocol described in Section 4.2.3 (Scheme 4.11).



Scheme 4.11: Formation of **1** from the transamidation of L-proline-phosphinecarboxamide with HDA.

$^{31}P\{^{1}H\}$ NMR spectra show the peaks corresponding to *cis*- and *trans*-L-proline-phosphinecarboxamide at −127.8 ppm and −131.6 ppm are rapidly converted into **1**, as evidenced by the formation of a new peak at −133.3 ppm (Figure 4.14(i)). Almost full conversion of L-proline-phosphinecarboxamide to **1** is observed after heating to 85 °C, in contrast to **2** and **6** which showed *ca.* 50% conversion at the same point (Figure 4.14(ii)). This is once again attributed to the poor nucleophilicity of L-proline compared to L-phenylalanine, disfavouring the reverse transamidation reaction with **1** to reform L-proline-phosphinecarboxamide.

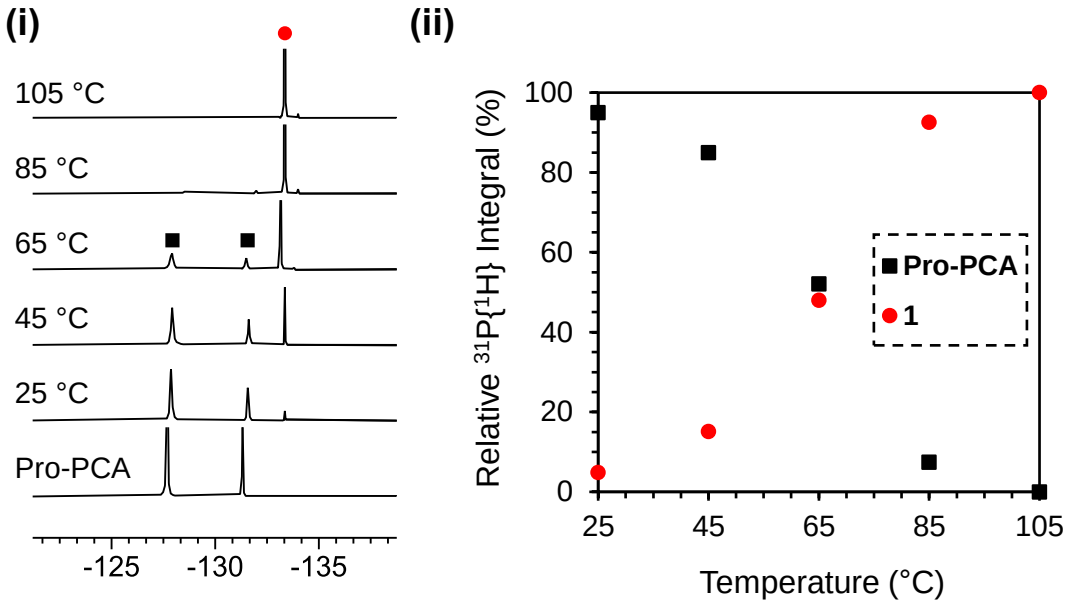


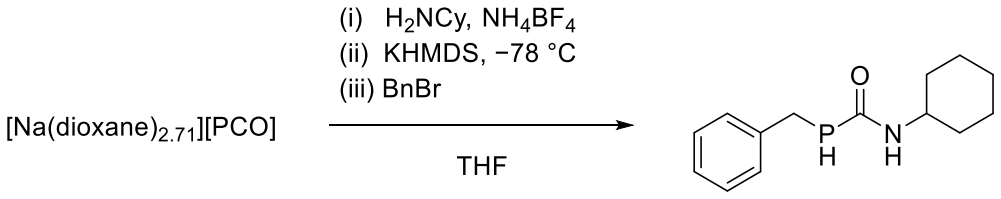
Figure 4.14: (i) $^{31}P\{^{1}H\}$ NMR spectrum showing the formation of **1** (●) upon heating a d_5-pyridine solution containing L-proline-phosphinecarboxamide (Pro-PCA) (■) and hexadecylamine at 25−105 °C for two minutes; (ii) change in the relative $^{31}P\{^{1}H\}$NMR integrals.

4.4.2 *P*-functionalised phosphinecarboxamide

This chapter has proposed that *N*-functionalised primary phosphinecarboxamides **2**–**8** decompose in solution upon heating to form HPCO. The analogous reactivity of *N*,*N*-functionalised L-proline-phosphinecarboxamide provides additional evidence for this

mechanism. HPCO is known to rapidly oligomerise and decompose in solution and is believed to be the source of PH_3 observed.[13,14] We were interested whether this reactivity could be deactivated by preventing the formation of HPCO. To do so, the solution phase reactivity of a *P*-functionalised secondary phosphinecarboxamide was studied.

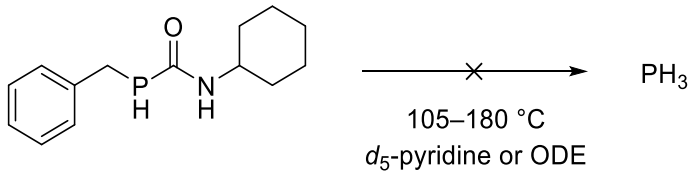
As surveyed in Chapter 1, *P*-functionalised phosphinecarboxamides may be prepared by the hydrophosphination of isocyanates; or alternatively by the deprotonation of an *N*-functionalised phosphinecarboxamide, followed by reaction with a suitable electrophile.[3–6,8,21,24] We elected to study *P*-benzyl-*N*-cyclohexyl-phosphine-carboxamide, which may be prepared from PCO^- and cyclohexylamine, followed by deprotonation by potassium bis(trimethylsilyl)amide (KHMDS) and reaction with benzyl bromide (Scheme 4.12). *P*-Benzyl-*N*-cyclohexyl-phosphinecarboxamide was previously reported by our group and can be prepared in moderate yield (48%).



Scheme 4.12: Synthesis of *P*-benzyl-*N*-cyclohexyl-phosphinecarboxamide.

4.4.2.1 Thermal decomposition *P*-benzyl-*N*-cyclohexyl-phosphinecarboxamide

Minimal decomposition was observed when a d_5-pyridine (d_5-py) solution containing *P*-benzyl-*N*-cyclohexyl-phosphinecarboxamide was heated at 105 °C for 120 minutes (Scheme 4.13; Figure 4.15). The experiment was repeated using 1-octadecene (ODE) as a solvent and heated for 30 minutes at 150 °C, 170 °C, and 180 °C.



Scheme 4.13: Thermal decomposition of *P*-benzyl-*N*-cyclohexyl-phosphinecarboxamide in d_5-pyridine (105 °C) and 1-octadecene (150–180 °C).

$^{31}P\{^{1}H\}$ NMR spectroscopy shows that *P*-benzyl-*N*-cyclohexyl-phosphinecarboxamide remains the predominant species in solution (−48.7 ppm) despite the increase in reaction temperature (Figure 4.15(i)). *P*-benzyl-*N*-cyclohexyl-phosphinecarboxamide does not appear to decompose into specific products, and instead shows the formation of multiple species between −125 and 34 ppm. Importantly, the peak at −242.5 ppm attributed to PH_3 has negligible intensity, supporting that *P*-functionalisation can be used to prohibit *in situ* PH_3 release (Figure 4.15(ii)).

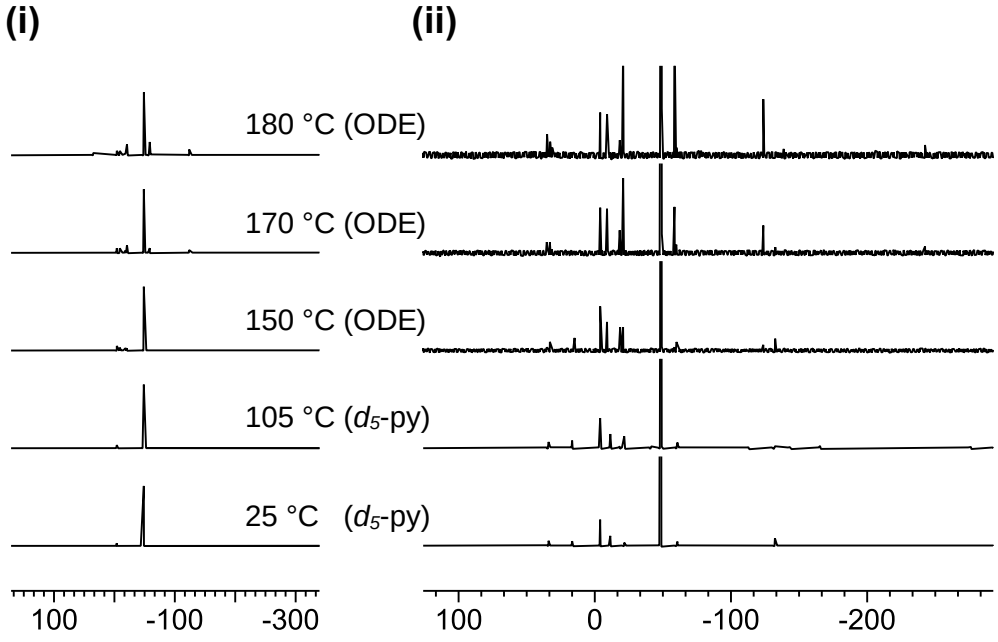
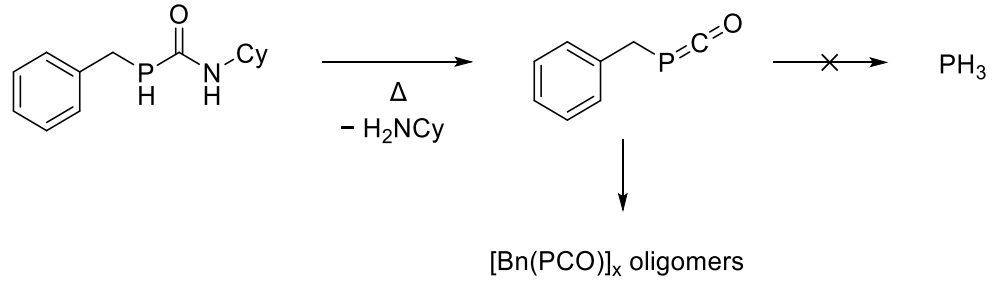


Figure 4.15: (i) $^{31}P\{^{1}H\}$ NMR spectra of d_5-pyridine (d_5-py) and ODE solutions containing *P*-benzyl-*N*-cyclohexyl-phosphinecarboxamide heated at 105–180 °C; (ii) expanded region to show resonances corresponding to the decomposition products.

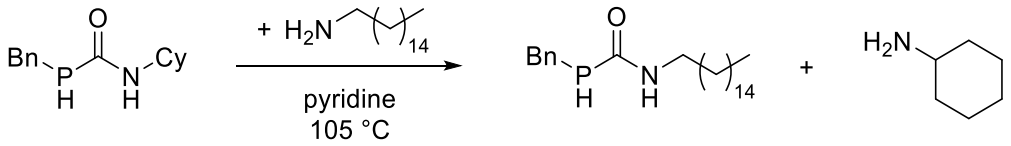
The formation of multiple decomposition products is to be expected. Assuming that *P*-benzyl-*N*-cyclohexyl-phosphinecarboxamide decomposes analogously to the *N*-functionalised phosphinecarboxamides though PCO^- formation, in this instance the corresponding benzyl phosphaketene will be produced (Scheme 4.14). Phosphaketenyl compounds derived from various elements (e.g. W, P, Ga, In) are known to be unstable due to the propensity of the weak C–P π-bond to oligomerise.[25] Without charge or steric stabilisation, phosphaketenes rapidly oligomerise and decompose.[26–29] In this case the benzyl substituent is unlikely to provide sufficient steric stabilisation with respect to oligomerisation and explains the multiple decomposition products observed.



Scheme 4.14: Postulated decomposition mechanism of *P*-benzyl-*N*-cyclohexyl-phosphinecarboxamide upon heating (Bn = benzyl).

4.4.2.2 Transamidation of *P*-benzyl-*N*-cyclohexyl-phosphinecarboxamide

Finally, the transamidation of *P*-benzyl-*N*-cyclohexyl-phosphinecarboxamide with HDA was studied as described in Section 4.2.3 (Scheme 4.15).



Scheme 4.15: Formation of *P*-benzyl-*N*-hexadecyl-phosphinecarboxamide from the transamidation of *P*-benzyl-*N*-cyclohexyl-phosphinecarboxamide with hexadecylamine.

$^{31}P\{^{1}H\}$ NMR spectra show the gradual conversion of *P*-benzyl-*N*-cyclohexyl-phosphinecarboxamide (−48.8 ppm) into a new signal at −49.5 ppm (Figure 4.16(i)). The proton-coupled spectrum reveals a doublet at −49.5 ppm ($^{1}J_{H-P}$ = 205.2 Hz), which is assigned to the transamidated product, *P*-benzyl-*N*-hexadecylamine-phosphine-carboxamide (Figure 4.16(ii)). Further evidence for this is given in the ^{1}H NMR spectra which shows the conversion of the amide resonance at 8.90 ppm into a new peak at 9.09 ppm.

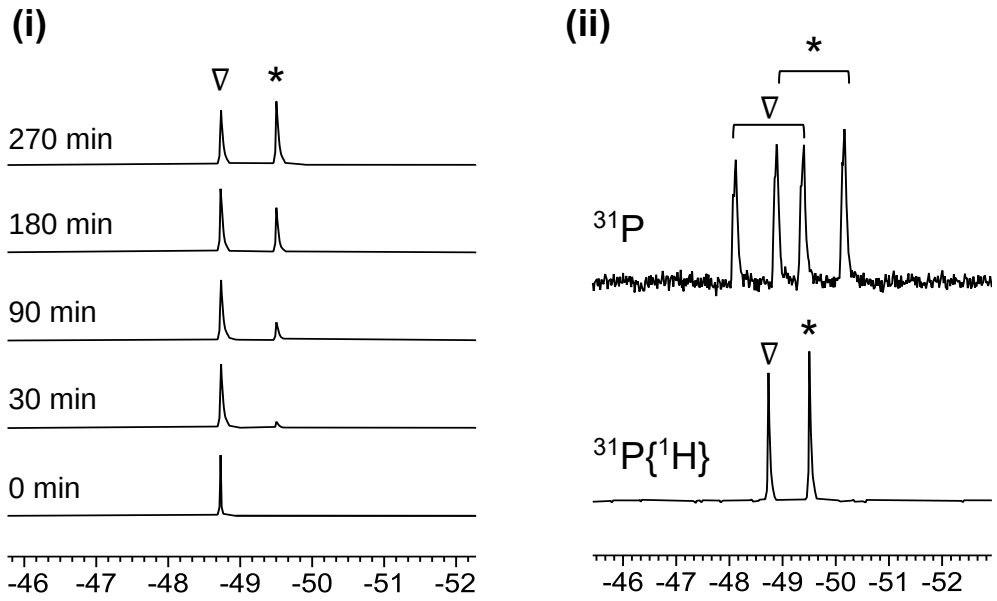


Figure 4.16: (i) $^{31}P\{^{1}H\}$ NMR spectra showing the formation of *P*-benzyl-*N*-hexadecyl-phosphinecarboxamide (*) from *P*-benzyl-*N*-cyclohexyl-phosphinecarboxamide (∇) upon heating in d_5-pyridine with hexadecylamine at 105 °C for 0–270 min; (ii) $^{31}P\{^{1}H\}$ and ^{31}P NMR spectra after 270 minutes of heating at 105 °C.

The transamidation reaction of *P*-benzyl-*N*-cyclohexyl-phosphinecarboxamide with HDA occurs more slowly than the corresponding reactions of *N*- and *N*,*N*-functionalised phosphinecarboxamides. 50% conversion is reached after heating *P*-benzyl-*N*-cyclohexyl-phosphinecarboxamide at 105 °C for 270 minutes, whereas **2** and L-proline-phosphinecarboxamide reached completion after 5 minutes. This discrepancy in

reactivity is rationalised by the inductive effect of the electron-donating benzyl substituent deactivating the phosphinecarboxamide moiety with respect to nucleophilic substitution.

4.5 Conclusions

This chapter has described the solution phase reactivity of *N*-, *N*,*N*-, and *P*-functionalised phosphinecarboxamides. Novel *N*-functionalised phosphinecarboxamides bearing carboxyl moieties (**2**–**8**) were prepared and characterised by ^{1}H, ^{13}C, ^{19}F, ^{31}P NMR and infrared spectroscopy. The thermal decomposition of these compounds was studied and it was revealed that they generate PH_3 *in situ* similarly to **1**.

L-Proline-phosphinecarboxamide was also found to produce PH_3 *in situ* upon thermal decomposition. PH_3 formation by an *N*,*N*-functionalised phosphinecarboxamide supports the intermediacy of HPCO and discounts a mechanism whereby PH_3 is directly generated alongside the corresponding isocyanate. This was also evidenced by the observation of PCO^- in the ^{31}P NMR spectra taken upon thermal decomposition of **5**. Furthermore, the inability of *P*-benzyl-*N*-cyclohexyl-phosphinecarboxamide to form PH_3 *in situ* confirms that HPCO is required, and that *P*-functionalisation may be used to prohibit its formation.

2, L-proline-phosphinecarboxamide, and *P*-benzyl-*N*-cyclohexyl-phosphinecarboxamide all undergo transamidation reactions with hexadecylamine upon heating to 105 °C. The *P*-functionalised phosphinecarboxamide transamidates at the slowest rate due to the deactivation of the phosphinecarboxamide moiety by the inductive effect of the electron-donating *P*-benzyl substituent.

4.6 References

1 J. M. Goicoechea and H. Grützmacher, *Angew. Chem. Int. Ed.*, 2018, **57**, 16968–16994.

2 E. N. Faria, A. R. Jupp and J. M. Goicoechea, *Chem. Commun.*, 2017, **53**, 7092–7095.

3 A. C. Behrle and J. A. R. Schmidt, *Organometallics*, 2013, **32**, 1141–1149.

4 M. Itazaki, T. Matsutani, T. Nochida, T. Moriuchi and H. Nakazawa, *Chem. Commun.*, 2020, **56**, 443–445.

5 T. M. Horsley Downie, J. W. Hall, T. P. Collier Finn, D. J. Liptrot, J. P. Lowe, M. F. Mahon, C. L. McMullin and M. K. Whittlesey, *Chem. Commun.*, 2020, **56**, 13359–13362.

6 B. Zhang, X. Ma, B. Yan, C. Ni, H. Yu, Z. Yang and H. W. Roesky, *Dalton Trans.*, 2021, **50**, 15488–15492.

7 T. M. Horsley Downie, M. F. Mahon, J. P. Lowe, R. M. Bailey and D. J. Liptrot, *ACS Catal.*, 2022, **12**, 8214–8219.

8 W.-P. Wang, X.-H. Cui, M. Li, X.-C. Wang and Z.-J. Quan, *Asian J. Org. Chem.*, 2022, **11**, e202200124.

9 T. P. Robinson and J. M. Goicoechea, *Chem. Eur. J.*, 2015, **21**, 5727–5731.

10 A. R. Jupp, G. Trott, É. Payen De La Garanderie, J. D. G. Holl, D. Carmichael and J. M. Goicoechea, *Chem. Eur. J.*, 2015, **21**, 8015–8018.

11 E. N. de Faria, 2020, Thesis (D.Phil.), University of Oxford.

12 A. Heuer-Jungemann, N. Feliu, I. Bakaimi, M. Hamaly, A. Alkilany, I. Chakraborty, A. Masood, M. F. Casula, A. Kostopoulou, E. Oh, K. Susumu, M. H. Stewart, I. L. Medintz, E. Stratakis, W. J. Parak and A. G. Kanaras, *Chem. Rev.*, 2019, **119**, 4819–4880.

13 A. Hinz, R. Labbow, C. Rennick, A. Schulz and J. M. Goicoechea, *Angew. Chem. Int. Ed.*, 2017, **56**, 3911–3915.

14 R. E. Schreiber and J. M. Goicoechea, *Angew. Chem. Int. Ed.*, 2021, **60**, 3759–3767.

15 R. Panzer, C. Guhrenz, D. Haubold, R. Hübner, N. Gaponik, A. Eychmüller and J. J. Weigand, *Angew. Chem. Int. Ed.*, 2017, **56**, 14737–14742.

16 A. Buffard, S. Dreyfuss, B. Nadal, H. Heuclin, X. Xu, G. Patriarche, N. Mézailles and B. Dubertret, *Chem. Mater.*, 2016, **28**, 5925–5934.

17 M. D. Tessier, K. De Nolf, D. Dupont, D. Sinnaeve, J. De Roo and Z. Hens, *J. Am. Chem. Soc.*, 2016, **138**, 5923–5929.

18 M. Green, *J. Mater. Chem.*, 2010, **20**, 5797–5809.

19 R. Tadmor, R. E. Rosensweig, J. Frey and J. Klein, *Langmuir*, 2000, **16**, 9117–9120.

20 L. Angelé, S. Dreyfuss, B. Dubertret and N. Mézailles, *Inorg. Chem.*, 2021, **60**, 2271–2278.

21 A. Jupp, 2016, Thesis (D.Phil.), University of Oxford.

22 H. K. J. Hall, *J. Am. Chem. Soc.*, 1957, **79**, 5441–5444.

23 W. A. J. Henderson and C. J. Schultz, *J. Org. Chem.*, 1962, **27**, 4643–4646.

24 E. N. Faria, A. R. Jupp and J. M. Goicoechea, *Dalton Trans.*, 2021, **50**, 6991–6996.

25 J. M. Goicoechea and H. Grützmacher, *Angew. Chem. Int. Ed.*, 2018, **57**, 16968–16994.

26 A. R. Jupp, M. B. Geeson, J. E. McGrady and J. M. Goicoechea, *Eur. J. Inorg. Chem.*, 2016, **2016**, 639–648.

27 L. Liu, D. A. Ruiz, D. Munz and G. Bertrand, *Chem*, 2016, **1**, 147–153.

28 Y. Mei, J. E. Borger, D.-J. Wu and H. Grützmacher, *Dalton Trans.*, 2019, **48**, 4370–4374.

29 M. K. Sharma, P. Dhawan, C. Helling, C. Wölper and S. Schulz, *Chem. Eur. J.*, 2022, **28**, e202200444.

Chapter 5

Synthesis and characterisation of InP quantum dots prepared from functionalised phosphinecarboxamides

5.1 Introduction and objectives

5.1.1 Controlling InP QD growth

Capping ligands are essential for controlling particle growth of colloidal QDs in solution.[1] Chapter 1 highlighted the various ways in which capping ligands affect growth, including the degree of steric stabilisation afforded by the side-chain substituent, the binding affinity of the coordinating motif to the metal species, and their ability to selectively stabilise distinct crystal facets.[2]

Capping ligands are widely employed to selectively control particle size and morphology in InP QD syntheses. Kim *et al.* showed that tetrahedrally shaped InP QDs could be prepared from $InCl_3$ and $P(NMe_2)_3$ using oleylamine ligands.[3] They attribute the uncommon geometry of the nanocrystals obtained to the absence of free acid in solution, in addition to the unique stabilisation of indium-rich {111} facets by oleylamine. Jeong and co-workers later modified this protocol to enable the isolation of InP tetrapods.[4]

Colloidal InP QD syntheses often exploit combinatorial strategies whereby all reactants are combined together in solution. Therefore, in addition to capping ligands, the other precursors present play an equally important role in dictating the growth and structural evolution of InP QDs in solution.

Elemental precursors (e.g. $P(NR_2)_3$, InX_3) are capable of influencing QD structure and growth. This was discussed earlier with the example of halide incorporation onto InP QD surfaces through the indium source (InX_3; X = F, Cl). The resulting halide-passivated InP QDs display enhanced PLQYs due to efficient trap passivation.[5] Another pertinent example of the influence of elemental precursors is the use of InP magic-sized clusters as

single source precursors to QDs. In these reactions InP MSCs are capable of templating QD formation, thereby directing the growth and structural evolution of the InP QDs.[6,7]

Structural control can also be imparted utilising non-conventional, low-valent indium precursors. Nozik and co-workers reported the preparation of InP nanorods from monodispersed indium droplets.[8] The In^0 droplets were found to template InP nanorod growth, promoting axial growth whilst restricting lateral growth. Yadav *et al*. showed that InP QDs with tetrahedral geometry could be obtained from indium(I) halides.[9] In this example, the low valent indium precursor acted as both an indium source and a reductant for the aminophosphine precursors used.

5.1.2 Influence of phosphorus precursors on QD growth

Phosphorus precursors may also be used to control the growth of InP QDs.[10] Mixtures of silylphosphines with different reactivities have been used to chemically resolve nucleation and growth events. Cossairt and co-workers reported the use of substituted triarylsilylphosphines for the preparation of InP QDs. They showed that a mixture of $P(SiMe_3)_3$ and $P(SiPh_3)_3$ could be used to achieve discrete nucleation and growth events.[11] Moreover, upon varying the ratio of the precursors in the binary mixture, the balance of the nucleation and growth processes could be modulated, thereby controlling QD size.

Taking a different approach, Bawendi and co-workers compared the reactivities of silyl- and germyl-phosphines for the preparation of InP QDs. They showed that the stronger P–Ge bond compared to the P–Si bond resulted in the slower consumption of $P(GeMe_3)_3$ compared to the silyl-congener.[12] Whilst the use of $P(GeMe_3)_3$ did not improve the

monodispersity of the InP QDs as desired, it is a good example of the creative approaches employed for controlling InP QD growth using phosphorus precursors.

The modification of phosphorus precursor substituent to impart control over InP QD growth is often referred to as side-chain engineering.[10] Facile functionalisation of phosphinecarboxamides and the ability to incorporate a variety of functional motifs make them attractive candidates for such studies. Moreover, the very novelty of using phosphinecarboxamides for the preparation of InP QDs warrants studying the effect of side-chain characteristics on QD growth. Accordingly the *N*-, *N*,*N*-, *P*-functionalised phosphinecarboxamides described in Chapter 4 are explored for the preparation of InP QDs.

5.1.3 Chapter outline

This chapter will describe the preparation of In(Zn)P/ZnS QDs using *N*- and *N*,*N*-functionalised phosphinecarboxamides bearing carboxyl substituents (**2**–**8** and L-proline-phosphinecarboxamide). The effect of the carboxyl substituent on QD particle size and dispersity is studied. The implications of the results obtained on the reaction mechanism are also discussed.

This chapter will also explore *P*-benzyl-*N*-cyclohexyl-phosphinecarboxamide as a phosphorus precursor to InP QDs. Its air-stability is evaluated and further *P*-functionalisation discussed.

Xuechun Bai contributed experimentally to this work under my supervision, and submitted a thesis on their work in fulfilment of Part II of the M. Chem. degree.

5.2 Preparation of In(Zn)P/ZnS QDs using carboxyl-functionalised phosphine-carboxamides

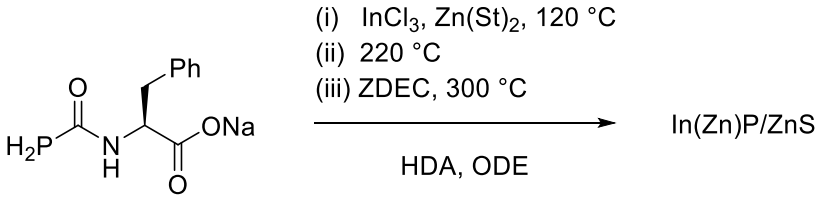
The reactivity described in Chapter 4 of carboxylate- (**2**, **3**, **4**, **5**, and L-proline-phosphinecarboxamide) and carboxylic acid-functionalised phosphinecarboxamides (**6**, **7**, and **8**), specifically their ability to generate PH_3, makes them promising phosphorus precursors to InP QDs. In order to test this, HDA-capped core/shell In(Zn)P/ZnS QDs were prepared following the protocol developed for **1** detailed in Chapter 3.

In order to compare results with the QDs prepared from **1**, reagent stoichiometry, concentration, scale, set-up, and heating profiles (i.e. number of steps, temperature, and duration) were all kept constant. By keeping reaction conditions consistent the effect of the side-chain substituent on the optical properties of the QDs formed can be compared and evaluated.

5.2.1 Carboxylate-functionalised phosphinecarboxamides

5.2.1.1 Preparation of In(Zn)P/ZnS QDs from 2–5

HDA-capped core/shell In(Zn)P/ZnS QDs were prepared from **2** following the protocol described in Chapter 3, details of which can be found in the experimental section (Chapter 7; Section 7.2.4.1). Despite the poor solubility of this salt at low temperatures (< 120 °C), the protocol did not require any modification or adaption while using **2** (Scheme 5.1).



Scheme 5.1: Synthesis of HDA-capped core/shell In(Zn)P/ZnS QDs from **2**. St = stearate ($O_2C(CH_2)_{16}CH_3$); HDA = hexadecylamine ($H_2N(CH_2)_{15}CH_3$); ODE = 1-octadecene ($H_2C{=}CH(CH_2)_{15}CH_3$); ZDEC = zinc diethyldithiocarbamate ($Zn[S_2CNEt_2]_2$).

The In(Zn)P QD cores prepared were found to be non-emissive. However, growth of an epitaxial ZnS shell using zinc diethyldithiocarbamate (ZDEC) induced emission. The PL emission spectrum of the core/shell In(Zn)P/ZnS QDs prepared from **2** shows a symmetrical peak at 556 nm with a FWHM = 89 nm (Figure 5.1). A broad, featureless absorption edge is observed, similarly to the QDs prepared from **1**. However, band edge excitation can be resolved by examining the PL excitation spectrum (λ_{ex} = 555 nm), which shows a peak at 511 nm. PL emission of the In(Zn)P/ZnS QDs prepared from **2** appears at a significantly shorter wavelength than that observed for **1** (λ_{max} = 613 nm), suggesting the formation of smaller QDs.

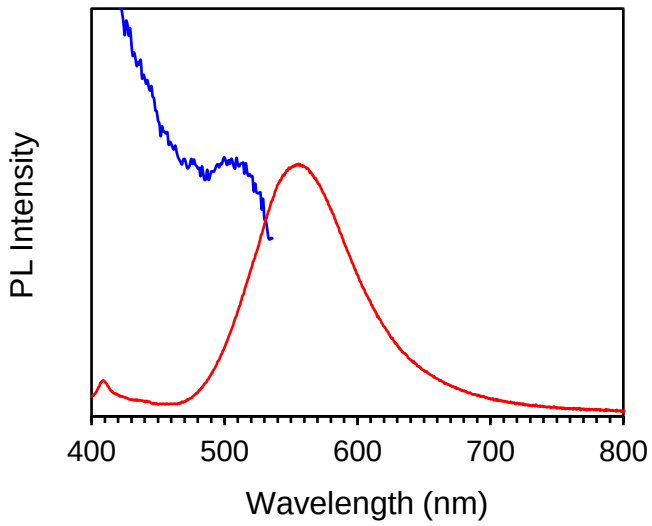


Figure 5.1: PL emission (red) and excitation (blue; λ_{ex} = 555 nm) spectra of a toluene solution containing In(Zn)P/ZnS QDs prepared from **2**.

Further evidence for the successful preparation of In(Zn)P/ZnS QDs from **2** is given by PXRD analysis. Broad, intense diffraction peaks are observed at 28.3, 47.4, and 56.0°, in good agreement with a cubic zinc blende structure and consistent with results obtained for the analogous QDs prepared from **1** (Figure 5.2).

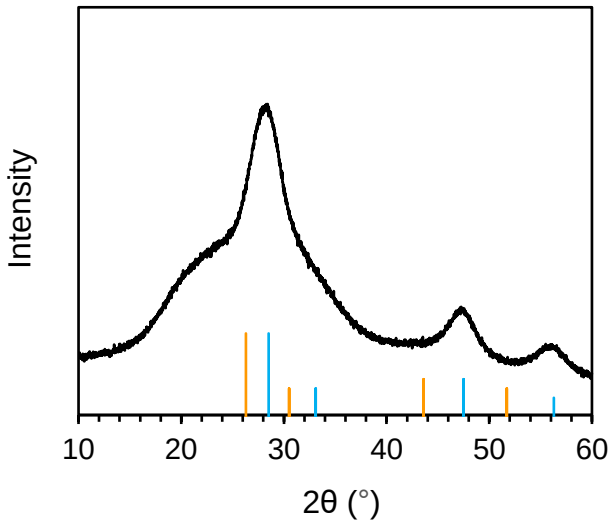
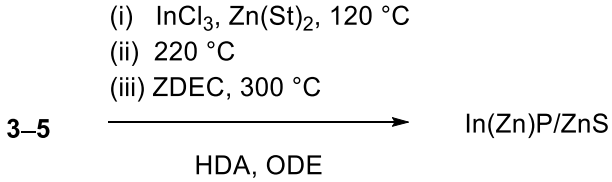


Figure 5.2: Powder X-ray diffraction pattern of core/shell In(Zn)P/ZnS QDs prepared from **2**. Diffraction patterns of zinc blende InP (orange) and ZnS (blue) shown for reference.

Following the successful use of **2** for the preparation of HDA-capped In(Zn)P/ZnS QDs, the analogous reactions using compounds **3**–**5** were studied. (Scheme 5.2). The preparation of QDs using **5** was attempted, and whilst the product appeared emissive, colloidal instability and solubility challenges precluded purification and analysis. This will be discussed further in Section 5.2.1.2.



Scheme 5.2: Synthesis of In(Zn)P/ZnS QDs from **3**–**5**. St = stearate; HDA = hexadecylamine; ODE = 1-octadecene; ZDEC = zinc diethyldithiocarbamate.

Spectroscopic and PXRD data are summarised in Table 5.1 for HDA-capped core/shell In(Zn)P/ZnS QDs prepared from **2**–**4**. Data for In(Zn)P/ZnS QDs prepared from **1** is also shown for reference. Imaging by scanning transmission electron microscopy (STEM) was not possible due extensive radiolysis of the samples under the high-energy electron beam. Preliminary studies using high-resolution transmission electron microscopy (HR-TEM) were found to overcome sample radiolysis, however insufficient data was collected before completion of this project, so these experiments will not be discussed.

Table 5.1: PL spectroscopic and PXRD data of In(Zn)P/ZnS QDs prepared from compounds **1**–**4**. PL emission $\lambda_{(max)}$ and full width at half maxima (FWHM) values given in nm and 2θ values in °.

Precursor	$\lambda_{(max)}$	**FWHM**	$2\theta_{(111)}$	$2\theta_{(220)}$	$2\theta_{(311)}$
1	613	114	28.1	47.2	55.7
2	556	89	28.4	47.3	56.1
3	563	96	28.1	47.5	56.1
4	562	83	28.1	47.5	56.1

All of the core/shell In(Zn)P/ZnS QDs prepared are found to be highly crystalline, with diffraction peaks consistent with a cubic zinc blende structure and in good agreement with one another (Table 5.1). The In(Zn)P/ZnS QDs prepared from **3** and **4** show PL emission peaks at 563 and 562 nm, respectively, in close agreement to that observed for **2** ($\lambda_{(max)}$ = 556 nm; Figure 5.3). The peaks also have comparably low line widths, with FWHM values measured between 83 and 96 nm.

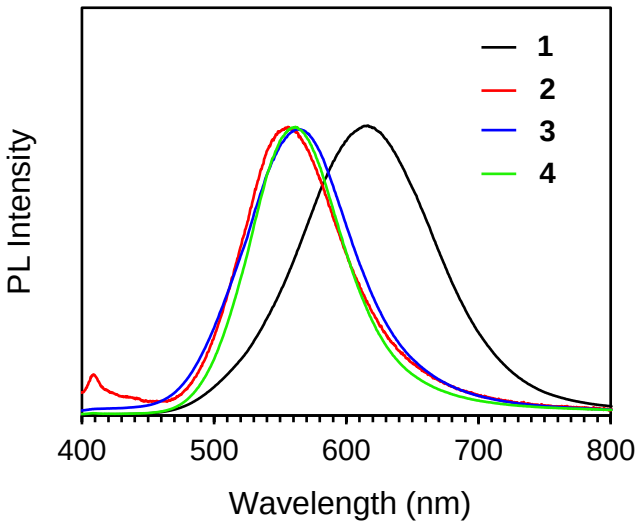


Figure 5.3: PL emission spectra of toluene solutions containing HDA-capped In(Zn)P/ZnS prepared from **2**–**4**. PL emission spectrum of QDs prepared from **1** shown for comparison.

The In(Zn)P/ZnS QDs show significantly blue-shifted PL emission compared to those prepared from **1**. The appearance of PL emission peaks at shorter wavelengths is indicative of the formation of QDs with reduced particle size. Moreover, an improvement in particle size distribution is also observed when using compounds **2**–**4** compared to **1**, reflected by the shorter FWHM. Investigations into the origin of these differences will be discussed in the next section.

The results obtained show that carboxylate-functionalised phosphinecarboxamides **2**–**4** are all effective precursors to InP QDs. The QDs prepared have similar photoluminescence profiles to one another, regardless of whether the side-chain consists of aromatic (**2** and **3**) or aliphatic (**4**) substituents.

5.2.1.2 Exploring the origin of size control

As mentioned, the QD synthetic conditions used to study **2**–**4** were kept constant so that any effect of the phosphinecarboxamide precursor on the PL profile of the corresponding

QDs could be compared. The reproducible blue-shift of PL λ_{max} values observed for QDs prepared from **2**–**4** relative to **1** suggests that functionalisation does in fact influence QD growth.

This influence is also exemplified in PL spectra of In(Zn)P/ZnS QDs prepared from blends of **1** and **4** (Figure 5.4). Upon increasing the ratio of **4**:**1** PL emission λ_{max} values decrease. A 1:1 mixture of **1** and **4** shows a significant blue-shift in λ_{max} from 613 nm to 573 nm, which is further reduced to 562 nm when only **4** is used. The gradual decrease in λ_{max} suggests that **4** is arresting the growth of QDs in solution, causing the reduction in particle size observed.

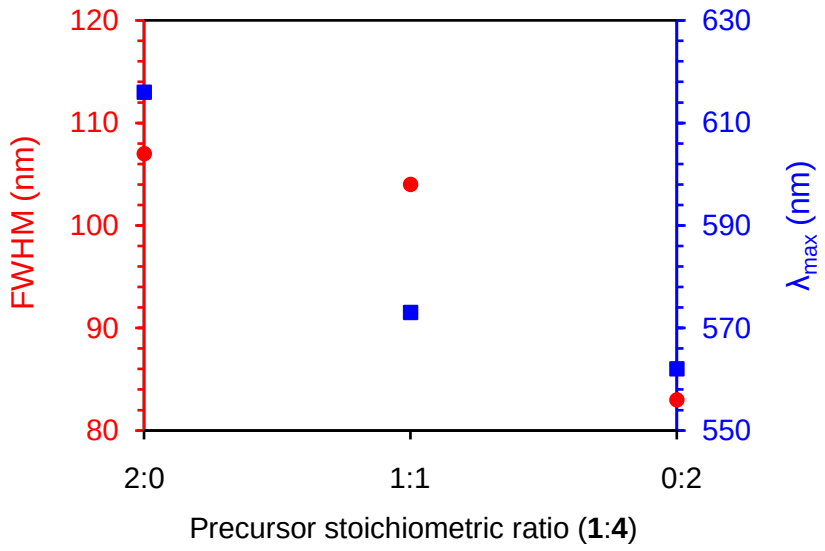


Figure 5.4: PL emission maxima (blue) and FWHM (red) of In(Zn)P/ZnS QDs prepared upon varying the stoichiometric ratio of **1** and **4**.

A reduction in PL emission line width is also observed upon increasing the ratio of **4**:**1**, with FWHM values reducing from 107 nm to 104 nm and 83 nm (Figure 5.4). The reduction in FWHM is consistent with more homogenous particle growth affording narrower particle size dispersion. The reduction suggests that in addition to slowing the

growth of the QDs, improved size focusing is achieved by the presence of the carboxylate group in **4**.

The control of QD size imparted upon side-chain functionalisation is reminiscent of the work of Gary *et al.*, who showed that InP QD growth could be slowed by substituting the methyl substituents in $P(SiMe_3)_3$ to phenyl groups.[11] However, Gary *et al.* attribute the size control afforded to the difference in reactivity of the two silylphosphines. $P(SiMe_3)_3$ is found to react more rapidly than $P(SiPh_3)_3$ as a result of the greater steric encumbrance of the phenyl substituents.

Whilst comparison to the work of Gary *et al*. highlights the similar control over QD particle size achieved upon modification of a side-chain substituent, the rationale behind the differing reactivities cannot be applied to phosphinecarboxamides **2**–**4**. In Chapter 4, compounds **1**, **2**, and **4** were all found to decompose at comparable rates by ^{31}P NMR spectroscopy (Figure 5.5(i)). This also applies to their *in situ* generation of PH_3 (Figure 5.5(ii)).

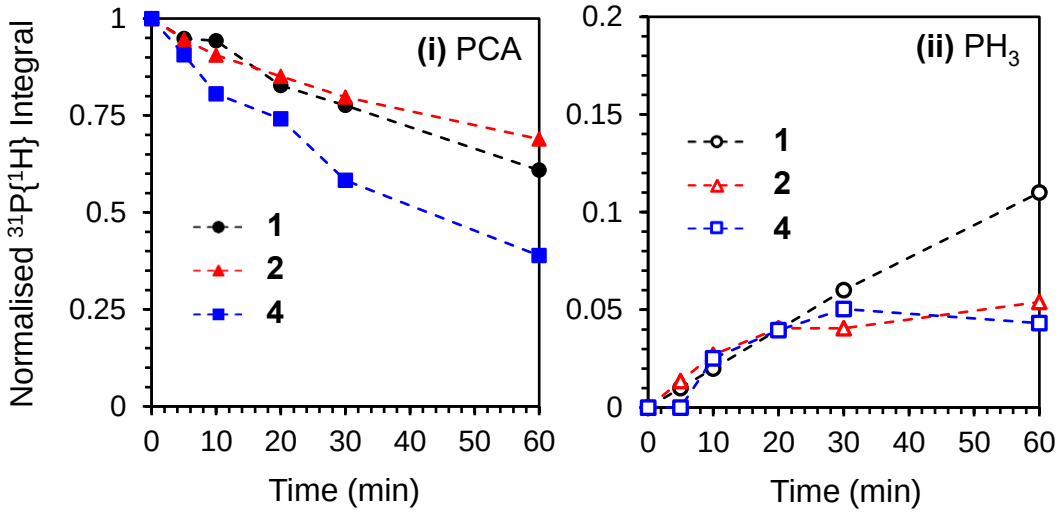
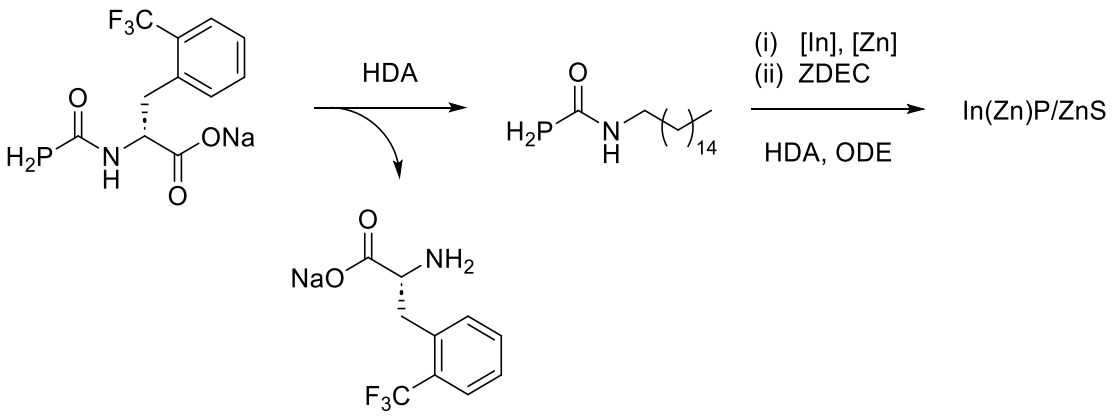


Figure 5.5: Normalised $^{31}P\{^1H\}$ NMR integrals of **1**, **2**, and **4** upon thermal decomposition at 105 °C: (i) phosphinecarboxamide peak (PCA; *ca*. −132 ppm); (ii) increase in PH_3 as a function of time.

Moreover, the relative decomposition rate and PH_3 release also neglects the transamidation process that occurs for **2** upon reaction with HDA, which suggests that **1** is the predominant species in solution upon reaching 105 °C (Chapter 4, Section 4.2.3). Although transamidation reactions were only studied using small-scale ^{31}P NMR spectroscopic experiments, evidence of transamidation by HDA occurring during QD synthesis conditions is given when using **3**.

Upon heating **3** with HDA in In(Zn)P QD growth conditions, a transamidation reaction is expected to occur, forming **1** and 2-(trifluoromethyl)-D-phenylalanine sodium salt (Scheme 5.3). The 2-(trifluoromethyl)-D-phenylalanine sodium salt produced is capable of coordinating to In(Zn)P and In(Zn)P/ZnS QD surfaces through its carboxylate functional group. As noted in Chapter 4, **3** was prepared as a structural analogue of **2** bearing a CF_3 substituent on the phenyl group. Therefore the CF_3 group can be employed as a discrete ^{19}F NMR spectroscopic handle to study the formation and subsequent surface binding of 2-(trifluoromethyl)-D-phenylalanine.



Scheme 5.3: Transamidation of **3** to form **1** and 2-(trifluoromethyl)-D-phenylalanine sodium salt, followed by In(Zn)P/ZnS QD formation. [In] = $InCl_3$; [Zn] = zinc stearate; ZDEC = zinc diethyldithiocarbamate; HDA = hexadecylamine; ODE = 1-octadecene.

The ^{19}F NMR spectrum of In(Zn)P QD cores prepared from **3** reveals a low intensity, broad peak at −62.7 ppm (Figure 5.6(i)). The peak is assigned to the trifluoromethyl group of surface-bound 2-(trifluoromethyl)-D-phenylalanine and its broad appearance is consistent with other QD surface ligands.[13,14] Surface-bound ligands experience spectral line broadening, which becomes more severe the closer the environment is to the surface.[15] Line broadening of surface-bound ligand environments occurs due to numerous factors, including the multiple binding modes that the carboxylate group can adopt, and the non-equivalence of ligand environments bound to different crystal facets.[15,16]

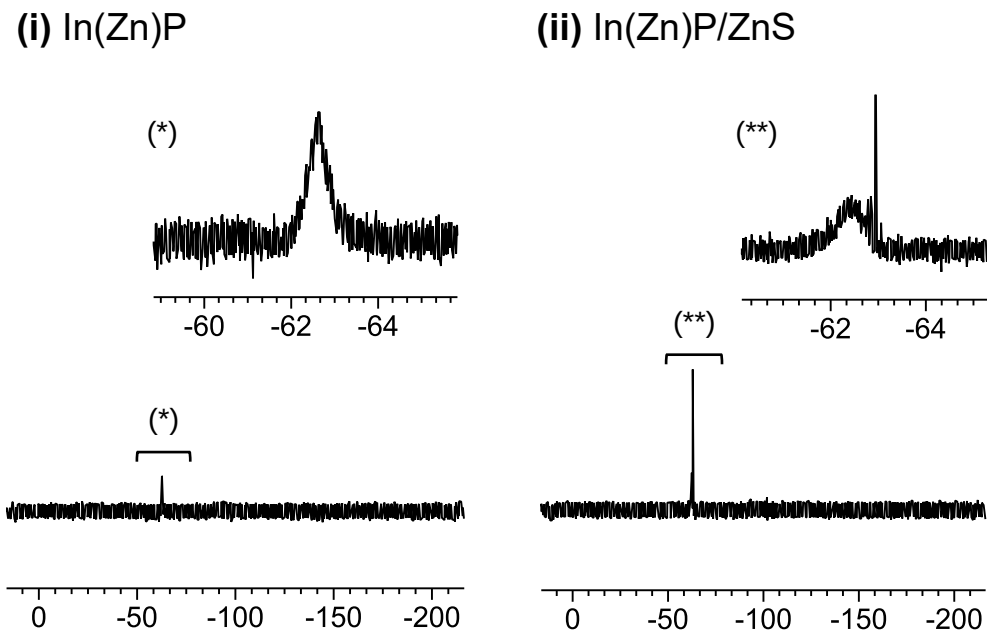


Figure 5.6: ^{19}F NMR spectrum of a $CDCl_3$ solution containing: (i) In(Zn)P QDs; (ii) core/shell In(Zn)P/ZnS QDs. Expanded regions show the broad resonances for clarity.

Surface-bound 2-(trifluoromethyl)-D-phenylalanine is also identified on core/shell In(Zn)P/ZnS QDs by a broad peak at −62.4 ppm (Figure 5.6(ii)). An additional sharp peak is observed at −62.9 ppm, which is attributed to dissociated free ligand.

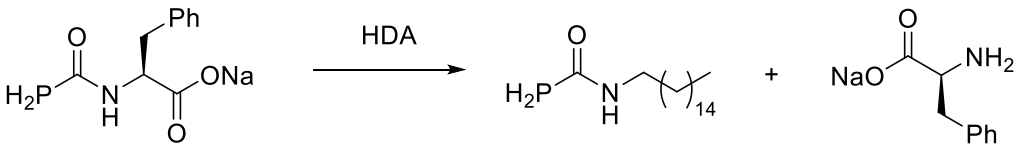
^{1}H NMR surface studies were also attempted on QDs prepared from **3** but did not provide any additional insight. This is due to the inability to distinguish and resolve surface-bound 2-(trifluoromethyl)-D-phenylalanine from the other surface ligand environments present in relatively high concentration (i.e. stearate and HDA). These results highlight the effectiveness of **3** as a ^{19}F NMR spectroscopic label, thereby providing valuable insight into the decomposition mechanism of phosphinecarboxamides.

Confirmation that transamidation reactions occur during QD growth conditions, as elucidated by multinuclear NMR spectroscopy, helps to rationalise the unsuccessful isolation and characterisation of QDs prepared from **5**. Assuming that the analogous transamidation reaction between **5** and HDA occurs within the early stages of QD growth, sodium 11-aminoundecanoate will be formed in addition to **1**. The bifunctional 11-aminoundecanoate ion present in solution is capable of chelating to the InP QD surface, displacing two capping ligands. The displacement of capping ligands will reduce the steric stabilisation of the QDs and result in colloidal destabilisation and precipitation.

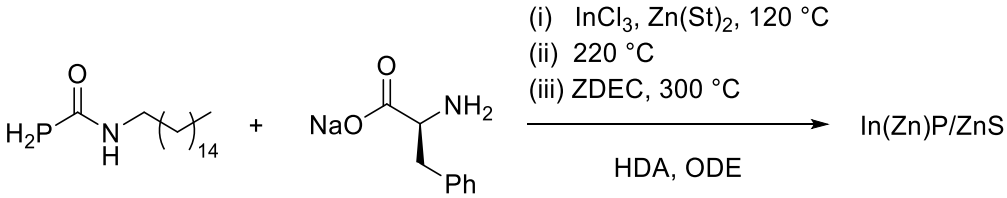
Furthermore, there is also the potential that 11-aminoundecanoate tethers multiple nanocrystals together during growth. Bifunctional linkers, such as the aminoalkanoic acids, are commonly employed for tethering nanoparticles to one another, although this is usually achieved by post-synthetic ligand exchange.[17] 11-Aminoundecanoate is also structurally reminiscent of anionic polymer flocculants commonly used in mineral processing applications for the selective aggregation and precipitation of inorganic minerals.[18] QD tethering would reduce the average separation between the particles during growth, consequently disfavouring the arrested precipitation process employed to achieve slow, controlled growth. The formation of 11-aminoundecanoate and the

accompanied colloidal destabilisation is also consistent with physical observations which found the QDs formed were highly aggregated and difficult to suspend.

Recognising that the transamidation reaction of carboxylate-functionalised phosphinecarboxamides with HDA persists during QD growth conditions, the relationship between this process and the associated size control afforded was studied. Chapter 4 described the transamidation reaction of **2** with HDA to form **1** (Scheme 5.4). If in fact the release of L-phenylalanine sodium salt upon transamidation is the origin of the difference in QD size observed when using **2**, addition of L-phenylalanine sodium salt to **1** for the preparation of In(Zn)P/ZnS QDs should reproduce the same result. To test this postulate, core/shell In(Zn)P/ZnS QDs were prepared from **1** with addition of L-phenylalanine sodium salt (Scheme 5.5).



Scheme 5.4: Transamidation of **2** with HDA to form **1** and L-phenylalanine sodium salt.



Scheme 5.5: Synthesis of HDA-capped core/shell In(Zn)P/ZnS QDs from **1** and L-phenylalanine sodium salt. St = stearate; HDA = hexadecylamine; ODE = 1-octadecene; ZDEC = zinc diethyldithiocarbamate.

The PL emission spectrum of In(Zn)P/ZnS QDs prepared from **1** and L-phenylalanine sodium salt shows a peak at 606 nm (Figure 5.7). The peak observed is in closer agreement to QDs prepared using **1** (λ_{max} = 613 nm) than from **2** (λ_{max} = 556 nm). Whilst the PL emission peak appears at a similar wavelength to QDs prepared from **1**, the

reduced FWHM (86 nm versus 114 nm for **1**) suggests that the addition of L-phenylalanine sodium salt improves size focussing and reduces polydispersity.

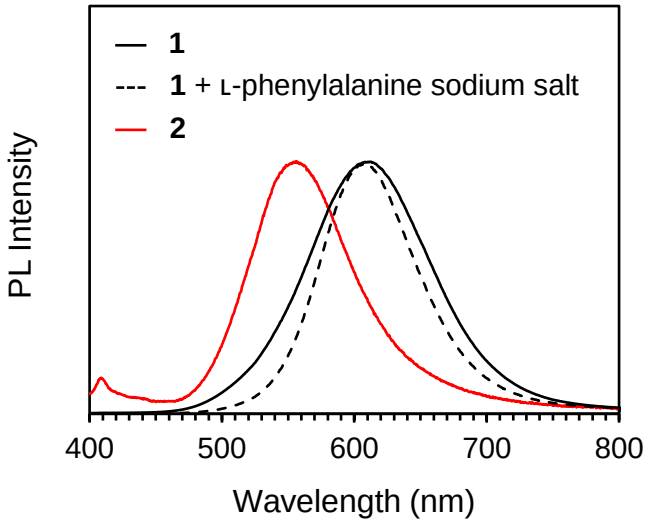


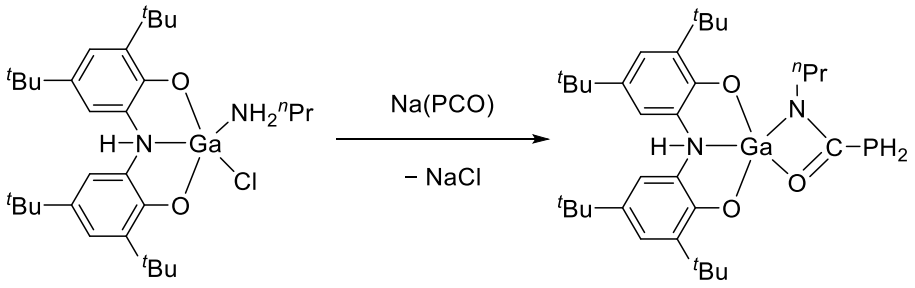
Figure 5.7: PL emission spectra of toluene solutions containing core/shell In(Zn)P/ZnS QDs prepared from **1** and **2**, showing the effect of the addition of L-phenylalanine sodium salt.

The addition of L-phenylalanine sodium salt in the preparation using **1** failed to reproduce QDs with a PL profile consistent to those from **2**. The disparity between the PL emission maxima, and consequently the size of QDs obtained, suggests that the release of the *N*-substituent upon transamidation of carboxylate-functionalised phosphinecarboxamides by HDA is not the cause for the size difference observed. Given that all of the other conditions were kept constant, this implies that there may be an alternative mechanism operating that has not yet been considered.

Failure to reproduce the result of **2** using the addition of exogenous L-phenylalanine sodium salt to **1** suggests that the carboxylate moiety must remain associated within the phosphinecarboxamide upon initial reaction with $InCl_3$. One mechanism to explain this could involve a salt metathesis reaction of the sodium carboxylate group and $InCl_3$.

However, this reaction would not preclude further reactivity at the phosphinecarboxamide moiety, such as transamidation or decomposition.

Alternatively, a mechanism could involve metalation of the phosphinecarboxamide group itself. Unpublished work from our group has shown that a stable *N*-propyl-phosphinecarboxamide gallium complex can be prepared using a supporting [ON(H)O] pincer scaffold.[19] In this example, the Ga[ON(H)O](Cl)(H_2N^nPr) complex reacts with sodium phosphaethynolate to form a phosphaketene. The gallium phosphaketene itself is unstable and undergoes a reaction with the amine adduct, forming a metalated phosphinecarboxamide (Scheme 5.6). Although the phosphinecarboxamide is not found to coordinate through the phosphide group, the example nevertheless supports the potential for an indium-bound phosphinecarboxamide species to be formed.



Scheme 5.6: Synthesis of a metalated *N*-propyl-phosphinecarboxamide from Ga[ON(H)O](Cl)(H_2N^nPr) and sodium phosphaethynolate.[19]

It is also possible that coordination through both the phosphinecarboxamide and carboxylate groups occurs. In this way, the carboxylate-functionalised phosphinecarboxamides would act as linkers between indium or zinc centres, synonymous to linkers found in metal-organic frameworks.[20–22] This would result in the formation of coordination clusters, although not strictly composed of InP like the magic-sized clusters known (Figure 5.8).[16] This may be plausible considering that the aliphatic

and aromatic substituents in **2**–**4** were purposely selected to be structural analogous of ligands used to stabilise InP MSCs.

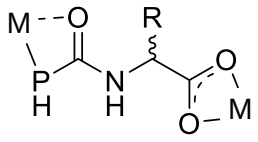


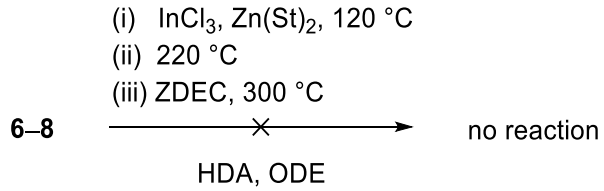
Figure 5.8: Carboxylate-functionalised phosphinecarboxamide as a bifunctional linker bridging between metal atoms (M = In or Zn).

Attributing the size control effect observed to intermediate coordination clusters is supported by the work of Park and co-workers. Park described the effect of using zinc oxo clusters ($Zn_4O(oleate)_6$ and $Zn_7O_2(oleate)_{10}$) during InP QD synthesis, where they found that the clusters supressed rapid precursor depletion and induced greater size uniformity in In(Zn)P QD cores.[23] Koh *et al*. have attributed similar observations to the formation of stable zinc-phosphorus complexes in the presence of carboxylate ligands.[24]

The decrease in QD size and improvement in monodispersity detailed in this work upon functionalisation with a carboxylate group (**2**–**4**) suggests that a similar mechanism could be operating that supresses growth. The presence of meta-stable intermediates which react slower that **1**, such as metal-phosphinecarboxamide coordination clusters, could rationalise the disparity in QD size observed.

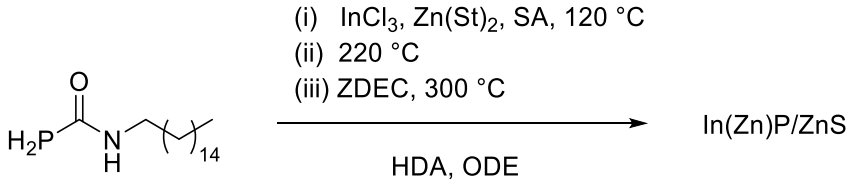
5.2.2 Carboxylic acid-functionalised phosphinecarboxamides

The preparation of HDA-capped core/shell In(Zn)P/ZnS QDs was attempted using carboxylic acid-functionalised phosphinecarboxamides (**6**–**8**; Scheme 5.7). In each case, no reaction was observed at either the core (i, ii) or core/shell (iii) growth stages.



Scheme 5.7: Attempted syntheses of In(Zn)P/ZnS QDs from **6**, **7**, and **8**. St = stearate; HDA = hexadecylamine; ODE = 1-octadecene; ZDEC = zinc diethyldithiocarbamate.

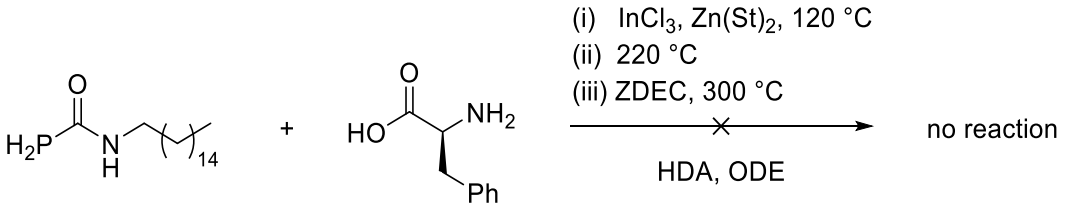
It is interesting that the protonation state of the carboxyl moiety has such a profound effect on the ability of **6**–**8** to act as phosphorus sources. One reason for this could be that acidic conditions do not favour In(Zn)P QD formation. However, this was discounted as the addition of two equivalents of extraneous stearic acid to a synthesis of In(Zn)P/ZnS QDs using **1** did not preclude QD formation, as evidenced by a sharp PL emission peak at 637 nm with FWHM = 94 nm. (Scheme 5.8).



Scheme 5.8: Synthesis of In(Zn)P/ZnS QDs from **1** upon addition of two equivalents of stearic acid (SA). St = stearate; HDA = hexadecylamine; ODE = 1-octadecene; ZDEC = zinc diethyldithiocarbamate.

An alternative reason for the inability of **6**–**8** to form In(Zn)P/ZnS QDs could be once again due to the respective transamidation reactions with HDA. Chapter 4 described the transamidation reaction of **6** with HDA to form **1**, releasing L-phenylalanine.

To determine whether this transamidation reaction prevents QD formation, the preparation of In(Zn)P/ZnS QDs was attempted using **1** with addition of L-phenylalanine (Scheme 5.9). This reaction was carried out analogously to that using the L-phenylalanine sodium salt described in Section 5.2.1.2.



Scheme 5.9: Attempted synthesis of In(Zn)P/ZnS QDs from **1** upon addition of L-phenylalanine. St = stearate; HDA = hexadecylamine; ODE = 1-octadecene; ZDEC = zinc diethyldithiocarbamate.

The addition of L-phenylalanine to the preparation using **1** was found to successfully preclude the formation of In(Zn)P/ZnS QDs. The effectiveness of L-phenylalanine to elicit the same outcome from **1** as observed for **6** is in contrast to the carboxylate example, where the addition of L-phenylalanine sodium salt to **1** did not achieve the same result as for **2** (Table 5.2). This suggests that in this case, the formation of L-phenylalanine by the transamidation of **6** by HDA is crucial in preventing In(Zn)P/ZnS QD formation.

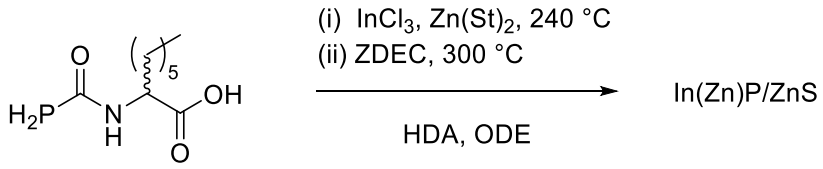
Table 5.2: PL spectroscopic data of In(Zn)P/ZnS QDs prepared from compounds **1**, **2**, and **6**, and control reactions with L-phenylalanine (sodium salt). PL emission $\lambda_{(max)}$ and full width at half maxima (FWHM) values given in nm.

Precursor	**$\lambda_{(max)}$**	**FWHM**
1	613	114
2	556	89
1 + L-phenylalanine sodium salt	606	86
6	no reaction	–
1 + L-phenylalanine	no reaction	–

One reason for this could be a condensation reaction of L-phenylalanine to form polypeptides. Lewis acids such as borates ($B(OR)_3$) and group IV metal complexes (MX_4; M = Ti, Zr; X = Cl, O^{i}Pr) are known to catalyse amino acid condensation.[25] Moreover, indium Lewis acid catalysts are frequently employed for ring-opening polymerisation.[26] The formation of polypeptides would likely destabilise the colloidal reaction mixture,

prohibiting QD growth. In addition, the H_2O generated by the condensation reaction would be capable of hydrolysing any InP QDs formed and quench emission.[27]

Whilst QD formation was not possible from **6**–**8** using the protocol developed thus far, core/shell In(Zn)P/ZnS QDs could be prepared from **7** by increasing the core growth temperature from 220 to 240 °C (Scheme 5.10).



Scheme 5.10: Modified synthesis of In(Zn)P/ZnS QDs from **7**. St = stearate; HDA = hexadecylamine; ODE = 1-octadecene; ZDEC = zinc diethyldithiocarbamate.

The In(Zn)P/ZnS QDs prepared are characterised by a UV-Vis absorption shoulder at 561 nm as well as a strong PL emission peak at 606 nm (Figure 5.9). Similarly to the carboxylate-functionalised phosphinecarboxamides (**2**–**4**), the QDs prepared from **7** show improved particle size dispersion, reflected by the relatively low FWHM of the PL emission peak (86 nm). PXRD analysis of the In(Zn)P/ZnS QDs prepared from **7** also show well-defined diffraction peaks at 28.3, 47.4, and 56.1°, in good agreement with the (111), (220), and (311) reflections of the expected cubic zinc blende structure.

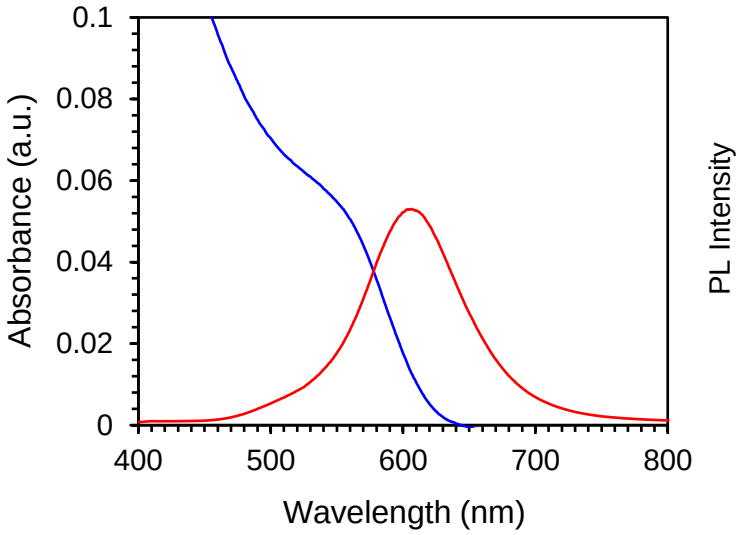
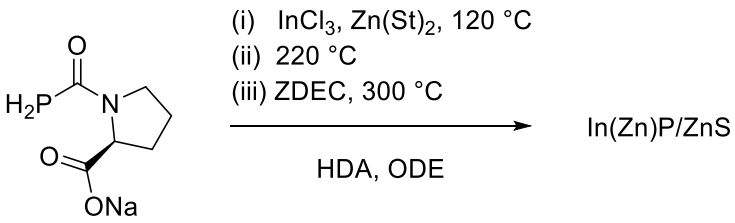


Figure 5.9: UV-Vis absorption (blue) and PL emission (red) spectra of a toluene solution containing HDA-capped core/shell In(Zn)P/ZnS QDs prepared from **7**.

Increasing the core growth temperature to 240 °C and removing the low-temperature annealing step at 120 °C is found to circumvent the inhibition of reactivity observed using the previous procedure for **7**. This may be due to a reduction in amino acid condensation in favour of InP QD growth, however the origin of this reactivity is unclear at the time of writing.

5.2.3 Preparation of In(Zn)P/ZnS QDs from L-proline-phosphinecarboxamide

Chapter 4 discussed how *N*,*N*-functionalised L-proline-phosphinecarboxamide showed *in situ* PH_3 release and transamidation reactivity comparable to other carboxyl-functionalised phosphinecarboxamides studied (**2**–**8**). L-Proline-phosphinecarboxamide is therefore also expected to be a suitable phosphorus precursor to InP QDs, and was studied following the protocol described for **2**–**4** (Section 5.2.1; Scheme 5.11).



Scheme 5.11: Synthesis of In(Zn)P/ZnS QDs from L-proline-phosphinecarboxamide. St = stearate; HDA = hexadecylamine; ODE = 1-octadecene; ZDEC = zinc diethyldithiocarbamate.

In(Zn)P QD cores prepared from L-proline-phosphinecarboxamide show a sharp PL emission peak at 607 nm, in contrast to QD cores prepared from **2**–**4**, which were non-emissive. Upon ZnS shell growth, a blue-shift in the PL emission peak to 590 nm is observed (Figure 5.10). The blue-shift results from greater excitonic confinement upon shell growth, and is consistent with core/shell QDs prepared from **1** (Chapter 3). Broad, featureless band edge absorption is also observed.

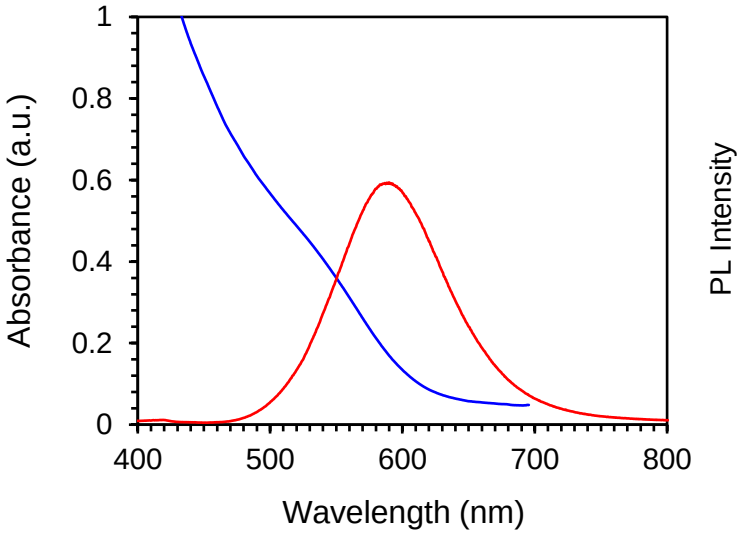


Figure 5.10: UV-Vis absorption (blue) and PL emission (red) spectra of a toluene solution containing HDA-capped core/shell In(Zn)P/ZnS QDs prepared from L-proline-phosphinecarboxamide.

The PL emission peak of In(Zn)/ZnS QDs prepared from L-proline-phosphine-carboxamide (590 nm) resides between those of the other carboxylate-functionalised

phosphinecarboxamides (**2**–**4**; *ca.* 560 nm) and **1** (613 nm). The disparity in PL peak position with those measured for **2**–**4** once again suggests that the origin of size control is more complex than the simple presence of carboxylate group in the phosphinecarboxamide.

An increase in PL emission FWHM is also observed upon shell growth from 85 to 97 nm. This is indicative of a greater degree of particle size dispersity upon ZnS shell growth, and is consistent with results obtained using **1** (Chapter 3). A reduction in polydispersity could be achieved by increasing the initial temperature ramp rate during shell growth. In the conditions described, the crude In(Zn)P QD cores and zinc diethyldithiocarbamate (ZDEC) are heated from room temperature to 300 °C over 27 minutes. ZDEC decomposes at 160 °C, so the time spent below this temperature could be reduced to minimise the potential for inhomogeneous QD growth occurring.[28]

PXRD analysis of the In(Zn)P cores and core/shell In(Zn)P/ZnS QDs prepared from L-proline-phosphinecarboxamide show the formation of highly crystalline nanoparticles. Diffraction peaks at 26.6, 43.7, and a broad shoulder at 51.1° are observed for the In(Zn)P QD cores, which shift to the corresponding high angles reflections at 28.4, 47.4, and 56.1° upon ZnS growth (Figure 5.11). The peaks are in agreement with the expected (111), (220), and (311) reflections of a cubic zinc blende structure, respectively.

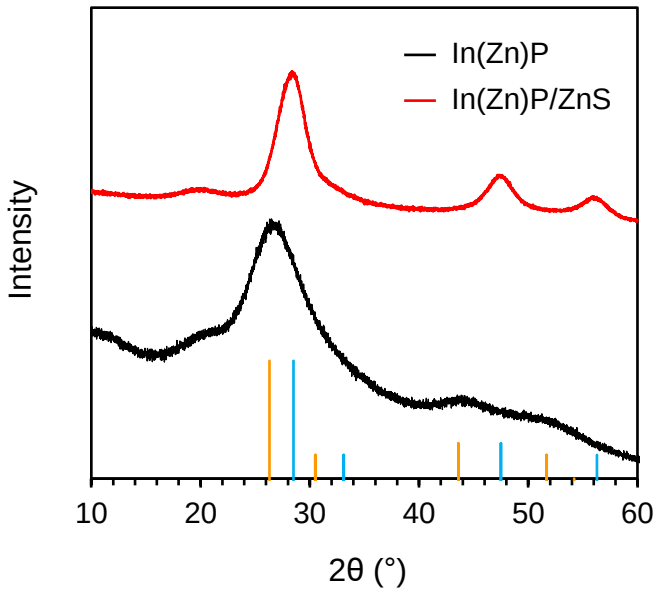


Figure 5.11: Powder X-ray diffraction pattern of In(Zn)P cores and core/shell In(Zn)P/ZnS QDs prepared from L-proline-phosphinecarboxamide. Diffraction patterns of zinc blende InP (orange) and ZnS (blue) shown for reference.

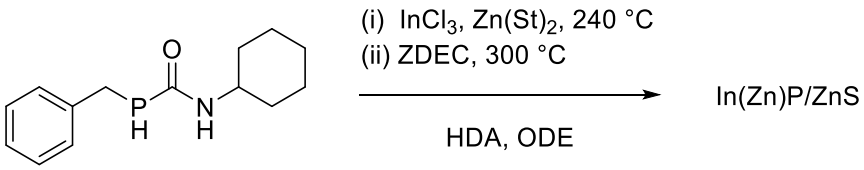
The successful isolation of In(Zn)P/ZnS QDs from carboxyl-functionalised phosphinecarboxamides demonstrates the robustness of the procedure developed and the utility of the phosphinecarboxamide moiety to act as an effective phosphorus precursor. Functionalisation with a carboxyl group has been found to enable size control over the QDs obtained. Moreover, in all of the examples discussed the QDs were more monodisperse than those prepared from **1**, as evidenced by the consistent decrease in PL emission FWHM values measured. The inability to image the QDs using electron microscopy precluded the investigation of any morphological changes to the QDs prepared upon carboxyl-functionalisation, however this will be the target of future work.

5.3 Preparation of In(Zn)P/ZnS QDs using *P*-functionalised phosphinecarboxamides

5.3.1 Preparation of In(Zn)P/ZnS QDs from *P*-benzyl-*N*-cyclohexyl-phosphinecarboxamide

Chapter 4 discussed how *P*-benzyl-*N*-cyclohexyl-phosphinecarboxamide does not decompose to form PH_3 *in situ* as observed for the *N*- and *N,N*-functionalised primary phosphinecarboxamides. This was rationalised by its inability to form HPCO, which is believed to be the source of reactive phosphorus species in solution (e.g. PH_3 and P_2H_4). In an attempt to confirm whether *P*-functionalisation accordingly prohibits QD formation, *P*-benzyl-*N*-cyclohexyl-phosphinecarboxamide was studied for the preparation of HDA-capped In(Zn)P/ZnS QDs.

Whilst no observable reaction occurred at 220 °C, *P*-benzyl-*N*-cyclohexyl-phosphine-carboxamide is unexpectedly found to act as a phosphorus precursor to In(Zn)P/ZnS QDs when the core growth temperature is increased to 240 °C (Scheme 5.12).



Scheme 5.12: Synthesis of core/shell In(Zn)P/ZnS QDs from *P*-benzyl-*N*-cyclohexyl-phosphine-carboxamide. St = stearate; HDA = hexadecylamine; ODE = 1-octadecene; ZDEC = zinc diethyldithiocarbamate.

The formation of In(Zn)/ZnS QDs is evidenced in the UV-Vis absorption spectrum, which shows a shoulder at 500 nm (Figure 5.12). This is accompanied by a PL emission peak at 542 nm indicative of QD formation. The relatively short PL emission wavelength measured suggests that the QDs formed have small particle diameters. This is consistent

with *P*-benzyl-*N*-cyclohexyl-phosphinecarboxamide being less reactive than *N*- and *N*,*N*-functionalised primary phosphinecarboxamides, resulting in slower particle growth.

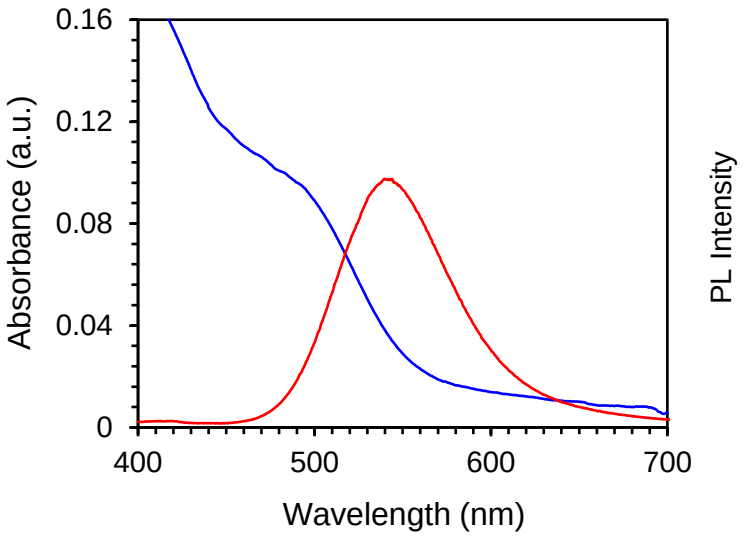


Figure 5.12: UV-Vis absorption (blue) and PL emission (red) spectra of a toluene solution containing HDA-capped core/shell In(Zn)P/ZnS QDs prepared from *P*-benzyl-*N*-cyclohexyl-phosphinecarboxamide.

The QDs obtained also have one of the lowest FWHM values measured out of all phosphinecarboxamides tested in this work (75 nm). The low FWHM value suggests the isolation of QDs with improved monodispersity. This may be a result of the slow growth afforded from the relatively unreactive *P*-functionalised phosphinecarboxamide. Angelé *et al.* highlighted how highly reactive phosphorus precursors rapidly convert into multiple species in solution, each of which have differing reactivities.[29] They also showed that by reducing the reactivity of the phosphorus precursor, polydispersity in QD particle size may be reduced.

Further support for the successful formation of In(Zn)P/ZnS QDs is given by PXRD analysis, which shows characteristic diffraction peaks at 28.5, 47.6, and 56.2°,

corresponding to the (111), (220), and (311) reflections of a cubic zinc blende structure (Figure 5.13).

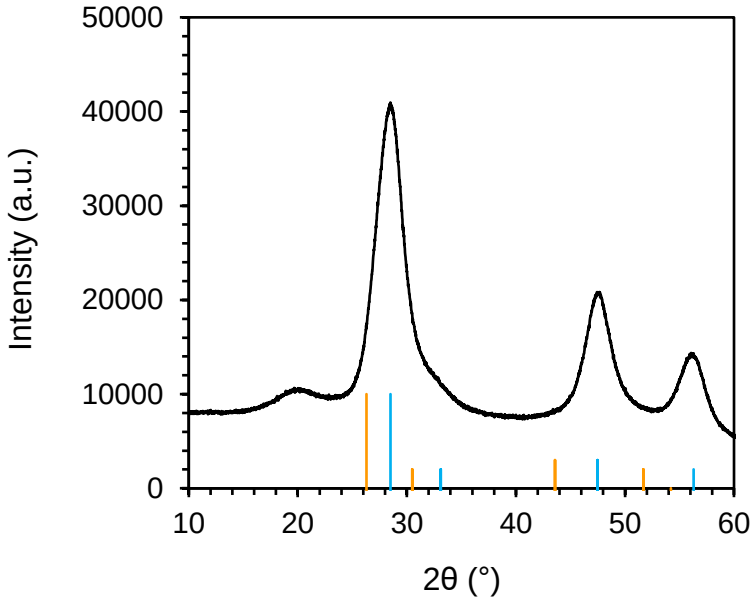


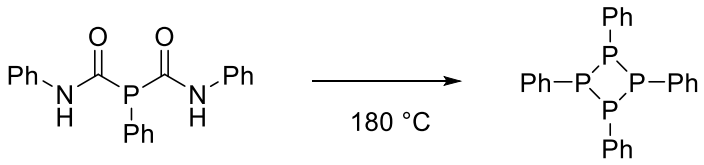
Figure 5.13: Powder X-ray diffraction pattern of core/shell In(Zn)P/ZnS QDs prepared from *P*-benzyl-*N*-cyclohexyl-phosphinecarboxamide. Diffraction patterns of zinc blende InP (orange) and ZnS (blue) shown for reference.

The isolation of InP QDs from *P*-benzyl-*N*-cyclohexyl-phosphinecarboxamide is confounding. No clear product was observed during thermal decomposition studies described in Chapter 4. Moreover, the formation of a relatively strong C–P σ-bond upon *P*-functionalisation (BDE = 513 kJ mol^{-1}) is expected to prohibit reactivity.[30]

Chapter 4 proposed that the thermal decomposition of phosphinecarboxamides occurs through PCO^- generation. The same decomposition reaction for *P*-benzyl-*N*-cyclohexyl-phosphinecarboxamide would afford the corresponding benzyl phosphaketene (BnPCO). Phosphaketenes are generally unstable with respect to oligomerisation and decomposition due to the highly reactive C=P π-bond.[31]

Phosphaketenes also readily decarbonylate by thermolysis or photolysis, releasing CO gas.[32] Alternatively, decarbonylation can be induced by ligand exchange with a suitable Lewis base. Examples include *N*-heterocyclic carbenes (NHCs), phosphines, and isonitriles.[33,34] The resulting base-stabilised phosphinidenes (RP) are highly reactive, requiring steric stabilisation for their manipulation and isolation.[35]

One route of reactivity of *P*-benzyl-*N*-cyclohexyl-phosphinecarboxamide could be the generation and subsequent coupling of transient phosphinidenes at high temperatures. Schneider *et al*. described the P–P coupling reactions of NHC-stabilised phosphinidenes to form cyclic oligophosphines.[36] Some of the earliest work investigating phosphinecarboxamide molecules revealed their propensity to undergo thermally-induced P–P coupling reactions. Korte and co-workers showed that upon heating phenylbis(phenylcarbamoyl)phosphine at 180 °C for 2 hours, the formation of tetra-phenylcyclotetraphosphine was observed (Scheme 5.13).[37] Whilst this is not directly attributed to phosphinidene generation and coupling, the role of radicals is proposed and discussed by Korte.

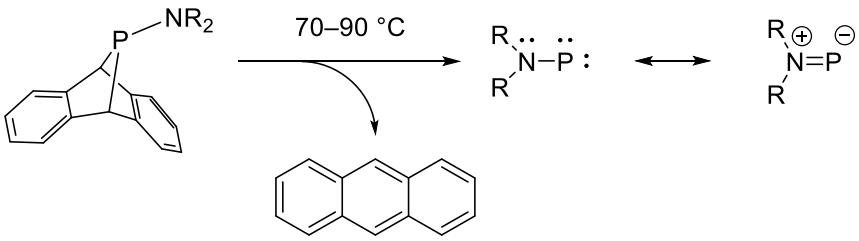


Scheme 5.13: Formation of tetraphenylcyclotetraphosphine by the thermally-induced P–P coupling of phenylbis(phenylcarbamoyl)phosphine.[37]

This example is closely related in structure to *P*-benzyl-*N*-cyclohexyl-phosphine-carboxamide and provides insight into the validity of P–P coupling occurring in this work. The fact that no QD formation occurs below 240 °C when using *P*-benzyl-*N*-cyclohexyl-phosphinecarboxamide supports that P–P oligomers may be formed before

reaching sufficiently high temperatures for QD growth. Matthews and Cartlidge have shown that P–P coupling of arylsilylphosphines is promoted by indium(III) halides.[38] Although they do not discuss whether the cyclic oligophosphanes produced are competent precursors to InP QDs, their work highlights the existence of similar P–P coupling reactions occurring in the presence of typical InP QD precursors.

Whilst P–P coupled products may form, a strong C–P σ-bond must consequently be cleaved to generate InP QDs. Another reaction route that may rationalise this is a phosphinidene transfer mechanism. Cummins and co-workers have reported phosphinidene transfer by dibenzo-7-phosphanorbornadiene, whereby two C–P bonds are thermolytically cleaved (Scheme 5.14).[39] In this example, C–P bond cleavage is driven by the gain of aromaticity of the anthracene by-product.



Scheme 5.14: Thermolytic formation of an aminophosphinidene by dibenzo-7-phosphanorbornadiene.[39]

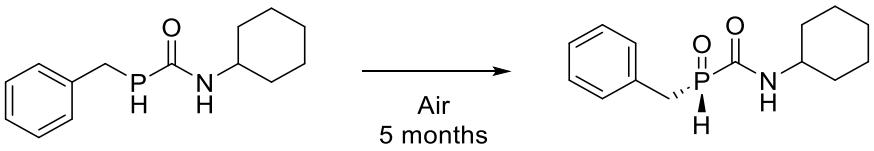
The presence of amine capping ligands may promote an analogous mechanism for *P*-benzyl-*N*-cyclohexyl-phosphinecarboxamide, however it is difficult to predict the products in this case without further study of intermediate species. The mechanism by which *P*-benzyl-*N*-cyclohexyl-phosphinecarboxamide acts as a phosphide precursor to InP QDs still remains unclear and is the target of future investigations (Chapter 6).

Regardless of the reaction mechanism, the demonstration of *P*-benzyl-*N*-cyclohexyl-phosphinecarboxamide as a suitable phosphorus precursor to InP QDs represents another

major accomplishment of this work. *P*-Functionalised secondary phosphinecarboxamides can be prepared through the hydrophosphination of isocyanates as well as derived from Na(PCO).[40–44] Having access to both routes to phosphinecarboxamides offers the extensive library of known functional groups to be incorporated and studied for the preparation of InP QDs.

5.3.2 Air stability of *P*-benzyl-*N*-cyclohexyl-phosphinecarboxamide

The unexpected reactivity of *P*-benzyl-*N*-cyclohexyl-phosphinecarboxamide for the preparation of In(Zn)P/ZnS QDs warrants evaluating its air stability. To do so, a solid sample of *P*-benzyl-*N*-cyclohexyl-phosphinecarboxamide was stored in a vial on the bench and exposed to air. The sample was then analysed by ^{31}P NMR spectroscopy after 5 months of air exposure (Scheme 5.15).



Scheme 5.15: Oxidation of *P*-benzyl-*N*-cyclohexyl-phosphinecarboxamide by exposure to air for 5 months.

The ^{31}P{^{1}H} NMR spectrum shows the prominent peak of *P*-benzyl-*N*-cyclohexyl-phosphinecarboxamide at −48.7 ppm, which appears as a doublet of doublets ($^{1}J_{H–P}$ = 206.3 Hz; $^{2}J_{H–P}$ = 7.2 Hz) in the proton-coupled spectrum (Figure 5.14). An additional peak is observed at 16.7 ppm, which is split into a doublet of triplets ($^{1}J_{H–P}$ = 482.3 Hz; $^{2}J_{H–P}$ = 14 Hz) upon proton-coupling. The peak at 16.7 ppm is in close agreement with the expected phosphine oxide product described by Jupp.[45]

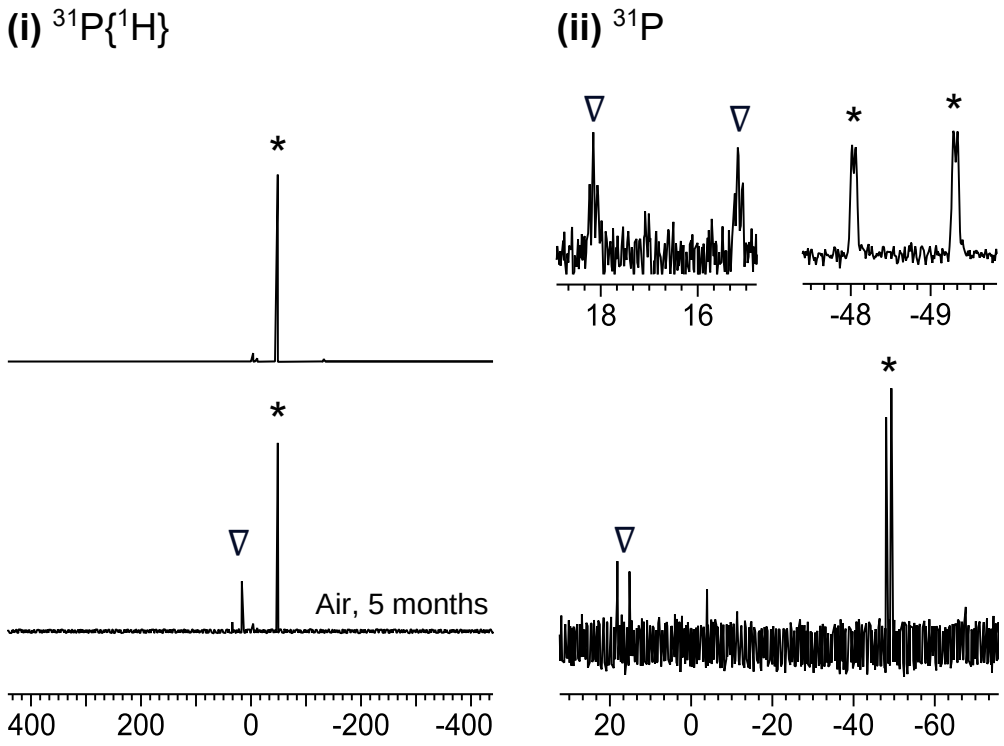


Figure 5.14: (i) $^{31}P\{^{1}H\}$ NMR spectra of d_5-pyridine solutions containing *P*-benzyl-*N*-cyclohexyl-phosphinecarboxamide (*) before and after exposure to air for 5 months; (ii) ^{31}P NMR spectrum showing the formation of the oxidised product (∇) in the 5 month sample.

The stability of *P*-benzyl-*N*-cyclohexyl-phosphinecarboxamide after exposure to air for 5 months demonstrates its comparable resilience to oxidation to the other *N*-functionalised phosphinecarboxamides discussed.[45] In this case the air-stability is less surprising, owing to the greater stability of secondary phosphines towards oxidation.[46,47]

Inspired by the ability of **1** to act as a phosphorus precursor to In(Zn)P/ZnS QDs after air exposure, the analogous reaction of *P*-benzyl-*N*-cyclohexyl-phosphinecarboxamide exposed to air for 5 months was tested. In(Zn)P/ZnS QDs were prepared following the protocol described in Section 5.3.1, and characterised by PL spectroscopy and PXRD.

PL emission spectroscopy shows a broad peak at 610 nm (Figure 5.15), while PXRD analysis bears the expected diffraction peaks at 28.5, 47.6, and 56.3°, in close agreement

with In(Zn)P/ZnS QDs prepared from *P*-benzyl-*N*-cyclohexyl-phosphinecarboxamide without air exposure.

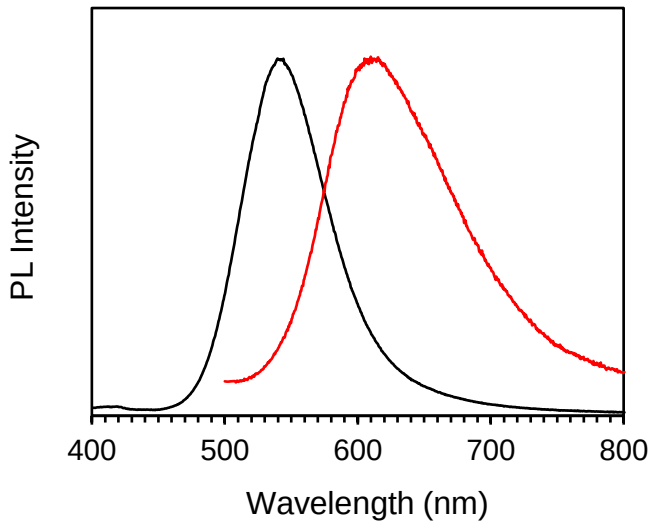


Figure 5.15: PL emission spectra of toluene solutions containing HDA-capped core/shell In(Zn)P/ZnS QDs prepared from *P*-benzyl-*N*-cyclohexyl-phosphinecarboxamide exposed to air for 5 months (red). Black trace shows In(Zn)P/ZnS QDs prepared without air exposure for reference.

The discrepancy between PL emission maxima with and without precursor air exposure is attributed to the oxidation process. The *P*-benzyl-*N*-cyclohexyl-phosphinecarboxamide oxide is expected to have distinct coordination characteristics that differ from the amine and carboxylate capping ligands. Accordingly, its presence is expected to disrupt the optimised QD growth conditions, which are known to be sensitive to changes in capping ligand character and concentration.[1,48] Moreover, for demonstration purposes the stoichiometry of the reaction was not adjusted to take into account the oxidation of *P*-benzyl-*N*-cyclohexyl-phosphinecarboxamide. As a consequence, there is a lower concentration of phosphorus precursor present which increases the likelihood of heterogenous particle-to-particle growth. This effect is reflected by the increase in

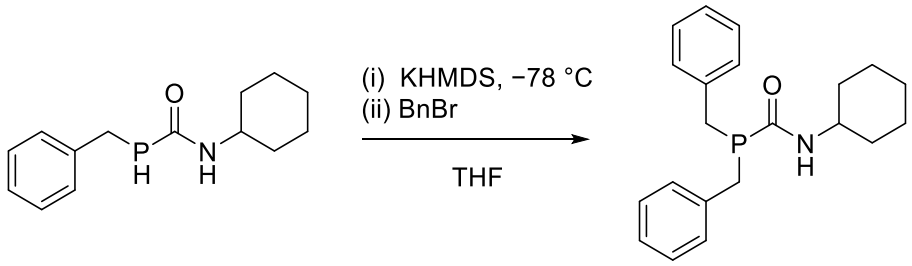
polydispersity in QD particle size observed upon exposure of the precursor to air, as the PL emission FWHM increases from 75 to 110 nm.

Nevertheless, this experiment represents an important proof-of-concept for the use of *P*-functionalised phosphinecarboxamides as a novel class of air-stable phosphorus precursor to InP QDs. Given that air-stability is a property reproducibly observed for various *N*-functionalised phosphinecarboxamides, it is likely that the same will be true for *P*-functionalised phosphinecarboxamides. These findings are a significant milestone of this work, introducing a second chemically-distinct class of novel phosphorus precursor to InP QDs. The implications of the contrasting, but equally effective reactivities of *N*- and *P*-functionalised phosphinecarboxamides on future work will be discussed in Chapter 6.

5.3.3 Synthesis and reactivity of *P*,*P*-benzyl-*N*-cyclohexyl-phosphinecarboxamide

Due to unexpected ability of *P*-benzyl-N-cyclohexyl-phosphinecarboxamide to act as a phosphorus source to InP QDs, it is necessary to investigate the related *P*,*P*-functionalised phosphinecarboxamide. If the reactivity of *P*-benzyl-*N*-cyclohexyl-phosphinecarboxamide resides in its decomposition to form a phosphaketene, *P*,*P*-functionalisation should prohibit this, similarly to how *N*,*N*-functionalisation precludes isocyanate formation (Chapter 4).

P,*P*-Benzyl-*N*-cyclohexyl-phosphinecarboxamide (**9**) was prepared by the deprotonation of *P*-benzyl-*N*-cyclohexyl-phosphinecarboxamide with KHMDS, followed by reaction with benzyl bromide (Scheme 5.16).



Scheme 5.16: Synthesis of *P*,*P*-benzyl-*N*-cyclohexyl-phosphinecarboxamide (**9**).

The ^{1}H NMR spectrum shows the expected benzyl environments: the methylene protons as two doublets at 2.83 and 3.19 ppm with shared geminal coupling ($^{2}J_{H–H}$ = 13.0 Hz); and the aromatic protons as a cluster of multiplets between 7.00–7.25 ppm (Figure 5.16). The cyclohexyl proton environments are observed between 0.92 and 1.68 ppm, in addition to a multiplet at 3.74 ppm, assigned to the amide proton. The absence of a phosphine proton environment and the relative peak integrals showing a 2:1 ratio of benzyl to cyclohexyl groups supports the formation of **9**. ^{31}P NMR spectroscopy provides further support for the successful preparation of **9** by the singlet observed at −3.69 ppm (Figure 5.17).

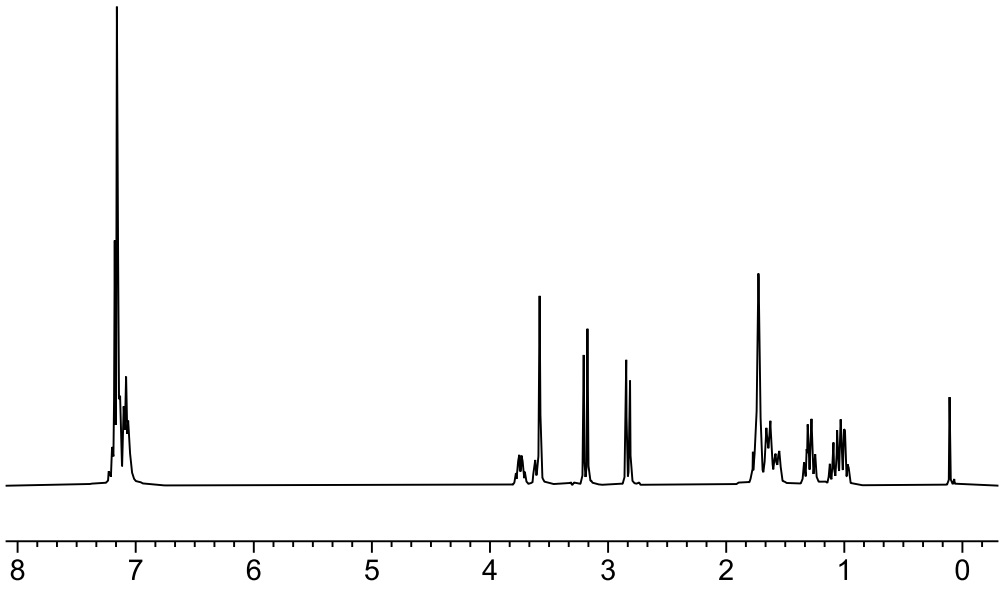


Figure 5.16: ^{1}H NMR spectrum of d_8-THF containing **9**.

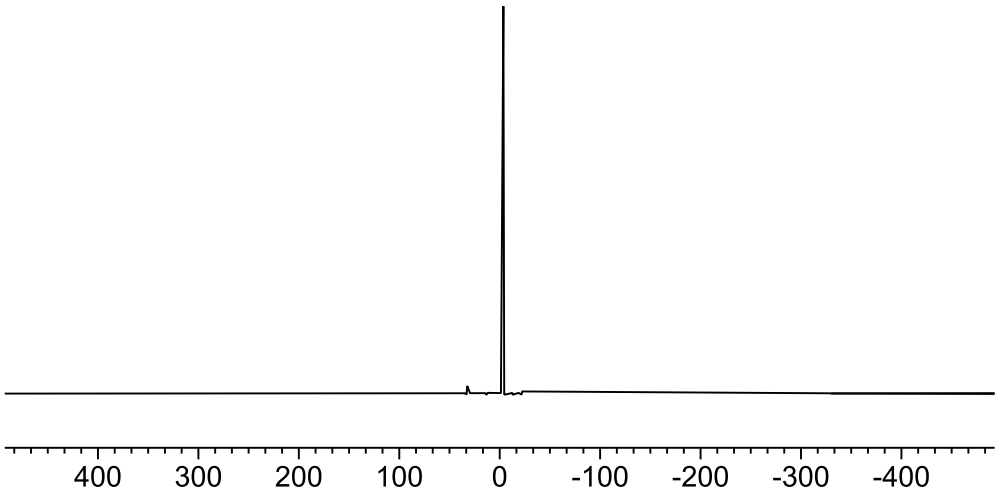
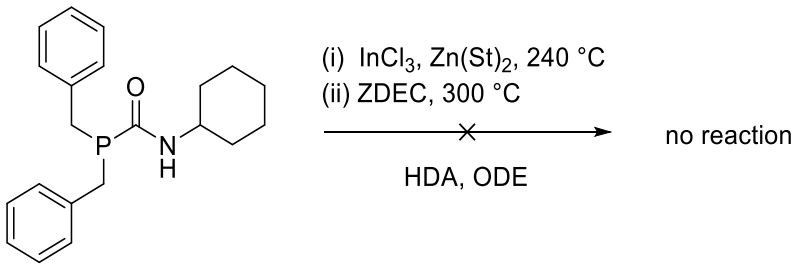


Figure 5.17: ^{31}P NMR spectrum of d_8-THF containing **9**.

Attempts to prepare In(Zn)P/ZnS QDs from **9** were unsuccessful (Scheme 5.17). This extended to modified experiments using higher reaction temperatures. This supports that *P*,*P*-functionalisation effectively deactivates the reaction mechanism by which *P*-benzyl-*N*-cyclohexyl-phosphinecarboxamide acts as a phosphorus precursors for InP QDs.



Scheme 5.17: Attempted synthesis of In(Zn)P/ZnS QDs from **9**.

These results suggest that a phosphaketene intermediate is required, and that *P*,*P*-functionalisation of a phosphinecarboxamide inhibits this reactivity. Further study is required to rationalise the confounding ability of *P*-benzyl-*N*-cyclohexyl-phosphinecarboxamide to act as a precursor to InP QDs. However, this result does support the potential intermediacy of a phosphaketene species.

5.4 Conclusions

This chapter has described the preparation of In(Zn)P/ZnS QDs from *N*-, *N*,*N*-, *P*-functionalised phosphinecarboxamides. Carboxylate-functionalised phosphine-carboxamides **2**–**4** are found to act as effective phosphorus precursors to InP QDs. Moreover, the use of **2**–**4** enables improved control over QD growth, affording smaller particles with reduced polydispersity. Attempts to reproduce this size control effect using **1** by the addition of the corresponding sodium salt produced upon transamidation were unsuccessful. The inability to reproduce the slow QD growth kinetics observed using control reactions suggests that a more complex decomposition mechanism than simply *in situ* PH_3 generation exists. This is further supported by the disparity in PL emission maxima observed for L-proline-phosphinecarboxamide compared to **2**–**4**, despite the presence of a carboxylate group.

The use of carboxylic acid-functionalised phosphinecarboxamides **6**–**8** was found to prohibit QD formation at 220 °C. This result could be reproduced upon addition of an extraneous carboxylic acid (L-phenylalanine) to a QD reaction using **1**. The inhibition is postulated to be a consequence of amino acid condensation to form polypeptides that destabilise the colloidal suspension. The inhibition can be overcome using **7** by reducing the reaction time at low temperatures (< 220 °C) and increasing the QD annealing temperature to 240 °C. All of the carboxyl-functionalised phosphinecarboxamides studied afforded InP QDs with improved particle size dispersity compared to **1**.

Finally, this chapter described *P*-benzyl-*N*-cyclohexyl-phosphinecarboxamide as an unexpected air-stable phosphorus precursor to InP QDs. The In(Zn)P/ZnS QDs obtained using *P*-benzyl-*N*-cyclohexyl-phosphinecarboxamide were among the most

monodisperse isolated thus far, showing promise for their continued development. The mechanism by which *P*-benzyl-*N*-cyclohexyl-phosphinecarboxamide acts as a phosphorus precursor is discussed. *P*,*P*-Functionalisation is shown to prohibit QD formation, providing valuable insight for future mechanistic studies.

5.5 References

1 M. Green, *J. Mater. Chem.*, 2010, **20**, 5797–5809.

2 G. Jia, S. Xu and A. Wang, *J. Mater. Chem. C*, 2015, **3**, 8284–8293.

3 K. Kim, D. Yoo, H. Choi, S. Tamang, J.-H. Ko, S. Kim, Y.-H. Kim and S. Jeong, *Angew. Chem. Int. Ed.*, 2016, **55**, 3714–3718.

4 Y. Kim, H. Choi, Y. Lee, W. Koh, E. Cho, T. Kim, H. Kim, Y.-H. Kim, H. Y. Jeong and S. Jeong, *Nat. Commun.*, 2021, **12**, 4454.

5 K. C. Dümbgen, J. Leemans, V. De Roo, M. Minjauw, C. Detavernier and Z. Hens, *Chem. Mater.*, 2023, **35**, 1037–1046.

6 M. R. Friedfeld, D. A. Johnson and B. M. Cossairt, *Inorg. Chem.*, 2019, **58**, 803–810.

7 Y. Kwon, J. Oh, E. Lee, S. H. Lee, A. Agnes, G. Bang, J. Kim, D. Kim and S. Kim, *Nat. Commun.*, 2020, **11**, 1–15.

8 J. M. Nedeljković, O. I. Mićić, S. P. Ahrenkiel, A. Miedaner and A. J. Nozik, *J. Am. Chem. Soc.*, 2004, **126**, 2632–2639.

9 R. Yadav, Y. Kwon, C. Rivaux, C. Saint-Pierre, W. L. Ling and P. Reiss, *J. Am. Chem. Soc.*, 2023, **145**, 5970–5981.

10 B. Chen, D. Li and F. Wang, *Small*, 2020, **16**, 1–20.

11 D. C. Gary, B. A. Glassy and B. M. Cossairt, *Chem. Mater.*, 2014, **26**, 1734–1744.

12 D. K. Harris and M. G. Bawendi, *J. Am. Chem. Soc.*, 2012, **134**, 20211–20213.

13 A. Cros-Gagneux, F. Delpech, C. Nayral, A. Cornejo, Y. Coppel and B. Chaudret, *J. Am. Chem. Soc.*, 2010, **132**, 18147–18157.

14 B. Fritzinger, R. K. Capek, K. Lambert, J. C. Martins and Z. Hens, *J. Am. Chem. Soc.*, 2010, **132**, 10195–10201.

15 J. De Roo, N. Yazdani, E. Drijvers, A. Lauria, J. Maes, J. S. Owen, I. Van Driessche, M. Niederberger, V. Wood, J. C. Martins, I. Infante and Z. Hens, *Chem. Mater.*, 2018, **30**, 5485–5492.

16 D. C. Gary, S. E. Flowers, W. Kaminsky, A. Petrone, X. Li and B. M. Cossairt, *J. Am. Chem. Soc.*, 2016, **138**, 1510–1513.

17 N. Rivera-González, S. Chauhan and D. F. Watson, *Langmuir*, 2016, **32**, 9206–9215.

18 V. H. Dao, N. R. Cameron and K. Saito, *Polym. Chem.*, 2016, **7**, 11–25.

19 R. Bowld, 2021, Thesis (M.Chem.), University of Oxford.

20 S. Ali Akbar Razavi and A. Morsali, *Coord. Chem. Rev.*, 2019, **399**, 213023.

21 H. Atallah, M. ELcheikh Mahmoud, F. M. Ali, A. Lough and M. Hmadeh, *Dalton Trans.*, 2018, **47**, 799–806.

22 B. Zhang, W. Wang, B. Liu and L. Hou, *Dalton Trans.*, 2021, **50**, 5713–5723.

23 K. Kim, Y.-H. Suh, D. Kim, Y. Choi, E. Bang, B. H. Kim and J. Park, *Chem. Mater.*, 2020, **32**, 2795–2802.

24 S. Koh, T. Eom, W. D. Kim, K. Lee, D. Lee, Y. K. Lee, H. Kim, W. K. Bae and D. C. Lee, *Chem. Mater.*, 2017, **29**, 6346–6355.

25 M. T. Sabatini, V. Karaluka, R. M. Lanigan, L. T. Boulton, M. Badland and T. D. Sheppard, *Chem. Eur. J.*, 2018, **24**, 7033–7043.

26 A. B. Kremer, R. J. Andrews, M. J. Milner, X. R. Zhang, T. Ebrahimi, B. O. Patrick, P. L. Diaconescu and P. Mehrkhodavandi, *Inorg. Chem.*, 2017, **56**, 1375–1385.

27 N. Mordvinova, P. Emelin, A. Vinokurov, S. Dorofeev, A. Abakumov and T. Kuznetsova, *Beilstein J. Nanotechnol.*, 2014, **5**, 1220–1225.

28 G. O. Siqueira, T. Matencio, H. V. da Silva, Y. G. de Souza, J. D. Ardisson, G. M. de Lima and A. de Oliveira Porto, *Phys. Chem. Chem. Phys.*, 2013, **15**, 6796–6803.

29 L. Angelé, S. Dreyfuss, B. Dubertret and N. Mézailles, *Inorg. Chem.*, 2021, **60**, 2271–2278.

30 Y.-R. Luo, *Comprehensive handbook of chemical bond energies*, CRC Press, Boca Raton , 2007.

31 V. Plack, J. R. Goerlich, A. Fischer and R. Schmutzler, *Zeitschrift für Anorg. und Allg. Chemie*, 1999, **625**, 1979–1984.

32 A. M. Tondreau, Z. Benkő, J. R. Harmer and H. Grützmacher, *Chem. Sci.*, 2014, **5**, 1545–1554.

33 L. Liu, D. A. Ruiz, D. Munz and G. Bertrand, *Chem*, 2016, **1**, 147–153.

34 M. M. Hansmann, R. Jazzar and G. Bertrand, *J. Am. Chem. Soc.*, 2016, **138**, 8356–8359.

35 U. Schmidt, *Angew. Chem. Int. Ed.*, 1975, **14**, 523–528.

36 H. Schneider, D. Schmidt and U. Radius, *Chem. Commun.*, 2015, **51**, 10138–10141.

37 H. Fritzsche, U. Hasserodt and F. Korte, *Angew. Chem. Int. Ed.*, 1964, **3**, 64.

38 A. J. Cartlidge and P. D. Matthews, *Inorganica Chim. Acta*, 2022, **533**, 120772.

39 W. J. Transue, A. Velian, M. Nava, C. García-Iriepa, M. Temprado and C. C. Cummins, *J. Am. Chem. Soc.*, 2017, **139**, 10822–10831.

40 A. C. Behrle and J. A. R. Schmidt, *Organometallics*, 2013, **32**, 1141–1149.

41 M. Itazaki, T. Matsutani, T. Nochida, T. Moriuchi and H. Nakazawa, *Chem. Commun.*, 2020, **56**, 443–445.

42 T. M. Horsley Downie, J. W. Hall, T. P. Collier Finn, D. J. Liptrot, J. P. Lowe, M. F. Mahon, C. L. McMullin and M. K. Whittlesey, *Chem. Commun.*, 2020, **56**, 13359–13362.

43 B. Zhang, X. Ma, B. Yan, C. Ni, H. Yu, Z. Yang and H. W. Roesky, *Dalton Trans.*, 2021, **50**, 15488–15492.

44 T. M. Horsley Downie, M. F. Mahon, J. P. Lowe, R. M. Bailey and D. J. Liptrot, *ACS Catal.*, 2022, **12**, 8214–8219.

45 A. Jupp, 2016, Thesis (D.Phil.), University of Oxford.

46 B. Stewart, A. Harriman and L. J. Higham, *Organometallics*, 2011, **30**, 5338–5343.

47 F. Horký, R. Franz, C. Bruhn and R. Pietschnig, *Chem. Eur. J.*, 2023, e202302518.

48 M. M. Green, *Curr. Opin. Solid State Mater. Sci.*, 2002, **6**, 355–363.

Chapter 6

Concluding remarks and future work

6.1 Conclusions

This thesis has reported the development of a novel method for the preparation of indium phosphide quantum dots (QDs) from phosphinecarboxamides ($RHPC(O)NR'_2$). The novel phosphinecarboxamides described are air-stable phosphorus-containing analogues of ureas and are prepared from the facile reaction of the 2-phosphaethynolate anion (PCO^-) with amines.

Thermal decomposition of $H_2PC(O)NH_2$ in solution is found to form PH_3 and P_2H_4, which were used *in situ* for the preparation of phenylacetate-capped InP magic-sized clusters. $H_2PC(O)NH_2$ was shown to undergo a transamidation reaction with the common QD capping ligand hexadecylamine to form *N*-hexadecyl-phosphinecarboxamide (**1**), which was also prepared independently by the reaction of hexadecylamine with PCO^-. **1** showed remarkable air-stability in addition to *in situ* PH_3 reactivity upon thermal decomposition.

Subsequently, the use of **1** as a phosphorus precursor to HDA-capped In(Zn)P and core/shell In(Zn)P/ZnS QDs was reported. The preparation of In(Zn)P/ZnS QDs from **1** stored in air for one month was also described, marking the first example of an air-stable phosphorus precursor to InP QDs. An improvement in QD size uniformity was afforded upon development of a protocol employing trioctylphosphine and palmitate capping ligands, highlighting the potential for further synthetic optimization to be achieved.

Motivated by the successful use of **1** for the preparation of InP QDs, the solution phase reactivity of *N*-, *N*,*N*-, and *P*-functionalised phosphinecarboxamides were investigated. Novel *N*-functionalised phosphinecarboxamides bearing carboxyl moieties (**2**–**8**) were all found to generate PH_3 *in situ* upon thermal decomposition, similarly to **1**. The analogous

production of PH_3 by *N*,*N*-functionalised L-proline-phosphinecarboxamide supported the intermediacy of HPCO during decomposition, discounting a mechanism whereby PH_3 is directly generated alongside an isocyanate. Transamidation reactions with hexadecylamine were observed for all phosphinecarboxamides studied, regardless of *N*- or *P*-functionalisation.

The preparation of In(Zn)P/ZnS QDs from *N*- and *N*,*N*-functionalised phosphine-carboxamides was reported. Carboxylate-functionalised phosphinecarboxamides **2**–**4** and L-proline-phosphinecarboxamide were shown to be effective phosphorus precursors to InP QDs, in addition to affording control over QD size. Failure to reproduce the size control effect using control reactions suggests that a more complex decomposition mechanism than *in situ* PH_3 generation operates. The use of carboxylic acid-functionalised phosphinecarboxamides **6**–**8** were found to prohibit QD formation at 220 °C, however this could be induced for **7** by increasing the reaction temperature to 240 °C. All of the carboxyl-functionalised phosphinecarboxamides studied afforded InP QDs with improved particle size dispersity compared to **1**.

Finally, the use of *P*-benzyl-*N*-cyclohexyl-phosphinecarboxamide as an unexpected air-stable phosphorus precursor to InP QDs is reported. *P*-Benzyl-*N*-cyclohexyl-phosphinecarboxamide was used to prepare In(Zn)P/ZnS QDs with low particle size dispersity, whilst *P*,*P*-functionalisation was found to completely inhibit this reactivity.

In conclusion, this thesis has contributed to the expansion of known phosphorus precursors to InP QDs. This work has introduced two chemically-distinct classes of air-stable phosphorus precursor, which at the time of writing is unprecedented. The broad applicability of the phosphinecarboxamides described for the preparation of InP QDs

presents the opportunity for the extensive library of literature-known compounds to be explored in the future.

6.2 Future work

6.2.1 Understanding and evaluating the QD size control effect

This work has described the differences in particle size of the QDs obtained from phosphinecarboxamides upon varying their functionality. However, the structural differences were only implied through changes in photoluminescence (PL) emission profiles. The inability to analyse the QDs by electron microscopy imaging precluded more extensive study of any structural and morphological influence by the phosphinecarboxamide precursors. Early experiments using high-resolution transmission electron microscopy (HRTEM) appeared to eliminate sample radiolysis issues observed during scanning TEM studies. Future work would seek to employ this imaging technique further to elucidate the structural characteristics of the InP QDs prepared.

Future work would also involve more mechanistic studies to fully understand the ambiguous mode of phosphide production by phosphinecarboxamides. The inability to reproduce the size control afforded for carboxylate-functionalised phosphine-carboxamides **2**–**4** using control reactions alludes to a more complex mechanism than transamidation and subsequent ligand-directed growth.

Ambient temperature multinuclear NMR studies of the speciation of $InCl_3$ and **2**–**4** in solution could be used to better understand whether stable indium-phosphinecarboxamide complexes are formed. The crystallisation of such species should be possible, particularly since **2** and **3** consist of stabilising phenylacetate substituents.

These substituents have previously been used to crystallographically characterise an InP magic-sized cluster.[1] X-ray crystallographic studies would provide further insight into the identity of possible intermediate species.

Mechanistic studies would also allow a better understanding of the confounding ability of *P*-benzyl-*N*-cyclohexyl-phosphinecarboxamide to act as a phosphorus precursor to InP QDs. The possibility of phosphinidene transfer and P–P coupling reactions occurring was discussed, however further investigation is required. ^{31}P NMR spectroscopy studies would be used to determine whether P–P coupled oligophosphanes are formed upon thermal decomposition of *P*-benzyl-*N*-cyclohexyl-phosphinecarboxamide. The formation of multiple products was described in Chapter 4, all of which have chemical shifts in the expected range for oligophosphanes (−180 to 20 ppm).[2] The formation of oligophosphanes should be easily identifiable, given the complex splitting patterns expected as a result of chemical and magnetic non-equivalence of the phosphorus nuclei.[3]

6.2.2 Towards monodisperse InP QDs

This thesis has addressed several challenges widely reported for the preparation of InP QDs. The identification and development of two distinct classes of air-stable phosphorus precursor marks a major breakthrough in the field. Future work will leverage the novel reactivity of these phosphinecarboxamides to tackle polydispersity challenges that frequently plague InP QD syntheses.

Preparing monodisperse InP QDs with narrow PL emission line widths comparable to prototypical II-VI QDs (e.g. CdSe) is a long-standing challenge.[4] This is further frustrated by the fact that even emerging QD materials, such as metal halide perovskites (e.g. $CsPbX_3$), can be prepared with high monodispersity with ease.[5] Particle size

inhomogeneity is often associated to the highly reactive nature of the traditional phosphorus precursors used.[6] Reiss highlighted how the rapid depletion of phosphorus monomers during synthesis leads to greater polydispersity in QD particle size.[7] Chan attributes this effect to fast monomer consumption promoting Ostwald ripening, whereby nanocrystals grow heterogeneously on one another with minimal size focussing.[8,9]

P-Benzyl-*N*-cyclohexyl-phosphinecarboxamide was used to produce InP QDs with a narrow PL emission line width (75 nm), indicative of reduced particle size dispersity. It is believed that the high thermal stability of *P*-benzyl-*N*-cyclohexyl-phosphinecarboxamide enables the slow, controlled release of reactive phosphorus species into solution. The narrow particle size dispersity observed for this relatively unoptimised preparation is impressive and is motivating for further improvements to be achieved.

An alternative way that phosphinecarboxamides may be used to obtain monodisperse QDs is through blending mixtures of precursors together. Cossairt and co-workers reported the use of a mixture of $P(SiMe_3)_3$ and $P(SiPh_3)_3$ with different reactivities for the resolution of InP QD nucleation and growth events.[10] $P(SiMe_3)_3$ was used as a phosphide source for nucleation, whilst the less reactive $P(SiPh_3)_3$ provided a slow but continuous supply during growth.[11] The distinct difference in reactivity of *N*- and *P*-functionalised phosphinecarboxamides could be exploited in an analogous fashion. The onset decomposition temperature of *N*-functionalised phosphinecarboxamides is 105 °C, whilst the *P*-functionalised congeners do not react until 240 °C. Such a large discrepancy in reactivity could be utilised to modulate the formation of InP QDs in solution – with *N*-functionalised phosphinecarboxamides acting as a phosphide source during nucleation

and the *P*-functionalised phosphinecarboxamide providing continual phosphide release during growth.

Detailed are just several ways in which phosphinecarboxamides could foreseeably be studied for the development of monodisperse InP QDs. The discovery of these novel precursors, and the extensive library of literature-known compounds already reported, will invariably permit the exploration of numerous approaches.

6.3 References

1 D. C. Gary, S. E. Flowers, W. Kaminsky, A. Petrone, X. Li and B. M. Cossairt, *J. Am. Chem. Soc.*, 2016, **138**, 1510–1513.

2 V. J. Eilrich and E. Hey-Hawkins, *Coord. Chem. Rev.*, 2021, **437**, 213749.

3 T. Wellnitz and C. Hering-Junghans, *Eur. J. Inorg. Chem.*, 2021, **2021**, 8–21.

4 E. M. Janke, N. E. Williams, C. She, D. Zherebetskyy, M. H. Hudson, L. Wang, D. J. Gosztola, R. D. Schaller, B. Lee, C. Sun, G. S. Engel and D. V Talapin, *J. Am. Chem. Soc.*, 2018, **140**, 15791–15803.

5 L. Protesescu, S. Yakunin, M. I. Bodnarchuk, F. Krieg, R. Caputo, C. H. Hendon, R. X. Yang, A. Walsh and M. V Kovalenko, *Nano Lett.*, 2015, **15**, 3692–3696.

6 D. K. Harris and M. G. Bawendi, *J. Am. Chem. Soc.*, 2012, **134**, 20211–20213.

7 R. Yadav, Y. Kwon, C. Rivaux, C. Saint-Pierre, W. L. Ling and P. Reiss, *J. Am. Chem. Soc.*, 2023, **145**, 5970–5981.

8 M. D. Clark, S. K. Kumar, J. S. Owen and E. M. Chan, *Nano Lett.*, 2011, **11**, 1976–1980.

9 P. M. Allen, B. J. Walker and M. G. Bawendi, *Angew. Chem. Int. Ed.*, 2010, **49**, 760–762.

10 D. C. Gary, B. A. Glassy and B. M. Cossairt, *Chem. Mater.*, 2014, **26**, 1734–1744.

11 B. Chen, D. Li and F. Wang, *Small*, 2020, **16**, 1–20.

Chapter 7

Experimental

7.1 General synthetic considerations

All reactions and product manipulations were carried out under an inert atmosphere of argon or dinitrogen using standard Schlenk or glovebox techniques (MBraun UNILab glovebox maintained at < 0.1 ppm O_2 and < 0.1 ppm H_2O) unless otherwise noted.

1,4-Dioxane (Alfa Aesar, 99+%, stab. 5−10 ppm BHT) was distilled from a sodium/benzophenone mixture. Acetonitrile (MeCN; Sigma Aldrich, CHROMASOLV® gradient grade for HPLC, ≥99.9%), 1,2-dimethoxyethane (DME; Sigma Aldrich, anhydrous, 99.5%), hexane (Sigma Aldrich, HPLC grade), pentane (Sigma Aldrich, HPLC grade), tetrahydrofuran (THF; Fisher, HPLC grade), and toluene (Sigma Aldrich, HPLC grade) were purified using an MBraun SPS-800 solvent system. Pyridine (Alfa Aesar, 99%) was degassed and dried over activated 3 Å molecular sieves before use. Ethanol (Sigma Aldrich, 99.8%) and methanol (Sigma Aldrich, 99.9%) were used as received. d_8-THF (Eurisotop, >99.5%), C_6D_6 (Sigma Aldrich, 99.5%), and d_5-pyridine (Eurisotop, >99.5%) were dried over CaH_2, vacuum distilled, and degassed before use. d_8-Toluene (Sigma Aldrich, 99.6%) was dried over Na/K, vacuum distilled, and degassed before use. d_6-DMSO and $CDCl_3$ were used as received. All dry solvents were stored under argon in gas-tight ampoules over 3 Å molecular sieves. 1-Octadecene (Sigma Aldrich, technical grade 90%), oleylamine (Sigma Aldrich, technical grade 70%), and tri-*n*-octylphosphine (Strem, 97%) were degassed under vacuum at 80°C for 16 hours and stored under argon before use. Deionised water (18.2 MΩ·cm) was obtained from a Purelab Flex machine. Bio-Beads S-X1 Support styrene divinylbenzene beads for size exclusion chromatography were used as received (1% cross-linkage, 40–80 µm bead size, 600–14,000 MW exclusion range).

The suppliers and purification procedures for commercially available chemicals are detailed in Table 7.1.

Table 7.1: Supplier and purification procedures for commercially available chemicals.

Reagent	Supplier	Purity	Purification
11-Aminoundecanoic acid	Sigma Aldrich	97%	Used as received
2-(trifluoromethyl)-D-phenylalanine	Fluorochem	98%	Used as received
2-Aminooctanoic acid	Sigma Aldrich	99%	Used as received
Ammonia	BOC	99.98%	Used as received
Benzyl bromide	Sigma Aldrich	98%	Used as received
^{t}BuOH	Alfa Aesar	99%	Refluxed over Mg/I_2, distilled
Coumarin 153	Sigma Aldrich	99%	Used as received
Cyclohexylamine	Alfa Aesar	98+%	Dried over CaH_2, vacuum distilled and degassed
Diethylcarbonate	Sigma Aldrich	99%	Used as received
H_2O_2 (aq. solution)	Alfa Aesar	35% w/w	Used as received
Hexadecylamine	Sigma Aldrich	98%	Used as received
Indium acetate	Sigma Aldrich	99.99%	Dried under vacuum
Indium chloride	Fluorochem	>99.9%	Dried under vacuum
KHMDS	Sigma Aldrich	95%	Used as received
L-Phenylalanine	Sigma Aldrich	99%	Used as received
L-Proline	Thermo Scientific	99%	Used as received
Myristic acid	Fluorochem	95%	Used as received
NaOH	Sigma Aldrich	97%	Used as received
Naphthalene	Sigma Aldrich	99+%	Sublimed under vacuum
$[NH_4][BF_4]$	Sigma Aldrich	> 97%	Dried under vacuum
Palmitic acid	Fluorochem	99%	Used as received
Phenylacetic acid	Alfa Aesar	99%	Used as received
Phosphorus	Sigma Aldrich	99.99%	Dried under vacuum

Sodium	Acros Organics	99.8%, oiled sticks	Washed with hexane, dried under vacuum
Stearic acid	Sigma Aldrich	95%	Used as received
Zinc stearate	Sigma Aldrich	10-12% zinc	Used as received
$[Zn][S_2CN(Et)_2]_2$	Sigma Aldrich	97%	Used as received

$[Na(dioxane)_x][PCO]$ (x = 2.50−2.71) was synthesised according to the preparation reported by Heift *et al.*, substituting ethylene carbonate for diethylcarbonate.[1] Phosphinecarboxamide,[2] *N*-cyclohexylphosphinecarboxamide,[3] *P*-benzyl-*N*-cyclohexylphosphinecarboxamide,[4] *P*,*P*-benzyl-*N*-cyclohexylphosphinecarboxamide,[4] and L-proline-phosphinecarboxamide were prepared according to literature procedures and stored at ambient temperatures in an inert atmosphere glovebox.[5,6] Indium phenylacetate, indium myristate, and indium palmitate were prepared using a modified preparation to that reported by Gary and co-workers.[7] In a typical synthesis, indium acetate (1000 mg, 3.34 mmol) and the carboxylic acid (33.4 mmol) were weighed out into a round-bottom flask and evacuated with stirring. The reaction mixture was heated to 80 °C to melt the carboxylic acid. The solution was allowed to off-gas acetic acid under reduced pressure for approximately 8 h at 80 °C to generate a molten $In(OOCR)_3$ solution. Afterward, the flask was filled with nitrogen, and a 20 mL portion of dry toluene was added. The $In(OOCR)_3$ product was then purified by washing with EtOH, MeOH, DCM, and cold hexane, and stored in an inert atmosphere glovebox. L-Phenylalanine sodium salt was prepared following literature methods by deprotonation with sodium hydroxide.[8]

7.2 Synthesis methods

7.2.1 Chapter 2 – Reactivity of phosphinecarboxamides in solution

7.2.1.1 Thermal decomposition studies

Thermal decomposition studies were carried out on d_5-pyridine solutions containing $H_2PC(O)NH_2$ and *N*-hexadecyl-phosphinecarboxamide (**1**) under an inert atmosphere in a J-Young tap NMR tube. The solutions were then heated in a silicone oil bath for the stated time and duration, and the formation of decomposition products monitored by ^{1}H and ^{31}P NMR spectroscopy.

7.2.1.2 Synthesis of phenylacetate-capped InP magic-sized clusters

$H_2PC(O)NH_2$ (80 mg, 1.04 mmol) and indium phenylacetate (1080 mg, 2.08 mmol) were dissolved in toluene (20 mL) and stirred at 110 °C for one hour. The solution turned from colourless to yellow and then red. The solution was concentrated and filtered to remove unreacted starting materials and triturated with hexane. The supernatant was removed by filtration and the product washed with hexane (3 × 10 mL). The volatiles were removed *in vacuo* and the product dried overnight to afford a red powder (400 mg).

7.2.1.3 Synthesis of myristate-capped InP magic-sized clusters

Myristate-capped InP MSCs were prepared according to the protocol described in Section 7.2.1.2 from $H_2PC(O)NH_2$ (30 mg, 0.390 mmol) and indium myristate (621 mg, 0.779 mmol). Due to the greater solubility of the myristate-capped MSCs in apolar solvents, hexane was used as a solvent and THF as an anti-solvent during purification.

7.2.1.4 Synthesis of 1 by transamidation of phosphinecarboxamide with hexadecylamine

$H_2PC(O)NH_2$ (10 mg, 0.065 mmol) and hexadecylamine (15 mg, 0.065 mmol) were dissolved in d_5-pyridine in a J-Young tap NMR tube. The solution was then heated in a silicone oil bath for the stated time and duration, and monitored by ^{1}H and ^{31}P NMR spectroscopy.

7.2.1.5 Synthesis of 1

$[Na(dioxane)_{2.71}][PCO]$ (1.33 g, 4.15 mmol), hexadecylamine (1.00 g, 4.15 mmol), and NH_4BF_4 (435 mg, 4.15 mmol) were dissolved in THF (40 mL) in a medium Schlenk tube. The resulting pale orange solution was stirred overnight at room temperature, after which the solvent was removed *in vacuo*. The crude product was redissolved in toluene (15 mL) and solids removed by filtration. Toluene was removed *in vacuo*, the yellow product washed with minimum hexane (*ca.* 10 mL), and subsequently dried *in vacuo* overnight, affording **1** as a yellow powder (1.071 g, 86%).

^{1}H NMR (400.2 MHz, C_6D_6, 298 K): δ (ppm) 4.73 (broad; 1H; N*H*), 3.30 (d; $^{1}J_{P–H}$ = 204.4 Hz; 2H; P*H*$_2$), 2.98 (m; 2H; NHC*H*$_2$), 1.02–1.39 (m; (C*H*$_2$)$_{14}$CH$_3$), 0.92 (t; $^{3}J_{H–H}$ = 7.0 Hz; 3H; (CH$_2$)$_{14}$C*H*$_3$). **^{1}H{^{31}P} NMR** (499.9 MHz, C_6D_6, 298 K): δ (ppm) 3.29 (s), other resonances remain unchanged. **^{31}P NMR** (162.0 MHz, C_6D_6, 298 K): δ (ppm) −132.5 (t; $^{1}J_{H–P}$ = 204.6 Hz). **^{31}P{^{1}H} NMR** (162.0 MHz, C_6D_6, 298 K): δ (ppm) −132.5 (s). **^{13}C{^{1}H} NMR** (151.0 MHz, d_5-pyridine, 298 K): δ (ppm) 172.4 (d; $^{1}J_{P–C}$ = 6.0 Hz; H_2PC(O)NH), 40.6 (NH*C*H$_2$), 32.4 (NHCH$_2$*C*H$_2$), 29.8–30.3 (*C*$_{14}$H$_{29}$). **CHN Analysis** (calculated for $C_{17}H_{36}NOP$): C 65.20%, H 7.63%, N 4.61%; found: C 65.12%, H 7.73%, N 4.78%.

7.2.2 Chapter 3 – Synthesis and characterisation of InP quantum dots prepared from phosphinecarboxamides

7.2.2.1 Synthesis of In(Zn)P QDs from 1

In a typical reaction **1** (54.5 mg, 0.181 mmol), $InCl_3$ (20 mg, 0.09 mmol), zinc stearate (114 mg, 0.181 mmol), and hexadecylamine (393 mg, 1.63 mmol) were added to a three-neck round bottom flask in an inert atmosphere glovebox. The solids were suspended in degassed 1-octadecene (ODE, 10 mL) and warmed to 120 °C (16 min, 6.25 °C/min) with stirring (500 rpm). The mixture was stirred at this temperature for 30 minutes before heating to 220 °C (10 °C/min) and stirred for a further 30 minutes. The resulting In(Zn)P QD solution was then rapidly cooled to room temperature, and an aliquot (3 mL) taken for purification and analysis.

7.2.2.2 Synthesis of In(Zn)P/ZnS QDs from 1

Zinc diethyldithiocarbamate (34 mg, 0.09 mmol) was added to an ODE solution (10 mL) containing crude In(Zn)P QDs (Section 7.2.2.1) and degassed under dynamic vacuum at room temperature for 20 minutes. The atmosphere was replenished with argon, the solution heated to 300 °C (17 min, 10 °C/min) and stirred for 30 minutes. The resulting core/shell In(Zn)P/ZnS QD solution was then rapidly cooled to room temperature for purification and analysis.

7.2.2.3 Synthesis of oleylamine-capped In(Zn)P/ZnS QDs from 1

1 (54.5 mg, 0.181 mmol), $InCl_3$ (20 mg, 0.09 mmol), and zinc stearate (114 mg, 0.181 mmol) were added to a three-neck round bottom flask in an inert atmosphere glovebox. The solids were suspended in oleylamine (10 mL) and the reaction mixture heated using the same temperature profile described in Section 7.2.2.1. Oleylamine-

capped core/shell In(Zn)P/ZnS QDs were prepared from the crude In(Zn)P QDs following the protocol described in Section 7.2.2.2.

7.2.2.4 Oxidation of 1 by H_2O_2

An aqueous H_2O_2 solution (0.38 mL, 6% v/v, 0.683 mmol) was added drop-wise to a stirring pyridine solution (5 mL) of **1** (103 mg, 0.342 mmol) affording a colourless solution. After stirring for four hours at room temperature the volatiles were *in vacuo*. The product oil was triturated with toluene and remaining volatiles removed *in vacuo* to afford the white solid product.

7.2.2.5 Synthesis of TOP-capped InP QDs from 1

Tri-*n*-octylphosphine-capped (TOP) InP QDs were prepared using a modified protocol reported by Angelé *et al.*[9] **1** (40 mg, 0.133 mmol) and indium palmitate (117 mg, 0.133 mmol) were added to a three-neck round bottom flask in an inert atmosphere glovebox. The solids were then suspended in ODE (16 mL) and TOP (2 mL), heated to 250 °C and stirred for 20 minutes. The solution was then rapidly cooled to room temperature and an aliquot taken for purification and analysis.

7.2.2.6 Synthesis of TOP-capped InP/ZnS QDs from 1

Zinc stearate (84 mg, 0.133 mmol) was added to a crude solution containing TOP-capped InP cores in ODE and TOP (Section 7.2.2.5). The solution was heated to 300 °C (27 minutes, 10 °C/min) and when the solution temperature reached 260 °C an ODE solution of zinc diethyldithiocarbamate (1.3 mL, 0.1 M) was rapidly injected. The reaction mixture was stirred for 30 minutes before rapidly cooling to room temperature.

7.2.2.7 Synthesis of In(Zn)P QDs from phenylacetate-capped InP MSCs

$H_2PC(O)NH_2$ (14 mg, 0.181 mmol) and indium phenylacetate (176 mg, 0.362 mmol) were dissolved in THF in a three-neck round bottom flask and heated at 70 °C for 30 minutes. THF was then removed *in vacuo*, followed by addition of zinc stearate (114 mg, 0.181 mmol) and hexadecylamine (393 mg, 1.63 mmol) to the flask in an inert atmosphere glovebox. The crude phenylacetate-capped InP MSCs and capping ligands were suspended in ODE (10 mL), heated to 220 °C and stirred for 1 minute before rapidly cooling.

7.2.2.8 Purification of QDs by precipitation and resuspension

Crude QD solutions were typically purified by precipitation and resuspension. The crude QD solution was diluted with hexane or toluene and centrifuged (3900 rpm, 20 minutes) to remove undissolved solids. The supernatant containing the QDs was recovered and then precipitated using an anti-solvent (e.g. EtOH, MeOH, or MeCN) followed by centrifugation (3900 rpm, 12 minutes). The supernatant was discarded and the QD solids resuspended in minimum hexane or toluene, followed by precipitation with the anti-solvent. This procedure was repeated three times for UV-Vis and PL spectroscopic analysis, and five to eight further times for transmission electron microscopy analysis.

7.2.2.9 Purification of QDs by size-exclusion chromatography

Size exclusion chromatography was used to purify QDs before PLQY measurements were taken.[10] A column was packed with toluene-swollen styrene divinylbenzene polymer beads (Bio-Beads S-X1, 600–14,000 MW exclusion range) and washed with toluene (180 mL) before use. A toluene solution containing QDs purified by precipitation/resuspension (2 cycles) was eluted through the column and the first eluate

was collected. The eluate containing the purified QDs was concentrated for further analysis. The column was washed with toluene (180 mL) and stored for reuse.

7.2.3 Chapter 4 – Reactivity of functionalised phosphinecarboxamides in solution

7.2.3.1 Synthesis of 2

[Na(dioxane)$_{2.5}$][PCO] (500 mg, 1.65 mmol) and L-phenylalanine (273 mg, 1.65 mmol) were dissolved in pyridine (30 mL) and water (3 mL) in a medium Schlenk tube. The resulting pale orange solution was stirred overnight at room temperature, after which the solution was filtered to a Schlenk tube and the solvent removed *in vacuo.* The product was washed with toluene (10 mL), and subsequently dried *in vacuo* overnight, affording **2** as a pale pink powder (350 mg, 86%).

^{1}H NMR (400.2 MHz, d_5-pyridine and a drop of distilled H_2O, 298 K): δ (ppm) 7.70 (m; 1H; N*H*), 7.58 (d; 2H; $^{3}J_{H–H}$ = 8.0 Hz; *meta*-*H*), 7.28 (t; 2H; $^{3}J_{H–H}$ = 8.0 Hz; *ortho*-*H*), 7.21 (t; 1H; $^{3}J_{H–H}$ = 8.0 Hz; *para*-*H*), 5.28 (m; 1H; NHC*H*), 3.77 (dd; $^{2}J_{H–H}$ = 13.6 Hz; $^{3}J_{H–H}$ = 4.9 Hz; 1H; NHCHC*H*$_a$H$_b$), 3.74 (dd; $^{1}J_{H–P}$ = 208.0 Hz; $^{2}J_{H–H}$ = 11.6 Hz; 1H; PH$_a$H$_b$), 3.68 (dd; $^{1}J_{H–P}$ = 209.1 Hz; $^{2}J_{H–H}$ = 11.5 Hz; 1H; PH$_a$*H*$_b$), 3.57 (dd; $^{2}J_{H–H}$ = 13.7 Hz; $^{3}J_{H–H}$ = 7.1 Hz; 1H; NHCHCH$_a$*H*$_b$). **^{1}H{^{31}P} NMR** (499.9 MHz, d_5-pyridine and a drop of distilled H_2O, 298 K): δ (ppm) 3.75 (d; $^{2}J_{Hb–Ha}$ = 11.2 Hz; 1H; PH$_a$H$_b$), 3.69 (d; $^{2}J_{Ha–Hb}$ = 11.6 Hz; 1H; PH$_a$*H*$_b$), other resonances remain unchanged. **^{31}P NMR** (162.0 MHz, d_5-pyridine and a drop of distilled H_2O, 298 K): δ (ppm) −131.8 (t; $^{1}J_{H–P}$ = 207.1 Hz). **^{31}P{^{1}H} NMR** (162.0 MHz, d_5-pyridine and a drop of distilled H_2O, 298 K): δ (ppm) −131.8 (s). **^{13}C{^{1}H} NMR** (151 MHz, d_5-pyridine and a drop of distilled H_2O, 298 K): δ (ppm) 177.5 (*C*OONa), 173.5 (d; $^{1}J_{P–C}$ = 7.6 Hz; H_2P*C*(O)NH), 140.5 (*ipso*-*C*), 131.1 (*ortho*-*C*), 129.2 (*meta*-*C*), 121.2 (*para*-*C*), 58.7 (NH*C*H), 39.6 (*C*H$_2$Ph).

CHN Analysis (calculated for $C_{10}H_{11}NNaO_3P$): C 48.59%, H 4.49%, N 5.67%; found: C 46.64%, H 4.31%, N 5.54%.

7.2.3.2 Synthesis of 3

[Na(dioxane)$_{2.5}$][PCO] (500 mg, 1.65 mmol) and 2-(trifluoromethyl)-D-phenylalanine (386 mg, 1.65 mmol) were dissolved in pyridine (30 mL) and water (3 mL) in a medium Schlenk tube. The resulting dark purple solution was stirred overnight at room temperature, after which the solution was filtered to a Schlenk tube and the solvent removed *in vacuo*. The resulting solids were washed with pyridine and toluene (20 mL, 50:50 v/v) and dried *in vacuo* overnight to afford **3** as a purple powder (349 mg, 67%).

^{1}H NMR (400.2 MHz, d_5-pyridine and a drop of distilled H_2O, 298 K): δ (ppm) 8.97 (d; $^{3}J_{H–H}$ = 8.7 Hz; 1H; N*H*), 8.02 (d; 1H; $^{3}J_{H–H}$ = 7.9 Hz; *meta*-*H*), 7.61 (t; 1H; $^{3}J_{H–H}$ = 7.9 Hz; *ortho*-*H*), 7.54 (t; 1H; $^{3}J_{H–H}$ = 7.9 Hz; *ortho*-*H*), 7.32 (t; 1H; $^{3}J_{H–H}$ = 7.9 Hz; *para*-*H*), 5.53 (m; 1H; NHC*H*), 4.06 (dd; $^{2}J_{H–H}$ = 14.6 Hz; $^{3}J_{H–H}$ = 4.8 Hz; 1H; NHCHC*H*$_a$H$_b$), 3.83 (dd; $^{1}J_{H–P}$ = 209.0 Hz; $^{2}J_{Hb–Ha}$ = 11.5 Hz; 1H; P*H*$_a$H$_b$), 3.75 (dd; $^{1}J_{H–P}$ = 209.8 Hz; $^{2}J_{Ha–Hb}$ = 11.6 Hz; 1H; PH$_a$*H*$_b$), 3.61 (dd; $^{2}J_{H–H}$ = 14.6 Hz; $^{3}J_{H–H}$ = 9.4 Hz; 1H; NHCHCH$_a$*H*$_b$). **^{1}H{^{31}P} NMR** (499.9 MHz, d_5-pyridine and a drop of distilled H_2O, 298 K): δ (ppm) 3.82 (d; $^{2}J_{Hb–Ha}$ = 11.7 Hz; 1H; P*H*$_a$H$_b$), 3.75 (d; $^{2}J_{Ha–Hb}$ = 11.7 Hz; 1H; PH$_a$*H*$_b$), other resonances remain unchanged. **^{31}P NMR** (162.0 MHz, d_5-pyridine and a drop of distilled H_2O, 298 K): δ (ppm) −131.8 (t; $^{1}J_{H–P}$ = 209.0 Hz; *P*H$_2$). **^{31}P{^{1}H} NMR** (162.0 MHz, d_5-pyridine and a drop of distilled H_2O, 298 K): δ (ppm) −131.8 (s). **^{13}C{^{1}H} NMR** (400.2 MHz, d_5-pyridine and a drop of distilled H_2O, 298 K): δ (ppm) 177.3 (*C*OONa), 173.7 (d; $^{1}J_{P–C}$ = 7.1 Hz; H$_2$P*C*(O)NH), 139.3 (*Ar*-*C*), 137.6 (*Ar*-*C*), 133.6 (*Ar*-*C*), 133.0 (*Ar*-

C), 126.84 (q, $^{1}J_{F–C}$ = 5.2 Hz), 121.2 (*Ar*-*C*), 57.8 (NH*C*H), 37.2 (*C*H_2Ph). **^{19}F NMR** (565.0 MHz, d_5-pyridine and a drop of distilled H_2O, 298 K): δ (ppm) −58.1 (s; 3F; C*F*$_3$).

7.2.3.3 Synthesis of 4

4 was prepared following the procedure described in Section 7.2.3.2 from [Na(dioxane)$_{2.5}$][PCO] (250 mg, 0.827 mmol) and 2-aminooctanoic acid (132 mg, 0.827 mmol), and isolated as an orange solid (83 mg, 42%).

^{1}H NMR (400.2 MHz, d_5-pyridine and a drop of distilled H_2O, 298 K): δ (ppm) 8.82 (d; $^{3}J_{H–H}$ = 7.7 Hz; 1H; N*H*), 5.19 (m; 1H; NHC*H*), 3.94 (dd; $^{1}J_{P–H}$ = 208.5 Hz; $^{2}J_{Hb–Ha}$ = 11.5 Hz; 1H; P*H*$_a$), 3.86 (dd; $^{1}J_{P–H}$ = 209.1 Hz; $^{2}J_{Ha–Hb}$ = 11.5 Hz; 1H; P*H*$_a$), 2.35 (m; 1H; CHC*H*$_a$), 2.20 (m; 1H; CHC*H*$_a$), 1.66 (m; 2H; CHCH_2C*H*$_a$), 1.26–1.17 (m; 6H; (C*H*)$_3$CH_3), 0.83 (t; $^{3}J_{H–H}$ = 7.1 Hz; 3H; C*H*$_3$). **^{1}H{^{31}P} NMR** (499.9 MHz, d_5-pyridine and a drop of distilled H_2O, 298 K): δ (ppm) 3.94 (d; $^{2}J_{Hb–Ha}$ = 11.7 Hz; 1H; P*H*$_a$H$_b$), 3.86 (d; $^{2}J_{Ha–Hb}$ = 11.7 Hz; 1H; PH$_a$*H*$_b$), other resonances remain unchanged. **^{31}P NMR** (162.0 MHz, d_5-pyridine and a drop of distilled H_2O, 298 K): δ (ppm) −131.1 (t, $^{1}J_{Ha–P}$ = 209.1 Hz, $^{1}J_{Hb–P}$ = 209.1 Hz, *P*H_2). **^{31}P{^{1}H} NMR** (162.0 MHz, d_5-pyridine and a drop of distilled H_2O, 298 K): δ (ppm) −131.1 (s). **^{13}C{^{1}H} NMR** (400.2 MHz, d_5-pyridine and a drop of distilled H_2O, 298 K): δ (ppm) 178.0 (*C*OONa), 173.4 (d; $^{1}J_{P–C}$ = 7.1 Hz; H_2P*C*(O)NH), 57.6 (NH*C*H), 34.6 (NHCH*C*H_2), 32.7 (*C*H_2CH_2CH_3), 30.4 (*C*H_2(CH)$_2$CH_3), 26.9 (CHCH_2*C*H_2), 23.6 (*C*H_2CH_3), 14.9 (*C*H_3).

7.2.3.4 Synthesis of 5

[Na(dioxane)$_{2.5}$][PCO] (500 mg, 1.65 mmol) and 11-aminoundecanoic acid (333 mg, 1.65 mmol) were dissolved in a mixture of THF (30 mL) and water (3 mL) in a medium Schlenk tube. The resulting dark purple solution was stirred overnight at room

temperature, after which the solution was filtered to a Schlenk tube and the solvent removed *in vacuo*. The resulting solids were washed with THF (20 mL) and dried *in vacuo* overnight, affording **5** as a light purple powder (281 mg, 59%).

^{1}H NMR (499.9 MHz, d_5-pyridine and a drop of distilled H_2O, 298 K): δ (ppm) 9.42 (s; 1H; N*H*), 4.04 (d; $^{1}J_{H\text{-}P}$ = 211.9 Hz; 2H; PH_2), 3.54 (m; 2H; NHCH_2), 2.68 (t; $^{3}J_{H–H}$ = 7.6 Hz; 2H; CH_2COOH), 1.99–1.18 (m; 16H; C_8H_{16}). **^{1}H{^{31}P} NMR** (499.9 MHz, d_5-pyridine and a drop of distilled H_2O, 298 K): δ (ppm) 4.04 (s), other resonances remain unchanged. **^{31}P NMR** (162.0 MHz, d_5-pyridine and a drop of distilled H_2O, 298 K): δ (ppm) −132.2 (t; $^{1}J_{P\text{-}H}$ = 209.9 Hz; *P*H_2). **^{31}P{^{1}H} NMR** (162.0 MHz, d_5-pyridine and a drop of distilled H_2O, 298 K): δ (ppm) −132.2 (s). **^{13}C{^{1}H} NMR** (400.2 MHz, d_5-pyridine and a drop of distilled H_2O, 298 K): δ (ppm) 183.9 (s; *C*OONa), 176.7 (d; $^{1}J_{P–C}$ = 8.2 Hz; H_2P*C*(O)NH), 42.3 (NH*C*H_2), 40.4 (*C*H_2COONa), 33.6–28.6 (C_8H_{16}). **CHN Analysis** (calculated for $C_{11}H_{23}NOPNa$): C 50.48%, H 8.81%, N 4.94%; found: C 49.25%, H 7.92%, N 4.62%.

7.2.3.5 Synthesis of 6

2 (350 mg, 1.42 mmol) and NH_4BF_4 (194 mg, 1.85 mmol) were dissolved in a mixture of pyridine (20 mL) and water (2 mL), and stirred overnight. The solvent was removed *in vacuo* and the crude product extracted in THF. The solution was then concentrated, forming an oil from which the white solid product could be obtained by trituration with hexane (20 mL). The solids were recovered by filtration and subsequently dried *in vacuo* overnight, affording **6** as a white powder (285 mg, 89%).

^{1}H NMR (499.9 MHz, d_5-pyridine, 298 K): δ (ppm) 12.55 (broad; 1H; COO*H*), 9.20 (d; $^{3}J_{H–H}$ = 8.2 Hz; 1H; N*H*), 7.44 (d; 2H; $^{3}J_{H–H}$ = 7.8 Hz; *meta*-*H*), 7.28 (t; 2H; $^{3}J_{H–H}$ = 7.8

Hz; *ortho*-<u>*H*</u>), 7.21 (t; 1H; $^{3}J_{H–H}$ = 7.8 Hz; *para*-<u>*H*</u>), 5.42 (m; 1H; NHC<u>*H*</u>), 3.78 (dd; $^{1}J_{P–Ha}$ = 209.7 Hz; $^{2}J_{Hb–Ha}$ = 10.8 Hz; 1H; P<u>*H*$_a$</u>H$_b$), 3.75 (dd; $^{1}J_{P-Hb}$ = 209.4 Hz; $^{2}J_{Ha–Hb}$ = 11.5 Hz; 1H; PH$_a$<u>*H*$_b$</u>), 3.61 (dd; $^{2}J_{Hb–Ha}$ = 13.7 Hz; $^{3}J_{H–Ha}$ = 5.2 Hz; 1H; NHCHC<u>*H*$_a$</u>H$_b$), 3.37 (dd; $^{2}J_{Ha–Hb}$ = 13.9 Hz $^{3}J_{H–Hb}$ = 8.2 Hz; 1H; NHCHCH$_a$<u>*H*$_b$</u>). **^{1}H{^{31}P} NMR** (499.9 MHz, *d*$_5$-pyridine, 298 K): δ (ppm) 3.77 (d; $^{2}J_{Hb–Ha}$ = 11.6 Hz; 1H; P<u>*H*$_a$</u>H$_b$), 3.74 (d; $^{2}J_{Ha–Hb}$ = 11.8 Hz; 1H; PH$_a$<u>*H*$_b$</u>), other resonances remain unchanged. **^{31}P NMR** (162.0 MHz, *d*$_5$-pyridine, 298 K) δ (ppm) −132.1 (t; $^{1}J_{P-H}$ = 209.1 Hz; <u>*P*</u>H$_2$). **^{31}P{^{1}H} NMR** (162.0 MHz, *d*$_5$-pyridine, 298 K): δ (ppm) −132.0 (s). **^{13}C{^{1}H} NMR** (151.0 MHz, *d*$_5$-pyridine, 298 K) δ (ppm) 175.7 (s, 1H, <u>*C*</u>OOH), 173.5 (d; $^{1}J_{P–C}$ = 7.6 Hz, H$_2$P<u>*C*</u>(O)NH), 139.0 (*ipso*-<u>*C*</u>), 130.1 (*ortho*-<u>*C*</u>), 129.0 (*meta*-<u>*C*</u>), 127.1 (*para*-<u>*C*</u>), 56.2 (NH<u>*C*</u>H), 38.60 (<u>*C*</u>H$_2$Ph). **IR** (cm^{-1}): *ν*(OH) 3281.

7.2.3.6 Synthesis of 7

7 was prepared following the procedure described in Section 7.2.3.5 from **4** (405 mg, 1.68 mmol) and NH_4BF_4 (176 mg, 1.68 mmol), and isolated as a white powder (94 mg, 25%).

^{1}H NMR (400.2 MHz, *d*$_5$-pyridine, 298 K): δ(ppm) 14.95 (broad; 1H; COO<u>*H*</u>), 9.78 (d; $^{3}J_{H–H}$ = 5.18 Hz; 1H; N<u>*H*</u>), 5.19 (m; 2H; NHC<u>*H*</u>), 3.91 (dd; $^{1}J_{P–Ha}$ = 209.3 Hz; $^{2}J_{Hb–Ha}$ = 11.6 Hz; 1H; P<u>*H*$_a$</u>H$_b$), 3.88 (dd; $^{1}J_{H–P}$ = 209.8 Hz; $^{2}J_{Ha–Hb}$ = 11.7 Hz; 1H; PH$_a$<u>*H*$_b$</u>), 2.16 (m; 1H; CHC<u>*H*$_a$</u>H$_b$), 1.99 (m; 1H; CHCH$_a$<u>*H*$_b$</u>), 1.66 (m; 2H; CHCH$_2$C<u>*H*$_2$</u>), 1.28–1.13 (m; 6H; C$_3$<u>*H*$_6$</u>CH$_3$), 0.79 (t; $^{3}J_{H–H}$ = 6.7 Hz; 3H; C<u>*H*$_3$</u>). **^{1}H{^{31}P} NMR** (499.9 MHz, *d*$_5$-pyridine, 298 K): δ (ppm) 3.92 (d; $^{2}J_{Hb–Ha}$ = 11.5 Hz; 1H; P<u>*H*$_a$</u>H$_b$), 3.89 (d; $^{2}J_{Ha–Hb}$ = 11.2 Hz; 1H; PH$_a$<u>*H*$_b$</u>), other resonances remain unchanged. **^{31}P NMR** (162.0 MHz, *d*$_5$-pyridine, 298 K) δ (ppm) –132.6 (t; $^{1}J_{H–P}$ = 209.0 Hz, <u>*P*</u>H$_2$). **^{31}P{^{1}H} NMR** (162.0 MHz,

d_5-pyridine, 298 K): δ (ppm) –132.6 (s). **^{13}C{^{1}H} NMR** (151.0 MHz, d_5-pyridine, 298 K) δ (ppm) 175.6 (*C*OONa), 173.5 (d; $^{1}J_{P–C}$ = 6.5 Hz, H_2PC(O)NH), 54.22 (NH*C*H), 32.9 (NHCH*C*H_2), 32.1 (*C*$H_2CH_2CH_3$), 29.5 (*C*$H_2(CH_2)_2CH_3$), 26.6 ($CHCH_2CH_2$), 23.0 (*C*H_2CH_3), 14.5 (*C*H_3). **IR** (cm^{-1}): *ν*(OH) 3256.

7.2.3.7 Synthesis of 8

8 was prepared following the procedure described in Section 7.2.3.5 from **5** (477 mg, 1.68 mmol) and NH_4BF_4 (194 mg, 1.85 mmol), and isolated as a white powder (184 mg, 42%).

^{1}H NMR (400.2 MHz, d_5-pyridine, 298 K): δ(ppm) 13.78 (broad; 1H; COO*H*), 9.20 (s; 1H; N*H*), 3.81 (d; $^{1}J_{H–P}$ = 207.0 Hz; 2H; P*H*$_2$), 3.47 (m; 2H; NHC*H*$_2$), 2.53 (t; $^{3}J_{H–H}$ = 8.1 Hz; 2H; C*H*$_2$COOH), 1.99–1.16 (16H; C_8*H*$_{16}$). **^{1}H{^{31}P} NMR** (499.9 MHz, d_5-pyridine, 298 K): δ (ppm) 3.81 (s), other resonances remain unchanged. **^{31}P NMR** (162.0 MHz, d_5-pyridine, 298 K) δ (ppm) −133.1 (t; $^{1}J_{H–P}$ = 207.7 Hz; *P*H_2). **^{31}P{^{1}H} NMR** (162.0 MHz, d_5-pyridine, 298 K): δ (ppm) −133.1 (s). **^{13}C{^{1}H} NMR** (151.0 MHz, d_5-pyridine, 298 K) δ (ppm) 176.5 (s; *C*OOH), 172.6 (d; $^{1}J_{C-P}$ = 6.0 Hz; H_2PC(O)NH), 40.7 (NH*C*H_2), 35.19 (*C*H_2COOH), 30.3–29.8 (*C*$_6$$H_{12}$), 27.6 (NHCH$_2$*C*$H_2$), 25.9 (*C*$H_2CH_2$COOH). **IR** ($cm^{-1}$): *ν*(OH) 3325.

7.2.3.8 Thermal decomposition studies

2–**8**, L-proline-phosphinecarboxamide, and *P*-benzyl-*N*-cyclohexyl-phosphinecarboxamide were each dissolved in d_5-pyridine in a J-Young tap NMR tube. A drop of distilled H_2O was added to the solutions containing sodium salts to aid solubilisation (**2**–**5**, and L-proline-phosphinecarboxamide). High temperature decomposition studies of *P*-benzyl-*N*-cyclohexylphosphinecarboxamide (150–180 °C) were carried out in degassed

1-octadecene. The solutions were then heated in a silicone oil bath for the stated time and duration, and the formation of decomposition products monitored by ^{1}H and ^{31}P NMR spectroscopy.

7.2.3.9 Transamidation studies

2, **6**, L-proline-phosphinecarboxamide, and *P*-benzyl-*N*-cyclohexyl-phosphine-carboxamide (1 equivalent, *ca.* 5–10 mg) were each dissolved in d_5-pyridine containing hexadecylamine (10 equivalents) in a J-Young tap NMR tube. The solutions were then heated in a silicone oil bath for the stated time and duration, and monitored by ^{1}H and ^{31}P NMR spectroscopy.

7.2.4 Chapter 5 – Synthesis and characterisation of InP quantum dots prepared from functionalised phosphinecarboxamides

7.2.4.1 Synthesis of In(Zn)P/ZnS QDs from carboxylate-functionalised phosphinecarboxamides 2–4

HDA-capped core/shell In(Zn)P/ZnS QDs were prepared from carboxylate-functionalised phosphinecarboxamides (**2**–**4** and L-proline-phosphinecarboxamide) following an identical protocol to that described in Sections 7.2.2.1 and 7.2.2.2. Precursor masses were calculated for a 2:1 stoichiometry of phosphinecarboxamide to $InCl_3$, based on $InCl_3$ as the limiting reagent (20 mg, 0.09 mmol). In order to compare results with the QDs prepared from **1**, all experimental parameters were kept constant, including: stoichiometry, concentration, volume, stir rate, and heating profile (number of steps, temperature, duration). The QDs were purified by precipitation and resuspension, and size-exclusion chromatography (Sections 7.2.2.8 and 7.2.2.9).

7.2.4.2 Synthesis of In(Zn)P/ZnS QDs by varying ratio of 1 and 4

HDA-capped core/shell In(Zn)P/ZnS QDs were prepared from a mixture of **1** and **4**, following the protocol described in Sections 7.2.2.1 and 7.2.2.2. Precursor masses were calculated for a 2:1 stoichiometry of phosphinecarboxamide to $InCl_3$, based on $InCl_3$ as the limiting reagent (20 mg, 0.09 mmol). The masses of **1** and **4** used at each ratio are shown in Table 7.2.

Table 7.2: Masses of **1** and **4** used at each stoichiometric ratio for the preparation of In(Zn)P/ZnS QDs.

(1) : (4)	**Mass of (1)** (mg)	**Mass of (4)** (mg)
1:0	54.5	0
0.5:0.5	27.3	21.8
0:1	0	43.6

7.2.4.3 Synthesis of In(Zn)P/ZnS QDs from 1 and L-phenylalanine sodium salt

L-Phenylalanine sodium salt (34 mg, 0.181 mmol) was added to a three-neck round bottom flask in an inert atmosphere glovebox along with **1** (54.5 mg, 0.181 mmol), $InCl_3$ (20 mg, 0.09 mmol), zinc stearate (114 mg, 0.181 mmol), and hexadecylamine (393 mg, 1.63 mmol). HDA-capped core/shell In(Zn)P/ZnS QDs were prepared following the protocol described in Sections 7.2.2.1 and 7.2.2.2. The In(Zn)P/ZnS QD product was purified by precipitation and resuspension (Section 7.2.2.8).

7.2.4.4 Synthesis of In(Zn)P/ZnS QDs from 7

7 (39.7 mg, 0.181 mmol), $InCl_3$ (20 mg, 0.09 mmol), zinc stearate (114 mg, 0.181 mmol), and hexadecylamine (393 mg, 1.63 mmol) were added to a three-neck round bottom flask in an inert atmosphere glovebox. The solids were suspended in ODE (10 mL) and warmed to 240 °C (22 min, 10 °C/min) with stirring (500 rpm). The mixture was stirred at this

temperature for 30 minutes before rapidly cooling to room temperature. A ZnS shell was grown on the In(Zn)P QD cores following the procedure described in Section 7.2.2.2. The In(Zn)P/ZnS QD product was purified by precipitation and resuspension (Section 7.2.2.8).

7.2.4.5 Synthesis of In(Zn)P/ZnS QDs from *P*-benzyl-*N*-cyclohexyl-phosphinecarboxamide

HDA-capped core/shell In(Zn)P/ZnS QDs were prepared from *P*-benzyl-*N*-cyclohexyl-phosphinecarboxamide (45.1 mg, 0.181 mmol) following the procedure described in Section 7.2.4.4. The In(Zn)P/ZnS QD product was purified by precipitation and resuspension (Section 7.2.2.8).

7.2.4.6 Synthesis of 9

A THF solution (10 ml) of *P*-benzyl-*N*-cyclohexyl-phosphinecarboxamide (100 mg, 0.401 mmol) was added dropwise to a stirring THF solution (10 mL) of KHMDS (80 mg, 0.401 mmol) at −78 °C. The solution turned pale yellow and was left to stir for four hours while warming to room temperature. Benzyl bromide (48 µL, 0.401 mmol) was added via microsyringe to immediately afford a white precipitate (KBr). The colourless solution was filtered to a Schlenk tube and the volatiles removed *in vacuo* to afford **9** as a white solid (78 mg, 57%).

^{1}H NMR (400.2 MHz, d_8-THF, 298 K) δ (ppm) 7.00–7.25 (m; 10H; Ar), 3.74 (m; 1H; N*H*), 3.19 (d; $^{2}J_{H–H}$ = 13.0 Hz; 2H; PC*H*$_a$H$_b$Ph), 2.83 (d; $^{2}J_{H–H}$ = 13.0; 2H; PCH$_a$*H*$_b$Ph), 1.68–1.50 (m; 4H), 1.29 (m; 2H), 1.16–0.92 (m; 4H). **^{31}P NMR** (162.0 MHz, d_8-THF, 298 K): δ (ppm) −3.69 (s).

7.3 Characterisation techniques

7.3.1 NMR spectroscopy

NMR samples were prepared under an inert atmosphere in J-Young NMR tubes equipped with a gas-tight valve. NMR spectra were acquired on a Bruker Avance III HD nanobay NMR equipped with a 9.4 T magnet (^{1}H 400.2 MHz, ^{31}P 162.0 MHz), a Bruker Avance III HD 600 with BB-F/^{1}H Prodigy nitrogen cryoprobe equipped with a 14.1 T magnet (^{19}F 564.0 MHz), a Bruker Avance III NMR equipped with a 11.75 T magnet (^{1}H 499.9 MHz, ^{31}P 202.4 MHz, ^{13}C 125.7 MHz), and a Bruker NEO 600 with broadband helium cryoprobe equipped with a 14.1 T magnet (^{1}H 600.4 MHz, ^{31}P 243.1 MHz, ^{13}C 151.0 MHz).

^{1}H and ^{13}C spectra are reported relative to $Si(CH_3)_4$ (δ_H 0 ppm, δ_C 0 ppm) and referenced to the most downfield residual solvent resonances where possible (*d*$_8$-THF: δ_H 3.58 ppm, δ_C 67.57 ppm; *d*$_5$-pyridine: δ_H 8.74 ppm, δ_C 150.35 ppm; C_6D_6: δ_H 7.16 ppm). ^{31}P spectra were externally referenced to 85% H_3PO_4 (δ_P 0 ppm). ^{19}F spectra were externally referenced to $CFCl_3$ (δ_F 0 ppm). All spectra were obtained at 25 °C unless otherwise specified. Data analysis was performed using MestReNova software.

7.3.2 UV-Vis and photoluminescence spectroscopy

Absorbance and photoluminescence data of toluene or hexane solutions containing purified QDs were collected on a Horiba Duetta spectrofluorometer at 25 °C. Solutions of air- and moisture-sensitive samples, such as the phenylacetate-capped InP MSCs, were prepared in an inert atmosphere glovebox in a quartz cuvette with a screw cap lid. Photoluminescence emission spectra were collected using an excitation wavelength of 365 nm.

7.3.3 Photoluminescence quantum yield (PLQY)

Photoluminescence quantum yields (PLQY) of purified QD solutions (toluene) were measured relative to a reference dye (coumarin 153 in ethanol, PLQY = 53%).[11] To avoid reabsorption of emitted photons the QD and reference dye solutions were diluted such that their absorbance was below 0.1. The concentration of the solutions was adjusted so that the respective absorbances at 422 nm were approximately equal. An excitation wavelength of 422 nm was used to prevent overlap with the emission regions. Absorbance and emission data were collected and the QY was calculated using Equation 7.1:

$$\Phi_{\mathrm{f},x} = \Phi_{\mathrm{f,st}} \cdot \frac{F_x}{F_{st}} \cdot \frac{f_{st}}{f_x} \cdot \frac{n_x^2(\lambda_{em})}{n_{st}^2(\lambda_{em})} \qquad (7.1)$$

where F is the integral photon flux, f is the absorption factor, n is the refractive index of the solvent, and Φ_f is the quantum yield. The index x denotes the QD sample, and the index *st* denotes the dye standard, coumarin 153.

7.3.4 Mass spectrometry

Matrix-assisted laser desorption-ionization time of flight (MALDI-TOF) mass spectra were collected on a Bruker AutoFlex MALDI TOF/TOF mass spectrometer calibrated using a Bruker protein calibration standard (5–20 kDa mass range). A THF solution containing phenylacetate-capped InP MSCs (0.2–2.0 mg mL^{-1}) was diluted with a stock solution of *trans*-2-[3-(4-*tert*-butylphenyl)-2-methyl-2-propenylidene]malononitrile (DCTB, 10.0 mg mL^{-1} in THF) and drop cast onto a MALDI plate. Data was collected in linear positive ion mode using a laser intensity of 15–30%. The laser pulse frequency

was kept at 2000 Hz and a single spectrum was recorded after 0.5–1 seconds of signal acquisition.

7.3.5 Powder X-ray diffraction

Powder X-ray diffraction (XRD) was performed on a PANalytical X'Pert Pro diffractometer with a copper X-ray source at 1.5418 Å (50 kV, 40 mA). QD core samples were drop cast on a silicon wafer placed on a spinning sample stage, and core/shell samples were drop cast onto a glass XRD slide placed on a flat sample stage. Data were collected in reflection geometry. The instrument was fitted with 0.04 rad. incident and receiving soller slits, an incident beam variable slit illuminating a 10 mm path, a 10 mm beam mask, incident and receiving antiscatter slits (1° and 5° respectively), and an X'Celerator detector preceded by a nickel filter. XRD reference patterns were from the Crystallography Open Database (COD) and the International Centre for Diffraction Data (ICDD): zinc blende InP: ICSD-24517 (ICSD release 2023.1); zinc blende ZnS: ICSD-230704 (ICSD release 2023.1).

7.3.6 Transmission electron microscopy

Transmission electron microscopy was performed on a JEM-ARM200F ACCELARM atomic resolution analytical electron microscope with a cold field emission source (CFEG) Cs probe corrected and a JEM-ARM300F GRAND ARM atomic resolution electron microscope. Toluene or hexane solutions containing QDs (< 0.5 mg mL^{-1}) were drop cast onto holey carbon film supported copper TEM grids (200 mesh), which were dried overnight under static vacuum (1 mbar) before analysis. High-angle annular dark-field images were captured in scanning mode (STEM) using a 200 kV accelerating voltage.

7.3.7 Elemental analyses

CHN elemental microanalyses were carried out by Elemental Microanalysis Ltd., Devon. Samples were submitted in Pyrex ampoules sealed under vacuum. All values are given as percentages.

Inductively coupled plasma mass spectrometry (ICP-MS) analyses were performed on a Perkin Elmer NexION 2000B instrument. Samples were prepared by digestion in a concentrated nitric acid solution (70% HNO_3 in H_2O), followed by dilution to afford a 0.3 M HNO_3 solution. Further dilutions were made using a 2% HNO_3 solution. All blanks, standards, and samples were also spiked with a 1.0 ng g^{-1} iridium solution to normalise for general instrument drift. Data was collected by the collision reaction mode with helium gas, and internal standards were also analysed by dynamic reaction mode with oxygen.

7.3.8 IR Spectroscopy

IR data were recorded on solid samples under ambient conditions. Spectra were recorded on a Bruker Tensor 27 FT-IR spectrometer with PIKE MIRacle ATR in absorbance mode.

7.4 References

1 D. Heift, Z. Benko and H. Grützmacher, *Dalton Trans.*, 2014, **43**, 831–840.

2 A. R. Jupp and J. M. Goicoechea, *J. Am. Chem. Soc.*, 2013, **135**, 19131–19134.

3 A. R. Jupp, G. Trott, É. Payen De La Garanderie, J. D. G. Holl, D. Carmichael and J. M. Goicoechea, *Chem. Eur. J.*, 2015, **21**, 8015–8018.

4 A. Jupp, 2016, Thesis (D.Phil.), University of Oxford.

5 E. N. Faria, A. R. Jupp and J. M. Goicoechea, *Chem. Commun.*, 2017, **53**, 7092–7095.

6 E. N. de Faria, 2020, Thesis (D.Phil.), University of Oxford.

7 D. C. Gary, M. W. Terban, S. J. L. Billinge and B. M. Cossairt, *Chem. Mater.*, 2015, **27**, 1432–1441.

8 A. Burakowski and J. Gliński, *J. Phys. Chem. B*, 2010, **114**, 12157–12161.

9 L. Angelé, S. Dreyfuss, B. Dubertret and N. Mézailles, *Inorg. Chem.*, 2021, **60**, 2271–2278.

10 Y. Shen, M. Y. Gee, R. Tan, P. J. Pellechia and A. B. Greytak, *Chem. Mater.*, 2013, **25**, 2838–2848.

11 C. Würth, M. Grabolle, J. Pauli, M. Spieles and U. Resch-Genger, *Nat. Protoc.*, 2013, **8**, 1535–1550.